AD-A220 471

DTIC
ELECTE
APR 16 1990
B
D

A NUMERICAL STUDY
OF PLASTICITY INDUCED CLOSURE
IN SHORT CRACKS
BY THE FINITE ELEMENT METHOD

DISSERTATION

DEPARTMENT OF THE AIR FORCE

AIR UNIVERSITY

AIR FORCE INSTITUTE OF TECHNOLOGY

Wright-Patterson Air Force Base, Ohio

90 04 13 198

REPORT DOCUMENTATION PAGE

Form Approved
OMB No. 0704-0188

1a. REPORT SECURITY CLASSIFICATION UNCLASSIFIED	1b. RESTRICTIVE MARKINGS

2a. SECURITY CLASSIFICATION AUTHORITY	3. DISTRIBUTION/AVAILABILITY OF REPORT
2b. DECLASSIFICATION/DOWNGRADING SCHEDULE	Approved for public release; distribution unlimited

4. PERFORMING ORGANIZATION REPORT NUMBER(S) AFIT/DS/ENY/90-1	5. MONITORING ORGANIZATION REPORT NUMBER(S)

6a. NAME OF PERFORMING ORGANIZATION School of Engineering	6b. OFFICE SYMBOL (If applicable) AFIT/ENY	7a. NAME OF MONITORING ORGANIZATION

6c. ADDRESS (City, State, and ZIP Code) Air Force Institute of Technology Wright-Patterson AFB, OH 45433	7b. ADDRESS (City, State, and ZIP Code)

8a. NAME OF FUNDING/SPONSORING ORGANIZATION	8b. OFFICE SYMBOL (If applicable)	9. PROCUREMENT INSTRUMENT IDENTIFICATION NUMBER

8c. ADDRESS (City, State, and ZIP Code)	10. SOURCE OF FUNDING NUMBERS			
	PROGRAM ELEMENT NO.	PROJECT NO.	TASK NO.	WORK UNIT ACCESSION NO.

11. TITLE (Include Security Classification)
A Numerical Study of Plasticity Induced Closure in Short Cracks by the Finite Element Method (U)

12. PERSONAL AUTHOR(S)
Eugene J. Bednarz, Major, USAF

13a. TYPE OF REPORT Dissertation	13b. TIME COVERED FROM _____ TO _____	14. DATE OF REPORT (Year, Month, Day) 1990 January	15. PAGE COUNT 169

16. SUPPLEMENTARY NOTATION

17. COSATI CODES			18. SUBJECT TERMS (Continue on reverse if necessary and identify by block number)
FIELD	GROUP	SUB-GROUP	Fatigue, fracture mechanics, crack closure, short cracks, finite element model, elastic-plastic viscoplasticity
20	11		

19. ABSTRACT (Continue on reverse if necessary and identify by block number)

Plasticity induced closure and its effect on the fatigue growth of short cracks were investigated analytically in a high strength titanium allow at room temperature as well as in a nickel base alloy at elevated temperature. The analysis consisted of subjecting a single-edge cracked specimen with an initial crack length of .001 inch to cyclic loading and allowing the crack to propogate. This was accomplished using a two-dimensional finite element code and a theoretical finite element model of a typical test geometry.

Visco II, the two-dimensional plane stress/plane strain finite element code uses constant strain triangular elements and incorporates the Bodner-Partom Viscoplastic Flow Law to handle non-linear material behavior. This is a time-dependent model which can easily be modified to handle time-independent behavior. The relations in this model are integrated through time by an explicit Euler extrapolation scheme. The overall solution technique involves the residual force method. Changing boundary conditions are incorporated through the use of a crack closure algorithm in addition to a crack growth procedure.

20. DISTRIBUTION/AVAILABILITY OF ABSTRACT ☒ UNCLASSIFIED/UNLIMITED ☐ SAME AS RPT. ☐ DTIC USERS	21. ABSTRACT SECURITY CLASSIFICATION UNCLASSIFIED	
22a. NAME OF RESPONSIBLE INDIVIDUAL Eugene J. Bednarz, Major, USAF	22b. TELEPHONE (Include Area Code) (505) 846-3432	22c. OFFICE SYMBOL WL/ARP

DD Form 1473, JUN 86 — Previous editions are obsolete.

Block 19. (Abstract continued):

The numerical simulations involved subjecting specimens of TI-6246 at room temperature (time-independent behavior) to cyclic loads with maximum nominal stress values of approximately 60 and 90 percent material yield strength and load ratios of -1.0 and 0.1 with a frequency of 1.0 Hz. The numerical simulations of specimens consisting of Inconel 718 at $1200^{\circ}F$ (time-dependent behavior) consisted of cyclic loads where the maximum nominal stress was .90 yield strength, the applied load ratio was 0.1, and the cyclic frequencies were .01 and 1.0 Hz.

The formation of a plastic wake and the effects of plasticity induced closure were observed in these specimens. Differences in the behavior of cracks grown by cyclic loading and those exhibiting no fatigue growth were thus investigated. In general, it was found that strain-related characteristics are highly dependent upon previous loading history. Stress-related characteristics, however, were found to be relatively insensitive.
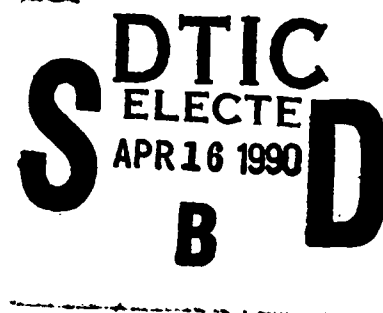
AFIT/DS/ENY/90-1

A NUMERICAL STUDY
OF PLASTICITY INDUCED CLOSURE
IN SHORT CRACKS
BY THE FINITE ELEMENT METHOD
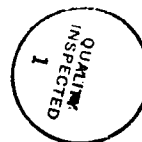
DISSERTATION

AFIT/DS/ENY/90-1   EUGENE J. BEDNARZ
                          MAJOR   USAF

DTIC
ELECTE
S APR 16 1990
B D

A NUMERICAL STUDY OF PLASTICITY INDUCED CLOSURE

IN SHORT CRACKS BY THE FINITE ELEMENT METHOD

Eugene J. Bednarz, B.S., M.B.A., M.S.
Major, USAF

Approved:

Accession For		
NTIS GRA&I	☑	
DTIC TAB	☐	
Unannounced	☐	
Justification		
By		
Distribution/		
Availability Codes		
Dist	Avail and/or Special	
A-1		

Anthony N Palazotto   5 Jan '90
Chairman

(signature)   5 Jan '90

Terry D. Hinnerichs   5 Jan 90

(signature)   3 Jan 90

(signature)   5 Jan 90

Accepted:

(signature)
Dean, School of Engineering

AFIT/DS/ENY/90-1

A NUMERICAL STUDY OF PLASTICITY INDUCED CLOSURE

IN SHORT CRACKS BY THE FINITE ELEMENT METHOD

DISSERTATION

Presented to the Faculty of the School of Engineering

of the Air Force Institute of Technology

Air University

in Partial Fulfillment of the

Requirements for the Degree of

Doctor of Philosophy

by

Eugene J. Bednarz, B.S., M.B.A., M.S.

Major, USAF

Acknowledgements

In completing the course of study and the research required for the degree of Doctor of Philosophy, I wish to extend my sincerest thanks and appreciation to a number of individuals. Several important individuals gave their valuable time and expertise in order that I complete this work. Others gave me their support.

To Dr Anthony Palazotto, my advisor, I want to express my most profound appreciation for his guidance, enormous understanding, and extreme patience over the past several years. Dr Palazotto, you provided me the tools necessary to complete this program. My sincerest thanks and deepest gratitude.

To Dr Ted Nicholas of the Wright Research and Development Center Materials Laboratory, thank you for your guidance and expertise. The cooperation you provided was instrumental in my success.

To my parents, Emil and Helen Bednarz, you have always had the deepest confidence in my abilities. I know that you would have been proud of me for completing this research and earning the Doctor of Philosophy degree. Remember, 'We are all products of our parents'.

Most importantly, I want to dedicate this work to my three beautiful daughters - Tifani, Leah and Ashley. Although you are many miles away, you are always in my heart. Tifani, Leah and Ashley - I love you.

To everyone involved in this research - my most profound thanks.

Table of Contents

List of Figures

List of Tables

List of Symbols

$(\,\dot{}\,)$	Time Rate of Change $(\,\,)$
a, A	Crack Length
a_i, A_i	Initial Crack Length
a_f, A_f	Final Crack Length
A	Hardening Recovery Coefficient (Bodner Model)
[B]	Strain Displacement Matrix
c_1, c_2, c_3	Timestep Algorithm Constants
[D]	Elastic Material Property Matrix
D_0	Limiting Value of Plastic Strain Rate in Shear (Bodner Model)
D_2^P	Second Invariant of the Plastic Strain Rate Tensor (Bodner Model)
dt	Time Increment
E	Elastic Modulus
J_2	Second Invariant of the Deviatoric Stress Tensor (Bodner Model)
[K]	Elastic Stiffness Matrix
K_I	Stress Intensity Factor (Mode I)
K_{eff}	Effective Stress Intensity Factor
l_0, l_1, l_2	Critical Crack Lengths
m	Work Hardening Rate Parameter (Bodner Model)
n	Rate Sensitivity Parameter (Bodner Model)
{P}	External Load Vector
{P_{clo}}	Closure Load Vector
P, P_σ, P_ϵ	Timestep Determination Parameters
{Q}	Internal Load Vector Due to Plasticity

r	Hardening Recovery Exponent (Bodner Model)
R	Load Ratio
S_{ij}	Components of the Deviatoric Stress Tensor
t	Time
{u}	Nodal Displacement Vector
W	Specimen Width
W_p	Plastic Work
Z	Material Hardness (Bodner Model)
Z_0	Initial Value of Hardness (Bodner Model)
Z_1	Maximum Value of Hardness (Bodner Model)
Z_2	Minimum Value of Hardness (Bodner Model)
$\dot{Z}_{rec}$	Rate of Thermal Recovery
$\dot{\epsilon}_{ij}{}^p$	Components of Deviatoric Viscoplastic Strain Rate Tensor
ϵ_e	*Effective Strain*
ϵ_{tol}	Strain Tolerance
λ	Proportionality Constant
σ_{ij}	Components of Stress
σ_o	Nominal Stress
σ_e	Effective Stress
σ_{tol}	Stress Tolerance
σ_{ys}	Material Yield Stress

ABSTRACT

Plasticity induced closure and its effect on the fatigue growth of short cracks were investigated analytically in a high strength titanium alloy at room temperature as well as in a nickel base alloy at elevated temperature. The analysis consisted of subjecting a single-edge cracked specimen with an initial crack length of .001 inch to cyclic loading and allowing the crack to propagate. This was accomplished using a two-dimensional finite element code and a theoretical finite element model of a typical test geometry.

Visco II, the two-dimensional plane stress/plane strain finite element code, uses constant strain triangular elements and incorporates the Bodner-Partom Viscoplastic Flow Law to handle non-linear material behavior. This is a time-dependent material model which can easily be modified to handle time-independent behavior. The relations in this model are integrated through time by an explicit Euler extrapolation scheme. The overall solution technique involves the residual force method. Changing boundary conditions are incorporated through the use of a crack closure algorithm in addition to a crack growth procedure. The numerical simulations involved subjecting specimens of TI-6246 at room temperature (time-independent behavior) to cyclic loads with maximum nominal stress values of approximately 60 and 90 percent of the material yield strength and load ratios of -1.0 and 0.1 with a frequency of 1.0 Hz. The numerical simulations of specimens consisting of Inconel 718 at 1200°F (time-dependent behavior) consisted of cyclic loads where the maximum nominal stress was .90 yield strength, the applied load

ratio was 0.1, and the cyclic frequencies were .01 and 1.0 Hz.

The formation of a plastic wake and the affects of plasticity induced closure were observed in these specimens. Differences in the behavior of cracks grown by cyclic loading and those exhibiting no fatigue growth were thus investigated. In general, it was found that strain-related characteristics are highly dependent upon previous loading history. Stress-related characteristics, however, were found to be relatively insensitive.

I. INTRODUCTION

Background

The United States Air Force places great emphasis on the principles of fracture mechanics in determining both aircraft construction and maintenance requirements [1-3]. The Engine Structural Integrity Program (ENSIP) provides standards for structural performance, design development, and verification requirements for turbine engines. This program assumes the existence of initial material defects which may be found by inspection or believed to exist based on statistical analyses. The subsequent prediction of material life considering these initial defects is an important aspect of this program. This emphasis on fracture mechanics also incorporates the use of Non-Destructive Examinations (NDEs) of aircraft components on a periodic basis to detect flaws, and Linear Elastic Fracture Mechanics (LEFM) principles to predict a remaining useful component life. Using these methods, if a given component is examined and it is determined that no flaws exist which can grow to a critical size prior to the next periodic examination or scheduled maintenance, then it is returned to service. This practice thereby allows for an efficient use of aircraft components which contain fatigue damage through Retirement for Cause (RFC) procedures.

One possible obstacle to these approaches, however, is the existence of short cracks and their apparent non-conservative growth patterns [4-20]. These flaws have exhibited growth at stress levels and sizes when LEFM analyses predict that no crack growth would occur. Furthermore, the growth rates of these short cracks are significantly higher than that predicted using LEFM principles.

The definition of a short crack is dependent on material, geometry, crack shape and other possible factors [15]. It is therefore not the same for all conditions. In general, then, a crack may be considered short when its growth rate cannot be predicted by LEFM principles. These crack sizes, however, are less than the crack detection limits of current NDE and inspection methods [15]. The immediate implication is that current procedures based on LEFM principles remain valid. So long as the flaws identified by these procedures remain in the 'long crack' regime, LEFM analyses will continue to predict fatigue crack growth accurately. As non-destructive examination and inspection methods improve, however, the crack detection limit will likely be reduced to the point where short cracks can be identified, and the non-conservative growth of these flaws will become a major factor in these procedures. An analysis of detectable flaws using linear elastic fracture mechanics principles could then significantly underestimate fatigue crack growth and, in turn, overestimate an aircraft component's serviceable life.

The overall consequence of this situation is two-fold. First, the use of multi-million dollar aircraft and the increasing cost of components indicate a need for a more accurate prediction of serviceable life. A non-conservative estimate based on LEFM principles could possibly result in the loss of an aircraft at a substantial financial penalty for the United States Air Force. Second, and most importantly, is the safety factor involved and possible loss of human life due to the overestimation of component life.

A need therefore exists to understand short crack behavior and the possible factors affecting the fatigue growth of such flaws. Based on

previous studies [21-23], the anomolous behavior of short cracks may be attributed to several factors. One involves microstructural considerations such as grain size and the resulting violation of the continuum assumption of fracture mechanics. A second involves the violation of LEFM assumptions, i.e., the plastic zone sizes of short cracks are relatively large when compared to their lengths.

It has also been suggested that the short crack fatigue response may be due to differences in the crack closure response of long and short cracks [22-34]. Crack closure may be envisioned as the premature contact of crack surfaces during the unloading portion of a fatigue cycle and is manifested in three mechanisms: asperity, oxide, and plasticity induced closure. Both asperity induced and oxide induced closure involve an interference between the crack surfaces which prevent them from completely closing when the applied load is reduced to zero. In the first case, this interference is due to surface roughness or asperities, whereas in the second case, it is due to oxides forming on the crack surfaces. The third form, plasticity induced closure, is concerned with the formation of plastically deformed material at and behind the crack tip. As the cracked material is subjected to positive tensile loading, plastic deformation occurs in the region surrounding the crack tip as the material yield strength is exceeded. During subsequent unloading, the surrounding elastic material compresses the plastic region causing the crack to close prematurely. It is this closure mechanism and its effect on short crack behavior which are the areas on which this research will concentrate.

With a thorough knowledge of the short crack phenomenon, the entire spectrum of crack growth, from initiation to failure, will be better

understood. The present research is thus aimed at developing a better understanding of short crack fatigue growth which, in turn, will lead to more accurate predictions of component serviceable life throughout all ranges of crack sizes. A more efficient and cost effective use of aircraft components and Air Force resources is ultimately envisioned.

Literature Review

A vast amount of research has been accomplished and literature published in the attempt to understand and explain short crack behavior. Recently, a number of works [17,35,36] have been published discussing the phenomenon of crack closure and its relation to short crack growth. Elber [31] found that closure can occur during the tensile portion of the fatigue cycle due to the presence of residual displacements in the crack wake. This plasticity induced closure results from the constraint existing around the wake of the crack tip by material which has been permanently deformed within the plastic zone which then leads to interference between the opposing crack surfaces.

Some efforts attempted to determine when and why LEFM analyses become non-conservative [37-39] based upon observations of short crack growth data. Others used plasticity-adjusted LEFM or elastic-plastic fracture mechanics to describe short crack behavior [5,40,41]. Another group considered analytical models which incorporated the effects of crack closure and residual crack tip plasticity [42-48].

In this first group of studies, Allen and Sinclair [37] observed that the limitations of linear elastic fracture mechanics in describing short crack behavior may be due to an inadequacy in describing the stress field as the crack length approaches zero. A nominal plastic

zone size was calculated assuming that the high near-tip stresses were redistributed over a zone through yielding and that this zone carries the same load that it would have in the absence of yielding. A value of K_{eff}, that stress intensity factor which produces the nominal plastic zone size, was then determined. With this value of K_{eff}, conventional LEFM was used to satisfactorily predict threshold stress intensity factors (those values of K_I below which a crack does not grow) for short flaws in center cracked, infinite width specimens of mild and 4340 steel.

Hobson [38] proposed a crack growth equation for short cracks which could be used in conjunction with LEFM to describe crack growth from crack initiation to failure in an aluminum alloy. Three zones of crack growth behavior were identified: a short crack zone where the crack grows to a length corresponding to the threshold stress intensity, an interactive zone where characteristics of both long and short crack growth are observed, and a long crack zone where LEFM principles apply. 'Best fit' analyses were then accomplished to correlate crack growth data with the proposed equations.

Taylor and Knott [39], in a correlative analysis, identified three similar regions of crack growth behavior based on the concept of a critical length. Below this value, cracks grow faster than that predicted by LEFM. Two values of crack length (l_1 and l_2) which are points of deviation from constant stress and constant stress intensity behavior, respectively, were determined. At crack lengths of l_1 and below, it was found that the initial crack length had no effect on fatigue strength. Below values of l_2, the LEFM or stress intensity approach becomes non-conservative in predicting fatigue failure. For a

5

wide range of materials, a correlation between the values of l_2 and size of the material microstructure was found.

Whereas these first efforts attempted to correlate short crack behavior with LEFM, the second group used plasticity-adjusted LEFM or elastic-plastic fracture mechanics principles to describe the short crack phenomenon.

Trantina and de Lorenzi [41] used a two-dimensional finite element model to analyze short crack behavior in a tension loaded double-edge cracked specimen. Plastic flow was described using the Ramberg-Osgood stress-strain law with a hardening exponent of 10 to evaluate the effects of elastic-plastic material behavior on the stress intensity factor. J-integral calculations by contour integrals and virtual crack extension were then used to determine an effective stress intensity factor value. Cyclic stress versus crack length data showed that deviations from LEFM began when applied stresses were about 0.7 of the material yield strength and the plastic zone size was approximately 0.1 of the crack length.

El Haddad [5,40] modified both elastic and elastic-plastic fracture mechanic solutions to correlate short crack behavior. By introducing an effective length, l_0, into relations for the stress intensity factor and J-integral and by expressing the stress intensity factor in terms of strain and length rather than stress and length, El Haddad was able to adequately correlate short crack behavior. Growth rate data for short flaws in notched specimens of several materials correlated well with long crack data under this approach.

The number of analytical investigations aimed at modeling plasticity induced closure have been limited. In the third group of

studies, Newman [42,44] used an analytical model of crack closure to study crack growth behavior and closure in small cracks. The closure model, based on the Dugdale model [43], was modified to leave plastically deformed material along the crack surface. A center cracked, tension specimen and symmetric cracks growing from circular holes were then analyzed. Crack opening stresses calculated using this model were then used to determine effective plastic zone corrected stress intensity factors and, in turn, applicable crack growth rates. Newman [44] used constant strain triangles in a two-dimensional finite element analysis which accounted for non-linear material behavior as well as changing boundary conditions under cyclic loading. To satisfy these boundary conditions, springs were attached to each boundary node, one to satisfy conditions in the x, or horizontal, direction and one in the y, or vertical, direction. For free nodes, the spring stiffness was set equal to zero, whereas for fixed or closed nodes, it was set to some large value. The particular spring stiffness, depending on the appropriate boundary condition, was then used to modify the elastic stiffness matrix as required. Assuming elastic-perfectly plastic material under constant amplitude or two-level block loading, crack growth rates were found consistent with experimental data.

Other finite element analyses have been used to analyze crack closure but have been complicated and computer intensive. Ogura, Ohji, and Ohkibu [45] and Nakagaki and Atluri [46] utilized higher order finite element models to study crack closure in various specimens.

Based upon the conclusions found in the preceeding literature, as well as those in other works [47-62], several items are indicated. First, the study of short cracks requires an elastic-plastic analysis.

LEFM analyses do not accurately predict short crack behavior. Second, numerous analytical models have been developed which can satisfactorily predict short crack behavior or closure in fatigued specimens. And third, numerical models, primarily finite elements, have been employed to either predict short crack behavior or crack closure effects. None, however, have been found which combine the two phenomena.

As a result, this research concentrates on a finite element analysis of plasticity induced closure and its effect on short crack fatigue growth. Initially short cracks growing from the edge of a finite-width specimen under constant amplitude fatigue cycling at various stress levels and stress ratios are investigated. Crack closure is traced using a two-dimensional elastic-plastic finite element analysis. Results are interpreted in terms of the influence of plasticity induced closure on the growth of small fatigue cracks. Observations as to the sensitivity of closure to the measurement location along the crack length are also discussed.

Approach

As previously stated, this research concentrates on developing a better understanding of plasticity induced closure and its effect on short crack behavior in a cyclically loaded specimen. The subject specimen studied here is composed of Titanium 6Al-2Sn-4Zr-6Mo (TI-6246) at room temperature and considered to be a homogeneous, isotropic material that deforms and/or strains under cyclic loading. Starting with an initial single-edge crack (a_i = .001 inch), the material is subjected to various load ratios and amplitudes in order to investigate the short crack phenomenon. A similar specimen, composed of Inconel 718

8

at 1200°F is also studied to incorporate viscoplastic effects. Two separate load frequencies are applied to isolate this phenomenon.

Visco II, an in-house computer program, was modified to incorporate the effects of crack closure. This finite element code employs constant strain triangular elements. It has the ability to apply saw-tooth shaped cyclic loads and to simulate crack growth through the release of finite element nodes. In addition, the Bodner-Partom constitutive relations [63-65] are employed to model material behavior during load increments. This elastic-viscoplastic model is primarily time-dependent, but can easily be made rate independent making it a versatile tool in this research effort. An explicit Euler extrapolation scheme is used to integrate these relations with respect to time and is further incorporated in Visco II using the residual force technique.

A finite element mesh was developed to model a single-edge cracked specimen (a_i = .001 inch, W = .10 inch) and was investigated to compare the effects of various cyclic loading profiles. For the TI-6246 specimen, external load was input as a saw-tooth stress-time pattern of constant amplitude with load ratios (ratio of minimum to maximum load) of -1.0 and 0.1. Maximum load amplitudes were applied to obtain nominal stresses of approximately 60 and 90 percent of the material yield strength. These resulted in initial stress intensity factors (K_I) of 6.69 and 10.04 KSI-IN$^{1/2}$ respectively. Cyclic load frequency in these cases was maintained at 1.0 Hz. In the study of Inconel 718, a load ratio of 0.1 and a nominal maximum stress value of .90 yield strength were maintained. The initial stress intensity factor for this specimen was 7.354 KSI-IN$^{1/2}$. However, the cyclic frequency took on values of 1.0 and .01 Hz.

II. Theory

In this research effort, a single-edge cracked specimen (a_i = .001 inch) is subjected to cyclic loading in order to study the effects of crack closure and the formation of a plastic wake as a short crack propagates. Using a finite element analysis, specimens composed of materials displaying entirely different characteristics (TI-6246 at room temperature and Inconel 718 at $1200°F$) are investigated. Inconel 718 exhibits non-linear, viscoplastic (time-dependent) material behavior at high temperatures, whereas TI-6246 at room temperature is considered non-linear, elastic-plastic (time-independent). Due to the variability of the materials involved, a viscoplastic flow law is required which can easily be modified to account for time independent relations. In addition, a finite element code is needed which incorporates cyclic loading, fatigue crack growth, and crack closure. This section discusses the applicable relations chosen to model plastic flow as well as finite element considerations required for such an analysis.

Bodner-Partom Viscoplastic Flow Law

The Bodner-Partom Viscoplastic Flow Law (Bodner model) satisfies the above requirements for both time-dependent and time-independent behavior and has been used successfully in the past to study viscoplasticity in a variety of analyses [66-71] including cyclically loaded specimens. This law, based on dislocation dynamics, suggests a continuous flow relation between stress and viscoplastic strain commencing at the onset of loading. As used here, this law assumes that the materials involved are isotropic and exhibit no kinematic hardening. The following discussion is intended to provide a basic understanding of

the Bodner model and present key items pertinent to this research. More detailed information may be obtained in works directly related to the model [63-65].

Formulation of the constituitive equations begins by recognizing that for small strains, total strain can be separated into elastic, as well as viscoplastic, strains such that

$$\epsilon_{ij} = \epsilon_{ij}{}^e + \epsilon_{ij}{}^p \tag{2.1}$$

Taking the time derivative of this equation, the total strain rate is then expressed as

$$\dot{\epsilon}_{ij} = \dot{\epsilon}_{ij}{}^e + \dot{\epsilon}_{ij}{}^p \tag{2.2}$$

where the elastic strain rate, $\dot{\epsilon}_{ij}{}^e$, is related to the stress rate through the time derivative of Hooke's law.

The determination of the viscoplastic strain rate, however, begins by squaring the rate form of the Prandtl-Reuss plastic flow equation,

$$\dot{\epsilon}_{ij}{}^p = \lambda S_{ij} \tag{2.3}$$

to obtain

$$\dot{\epsilon}_{ij}{}^p \dot{\epsilon}_{ij}{}^p = \lambda^2 S_{ij} S_{ij} \tag{2.4}$$

where $\dot{\epsilon}_{ij}{}^p$ are components of the deviatoric viscoplastic strain rate tensor, S_{ij} are components of the deviatoric stress tensor, and λ is a proportionality constant. Then by substituting the following relations,

$$J_2 = (S_{ij} S_{ij})/2 \tag{2.5}$$

11

and $D_2^P = (\dot{\epsilon}_{ij}^P \dot{\epsilon}_{ij}^P)/2$ $\qquad$ (2.6)

one obtains

$$D_2^P = \lambda^2 J_2 \qquad (2.7)$$

Here, D_2^P is defined as the second invariant of the plastic strain rate and J_2 is the second invariant of the deviatoric stress tensor.

Based on experimental work, Bodner and Partom expressed D_2^P as

$$D_2^P = D_0^2 \exp[-(Z^2/3J_2)^n((n+1)/n)] \qquad (2.8)$$

In this relation, D_0 is the limiting value of the plastic strain rate in shear, Z is a measure of material hardness, and n a rate sensitivity parameter. Further, the evolution equation for Z is assumed to consist of a hardening term due to plastic work, W_p, and can be described as

$$\dot{Z} = (\partial Z/\partial W_p)(dW_p/dt) \qquad (2.9)$$

Here, $(\partial Z/\partial W_p)$ is assumed to be of the form

$$(\partial Z/\partial W_p) = m(Z_1 - Z) \qquad (2.10)$$

where m is a parameter controlling the rate of material work hardening and Z_1 is the maximum value of Z attainable. W_p is the relative amount of plastic work done from some initial state and is expressed in the form

$$W_p = \int S_{ij} \dot{\epsilon}_{ij}^P dt = 2(D_2^P J_2)^{1/2} \qquad (2.11)$$

Most materials exhibit some thermal recovery of hardening or relaxation of accumulated plastic work at high temperatures. To model

12

this particular behavior, the change in hardness can be modified by adding the term

$$\dot{Z}_{rec} = -A((Z-Z_2)/Z_1)^r Z_1 \qquad (2.12)$$

In this relation, Z_2 is the value of Z in a completely non-work hardened condition indicating the minimum value of material hardness, whereas A and r are the hardening recovery coefficient and exponent respectively. Then, by integrating the resulting equation for the change in hardness using equation (2.10), material hardness takes on the form

$$Z = Z_1 + (Z_0 - Z_1)\exp(-mW_p/Z_0) - A((Z-Z_2)/Z_1)^r Z_1 \qquad (2.13)$$

where Z_0 is defined as the initial value of hardness prior to any plastic deformation.

For strictly time independent behavior, the thermal recovery term in equation (2.13) is negligible and can therefore be disregarded in the evaluation of material hardness. This can be accomplished by setting the values of A, r, and Z_2 to zero in the $\dot{Z}_{rec}$ term without affecting the overall solution of the Bodner equations.

The specific procedure used to solve the Bodner equations is an Euler extrapolation scheme which integrates the equations with respect to time. This is accomplished for each element in the finite element code as follows:

$$Z^i = Z_1 + (Z_0 - Z_1)\exp[-mW_p^{i-1}/Z_0] \qquad (2.14)$$

$$(D_2^P)^i = D_0^2 \exp[-((Z^i)^2/3J_2^{i-1})^n((n+1)/n)] \qquad (2.15)$$

$$(\dot{\epsilon}_{ij}^P)^i = [(D_2^P)^i/J_2^{i-1}]^{1/2}(S_{ij})^{i-1} \qquad (2.16)$$

13

$$\{d\epsilon_{ij}^{P}\}^{i} = \{\dot{\epsilon}_{ij}^{P}\}^{i} dt^{i} \tag{2.17}$$

$$\dot{Z}_{rec}^{i} = -A((Z^{i}-Z_{2})/Z_{1})^{r}Z_{1} \tag{2.18}$$

$$W_{p}^{i} = W_{p}^{i-1} + (S_{ij})^{i-1}\{d\epsilon_{ij}^{P}\}^{i} + \dot{Z}_{rec}^{i} dt^{i}/[m(Z_{1}-Z^{i})] \tag{2.19}$$

where the superscript i refers to the current timestep.

Material Constants

The constants used in the Bodner model are both material and temperature dependent and must therefore be evaluated for each material at the specific temperature of interest. The Bodner constants for Inconel 718 at $1200^{\circ}F$ have previously been determined by Beaman [72] and are presented in Table 2.1. These values were subsequently verified by Mercer [73] and have been shown to model the particular material behavior satisfactorily.

Material constants for TI-6246 at room temperature have not been previously evaluated for use with the Bodner model and must therefore be determined from available experimental data. Following the procedures developed by Beaman [72] and Stouffer [74] in conjunction with experimental stress-strain data provided by the WRDC Materials Laboratory, values for these Bodner constants were determined and are listed in Table 2.2. An overview of the steps involved in this approach is included in Appendix A. Note that the parameters affecting thermal recovery (A, r, and Z_2) have been given the value of zero. TI-6246 at room temperature exhibits time independent behavior and the thermal recovery term in equation (2.13) is negligible.

The values of the Bodner constants determined for TI-6246 at room temperature were subsequently verified by analytically loading a

14

Table 2.1

Bodner Coefficients for Inconel 718 at 1200°F

Parameter	Description	Value
E	Elastic Modulus	23.568×10^3 KSI $(16.250 \times 10^4$ MPa$)$
n	Strain Rate Exponent	3.0
D_0	Limiting Value of Strain Rate	10^6 sec^{-1}
Z_0	Limiting Value of Hardness	235.3 KSI (1622 MPa)
Z_1	Maximum Value of Hardness	260.3 KSI (1795 MPa)
Z_2	Minimum Value of Hardness	104.1 KSI (718 MPa)
m	Hardening Rate Exponent	2.875 KSI^{-1} $(.417$ MPa$^{-1})$
A	Hardening Recovery Coefficient	1.5×10^{-3} sec^{-1}
r	Hardening Recovery Exponent	7.00

(1 Kbar = 100 MPa = 14.504 KSI)

Table 2.2

Bodner Coefficients for TI-6246 (Room Temperature)

Parameter	Description	Value
E	Elastic Modulus	16.275×10^3 KSI $(11.221 \times 10^4$ MPa$)$
n	Strain Rate Exponent	2.0
D_0	Limiting Value of Strain Rate	10^4 sec^{-1}
Z_0	Limiting Value of Hardness	351.72 KSI (2425.0 MPa)
Z_1	Maximum Value of Hardness	396.87 KSI (2736.3 MPa)
Z_2	Minimum Value of Hardness	0.0
m	Hardening Rate Exponent	.069 KSI^{-1} $(.01$ MPa$^{-1})$
A	Hardening Recovery Coefficient	0.0
r	Hardening Recovery Exponent	0.0

(1 Kbar - 100 MPa - 14.504 KSI)

16

uniaxial, two-element finite element model under a similar stress range and approximate strain rate of .005 in/min. Applied loads ranged from 0 to 176 KSI to coincide with the experimental data. The Visco code, however, is not governed by strain rate but instead uses a load versus time input format. The strain rate of .005 in/min was approximated by varying the rate at which the load was applied until a strain rate approximating .005 in/min was obtained. The experimental stress-strain data and the results from the two-element finite element model are presented in Figure 2.1. Since Visco is load or stress driven, strain rates cannot be maintained during cyclic loading. For this reason, further analysis of TI-6246 material constants could not be performed. The results of the two-element finite element model, therefore, were deemed sufficient to verify the Bodner constants for this research.

Finite Element Considerations

Visco II, the computer program used in this research, is a two-dimensional, plane stress/strain, finite element code which uses constant strain triangular elements. The overall solution technique is the residual force method and key features incorporated within this program are a Gauss-Siedel iterative procedure coupled with a crack closure algorithm to solve for equilibrium, the Euler extrapolation scheme previously discussed to model elastic-viscoplastic material behavior, a data storage/restart capability to handle extensive cyclic loading, and a procedure to simulate crack growth. It should be pointed out that Visco II is an extension of the Visco program developed by Hinnerichs [71,75], modified to meet the needs of this particular research effort.
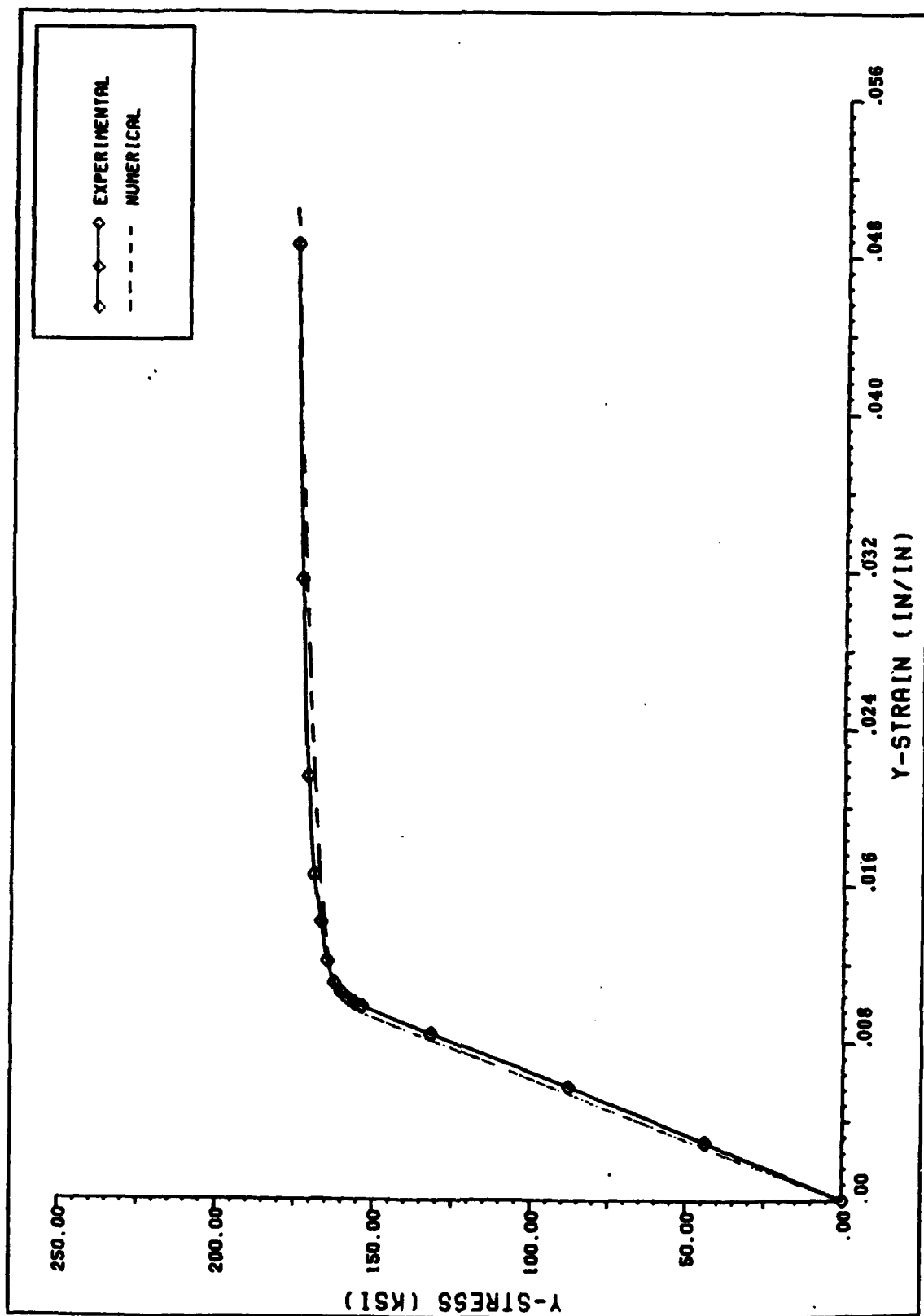
17

Figure 2.1

Stress-Strain Data -   TI-6246

18

Residual Force Method. The basic concept in the residual force method is that the elastic stiffness matrix remains constant throughout an analysis and plasticity effects are incorporated into the solution through the inclusion of a plastic load vector. The resulting equilibrium equations then take on the form:

$$[K]\{u\}^i = \{P\}^i + \{Q\}^i \tag{2.20}$$

where $[K]$ is the constant elastic stiffness matrix, $\{u\}^i$ is the nodal displacement vector, $\{P\}^i$ is a vector of externally applied loads, and $\{Q\}^i$ is the vector of internal loads developed due to the accumulation of plastic deformation. The superscript i in this relation refers to the current timestep. The algorithm employed in Visco II, then, takes on the following form:

1. Compute the current time,

$$t^i = t^{i-1} + dt^i \tag{2.21}$$

2. Calculate the plastic strain rate using the Bodner model/Euler extrapolation scheme (see Eq 2.16),

$$\{\dot{\epsilon}_{ij}^{\,P}\}^i = [(D_2^{\,P})^i/J_2^{\,i-1}]^{1/2}\{S_{ij}\}^{i-1} \tag{2.22}$$

3. Compute the plastic strain increments,

$$\{d\epsilon_{ij}^{\,P}\}^i = \{\dot{\epsilon}_{ij}^{\,P}\}^i dt^i \tag{2.23}$$

4. Calculate the plastic load vector (elementwise),

$$\{Q\}^i = \int [B]^T [D] \{\epsilon_{ij}^{\,P}\}^i dvol \tag{2.24}$$

19

where

$$(\epsilon_{ij}{}^{P})^{i} = (\epsilon_{ij}{}^{P})^{i-1} + (d\epsilon_{ij}{}^{P})^{i} \qquad (2.25)$$

5. Compute the current external loads,

$$(P)^{i} = (P)^{i-1} + (\dot{P})^{i}dt^{i} \qquad (2.26)$$

6. Calculate nodal displacements using the Gauss-Siedel technique,

$$(u)^{i} = [K]^{-1}\sum_{j=1}^{N}((P)^{i} + (Q)^{i}) \qquad (2.27)$$

7. If closure has occurred, determine the resultant nodal forces and modify the external load vector accordingly,

$$(P)^{i} = (P)^{i} + (P_{clo})^{i} \qquad (2.28)$$

and re-solve for nodal displacements

8. Calculate total strains for each individual element,

$$(\epsilon_{ij})^{i} = [B](u)^{i} \qquad (2.29)$$

9. Compute resultant stresses,

$$(\sigma_{ij})^{i} = [D]((\epsilon_{ij})^{i} - (\epsilon_{ij}{}^{P})^{i}) \qquad (2.30)$$

10. Modify current timestep size and continue procedure until analysis is completed.

20

With this procedure, time is incremented directly and the resultant displacements, stresses and strains are subsequently evaluated. The particular timestep, dt, is determined subject to stress and strain tolerances and an algorithm relating these constraints to changes in the current timestep size [75-77]. This approach thereby maximizes the allowable timestep and thus minimizes computational requirements. The stress and strain parameters, P_σ and P_ϵ, used for developing timestep sizes, are functions of effective stress and effective strain and are defined as follows [75-77]:

$$P_\sigma = (\sigma_e^{\ i} - \sigma_e^{\ i-1})/(\sigma_e^{\ i-1} \sigma_{tol}) \tag{2.31}$$

$$P_\epsilon = (d\epsilon_e^{\ P})^i / \epsilon_{total}^{\ i} \epsilon_{tol} \tag{2.32}$$

P_σ and P_ϵ are evaluated for each element during each timestep and the parameter P is set equal to the largest value. The timestep is then determined according to a generalized set of relationships:

$$dt^i = c_1 dt^{i-1} \quad \text{if} \quad c_2 \le P \le c_3 \tag{2.33}$$

where c_1 is a proportionality constant, and the values of c_2 and c_3 form intervals for the value of P. By controlling the size of subsequent timesteps in this manner, the levels of accuracy inherent in the equilibrium and compatability relations are also determined. The evaluation of these constants is discussed in a following section related to finite element modeling.

Gauss-Siedel Technique. The equilibrium equations are solved in Visco II using a Gauss-Siedel iterative technique [75]. Nodal

21

displacements are determined individually and assumed to be a function only of those nodes directly connected to the one in question. At the completion of each iteration, the change in nodal displacements is used to calculate a tolerance limit which is then used to check for convergence. This is dependent upon the initialization of nodal displacements which is normally set to zero. However, displacements from previous solutions, representing a more accurate 'guess', will speed the convergence of this technique. Additionally, an overrelaxation factor is employed in order to speed the process [71].

If negative displacements occur along the crack face indicating crack closure, Visco II performs an iterative closure routine. This procedure first resets applicable nodal displacements to zero (as negative values are physically impossible), and then calculates a resultant nodal force required to insure a zero displacement using the following relation:

$$\{P_{clo}\}^i = \sum_{N=1}^{3} \int [B]^T \{\sigma_{ij}\} dvol \tag{2.34}$$

$\{P_{clo}\}^i$ is the vector of external forces at the closed nodes and is a function of stresses in the three adjacent elements. These forces are then added to the external load vector and the solution for equilibrium is repeated. This procedure thus incorporates the changing boundary conditions involved in crack closure without modifying the stiffness matrix as is the case in other closure routines [42,47,50]. Since nodal displacements will change with the addition of these closure loads, this crack closure algorithm is repeated after the equilibrium solution until the difference in closure loads on subsequent iterations is less than a specified tolerance value. This procedure can be visualized in the

22

i) **NO CLOSURE:**
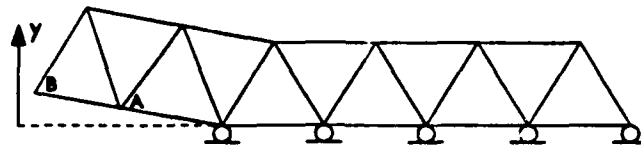
$\{u\}' > 0$

ii) **NEGATIVE DISPLACEMENTS:**
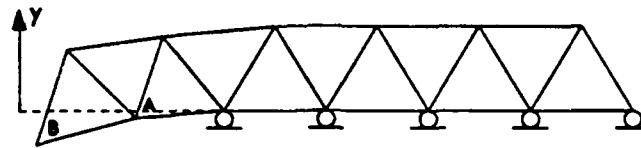
$\begin{Bmatrix} u_A \\ u_B \end{Bmatrix} = \begin{Bmatrix} (-) \\ (-) \end{Bmatrix}$

iii) **RESET DISPLACEMENTS TO ZERO:**
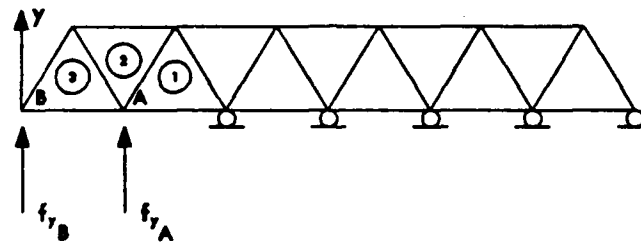
$\begin{Bmatrix} u_A \\ u_B \end{Bmatrix} = \begin{Bmatrix} 0 \\ 0 \end{Bmatrix}$

iv) **DETERMINE CLOSURE LOADS:**

$\{\varepsilon_{ij}\}' = [B]\{u\}'$

$\{\sigma_{ij}\}' = [D]\{\{\varepsilon_{ij}\}' - \{\varepsilon_{ij}{}^P\}'\}$

$\{P_{cls}\}' = \Sigma \int [B]\{\sigma_{ij}\}' dvol$

v) **RE-SOLVE EQUILIBRIUM:**

$\{u\}' = [K]^{-1}\{\{P\}' + \{P_{cls}\}' + \{Q\}'\}$

Figure 2.2

Finite Element Crack Closure

23

Figure 2.3

Equilibrium/Closure Solution Algorithm

diagram in Figure 2.2 and flowchart in Figure 2.3. Because the procedure is only performed when negative displacements occur at nodes along the crack surface, subsequent crack opening is easily handled. Crack openin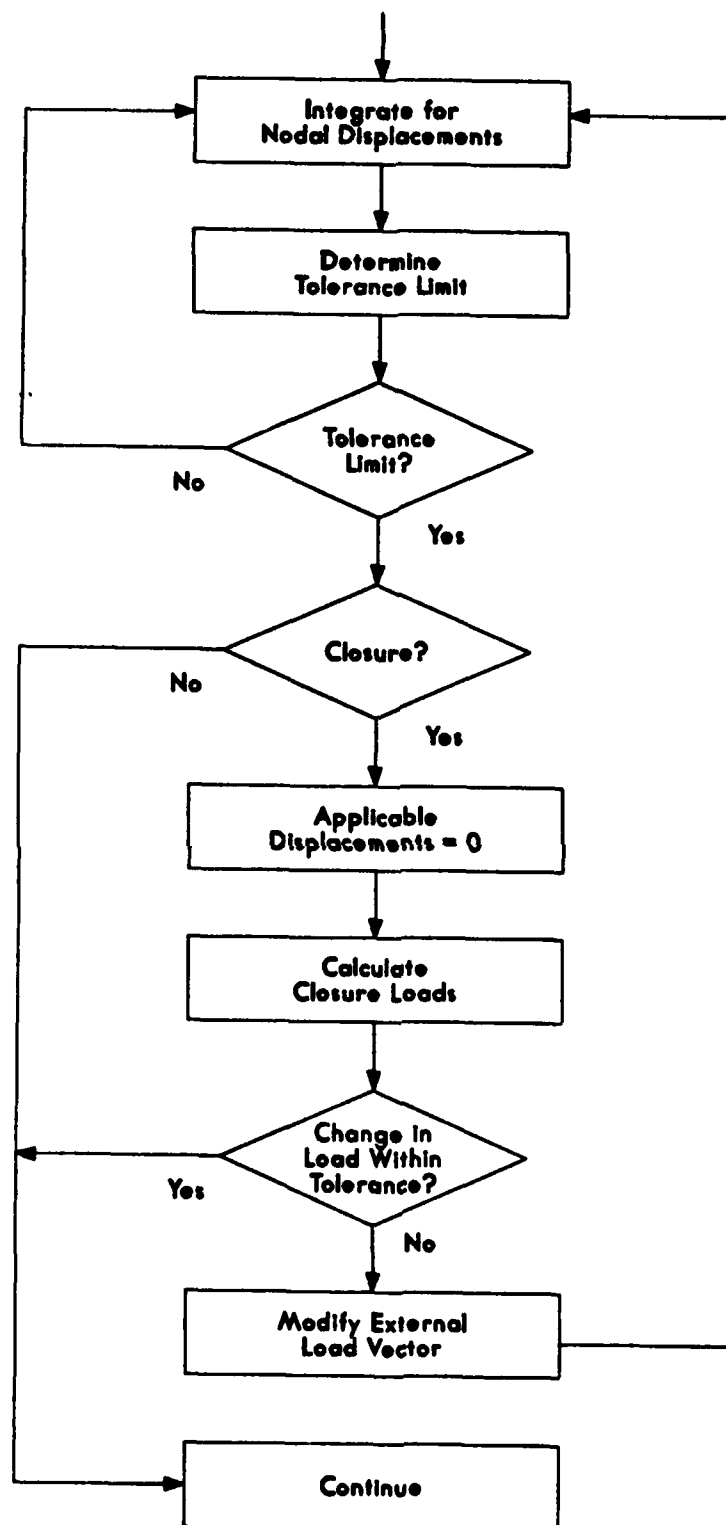g is indicated by a lack of negative displacements and the crack closure algorithm is, thus, not performed. Additionally, by compensating for crack closure through the inclusion of an internal load vector, the global stiffness matrix remains constant and does not require any modifications during the above routine.

Crack Growth. In Visco II, crack growth is simulated through the use of a node release algorithm [71,75]. When a node is to be released, the forces at that node required to maintain a zero displacement are evaluated using equation (2.34). This is equivalent to an oppositely directed force and is then applied to the node and reduced linearly over time (Figure 2.4). The boundary condition that had previously been in effect is conveniently handled in the Gauss-Siedel technique previously discussed. The stiffness matrix is initially developed on an individual nodal basis in which only adjacent nodes contribute to one's displacement. When a node is fixed, its equilibrium equation is skipped over in the iterative solution procedure. As that node is released, however, its equilibrium equation is then included. By handling crack growth and changing boundary conditions in this manner, refactoring of the stiffness matrix is not required.

Data Storage/Restart Capability. Visco II further includes a routine which provides for the ability to store data at the completion of the finite element analysis and subsequent ability to restart the program using this data as initial conditions. In this manner, it is

25

possible to continue an extensive analysis indefinitely without being limited by computer restraints. Additionally, this capability provides a method to perform a finite element analysis at any point in a fatigue crack growth study, the only requirement being that initial conditions are known or available. This program modification is outlined in Appendix B.
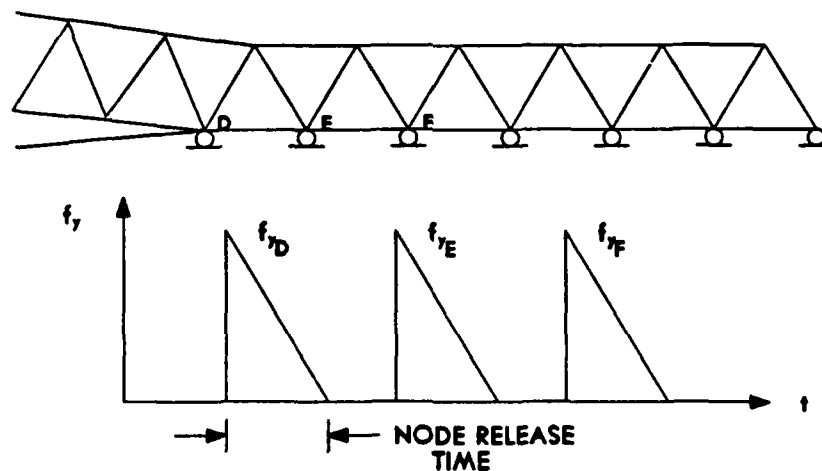

Figure 2.4

Node Release Method (a) Finite Element Cracktip
(b) Node Unload Method

26

III. Finite Element Model

In the previous chapter discussing theory, several programming considerations were presented which could be used to solve a generalized elastic-viscoplastic flow problem using the finite element method. These were incorporated into the finite element code, Visco II, and included the particular viscoplastic flow law (Bodner model) and associated material parameters, solution procedures such as the residual force method and Gauss-Siedel iterative technique, as well as several other considerations relevant to this research. In the sections to follow, however, more specific information is presented which is a function of this particular research effort. Included here are the investigation and selection of suitable programming variables, validation of program subroutines, and the determination of an appropriate finite element mesh. The information determined in these areas was based on a series of preliminary studies conducted as an integral part of this research effort and are included in this chapter for completeness.

Investigation of Programming Variables.

Within the residual force algorithm employed in Visco II, the accuracy of the equilibrium and compatibility relations is controlled through the use of the stress and strain tolerances coupled with a set of relations to modify the current timestep size as discussed in chapter 2. These relations are of the form:

$$dt^i = c_1 dt^i \qquad \text{if} \quad c_2 \leq P \leq c_3 \qquad (2.33)$$

where P is the greatest value of P_σ and P_ϵ determined by equations

(2.31) and (2.32), c_1 is a proportionality constant, and c_2 and c_3 form intervals around P. In order to determine the optimal values of these parameters, a one-dimensional case was investigated. A two-element model was subjected to a uniaxial, fully reversed, cyclic load in which the values of c_1, c_2, and c_3 were varied to study their effects on accuracy and computer time requirements, the results of which are shown in Figures 3.1 and 3.2. In these figures, t(cps) refers to the computer time required to complete one entire load cycle, whereas r is the amount of drift or ratcheting exhibited in the stress-strain curve over the same period. The values of 'base r' and 'base t' are those initially obtained using the relations for timestep change set forth by Hinnerichs [71,75] and used in subsequent studies [67-70]. Based upon these results, the complete set of relations take on the following form:

$$dt^i = .9dt^i \qquad \text{if} \qquad 1.0 \leq P \tag{3.1}$$

$$dt^i = 1.0dt^i \qquad \text{if} \qquad .85 \leq P < 1.0 \tag{3.2}$$

$$dt^i = 1.1dt^i \qquad \text{if} \qquad .70 \leq P < .85 \tag{3.3}$$

$$dt^i = 1.2dt^i \qquad \text{if} \qquad P < .70 \tag{3.4}$$

The equilibrium equations are solved for in the residual force method employed here using the Gauss-Siedel iterative technique. These equations, in matrix form,

$$[K]\{u\}^i = \{P\}^i + \{Q\}^i \tag{2.20}$$

are solved for the nodal displacements during each timestep. The number of iterations required to solve these equations is controlled by a
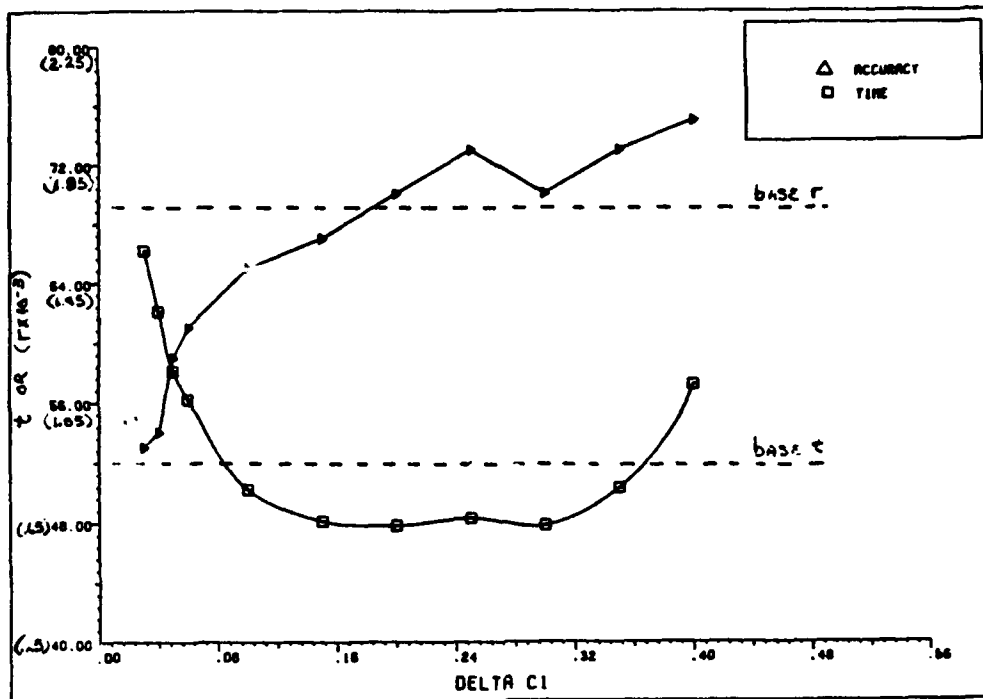
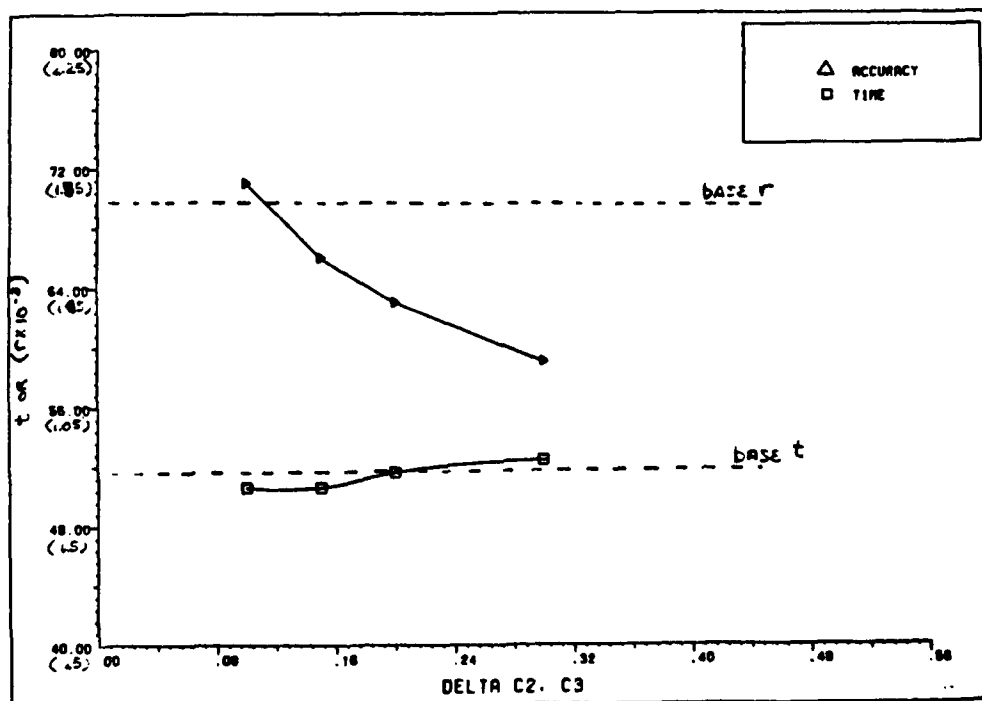Figure 3.1

Effect of Varying c_1 in Timestep Algorithm

Figure 3.2

Effect of Varying of c_2 and c_3 in Timestep Algorithm

'force unbalance' term which represents the numerical error in the equilibrium solution. At the completion of each iteration, the force unbalance is determined by summing the forces resulting from the incremental displacements calculated during that iteration. This procedure continues until this value is less than some tolerance value or the number of iterations exceeds a predetermined number [71].

The center cracked panel employed by Henkel [68] was subjected to a fully reversed cyclic load with a stress intensity factor of 35 KSI-$IN^{1/2}$ to investigate this concept. In this study, values of the force unbalance tolerance, maximum number of iterations allowed, and the overrelaxation factor were all varied. In each instance, the value of the force unbalance diminished at an exponential rate until additional iterations did not affect its final value. Further, changes in the force unbalance tolerance and overrelaxation factor did not substantially improve this value. This study showed that although the accuracy of the equilibrium solution could not be significantly improved by varying the tolerance values within the Gauss-Siedel technique, the amount of computer time required could be reduced by limiting the number of iterations allowed.

The stress and strain tolerances employed in the residual force method were further investigated by subjecting a single-edge cracked specimen to cyclic loading at a nominal stress value of approximately 60 percent material yield strength and a load ratio of 0.1. The stress and strain tolerances, σ_{tol} and ϵ_{tol} respectively, were found to optimize the tradeoff between accuracy and computational requirements at a value of .10. That is, the amount of change in stress or strain in any

element is not allowed to exceed ten percent during a single time increment. If this amount of change is exceeded, then the current timestep is reduced and the solution repeated. At tolerances less than ten percent, these values were frequently exceeded which resulted in significantly higher computational requirements. Under these circumstances and the additional requirement to analyze the specimens under a nominal stress of .90 yield strength, these particular tolerance values were deemed appropriate for the analysis conducted.

Results obtained from these analyses agreed with those obtained by Henkel [68] and were subsequently verified by Mercer [73] in an independent study using an implicit solution technique. Representative strain fields under similar conditions may be found in works by Wilson [70] and Henkel [68].

Crack Closure

Within the Gauss-Siedel technique employed in Visco II is the crack closure algorithm previously discussed in chapter 2. When closure occurs, a resultant internal force using

$$\{P_{clo}\}^i = \sum_{N=1}^{3} \int [B]^T \{\sigma_{ij}\} dvol \tag{2.34}$$

is determined and applied to the closed node by modifying the external load vector:

$$\{P\}^i = \{P\}^i + \{P_{clo}\}^i \tag{2.28}$$

In this manner, the global stiffness matrix does not require modification and thus maintains the overall solution technique employed by the residual force method.

31

This closure algorithm was applied to the center cracked panel investigated by Henkel [68] using a stress intensity factor of 45 KSI-IN$^{1/2}$ and load ratio of -1.0. In Henkel's work, where the displacements at closed nodes were simply reset to zero, residual force unbalances on the order of 2000-3000 were evident at the point of full negative load. Through the use of this closure algorithm, the magnitudes of the force unbalance were reduced to less than 100 at the same load points. By thus reducing the residual force unbalance in the Gauss-Siedel equilibrium solution, the overall accuracy was improved. Further verification of this routine was accomplished by analyzing a center cracked panel with a stress intensity factor of 35 KSI-IN$^{1/2}$ under fully reversed loading. The results of this analysis were compared to those obtained by Mercer [73] for the identical specimen using a completely different finite element code. Stresses obtained from these two programs for elements ahead of the crack tip are displayed in Figure 3.3

Crack Growth

Crack growth is simulated using the node release method previously discussed and has been successfully used in several past finite element analyses [69,71,75]. Node release (crack growth) is assumed to occur at the point of maximum load application ,i.e., at the one-quarter cycle point for R - -1.0 and at the one-half cycle point for R - 0.1. This allowed the forces to be reduced at the released node as the total external loads were also being reduced, the result being that stresses near the new crack tip did not increase significantly during the node release process. This condition may have resulted had node release
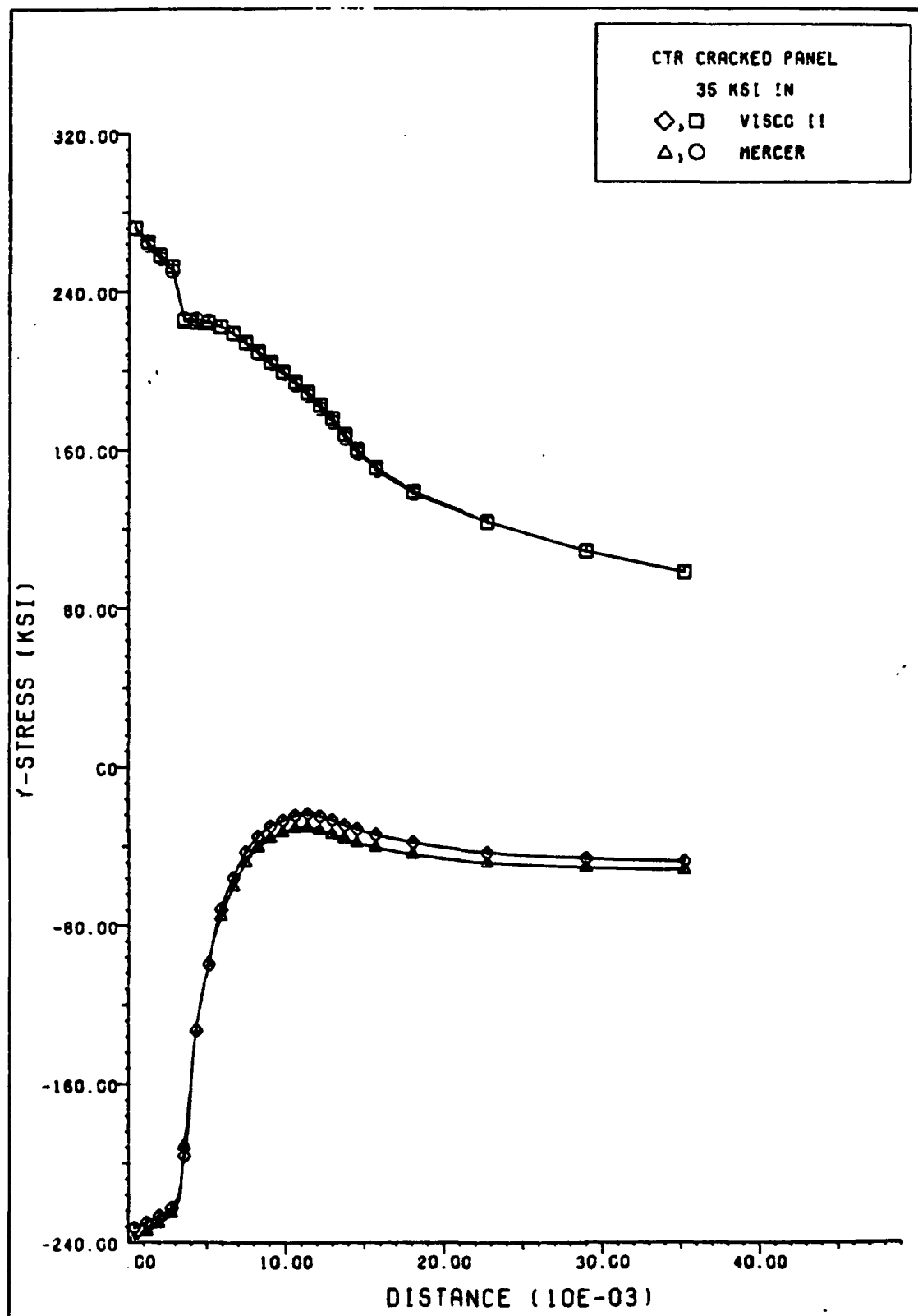
32

Figure 3.3

Crack Closure Algorithm Results

33

occurred during an increase in external loads. As explained in chapter 2, when a node is released, a force is initially calculated and internally applied to that node to maintain a zero displacement. This force is then reduced over a specific time interval, the node release time, until that node is no longer restrained. For the finite element simulation here, the node release time was arbitrarily set equal to one-half the time from maximum load application to the point of minimum positive load. Hence, for R - -1.0, this time was set at .125 seconds, whereas the release time was .25 seconds for a load ratio of 0.1. In this manner, the node release algorithm was completed prior to any externally applied compressive forces or the beginning of a subsequent load cycle.

Due to the proposed experimentation, it was anticipated that approximately 10-15 nodes would be released during the computer analysis, thus allowing for crack growth approximately one and one-half to two crack lengths. The release of a node was assumed to occur only after a steady state condition was reached in front of the crack tip. Since it was not feasible to attain true steady state conditions prior to the release of each node, a preliminary study was accomplished to determine an optimal interval between subsequent node releases. A single-edge cracked specimen was loaded at approximately 60 percent material yield strength and load ratios of both -1.0 and 0.1 were applied in two separate cases. Crack tip stress distributions ahead of the crack tip and displacements behind the crack tip remained virtually unchanged after one complete load cycle in both instances. Plastic strains ahead of the crack tip, however, required several cycles to reach a near steady state condition. In particular, after two complete

load cycles, the change in the average amount of plastic strains in the three elements immediately in front of the crack tip was less than four percent (Figure 3.4). Additional cycles were therefore deemed unnecessary when considering the amount of crack growth anticipated. For this reason, during the computer analysis of the single-edge cracked specimens, a node is released during one load cycle and another complete load cycle is run to allow for the stabilization of stress and strain conditions. On the following cycle, data are collected as required and the procedure (Figure 3.5) is repeated until the desired crack growth is attained.

Finite Element Mesh

In consideration of the proposed experimentation and the results of preliminary studies, a finite element mesh (Figure 3.6) consisting of constant strain triangular elements was developed. Due to symmetry, half of the specimen has been modeled and necessary displacement boundary conditions applied at the nodes along the axis of symmetry. The entire mesh includes 389 elements and 231 nodes. The fine portion of the mesh in the vicinity of the crack tip, shown in Figure 3.7, consists of elements 1.6×10^{-4} inches in height and width and thus an area of 1.28×10^{-8} inches squared. These elements extend 2.56×10^{-3} inches ahead of the crack tip (approximately two and one-half crack lengths) in order to accomodate the experimental crack growth data.

The size of the fine mesh elements is based upon previous work, experimental measurement accuracies, one-dimensional analyses, and stress intensity factor calculations. Initial estimates were obtained by comparing crack tip element sizes and initial crack lengths in
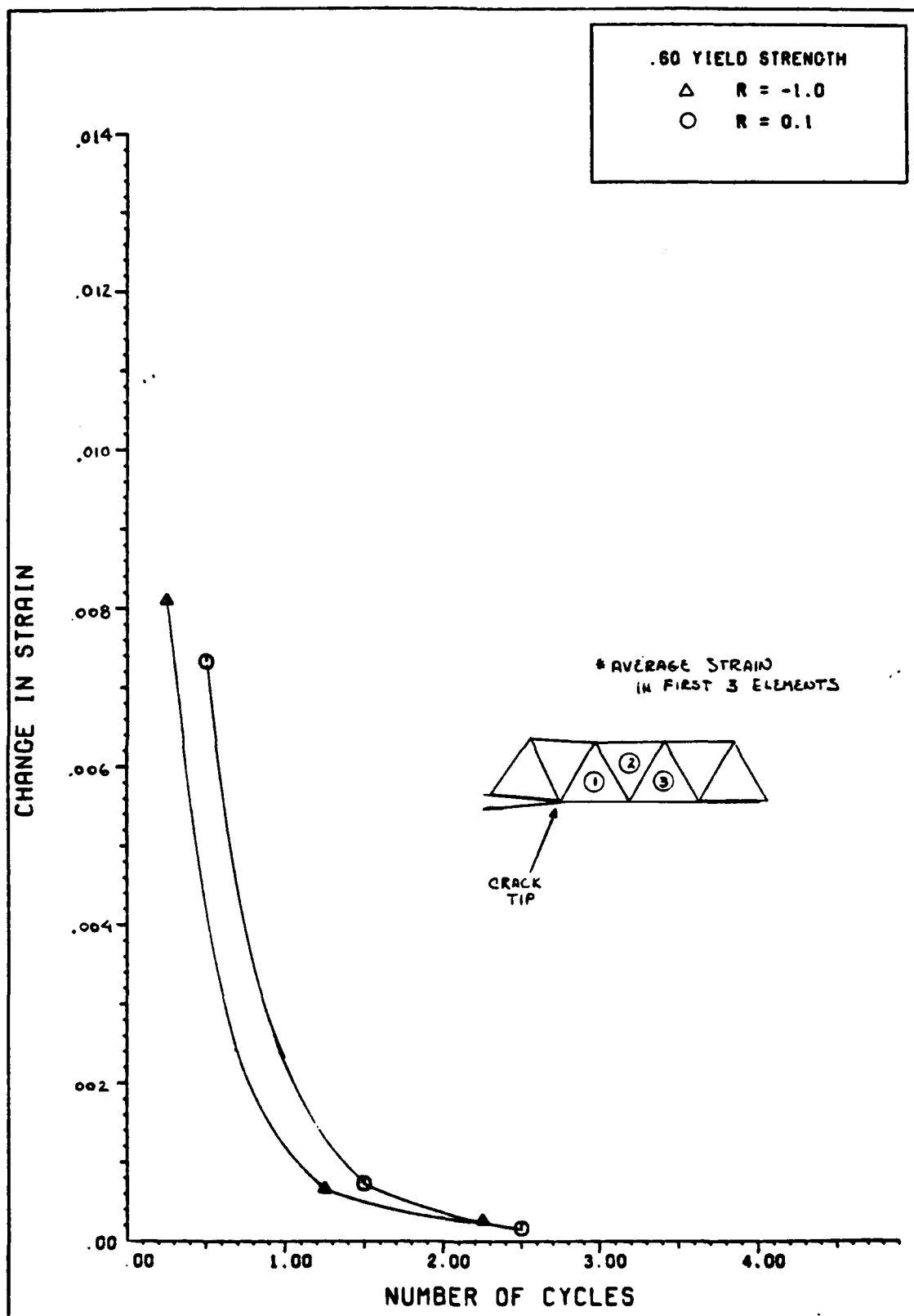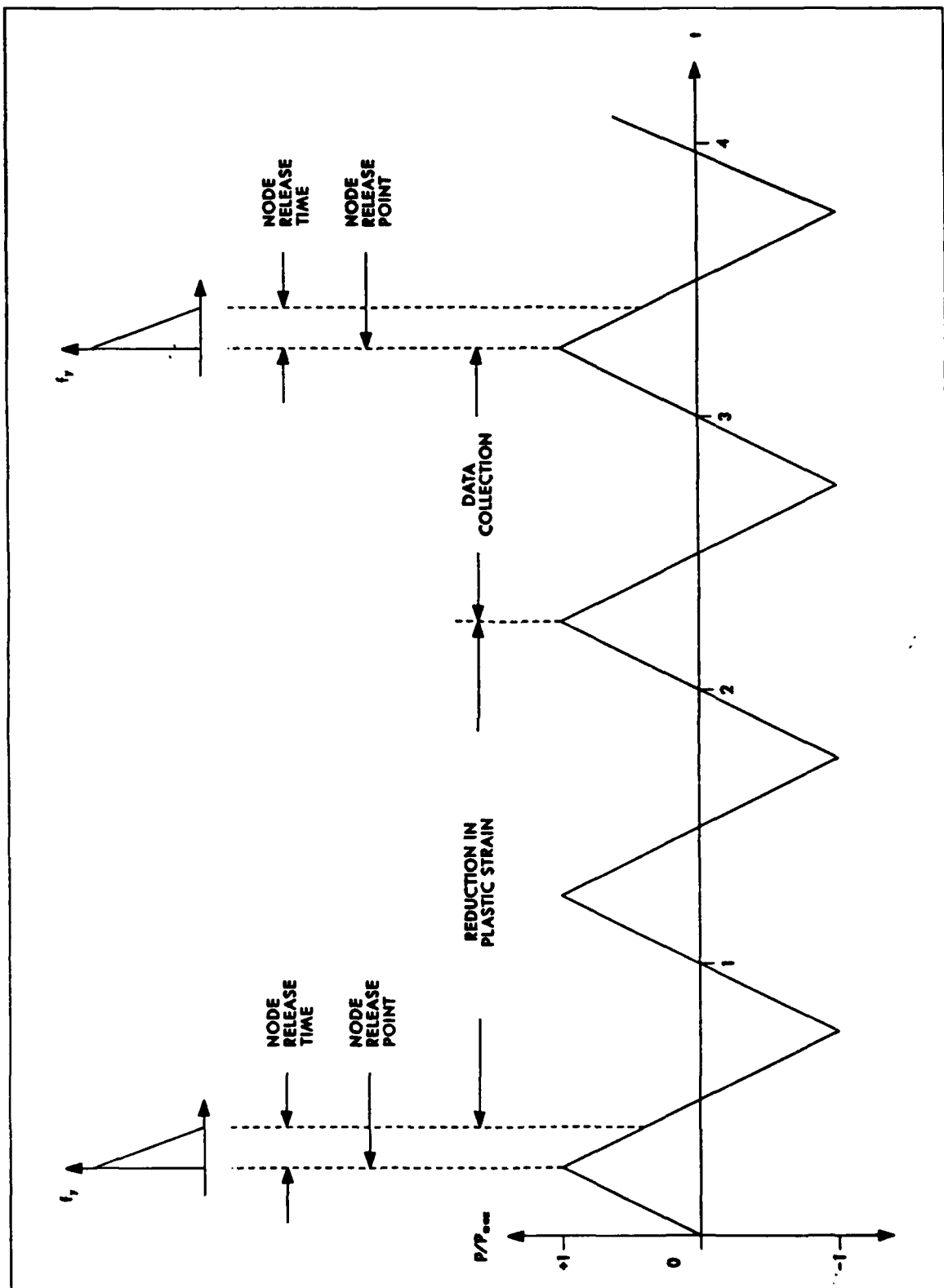
35

Figure 3.4

Changes in Plastic Strain
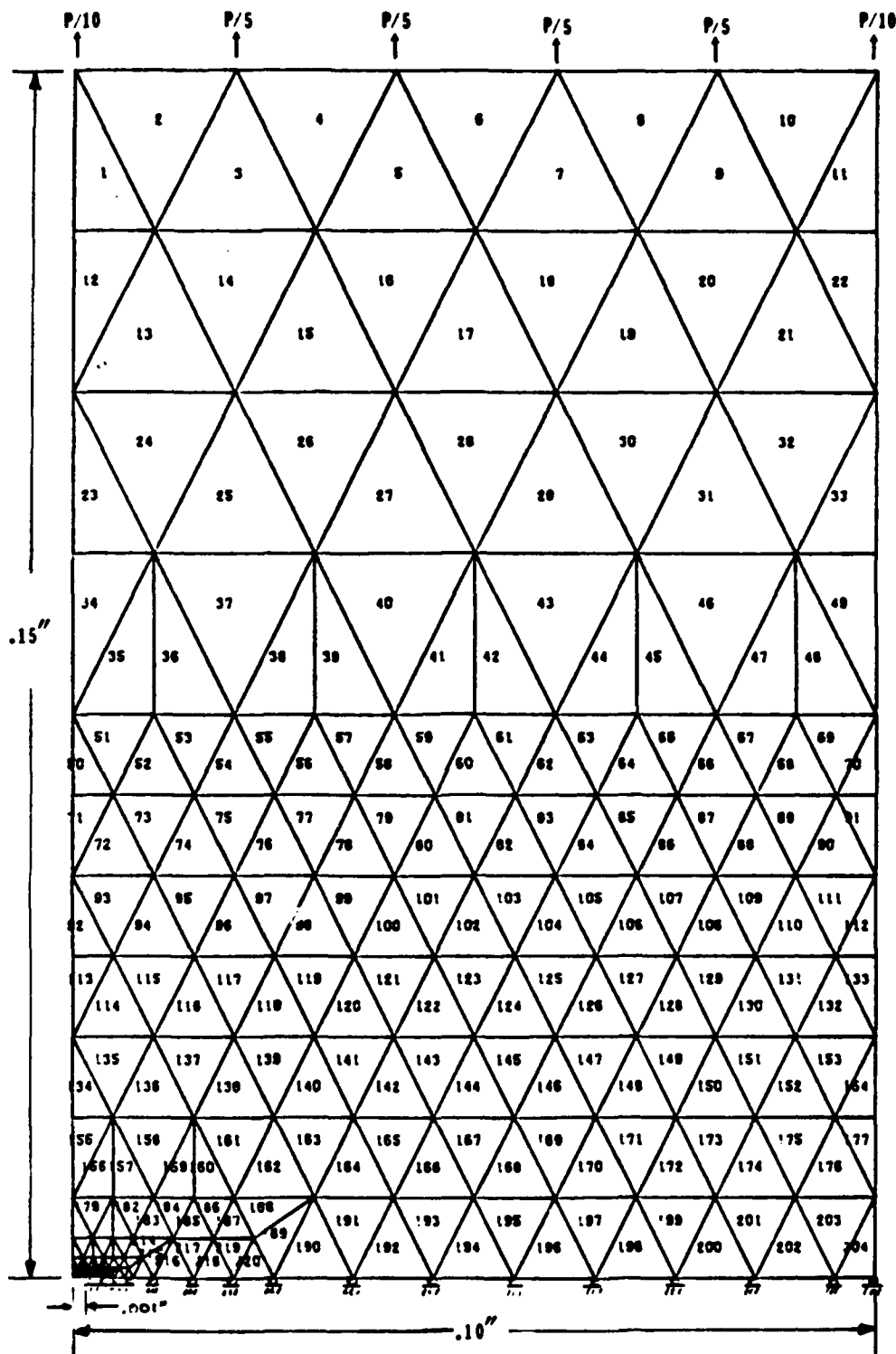
Figure 3.5

Finite Element Crack Growth Procedure

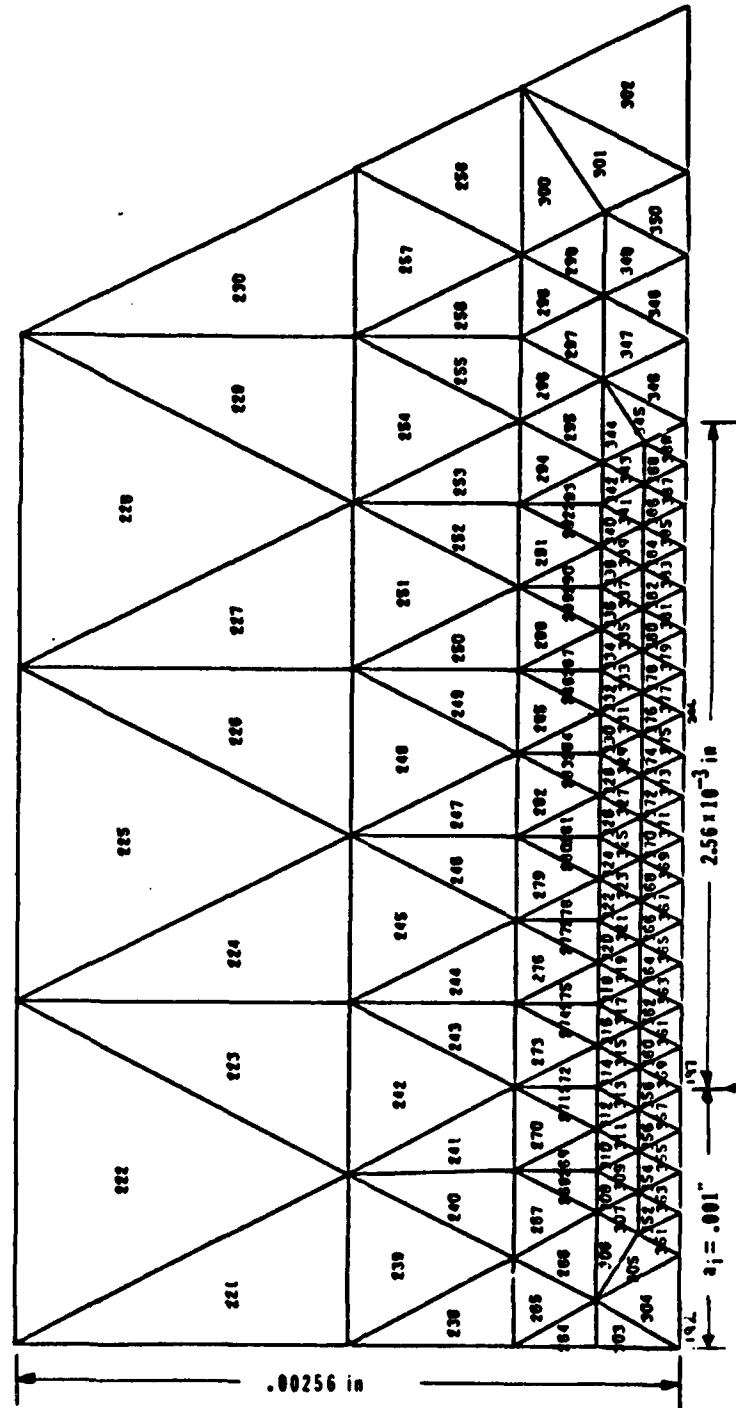Figure 3.6

Finite Element Mesh - Single Edge Crack

38

Figure 3.7

Crack Tip Finite Element Mesh

39

previous studies. Henkel [68] used elements measuring 7.8125×10^{-4} inches in height and width for a center cracked panel (2a - .2734 inches) to study crack closure characteristics under cyclic loading. Hinnerichs [71] employed the same element size to study viscoplastic creep in several center cracked panels (2a - .2734, .4733, and .6234 inches). Comparative elements for a single-edge cracked specimen (a - .001 inch) based on initial crack length would then measure approximately 6.0×10^{-6} inches. In addition, data obtained from experimental results [22] and studies of the methods involved indicated an accuracy of 1μm (3.9×10^{-5} inch) in measuring crack lengths on the order of 25μm ($.98 \times 10^{-3}$ inch) [78].

A one-dimensional uniaxial finite element analysis was also accomplished using small elements (2.0×10^{-5} inch) to determine if the Visco II code and associated computer resources could accomodate a small-sized element. In question was the ability to maintain a sufficient level of accuracy in the solution algorithms when element size was reduced. Proposed element sizes (in terms of linear dimensions) for this research effort were over 1500 times smaller than any element previously used. By applying several stress values under fully reversed cyclic loads, it was determined that the size of an element was not a limiting factor as long as the resultant stresses did not significantly exceed the material yield strength. This indicates that the element size would certainly be a factor when the final mesh was developed. Since the stresses in a constant strain triangle are calculated at its centroid, as the element size is reduced, the point of stress calculation grows closer to the crack tip. This results in higher crack tip element stresses for a given external load. As an

example, in an elastic analysis the stress in the y-direction in the vicinity of the crack tip is related by [79,80]:

$$\sigma_y = (K_I/\sqrt{2\pi r})\cos\theta/2(1+\sin\theta/2\sin3\theta/2) \tag{3.5}$$

For a single-edge cracked specimen, K_I, the stress intensity factor can be approximated by [79]:

$$K_I = [1.99 - .41(a/W) + 18.7(a/W)^2 - 38.48(a/W)^3$$

$$+ 53.85(a/W)^4] \sigma a^{1/2} \tag{3.6}$$

For the specimen investigated here, this reduces to:

$$K_I = .062357609\sigma \tag{3.7}$$

Thus, for a crack tip element of size 2.0×10^{-5} inch, the approximate stress is 8.472σ and an element size of 4.0×10^{-5} inch has an approximate crack tip stress of 5.99σ.

As a result of the above considerations and the requirement for crack growth of approximately 2-3 crack lengths, the mesh with fine elements measuring 1.6×10^{-4} inches was constructed. Although smaller element sizes may have been utilized, particularly at loads of 60 percent yield strength, the larger load of 90 percent yield strength precipitated the use of these elements. In addition, a mesh including smaller elements over the same region would require substantially more elements and incur excessive computer resources to simulate crack growth over a similar distance.

Finally, an external load was applied to the final mesh and a calculation of the stress intensity factor performed. For an externally

applied stress of .04913 KSI, K_I was analytically determined to be 3.088 KSI-IN$^{1/2}$ using equation (3.7). Using an extrapolation technique with the finite element mesh, a value of 3.014 KSI-IN$^{1/2}$ was found (Figure 3.8). This indicated an error of less than 2.5 percent.

Experimentation

Specimens composed of a high strength titanium alloy, TI-6246, and whose geometry is shown in Figure 3.9, were subjected to cyclic loading in experiments conducted by the WRDC Materials Laboratory [22,23]. Several values of load ratio, R (ratio of minimum load amplitude to maximum load amplitude), and various stress levels were applied. In particular, load ratios of -1.0 (fully reversed loading) and 0.1 were investigated in conjunction with maximum load amplitudes resulting in nominal stress values of both 60 and 90 percent material yield strength. Under these conditions, growth data for small surface flaws were obtained. The particular flaw sizes monitored for these load conditions are shown in Table 3.1.

The analysis of the experimental data involves a three-dimensional elastic analysis of a surface flaw; However, it is proposed that experimental results may be approximated using a two-dimensional finite element analysis of a single-edge cracked specimen. The crack length, a, in this case would be equal to one-half the actual surface flaw length (Figure 3.10). Although the dimensionality between the two cases is different, the finite element model should yield comparable results as long as the surface flaw is semi-circular (aspect ratio = a/r = 1.00) and through-the-thickness stresses are uniform. Experimental results confirmed the first of these requirements in that
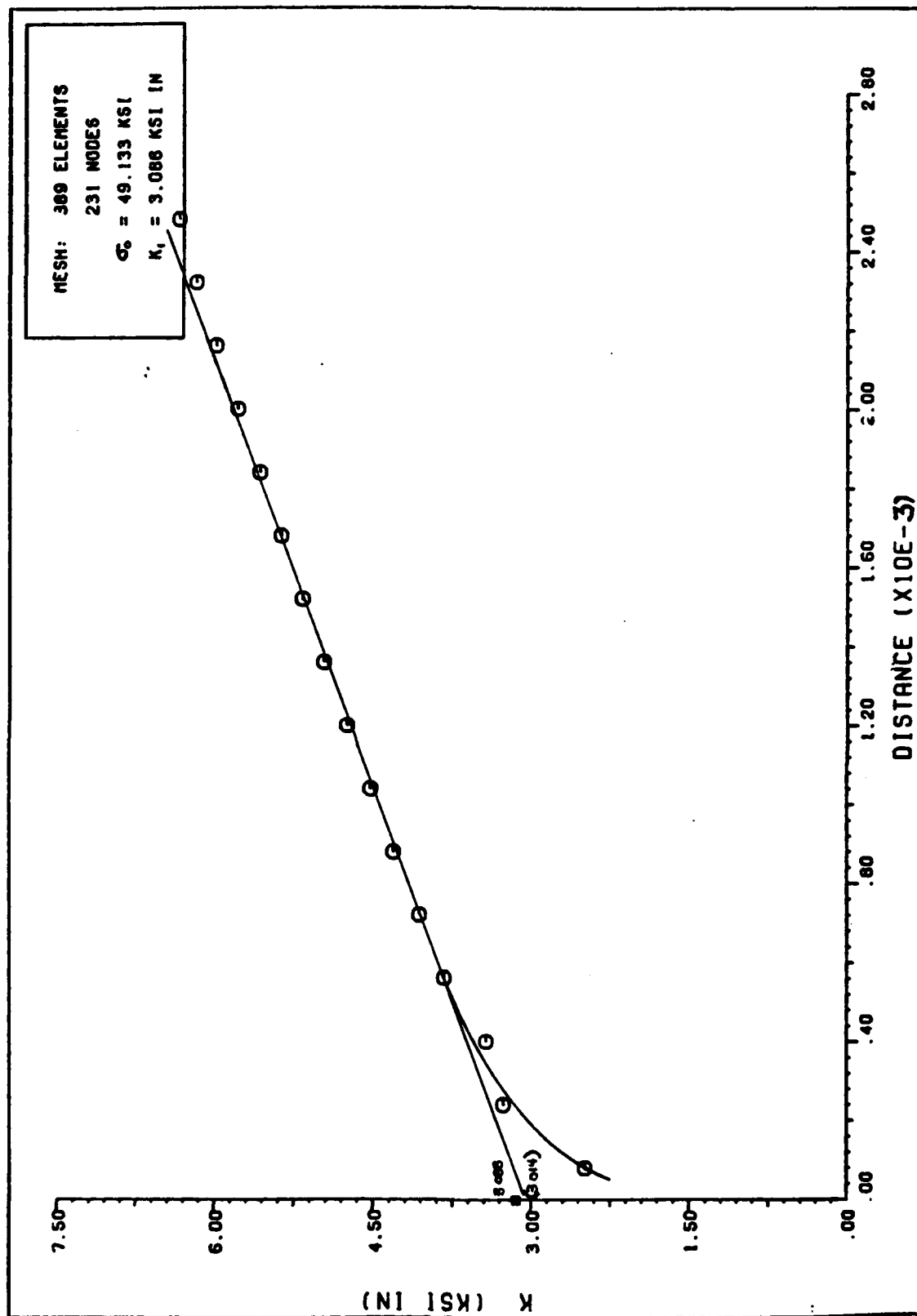
Figure 3.8

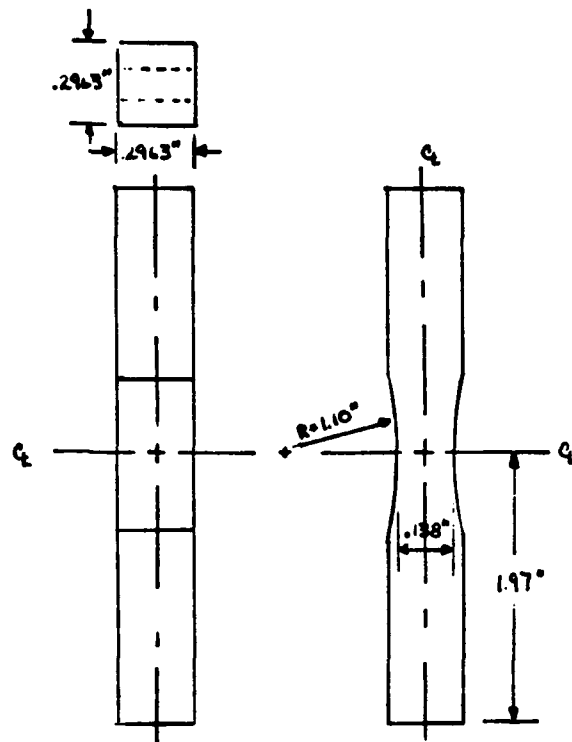Stress Intensity Factor Interpolation
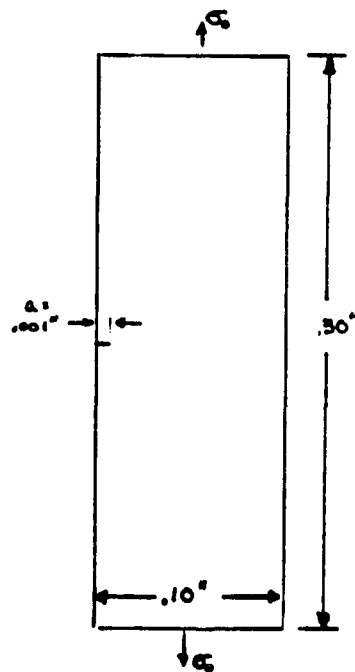
43

Figure 3.9

Experimental Specimen Geometry
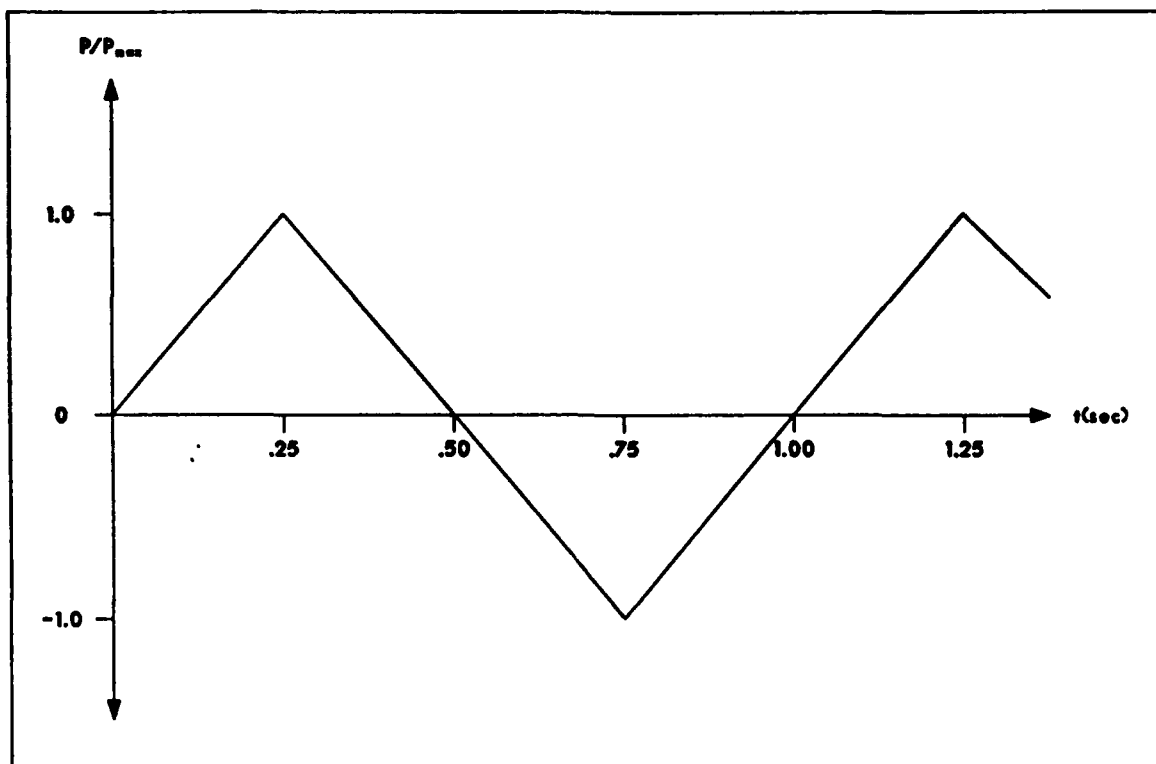

Figure 3.10

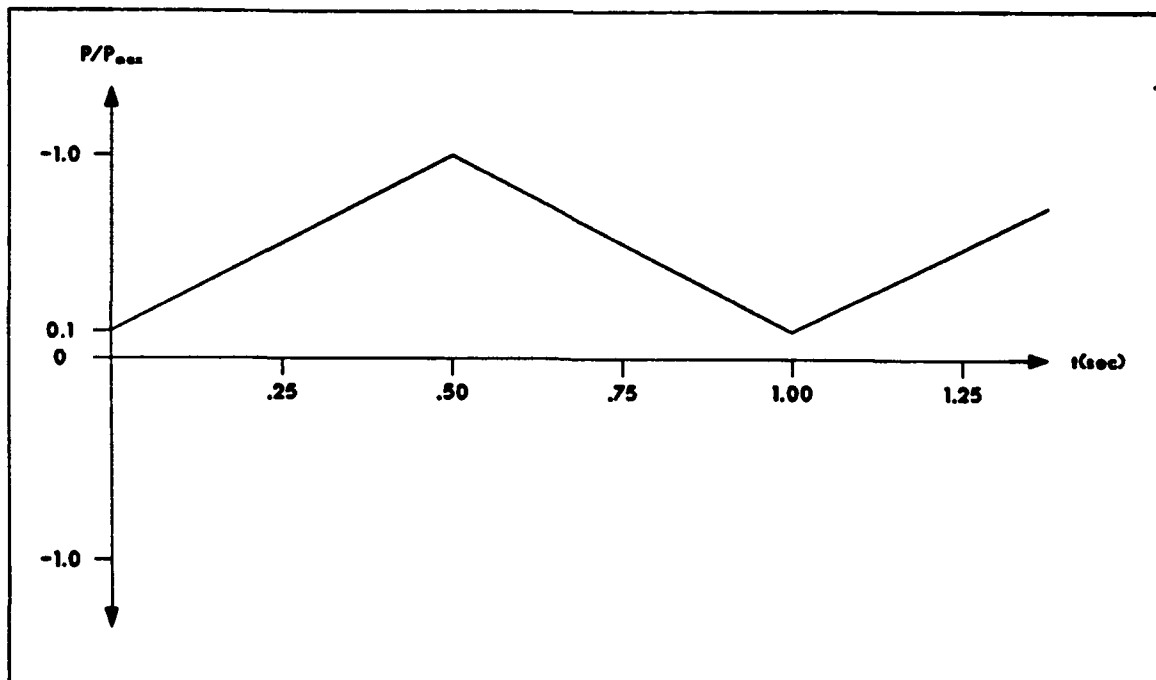Single-Edge Cracked Specimen

Figure 3.11

Load-Time Pattern (R = -1.0)

Figure 3.12

Load-Time Pattern (R = 0.1)

Table 3.1

Experimental Crack Sizes

LOAD	R = -1.0	R = 0.1
$\sigma = .60\sigma_{ys}$	44 - 530μm	60 - 1070μm
	.001732 - .02086 in	.002362 - .04213 in
$\sigma = .90\sigma_{ys}$	44 - 860μm	44 - 814μm
	.001732 - .03386 in	.001732 - .03205 in

Table 3.2

Loading Data

SPECIMEN	σ	LOAD (LB)	K_I(KSI-IN$^{1/2}$)
TI-6246	$.60\sigma_{ys}$	10650.0 (106.5 KSI)	6.69
TI-6246	$.90\sigma_{ys}$	15975.0 (159.75 KSI)	10.04
Inconel 718	$.90\sigma_{ys}$	11700.0 (117.0 KSI)	7.354

46

the surface flaw remained nearly semi-circular (a/r = 1.03) and subsequent analysis by the Materials Laboratory verified the existence of a uniform stress distribution through the specimen thickness [22].

Loads, as previously stated, included nominal stress values of approximately 60 and 90 percent yield strength in conjunction with load ratios of -1.0 and 0.1. For TI-6246 (yield strength = 168 KSI), the applied loads in the finite element analysis are shown in Table 3.2 and resulted initial maximum stress intensity factors of 6.69 KSI-IN$^{1/2}$ and 10.04 KSI-IN$^{1/2}$ when evaluated using equation (3.6). The loads were applied in a triangular saw-toothed load-time pattern at a frequency of 1.0 Hz. These patterns, for the two load ratios, are shown in Figures 3.11 and 3.12. For Inconel 718 (yield strength = 130 KSI), the applied load is shown in Table 3.2. A nominal stress value of 90 percent yield strength and a load ratio of 0.1 were maintained, whereas the load frequency was assumed to be 1.0 and 0.01 Hz.

IV. Results and Discussion

The effects of plasticity induced closure on the fatigue growth of short cracks was investigated by analyzing a single-edge cracked specimen using the Visco II finite element code. A specimen model consisting of TI-6246 at room temperature was subjected to four separate load conditions in which the load ratio and nominal stress values were varied while the load frequency remained constant at 1.0 Hz. A second model composed of high temperature Inconel 718 was analyzed using two cases where the load ratio and nominal stress value remained constant, but load frequency was varied in order to observe the viscoplastic effects. These case studies are outlined in Table 4.1. In each of these cases, comparisons are made between the case in which a crack is allowed to grow from an initial crack length of .001 inch to some final crack length (.0026 in for TI-6246 and .0018 in for Inconel 718), and the case

Table 4.1

Finite Element Case Studies

Case	Material	Stress (σ/σ_{ys})	R	a_f (in)	Freq (Hz)
A	TI-6246	.60	-1.0	.0026	1.0
B	TI-6246	.60	0.1	.0026	1.0
C	TI-6246	.90	-1.0	.0026	1.0
D	TI-6246	.90	0.1	.0026	1.0
E	Inconel 718	.90	0.1	.0018	1.0
F	Inconel 718	.90	0.1	.0018	.01

where the initial crack length is set equal to that of the grown crack in an undeformed material where crack extension has not occurred. A graphic representation of this finite element crack growth is shown in Figure 4.1. Crack growth is obtained through the use of the node release algorithm discussed in Chapter 2. By analyzing the two cracks in this manner, the effects of fatigue crack growth history and the formation of a plastic wake can be better isolated.

For the two materials, data have been obtained from the finite element analyses and are presented in several categories. These include displacements along the crack surface, stress-strain values immediately in front of the crack tip, stress distributions ahead of the crack tip, plastic strains along, as well as in front of, the crack, closure data, and load-displacement relationships.

Results for TI-6246

The single-edge cracked specimen model consisting of TI-6246, a high strength titanium alloy at room temperature, was numerically subjected to external loads of 10650 and 15975 pounds resulting in nominal stress values of approximately 60 and 90 percent of the material yield strength, respectively. At the initial crack length of .001 inch, these loads represent stress intensity factors of approximately 6.69 and 10.04 KSI-IN$^{1/2}$. In all but one case, ten finite element nodes were released during the analysis which resulted in a crack extension of · .0016 inch (a_f = .0026 inch). In case B, a total of fifteen nodes were released (a_f = .00324 inch). Results and trends observed at this last crack length, however, did not differ significantly from those at the shorter final crack length. Therefore, the results obtained from all
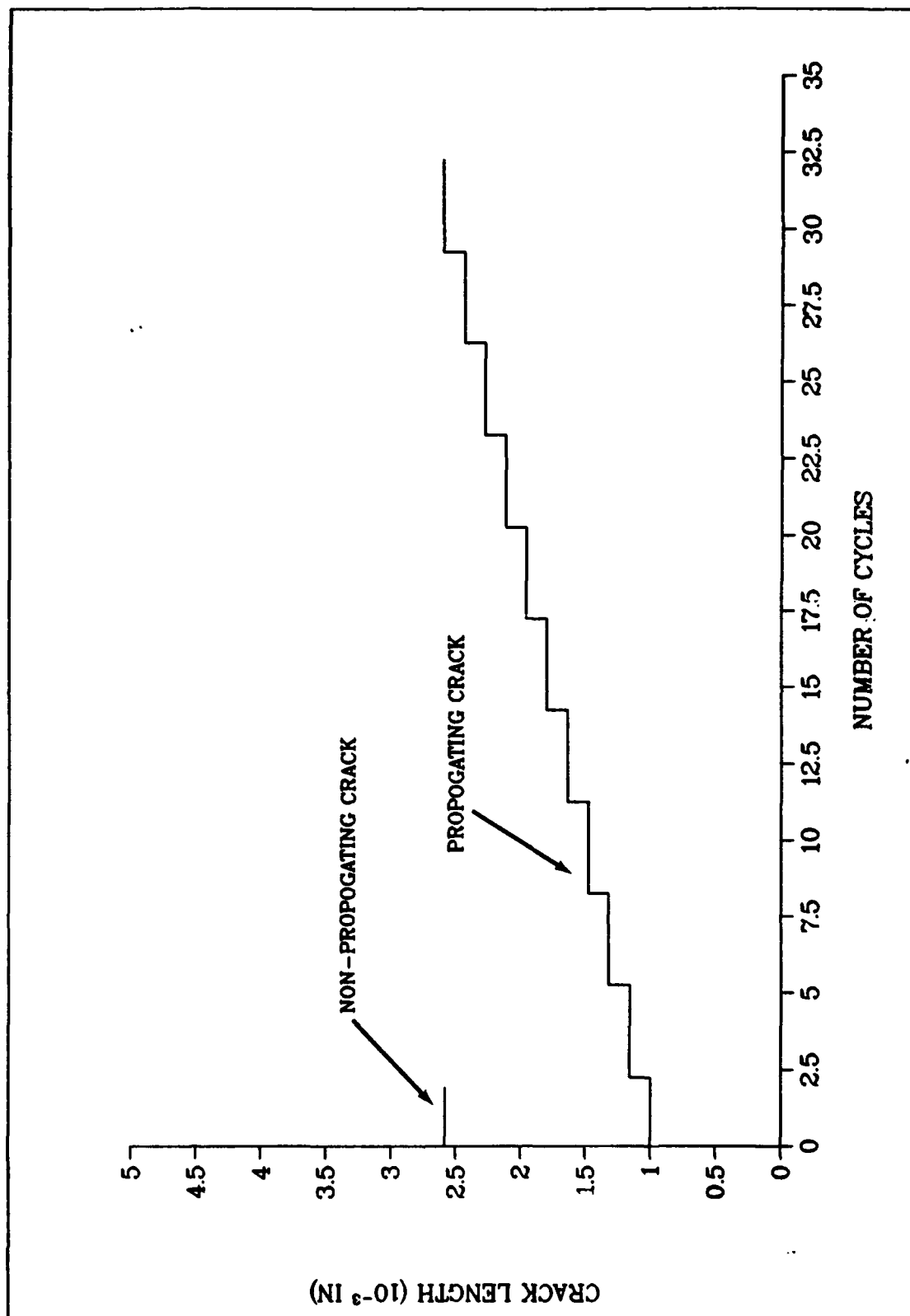
Fig 4.1: Finite Element Crack Growth

50

four cases are presented for the same final crack length (a_f = .0026 inch) for reasons of comparison and continuity.

The y-displacement profiles behind the crack tip at minimum loading show significant differences between the propagated and non-propagated cracks. In cases A and C, Figures 4.2 and 4.4, where the load ratio is -1.0, the displacements in the non-propagated crack are much greater and occur immediately behind the crack tip. The displacements in the propagated cracks occur at a distance of .00176 in behind the crack tip (in the vicinity of the original crack tip) and are considerably less. Similar results are shown in Figures 4.3 and 4.5 for the cases where the load ratio is 0.1. In these cases, the non-propagated crack remains fully open at minimum load and the maximum displacement in the vicinity of the crack tip occurs at the node directly behind the tip. The displacement profile of the propagated crack indicates that the crack remains closed for several nodes adjacent to the crack tip and then opens gradually up to the location of the original tip. At this point, the displacement increases significantly. These findings show that for the non-propagated crack, the crack tip is fully open and maximum displacement occurs at the node directly behind the crack tip. For the propagated crack, however, the crack remains closed for several nodes behind the crack tip and then opens gradually as distance from the crack tip increases. The discontinuity which occurs in the vicinity of the original crack tip (Figures 4.3 and 4.5) indicates that under cyclic loading the displacements take on unusually high values directly behind the crack tip when no history from prior fatigue cycling and crack extension are considered. It is unrealistic to represent displacement profiles behind
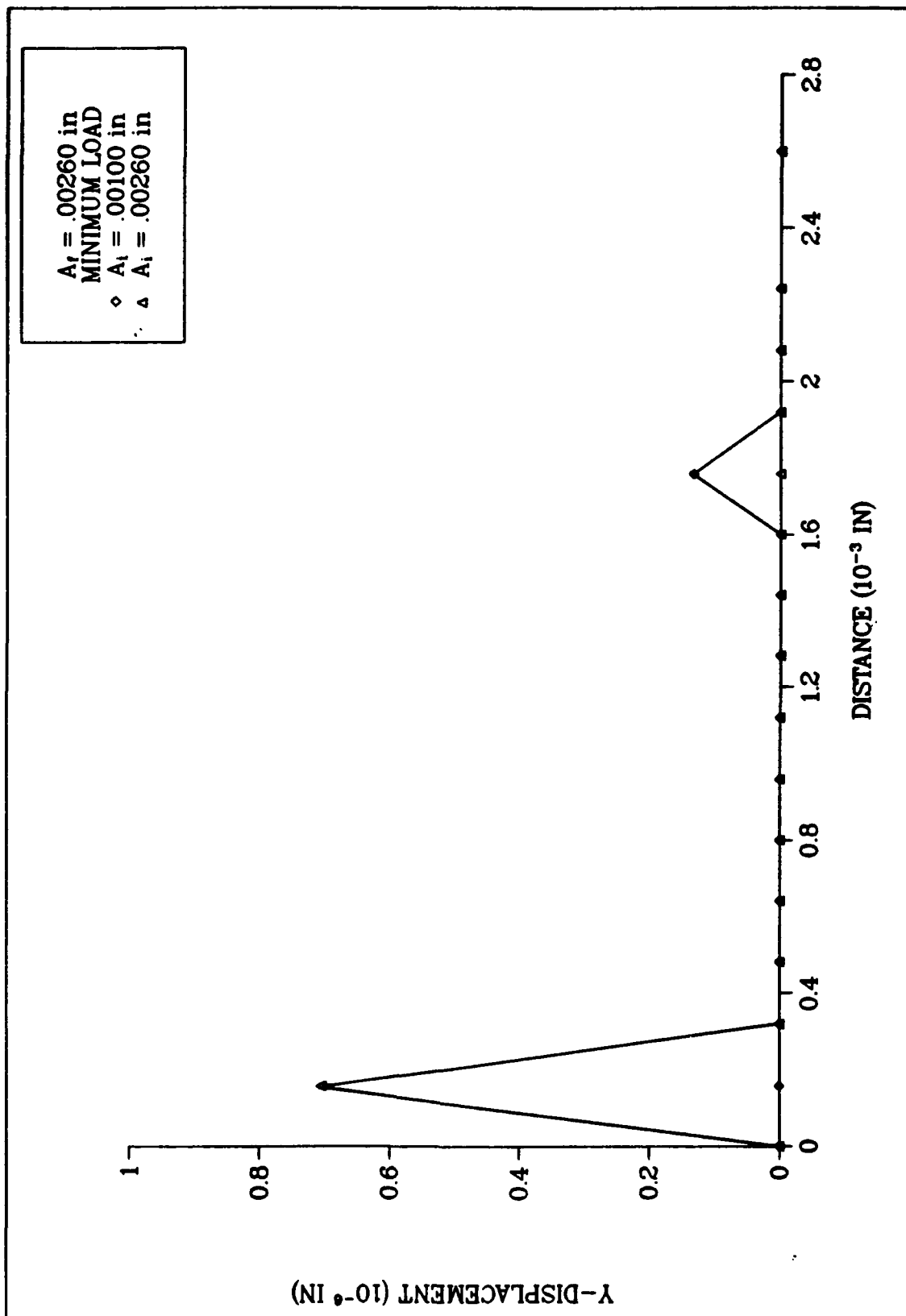
51

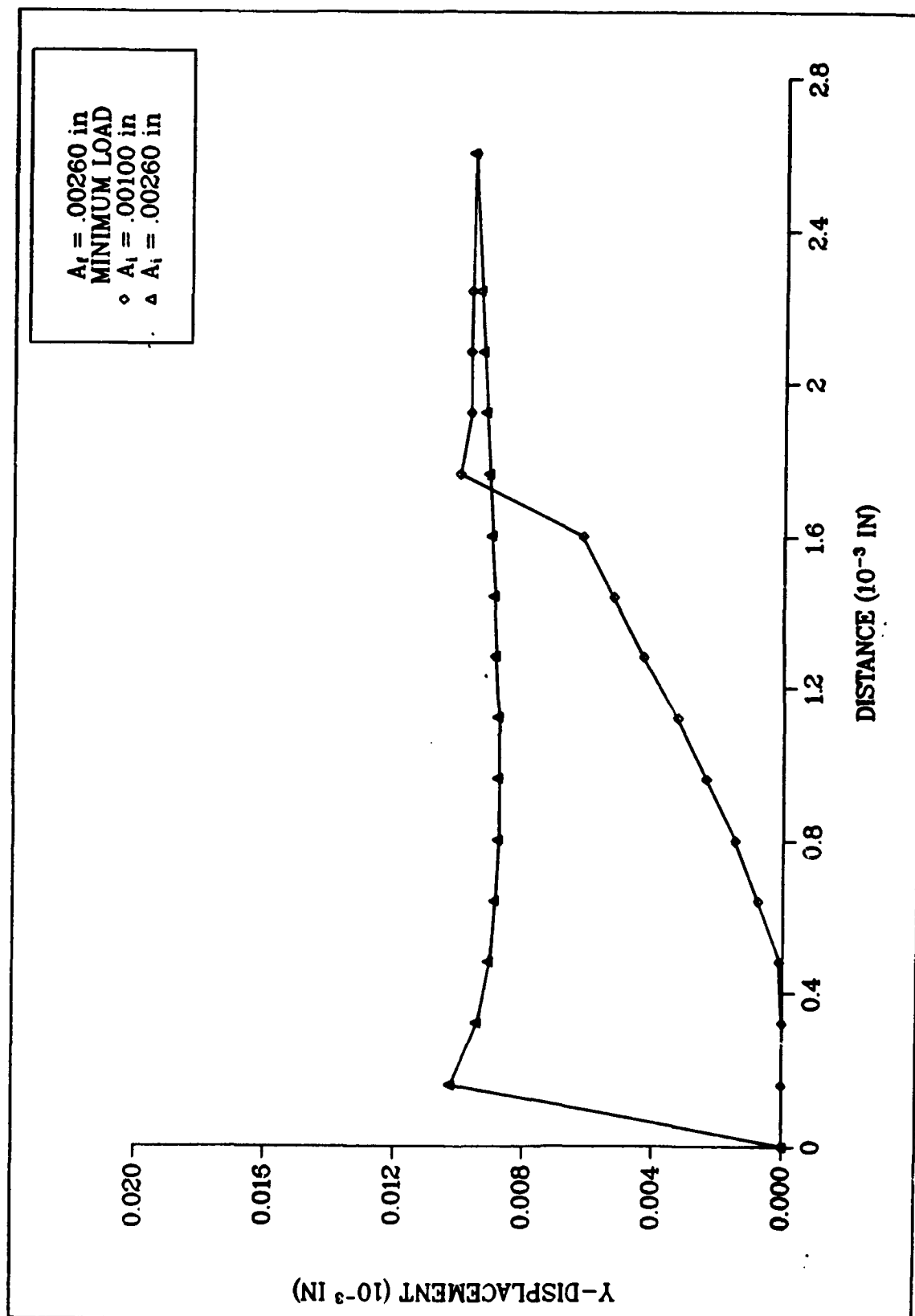Fig 4.2: Displacements Behind Crack Tip (Case A/Min Load)

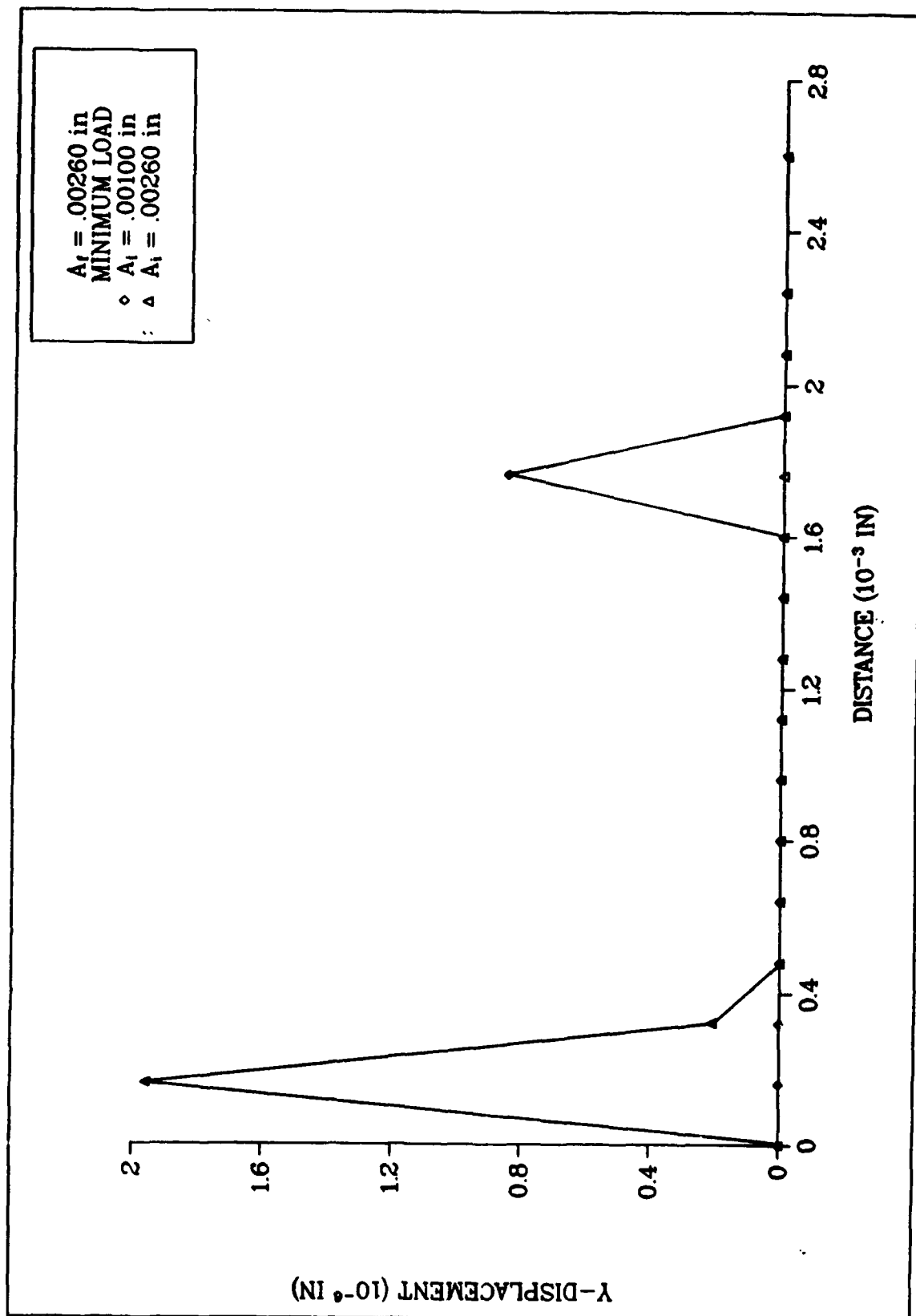Fig 4.3: Displacements Behind Crack Tip (Case B/Min Load)

53

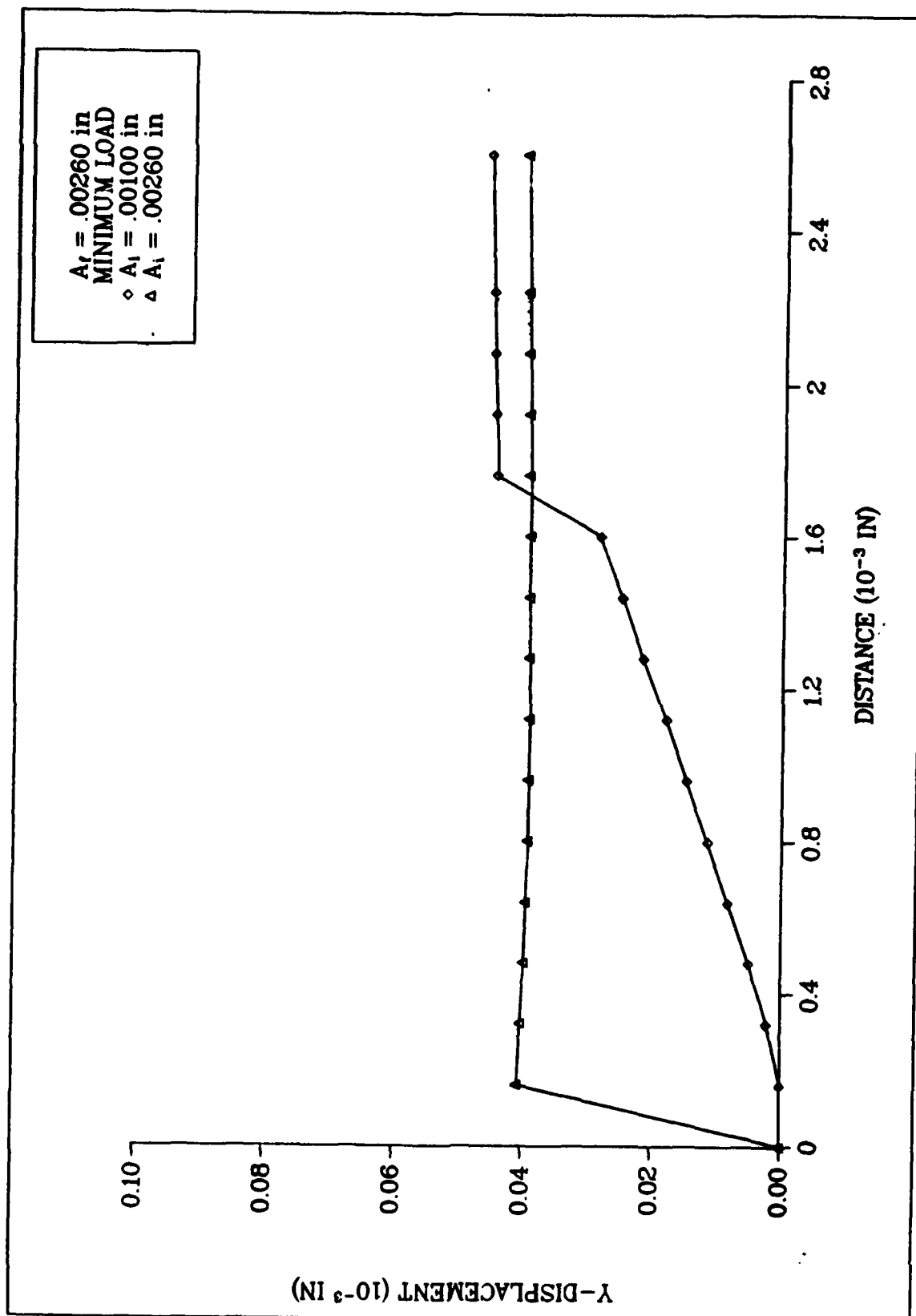Fig 4.4: Displacements Behind Crack Tip (Case C/Min Load)

Fig 4.5: Displacements Behind Crack Tip (Case D/Min Load)

a propagating crack in a finite element model which does not include the cumulative effects of crack propagation.

Analysis of the y-displacement profiles behind the crack tip at maximum loading yields similar results to those observed at minimum loading. In each case, Figures 4.6 to 4.9, the displacements directly behind the crack tip observed in the non-propagated cracks are greater than those of the propagated cracks. The existence of a plastic wake resulting from cyclic loading and crack extension reduces the amount of displacement along the crack surface. The displacements which are measured past the original crack tip, i.e., further than .0016 in, are nearly identical for all four cases. The effects of cyclic loading and crack extension do not occur over the original .001 inch crack length. The larger displacements always correspond to the non-propagated crack. The difference between these profiles corresponds to the plastic wake which forms behind the propagating crack. Therefore, the plastic wake is not modeled unless nodes are released in the finite element model simulating crack growth.

The stress/strain curves for elements immediately in front of the crack tip are displayed in Figures 4.10 through 4.13. In each case, the maximum and minimum stresses observed do not differ significantly between the propagated and non-propagated cracks. The stresses, therefore, do not appear to be affected by crack growth history. The strains exhibited by the non-propagated cracks, however, are greater in each case. Under a nominal stress value of 60 percent yield strength, Figures 4.10 and 4.11, the non-propagated crack exhibits strains approximately 25 percent greater than the propagated crack. At higher loads, as in Figure 4.13, this increase in strain is nearly doubled.
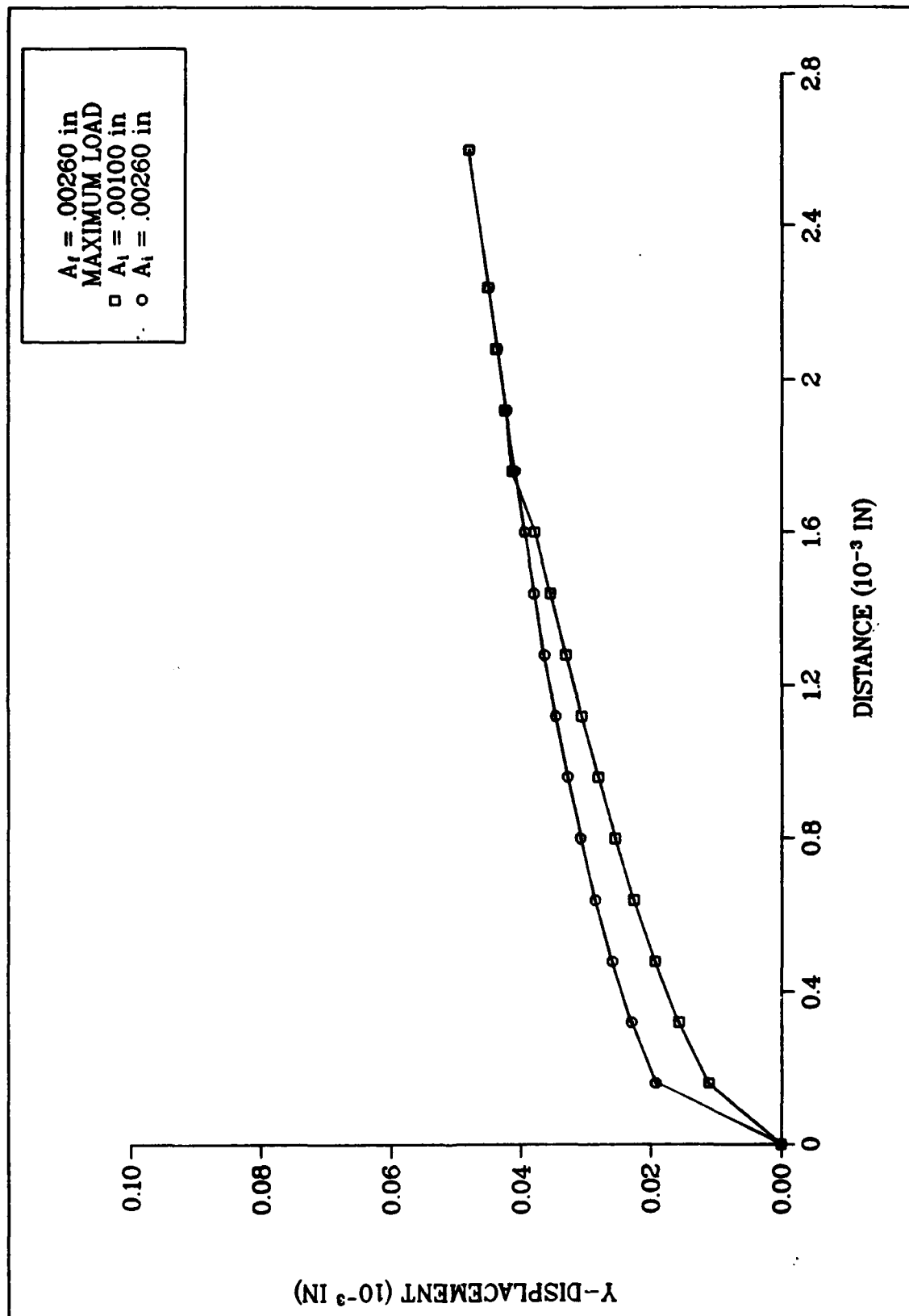
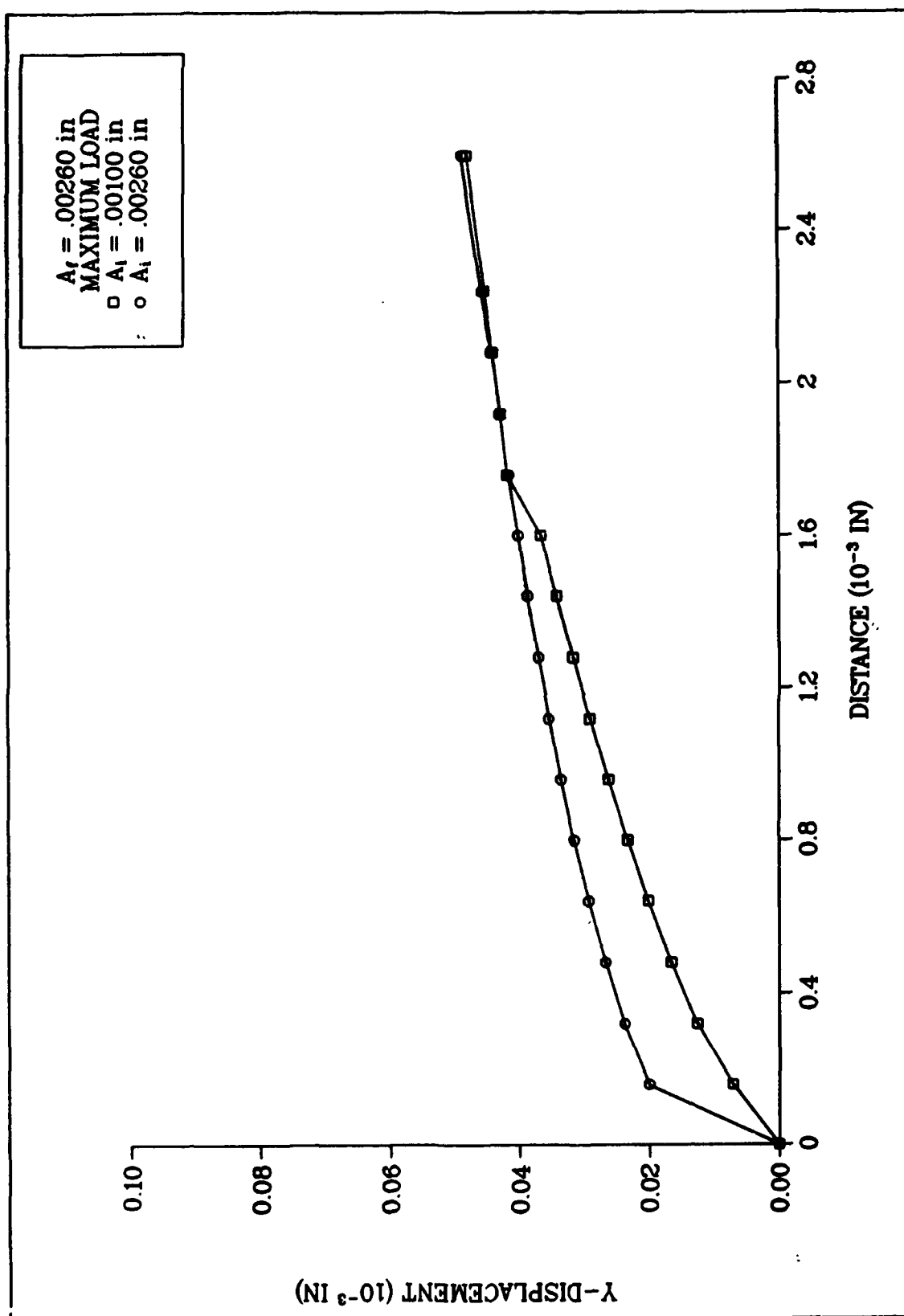Fig 4.6: Displacements Behind Crack Tip (Case A/Max Load)

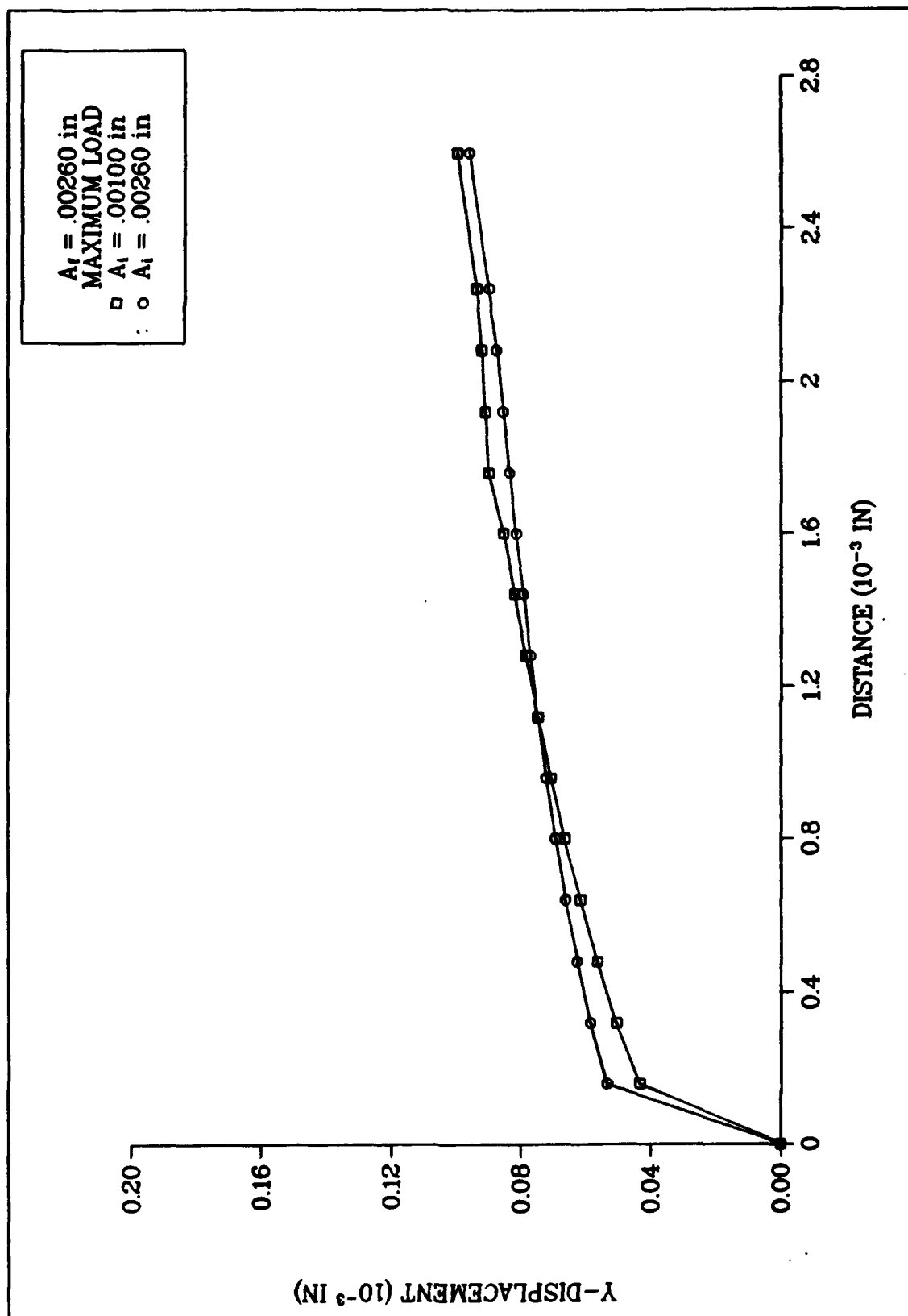Fig 4.7: Displacements Behind Crack Tip (Case B/Max Load)

58

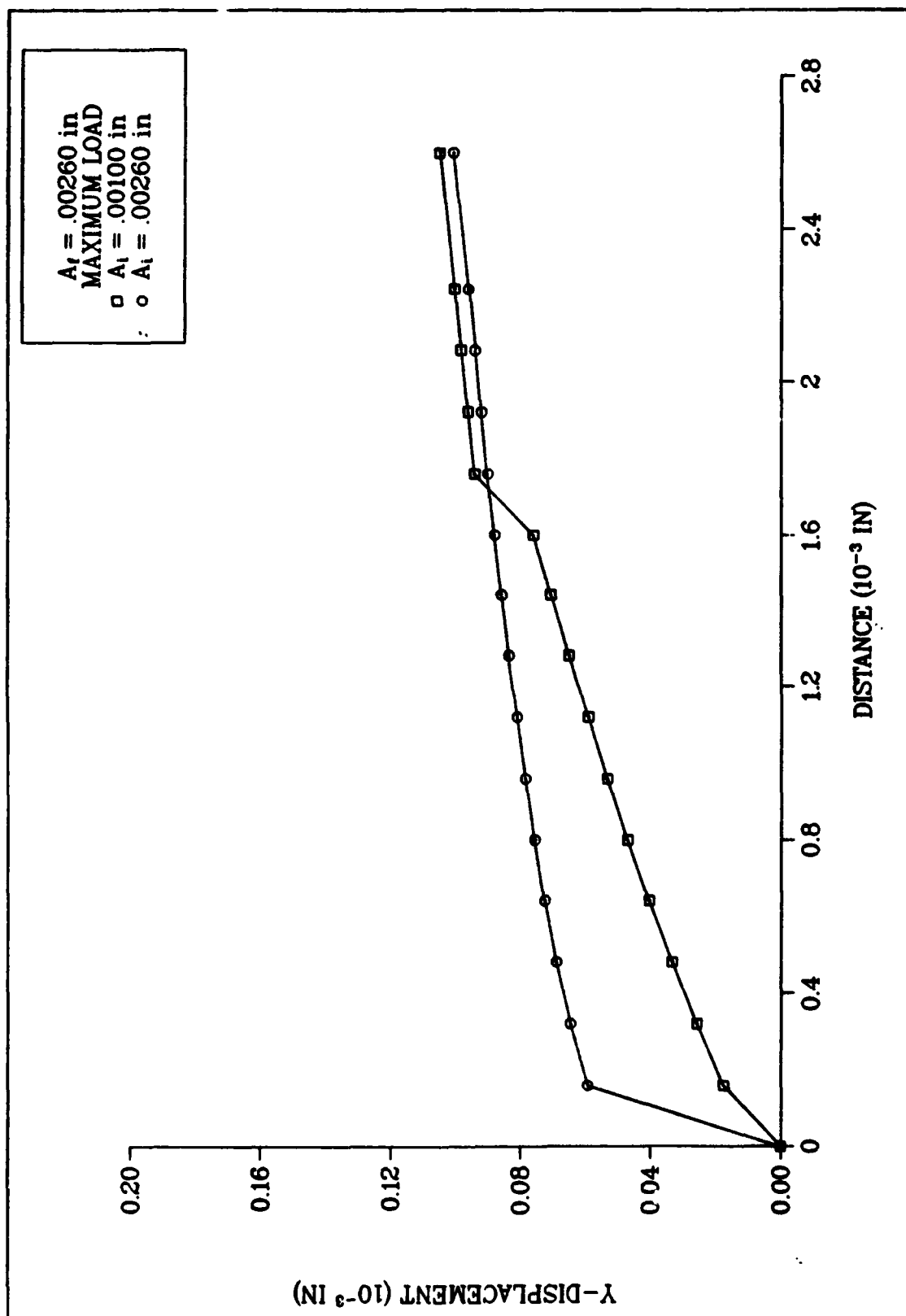Fig 4.8: Displacements Behind Crack Tip (Case C/Max Load)

Fig 4.9: Displacements Behind Crack Tip (Case D/Max Load)
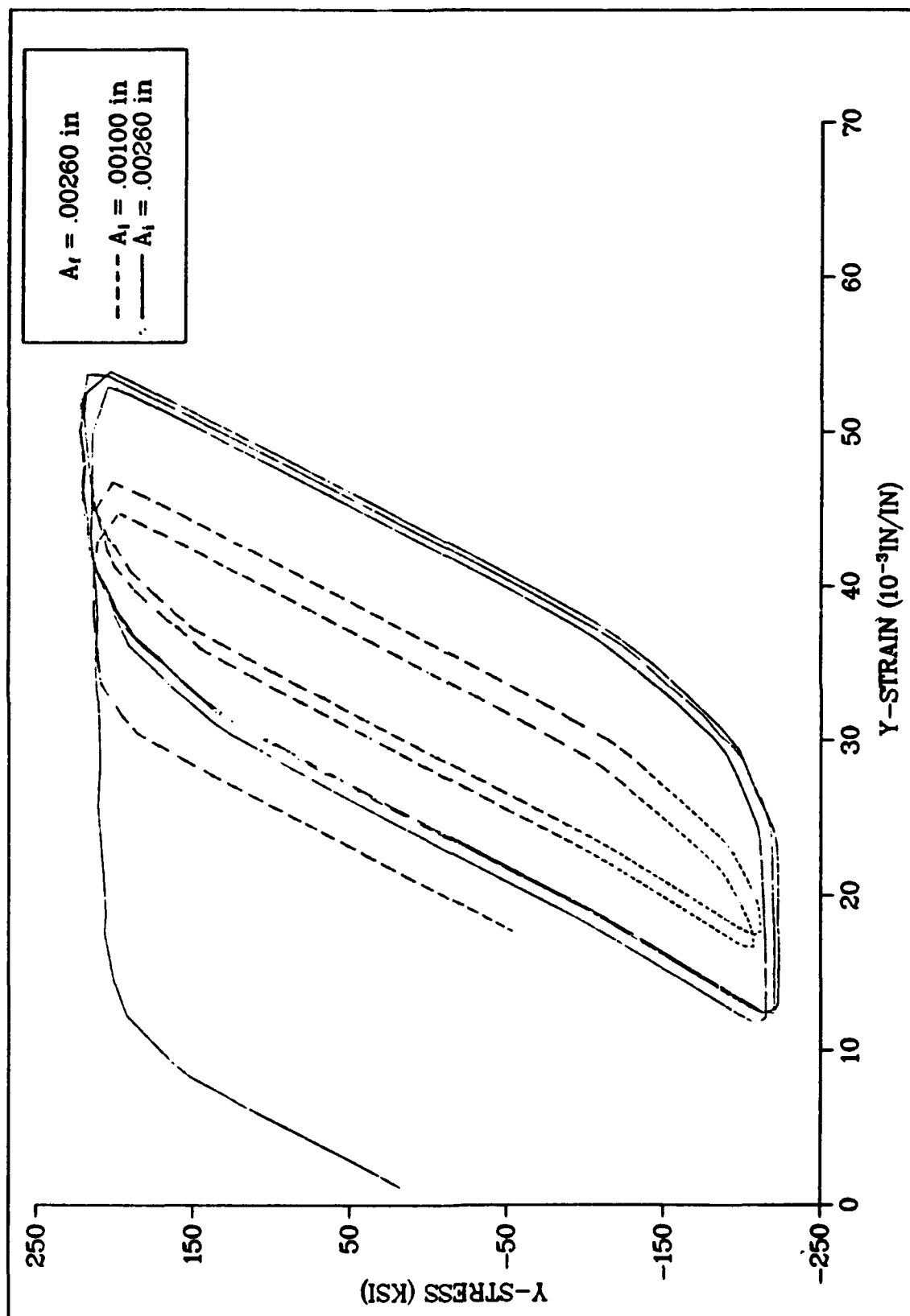
60

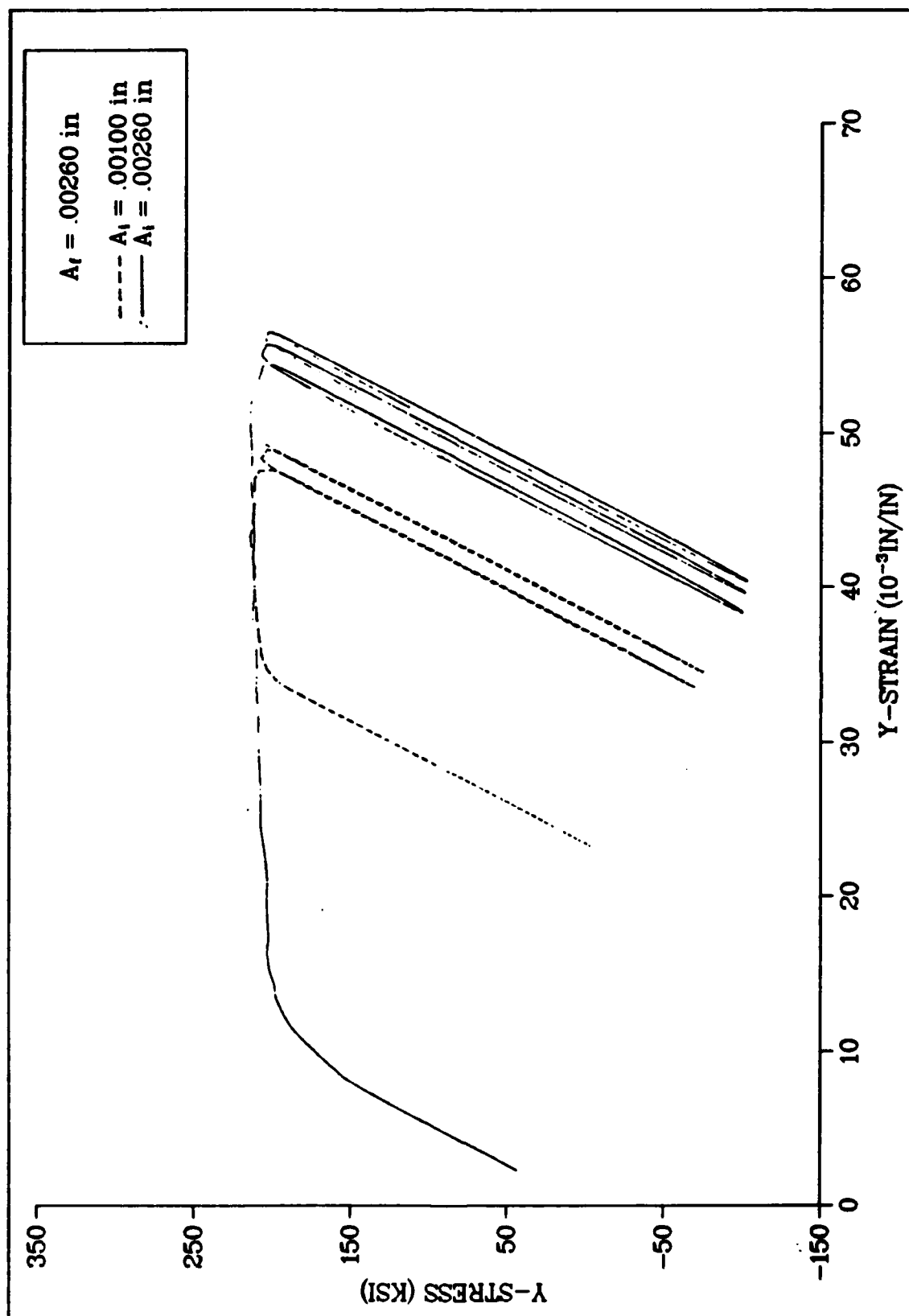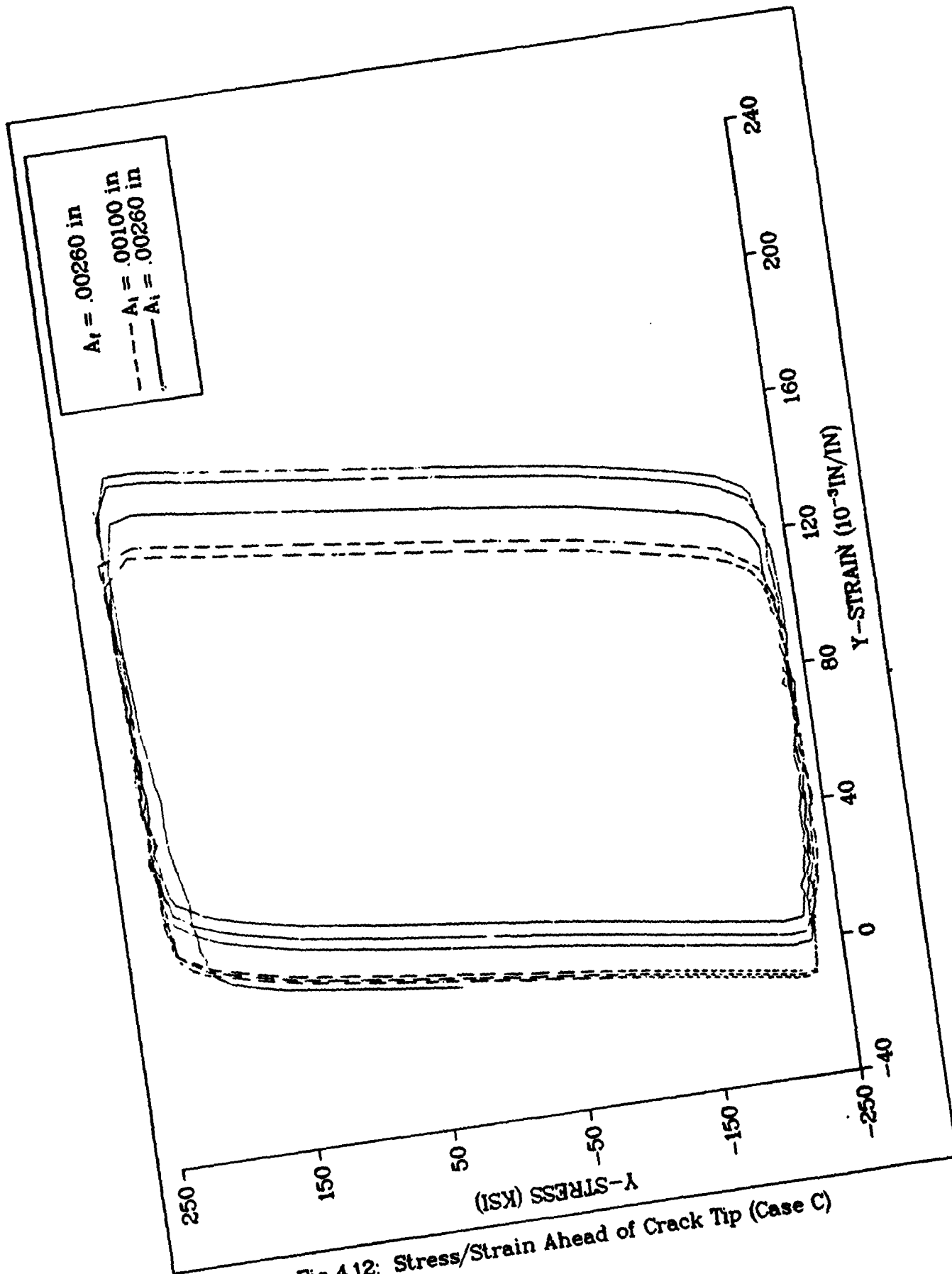Fig 4.10: Stress/Strain Ahead of Crack Tip (Case A)

61

Fig 4.11: Stress/Strain Ahead of Crack Tip (Case B)

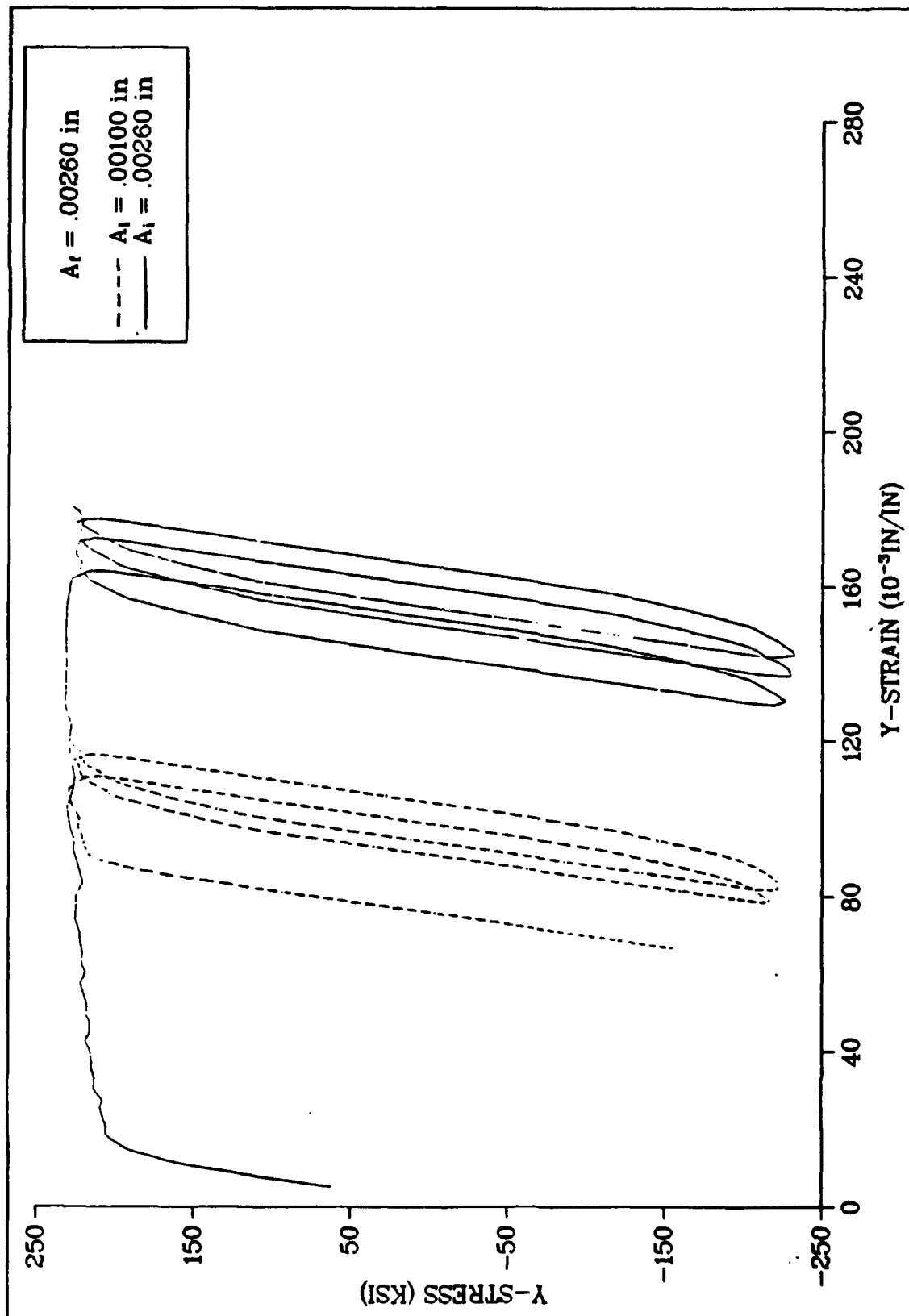Fig 4.12: Stress/Strain Ahead of Crack Tip (Case C)

63

Fig 4.13: Stress/Strain Ahead of Crack Tip (Case D)

64

The strains immediately ahead of the crack tip are therefore related to crack growth history. The plastic wake formed as a result of crack growth limits the amount of strain exhibited. Since the non-propagated crack is not subjected to this limitation, it shows higher strain values.

As illustrated in Figures 4.10 through 4.13, the stresses ahead of the crack tip do not differ significantly between propagated and non-propagated cracks. Figures 4.14 through 4.17 show the stress profiles ahead of the crack tip. The y-stress at full positive load is greatest near the crack tip and reduces gradually as the distance from the crack tip is increased. At minimum loading, the negative stresses increase rapidly over the first five elements in front of the crack tip and then level off for each case except for case C where the load ratio is -1.0 and nominal stress is .90 yield strength. Here the high compressive forces are nearly constant over the first six elements and then begin to increase gradually.

The distribution of plastic strain in the y-direction at maximum tensile load for the four cases is presented in Figures 4.18 to 4.21. The differences between the propagated and non-propagated cracks are obvious. In each instance, the non-propagated crack exhibits no plastic strain along the crack length and has a slightly greater strain at the crack tip. The non-propagated cases show an increase in plastic strain as the crack tip is approached and do not exhibit as great a strain in the crack tip vicinity. As the crack is allowed to grow, plastic strains are accumulated along the crack surface. These residual strains restrict the amount of plastic strain observed in the crack tip element. Ahead of the crack tip, the plastic strains in the non-propagated cracks
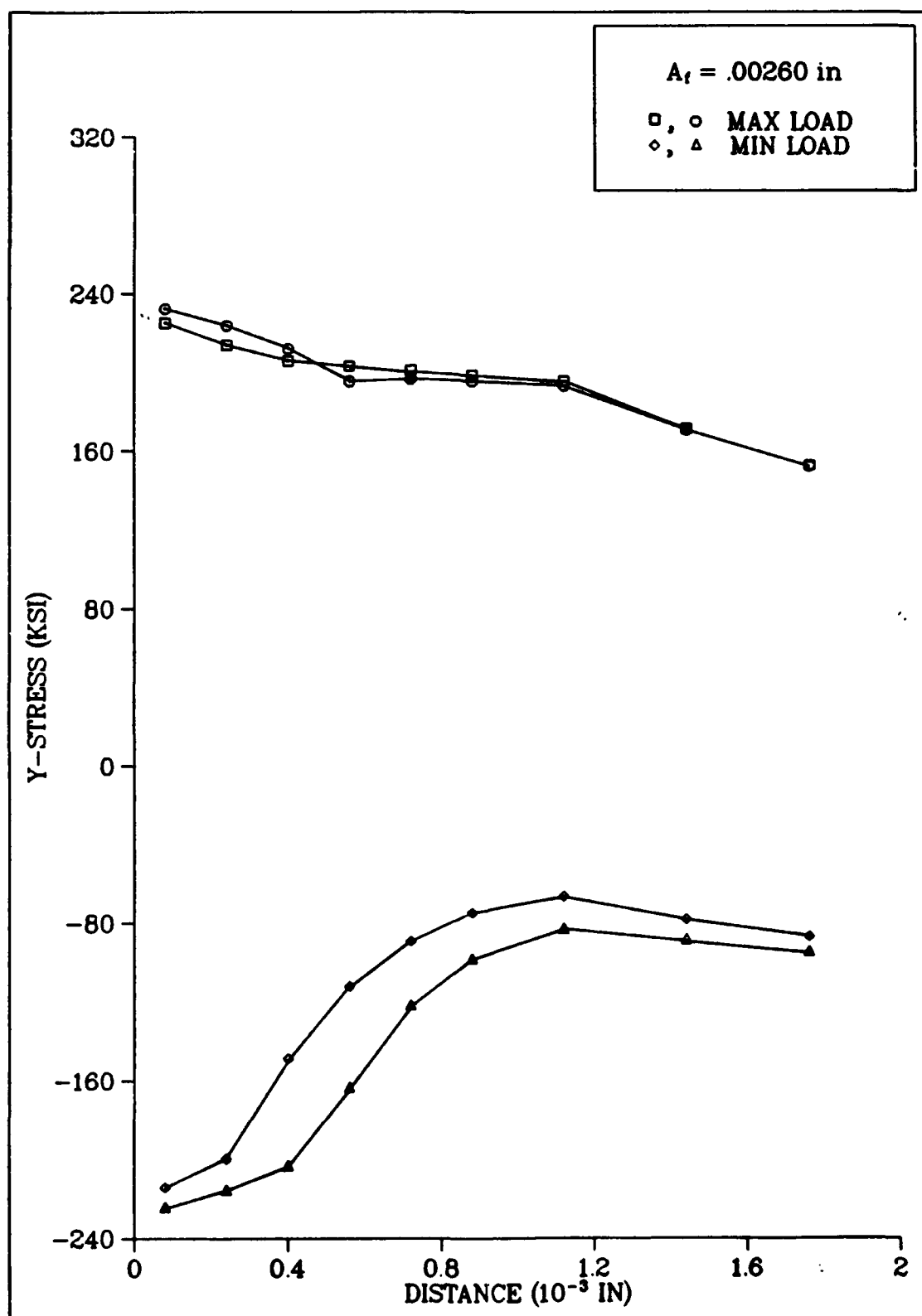
Fig 4.14: Stresses Ahead of Crack Tip (Case A)

66
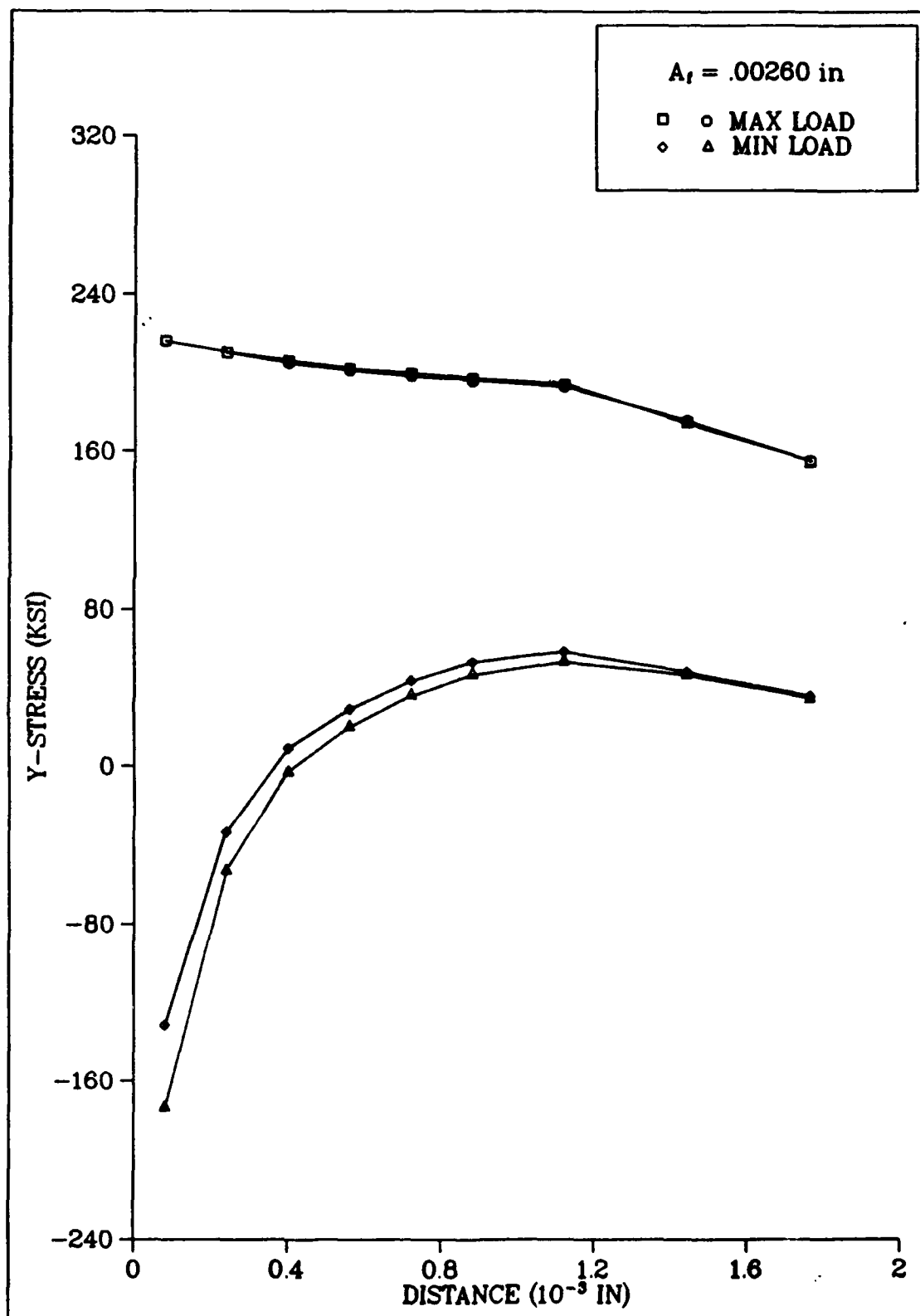
Fig 4.15: Stresses Ahead of Crack Tip (Case B)
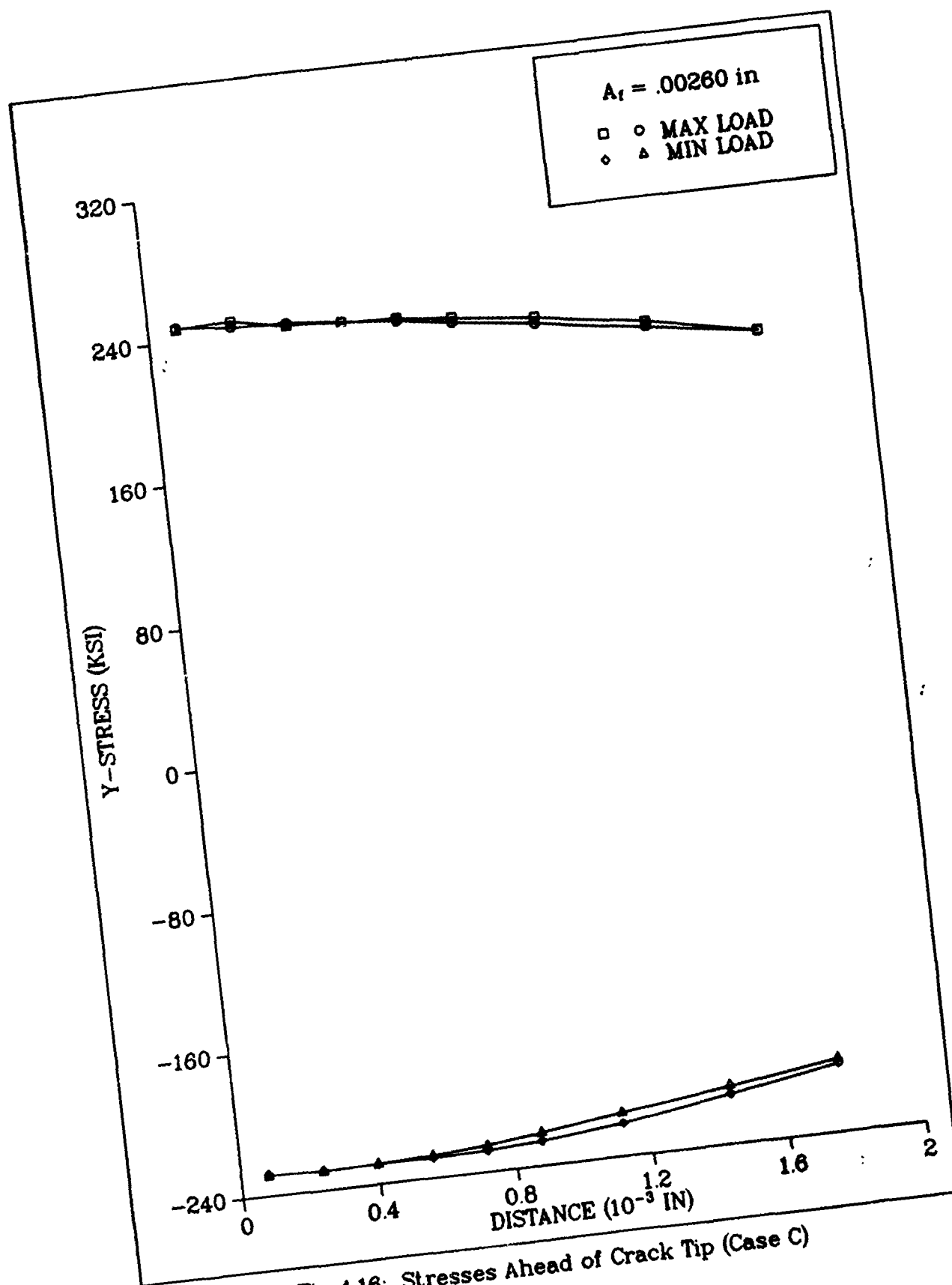
Fig 4.16: Stresses Ahead of Crack Tip (Case C)

68
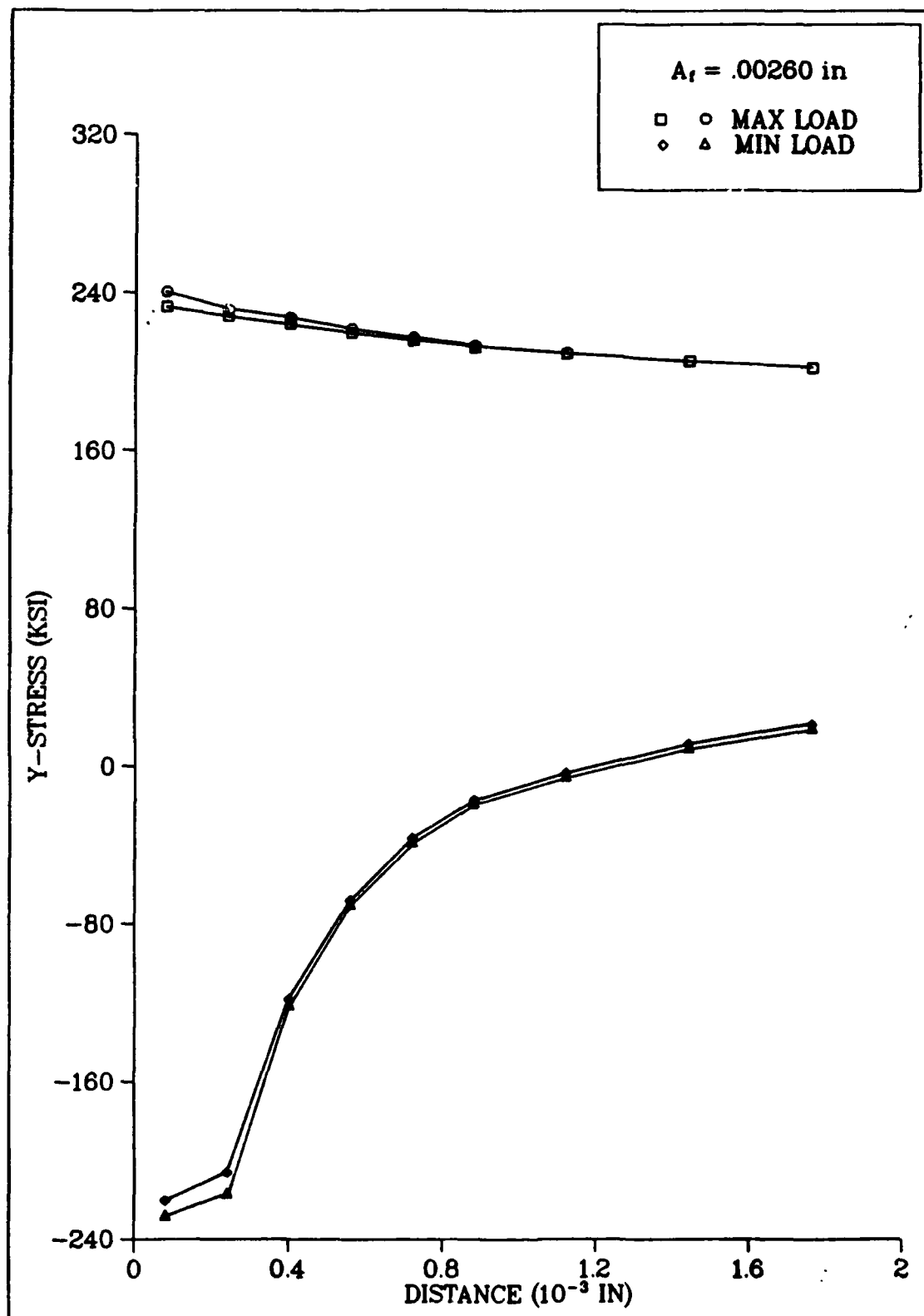
Fig 4.17: Stresses Ahead of Crack Tip (Case D)
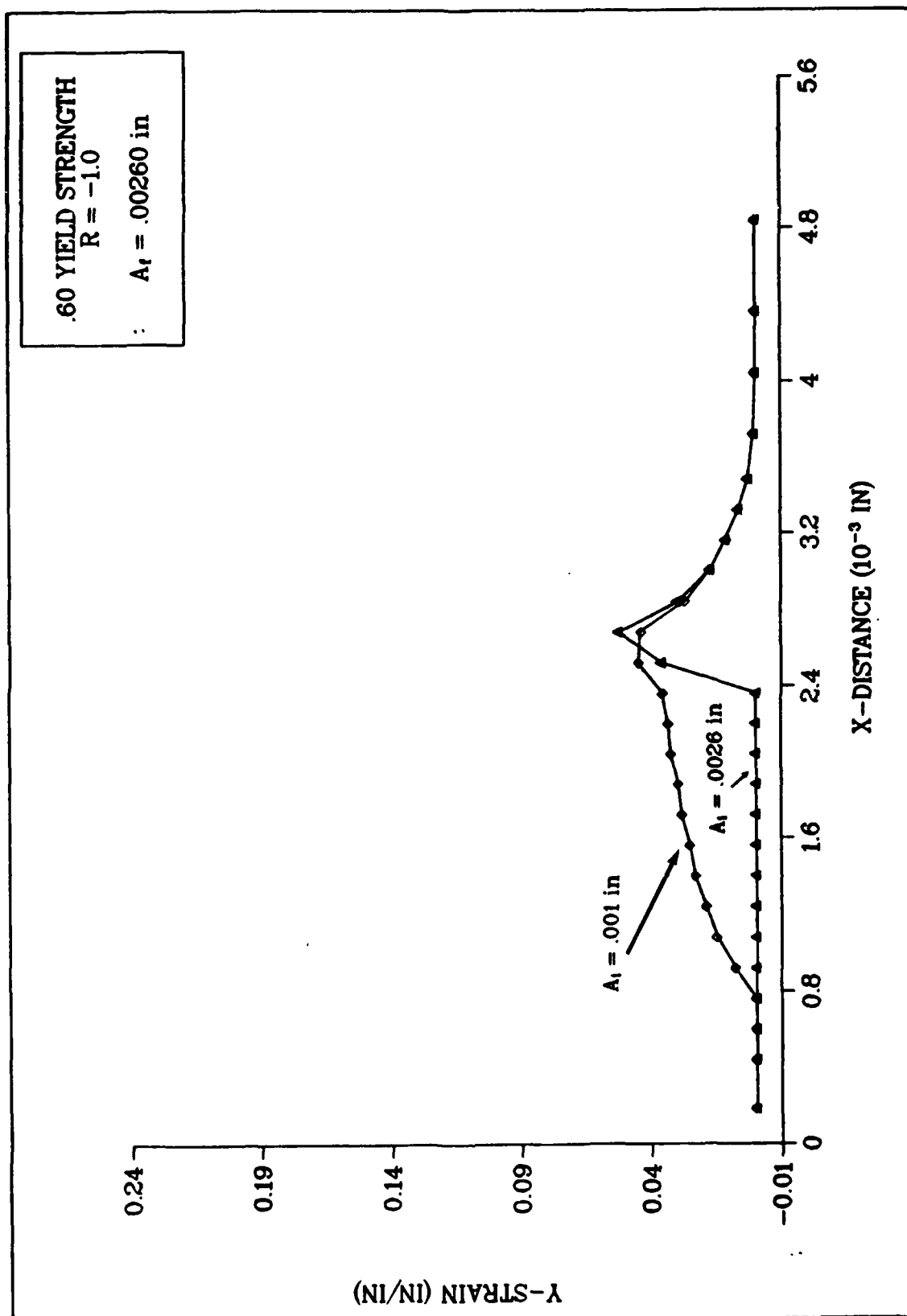
Fig 4.18: Plastic Strain Along X-Axis (Case A)
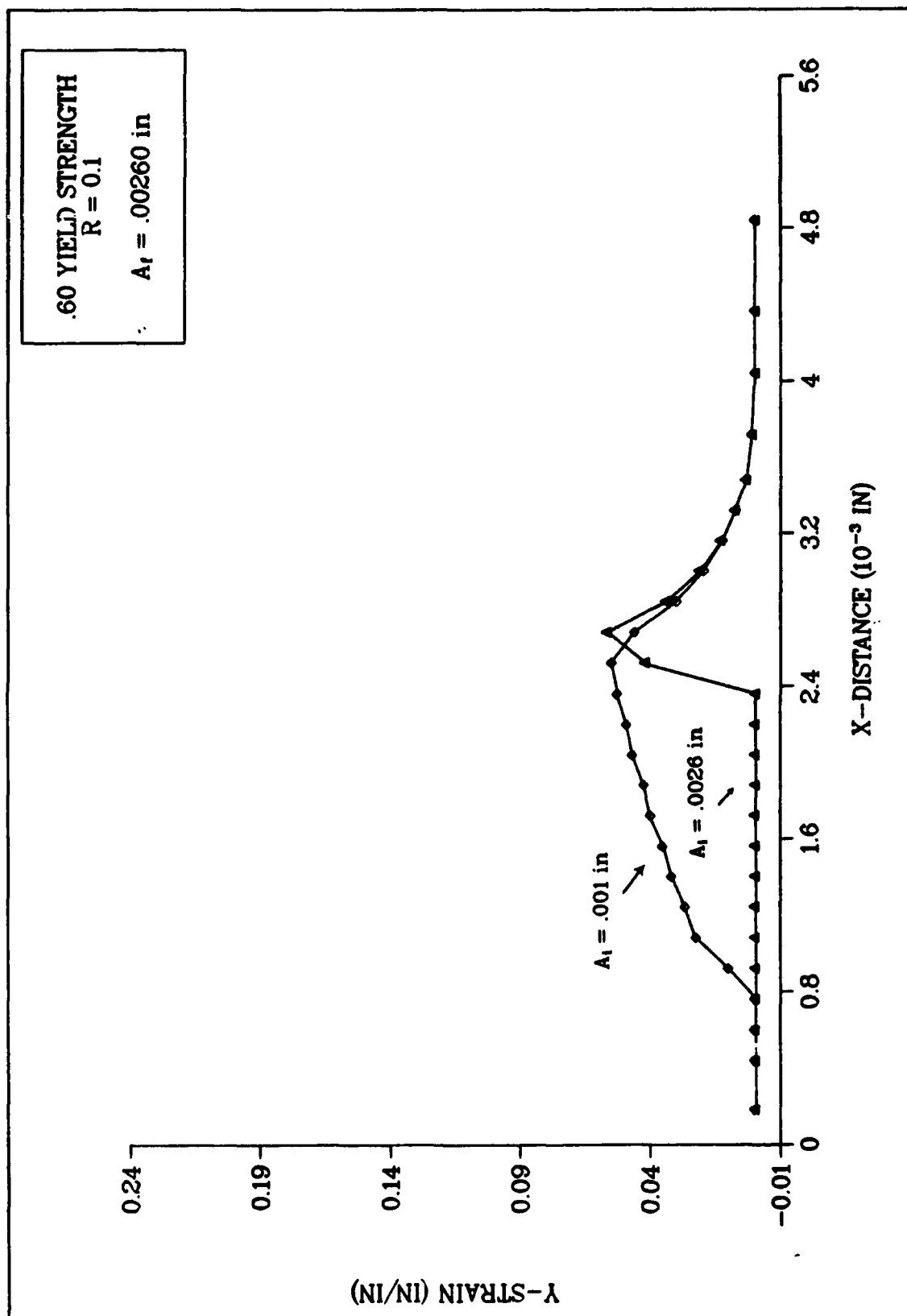
Fig 4.19: Plastic Strain Along X-Axis (Case B)

71
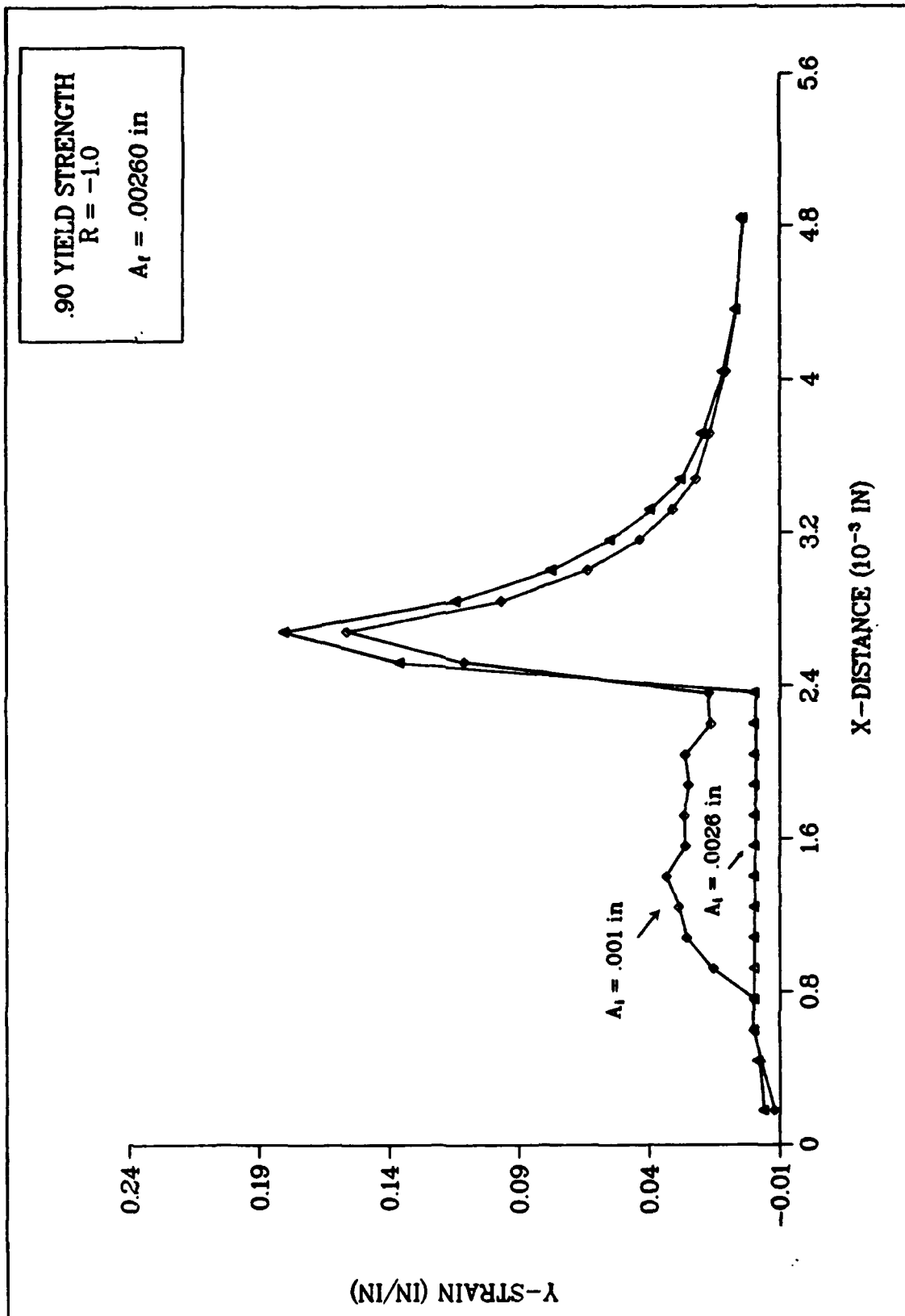
Fig 4.20: Plastic Strain Along X–Axis (Case C)

The figure shows a plot with axes labeled "Y–STRAIN (IN/IN)" and "X–DISTANCE (10^{-3} IN)". A legend box contains:

.90 YIELD STRENGTH
R = -1.0
A_f = .00260 in

Curve labels: A_i = .001 in and A_i = .0026 in

Fig 4.21: Plastic Strain Along X-Axis (Case D)

73

decrease asymptotically and approach those of the propagated cracks within several elements. In addition, the amount of plastic strain exhibited appears to be a function of both the nominal stress applied and the load ratio. In cases B and D, in Figures 4.19 and 4.21 where the load ratio is -1.0, the nominal stress is increased from 60 to 90 percent yield strength. The plastic strain observed in the propagated cracks rises dramatically in both cases. The plastic strain then appears to vary directly with load magnitude. When the load ratio is increased, a similar condition exists. At a load ratio of 0.1, the plastic strains along the crack 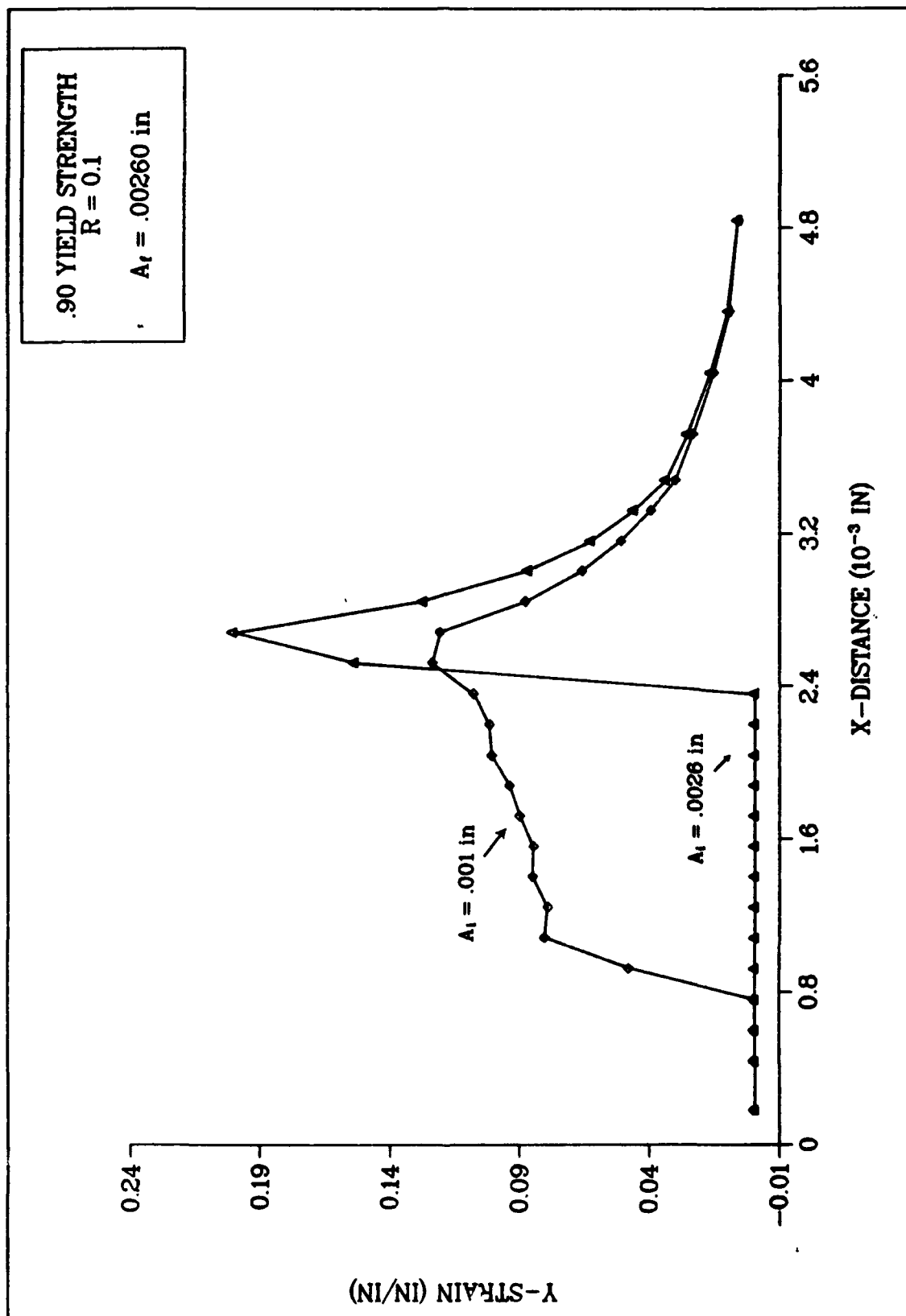length are greater than those with a load ratio of -1.0. The compressive forces present with the negative load ratio limit the accumulation of plastic strain.

Analysis of the y-direction plastic strains at maximum load yield several findings. No residual strains are exhibited behind the crack tip for the non-propagated crack. Ahead of the crack tip, however, these strains slightly exceed those of the propagated crack near the tip and then asymptotically approach those of the propagated crack at greater distances from the crack tip. The distance over which the plastic strains are measureable ahead of the crack tip, i.e., the size of the plastic zone, is approximately equal to the initial crack length of .001 inch. This condition is typical of short crack phenomena. The plastic strains immediately ahead of the crack tip are higher for the non-propagated crack than for the propagated crack. Further, by observing the strains behind the crack tip, it is seen that the plastic residual strains increase significantly as the nominal applied stress increases from 0.6 to 0.9 of the yield stress in the case of R = 0.1. However, for fully reversed loading, R = -1.0, the residual plastic

strains are lower and become smallest at the highest stress level. This indicates that severe compression develops in the wake under fully reversed loading and the plastic wake is compressed the most at the higher stress level in the region directly behind the crack tip.

By comparing the y-displacements behind the crack tip with corresponding residual strain data, several findings are made. The differences in the y-displacements for the non-propagated crack (larger displacements) and the propagated crack (smaller displacements) correspond to the plastic wakes behind the crack tip formed during crack growth. For the lower stress level, i.e., 0.6 yield stress, the plastic wake is larger for R = 0.1 than for the case where R = -1.0. This agrees with the amount of residual plastic strain observed in those cases. At the higher stress level, i.e., 0.9 yield stress, the larger plastic wake at R = 0.1 is observed in both the displacement profile and the strain profile. For R = -1.0, larger displacements occur at maximum load but the size of the plastic wake is similar to those of the lower stressvalues near the crack tip. At larger distances from the crack tip, residual strains decrease while maximum displacements become larger for the propagated crack than for the non-propagated crack. The highest amount of plastic deformation occurs for the higher stress level (0.9 yield stress) at R = 0.1.

Evidence of the increased amount of plasticity along the crack length due to fatigue crack growth is observed in several forms of closure data. Figures .22 through 4.25 present crack closure and opening data as a function of crack length. Here, P(clo) is the load at which some point on the crack closes. In the finite element analysis, this occurs when a node on the crack surface exhibits a
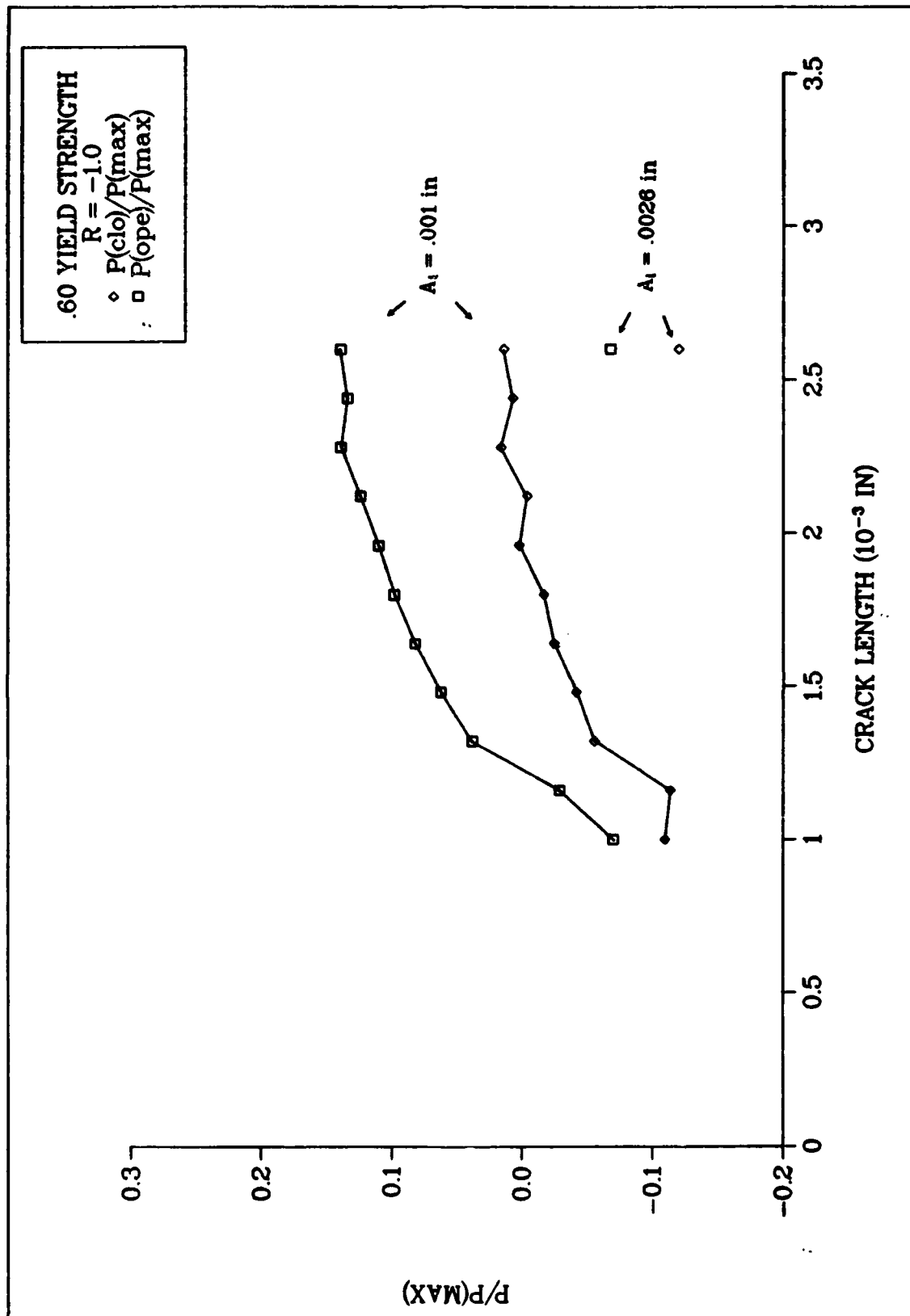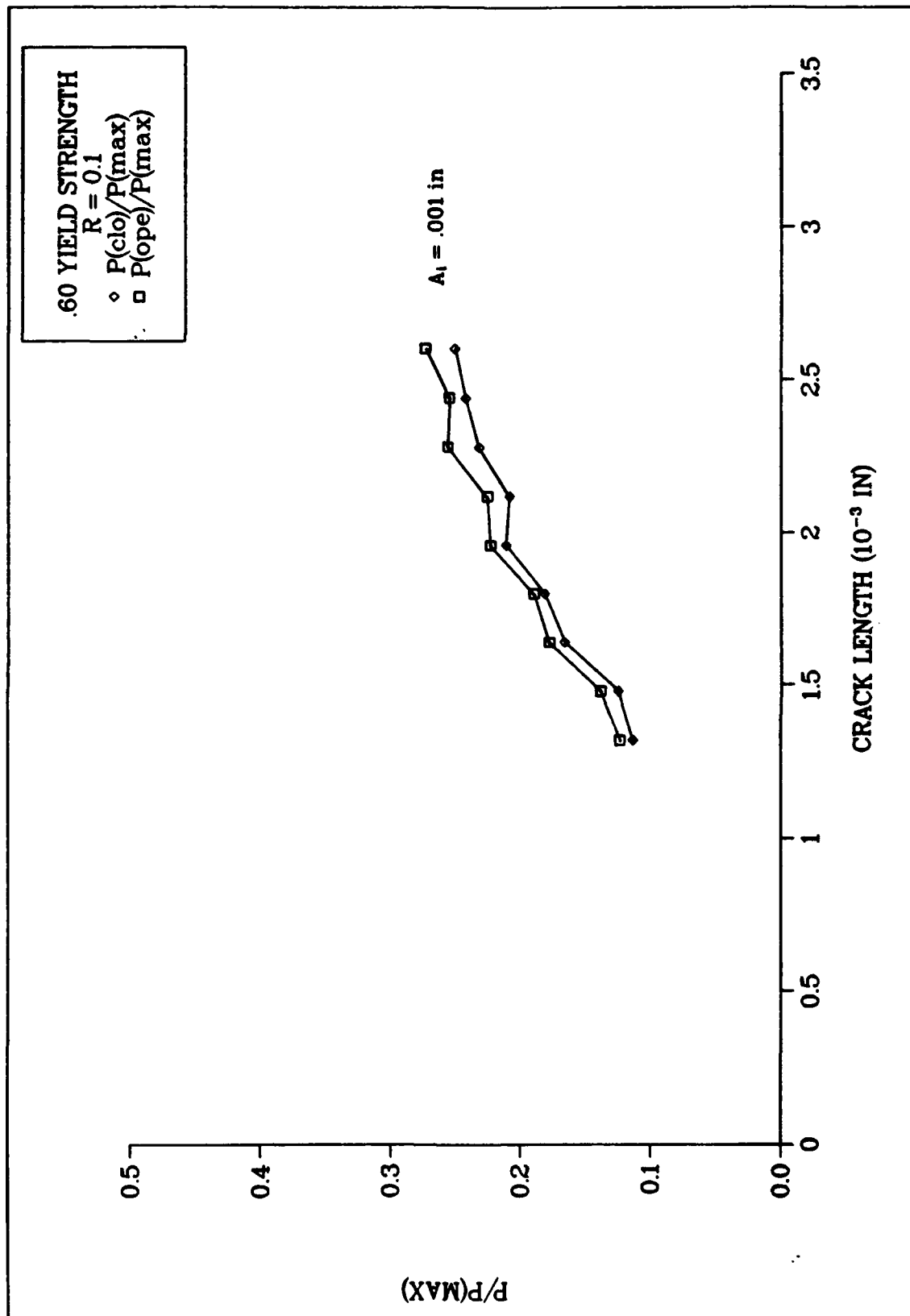
75

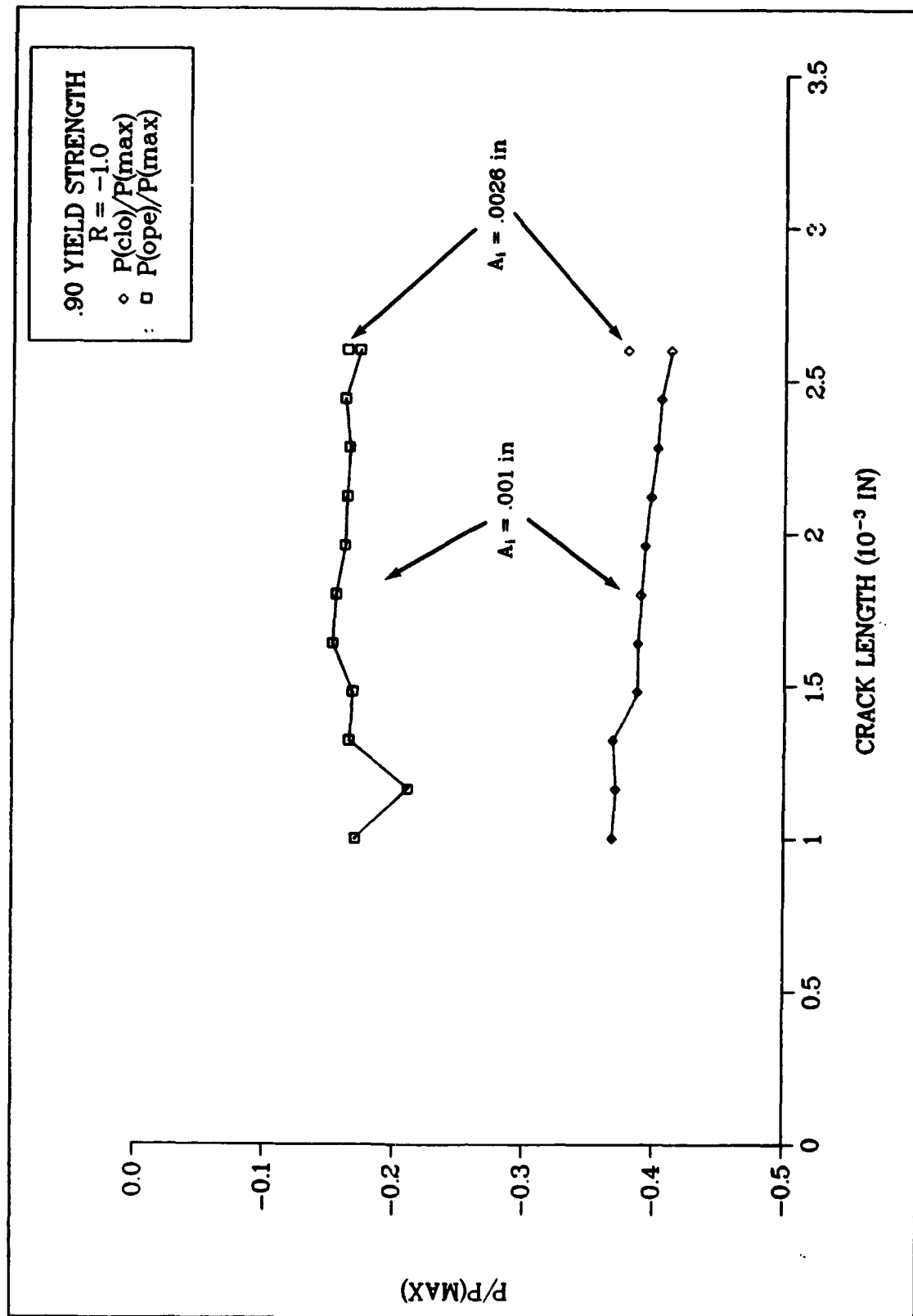Fig 4.22: Crack Closure (Case A)

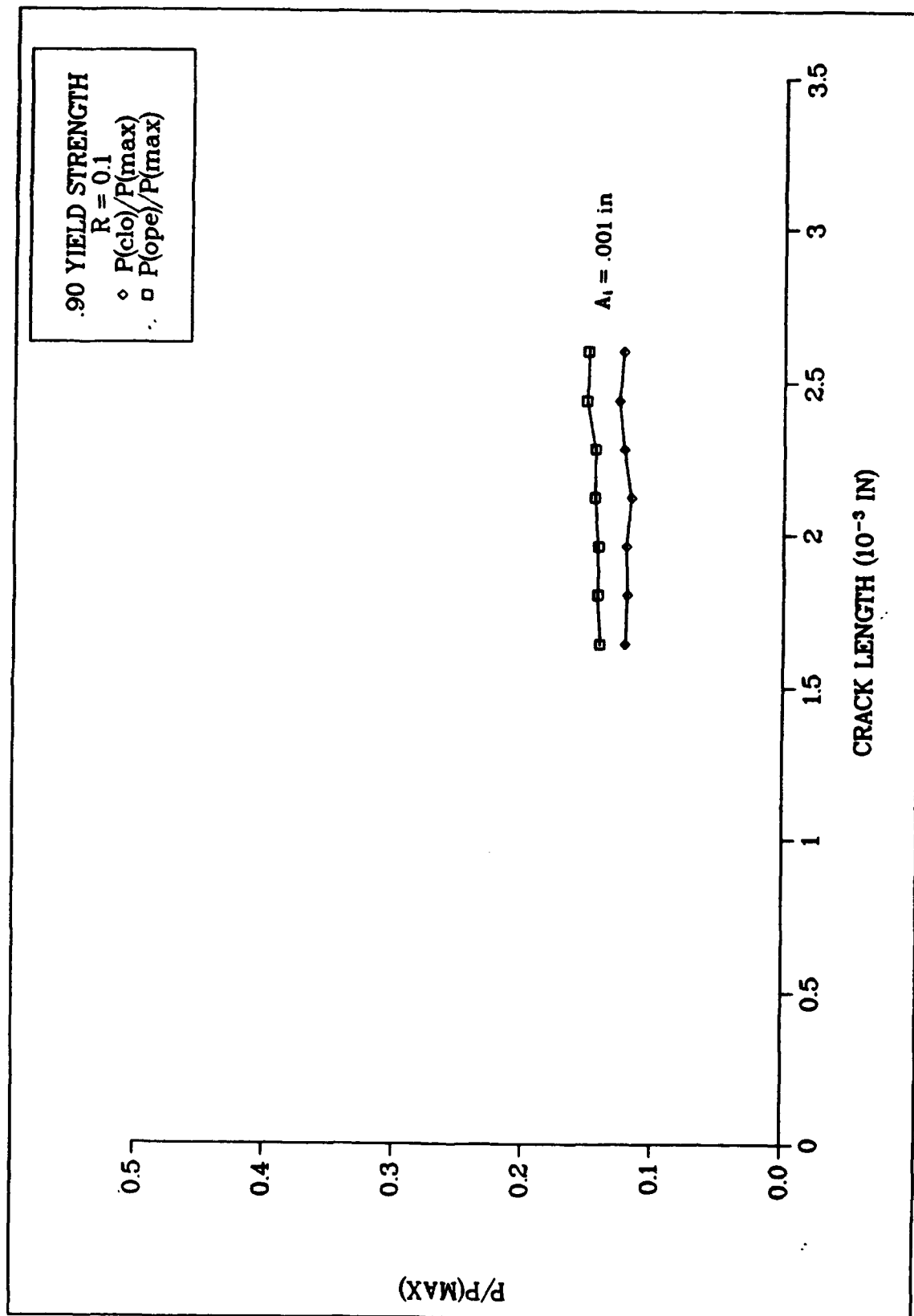Fig 4.23: Crack Closure (Case B)

77

Fig 4.24: Crack Closure (Case C)

78

Fig 4.25: Crack Closure (Case D)

negative displacement, thereby initiating the crack closure algorithm. P(ope) is the first point during reloading when all nodes along the crack surface exhibit positive displacements. At 60 percent material yield strength, both closure and opening values continue to increase as the crack propagates. As the crack grows and the plastic wake forms, there is a corresponding increase in residual compressive forces within the material during unloading. As a result, less external compression is required to close the crack and greater tension is required before the crack reopens on subsequent loading. In cases C and D, Figures 4.24 and 4.25, the nominal stresses are greater. The closure data here does not show the increases that are evident at lower stress values. In these cases, the closure and opening values are nearly constant. There appears to be a limit in closure loads which is a function of the load conditions. For fully reversed loading as in case C, the closure load decreases as the crack extends. As the size of the plastic area is reduced because of high compressive stresses, the residual compressive stresses are also reduced. As a result, greater forces are required to close the crack.

The difference between crack opening and crack closure discussed above is most noticeable for the cases where R = -1.0 which exhibit large hysteresis loops under fully reversed loading. This hysteresis is largest at the higher stress level of 0.9 yield stress (Figures 4.10 and 4.12). Further, closure continues to develop over the total amount of crack extension at the lower stress level of 0.6 yield stress. If the crack does not propagate, the closure load at the final crack length is approximately the same as for the crack before it was allowed to grow. At higher stress levels the closure load does not vary considerably as

the crack extends. At the higher stress levels the plastic deformation occurring behind the crack tip reaches an equilibrium condition with little or no extension. This is also observed for the case where the nominal stress is 0.9 yield stress and fully reversed loading occurs. The closure load for the longer crack length with no plastic strain history is nearly the same for the propagated crack. At this higher stress level, but where R - 0.1, the closure load reaches a value slightly greater than the minimum load after crack extension and then remains constant. For the non-propagated crack, no closure develops and therefore the closure load must be less than the minimum load applied.

Another method of measuring closure is to observe the closure load as a function of crack length. Closure load has been converted to closure stress intensity using the elastic stress intensity solution for the single edge cracked specimen and these data have been plotted against K(max) for all four cases in Figures 4.26 to 4.29. At lower applied stresses (Figures 4.26 and 4.27), K(clo) and K(ope) for the propagating crack increase with K(max). At higher applied stresses (Figures 4.28 and 4.29), the same is not true. At a load ratio of -1.0, the values of K(clo) and K(ope) decrease with an increase in K(max) and remain nearly constant at a load ratio of 0.1. The higher compressive stresses ahead of the crack tip result in lower values of K(clo) and K(ope).

For plasticity induced closure, analytical and experimental results indicate that K(clo) or K(ope) increases linearly as K(max) increases [32]. For R - 0.1, K(clo) increases with K(max) for the lower applied stress. For the higher applied stress, K(clo) decreases with increases in K(max). This indicates that there is no single-valued function of
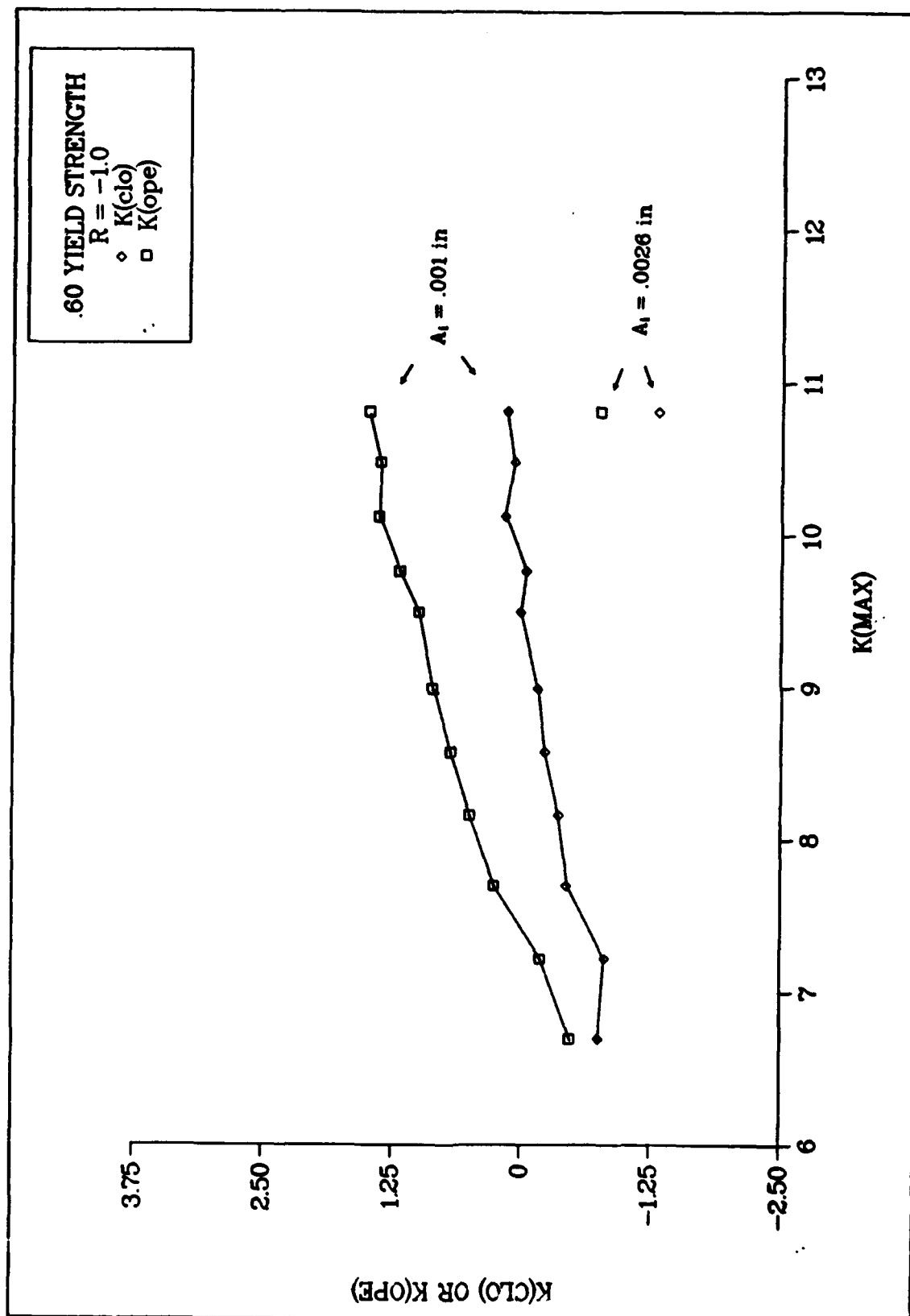
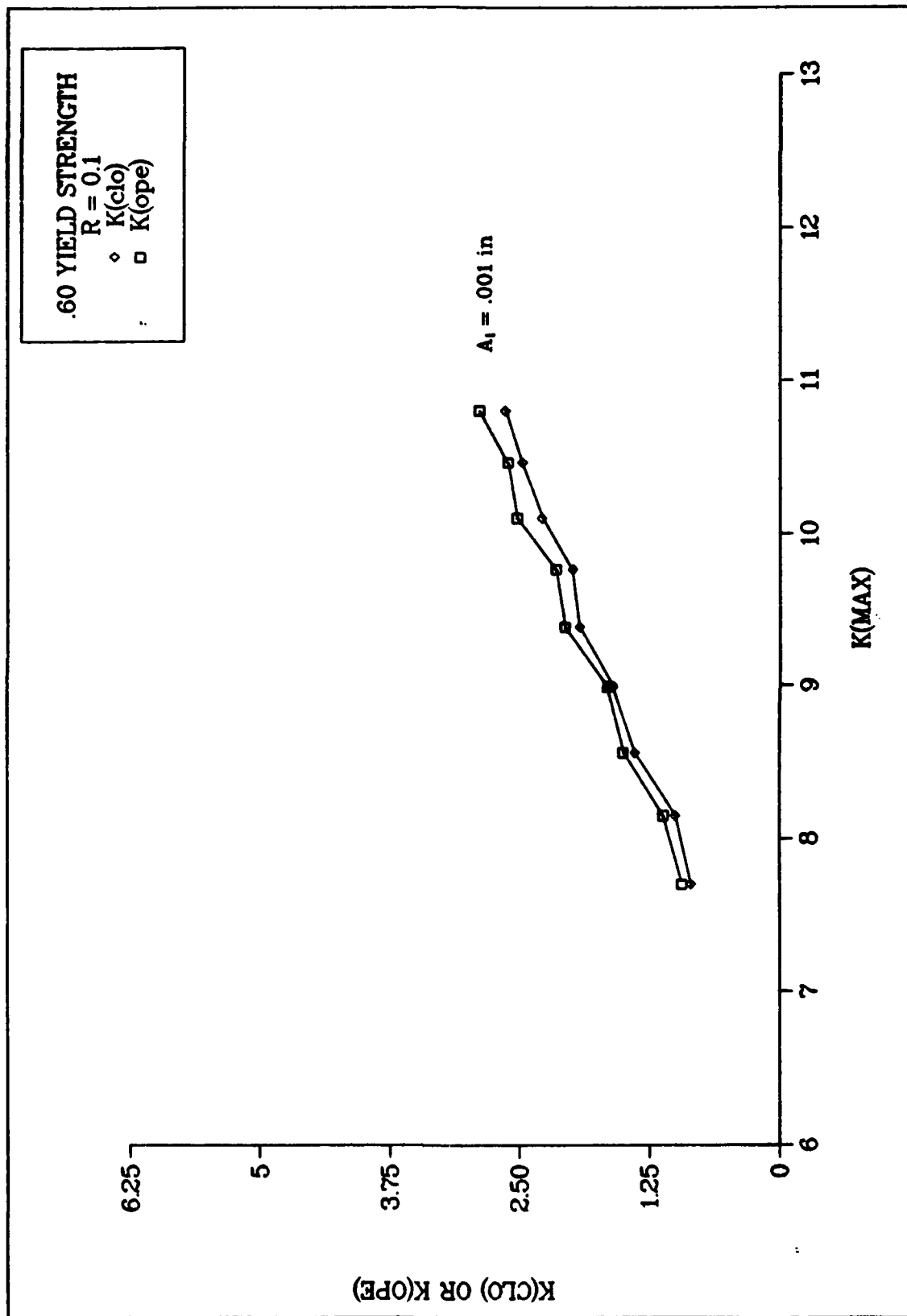Fig 4.26: Crack Closure As a Function of K (Case A)

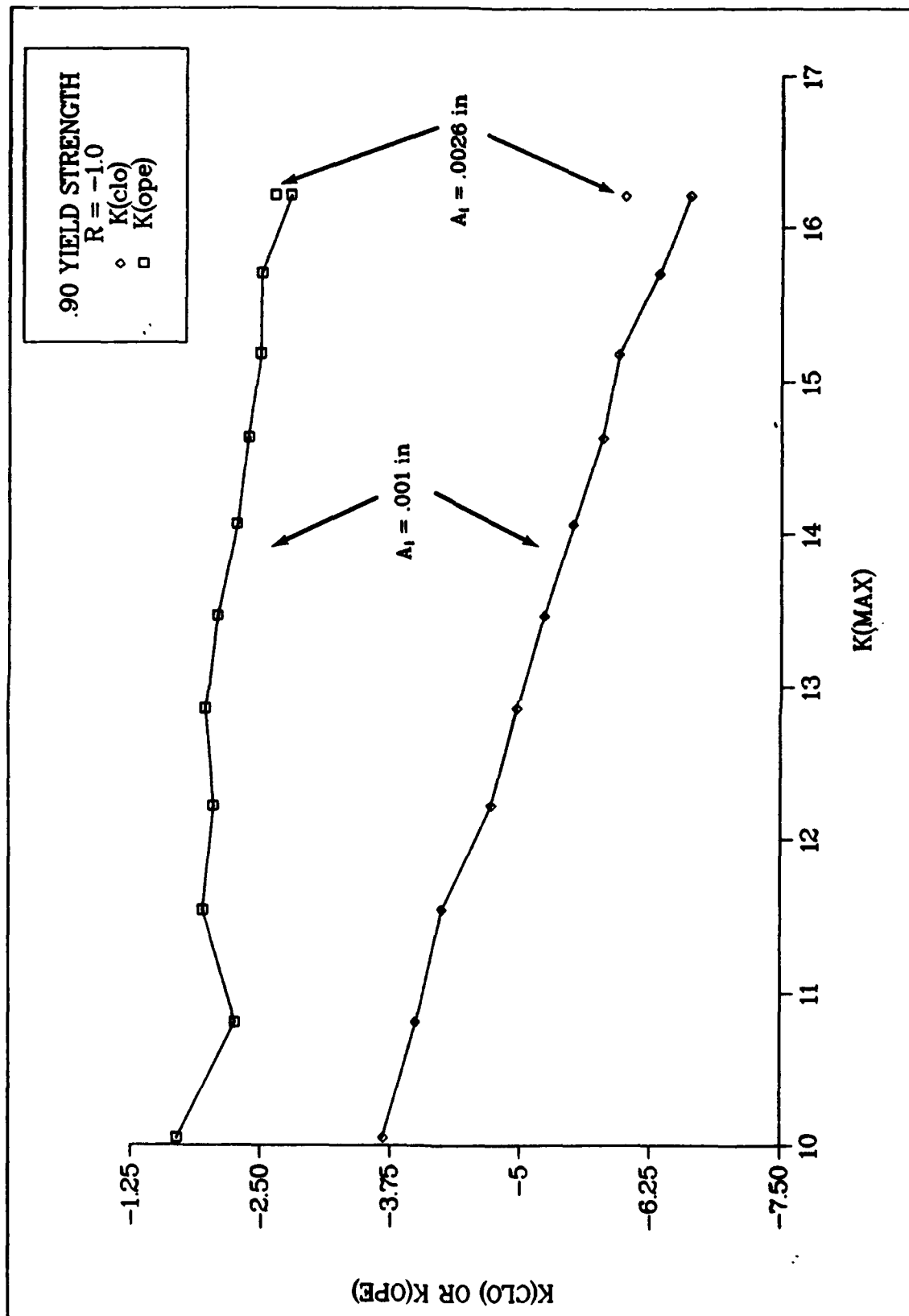Fig 4.27: Crack Closure As a Function of K (Case B)

Fig 4.28: Crack Closure As a Function of K (Case C)
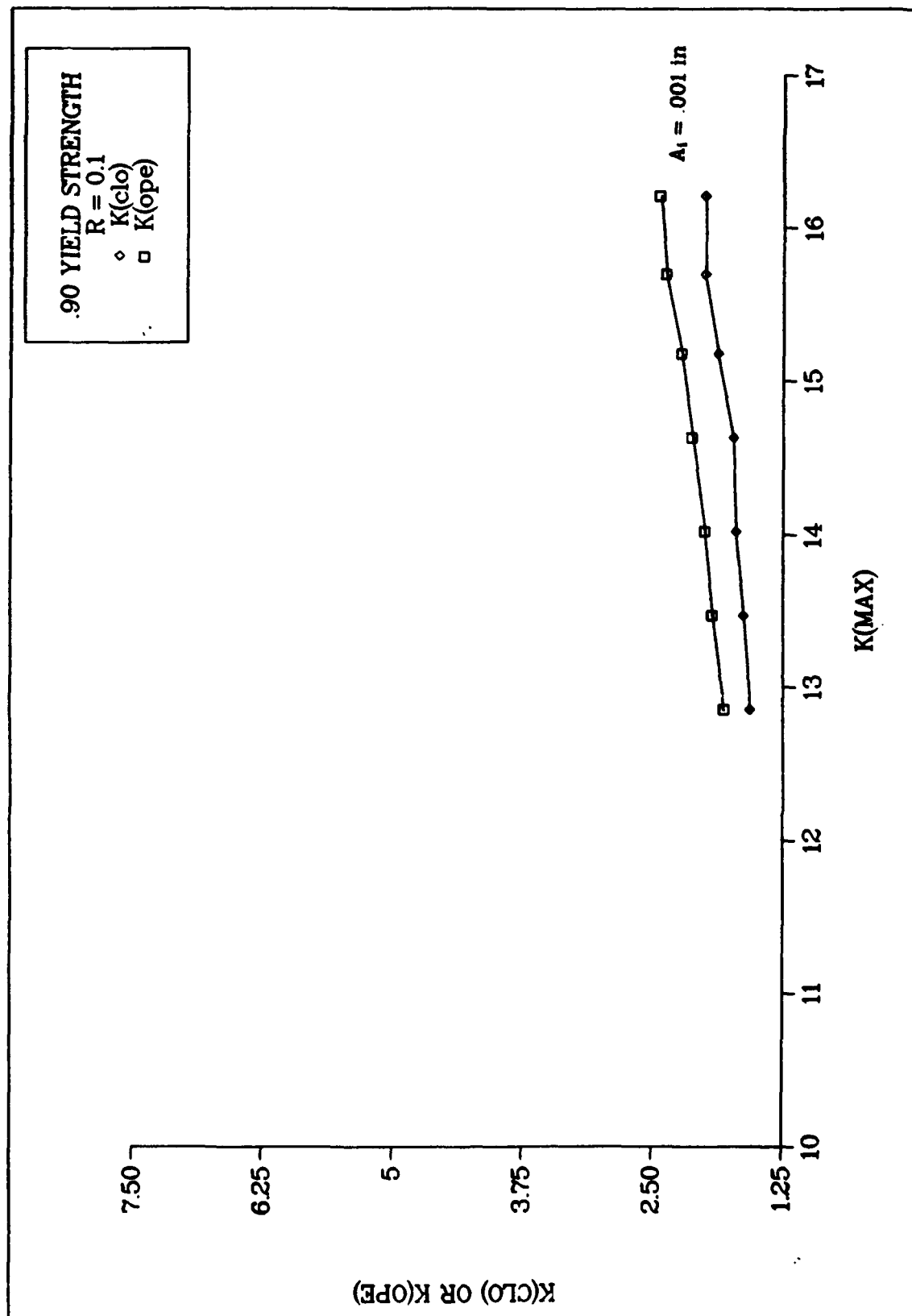
Fig 4.29: Crack Closure As a Function of K (Case D)

K(clo) against K(max) for R = 0.1. At the higher stress levels there are compressive stresses generated ahead of the crack tip because of the higher stress range coupled with the maximum stress being limited by the yield stress. This results in a residual deformation pattern caused by cyclic plasticity leading to lower values of K(clo). At a stress ratio of R = -1.0 and at the higher stress level, the value of K(ope) remains relatively constant at a sightly negative value while K(clo) decreases with increasing crack extension. K(ope) and K(clo) for the non-propagating crack do not differ significantly from the propagating crack at the final crack length. Closure here appears to be a result of cyclic plastic deformation at or near the crack tip rather than as a result of the residual plastic wake behind the propagating crack. At the lower stress level, however, K(ope) and K(clo) for the non-propagating crack differ significantly from the propagating crack. Here K(ope) increases faster than K(clo) as K(max) increases.

As previously discussed, closure may be analytically determined as the point where nodal displacements become either negative or zero in the finite element code. Experimentally, however, closure data is normally determined through the use of load-displacement curves obtained from measurements taken from a test specimen. Out of necessity, these measurements are usually taken at or near the crack mouth. Figures 4.30 through 4.53 present load-displacement and load-delta displacement for three nodes along the crack surface. Node 192 represents the crack mouth, whereas nodes 205 and 206 are those immediately adjacent to the crack tip. Figure 3.7 shows this node numbering scheme. The closure load determined from load-displacement data is that point at which the curve becomes non-linear. At points distant from the crack tip, this

86

Fig 4.30: Load – Displacement (Case A/Elem 192)

Fig 4.31: Load — Delta Displacement (Case A/Elem 192)

Fig 4.32: Load — Displacement (Case A/Elem 205)

The chart contains the following labels:

.60 YIELD STRENGTH
R = -1.0
A_f = .00260 in
A_i = .00100 in

Y-axis: P/PMAX (1, 0.6, 0.2, -0.2, -0.6, -1.)

X-axis: DISPLACEMENT (10^{-3}IN) (0.000, 0.004, 0.008, 0.012, 0.016, 0.020, 0.024, 0.028)

89

.60 YIELD STRENGTH
R = −1.0
A_f = .00260 in
A_i = .00100 in

Fig 4.33: Load − Delta Displacement (Case A/Elem 205)

Fig 4.34: Load − Displacement (Case A/Elem 206)

91

Fig 4.35: Load — Delta Displacement (Case A/Elem 206)

Fig 4.36: Load – Displacement (Case B/Elem 192)

93

Fig 4.37: Load – Delta Displacement (Case B/Elem 192)

94
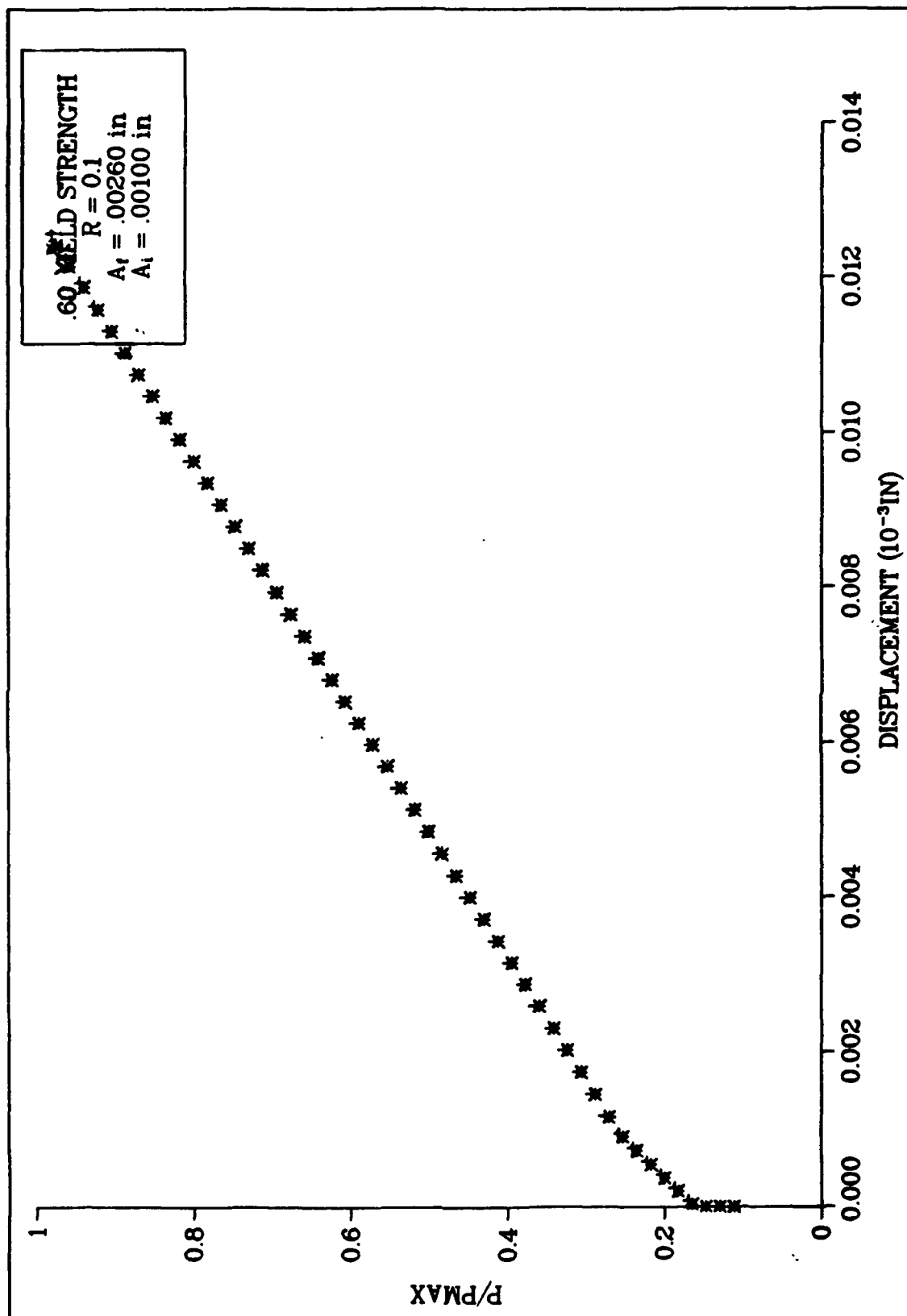
Fig 4.38: Load – Displacement (Case B/Elem 205)

95

.60 YIELD STRENGTH
R = 0.1
A_f = .00260 in
A_i = .00100 in
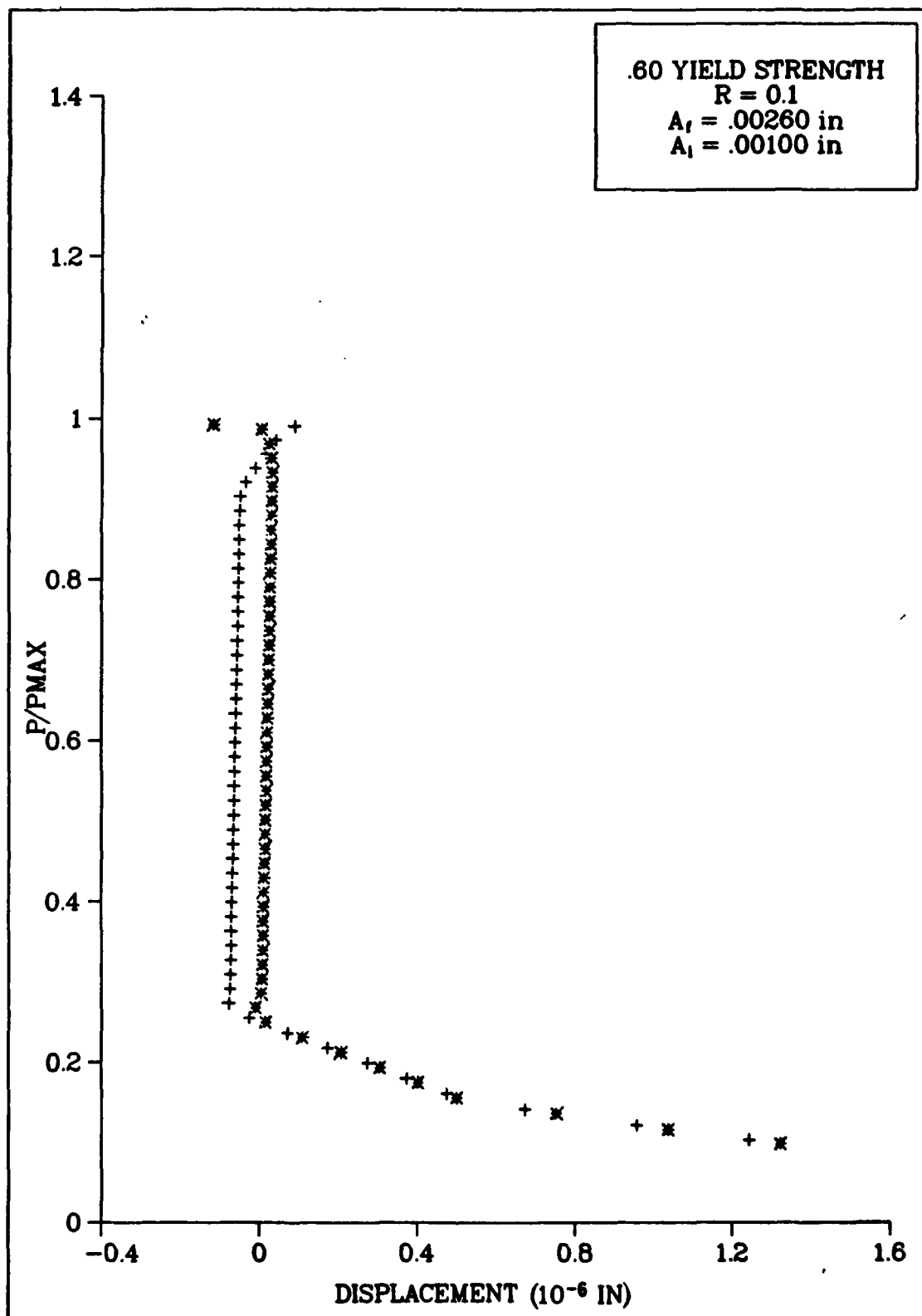
Fig 4.39: Load − Delta Displacement (Case B/Elem 205)
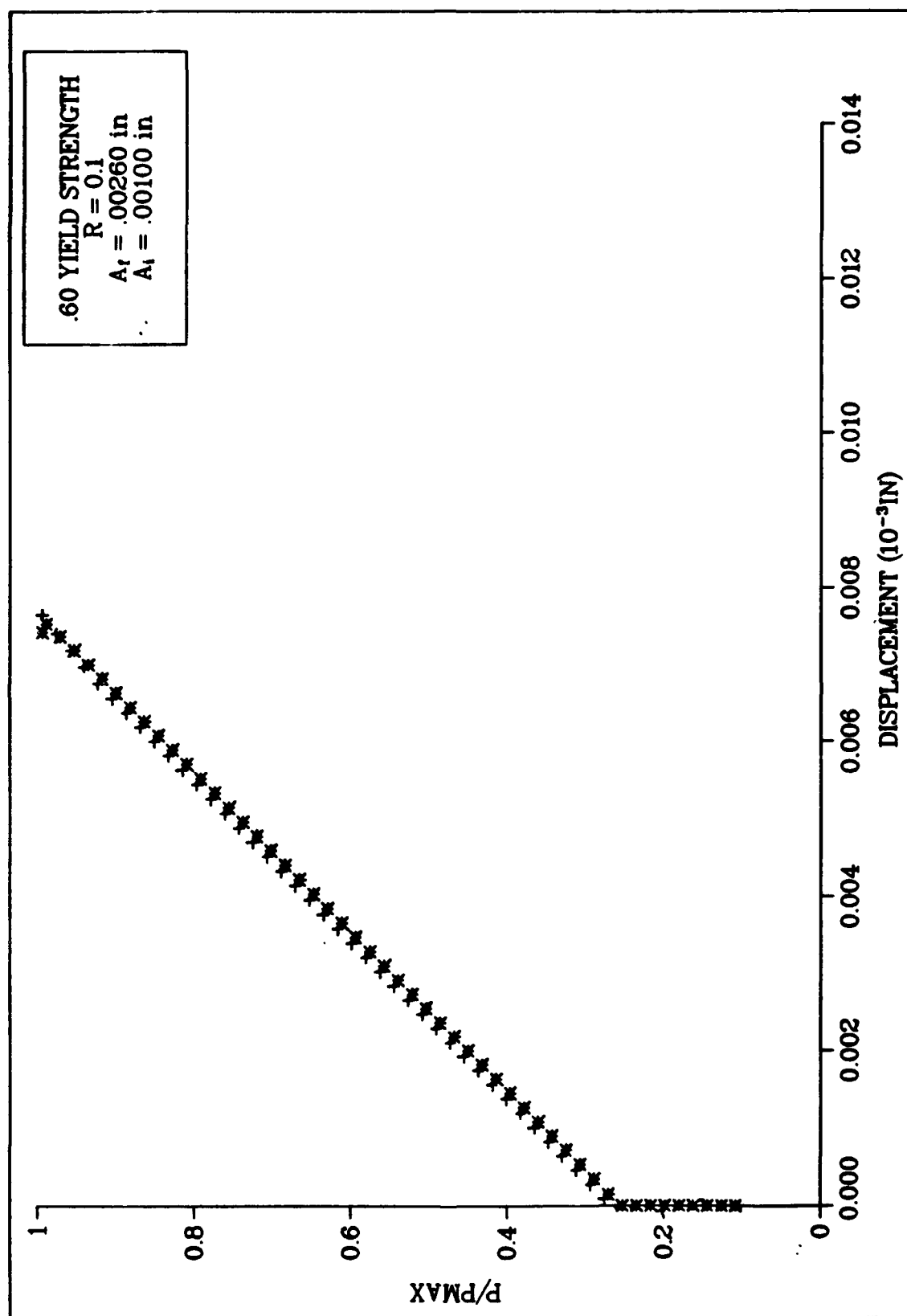
Fig 4.40: Load – Displacement (Case B/Elem 206)
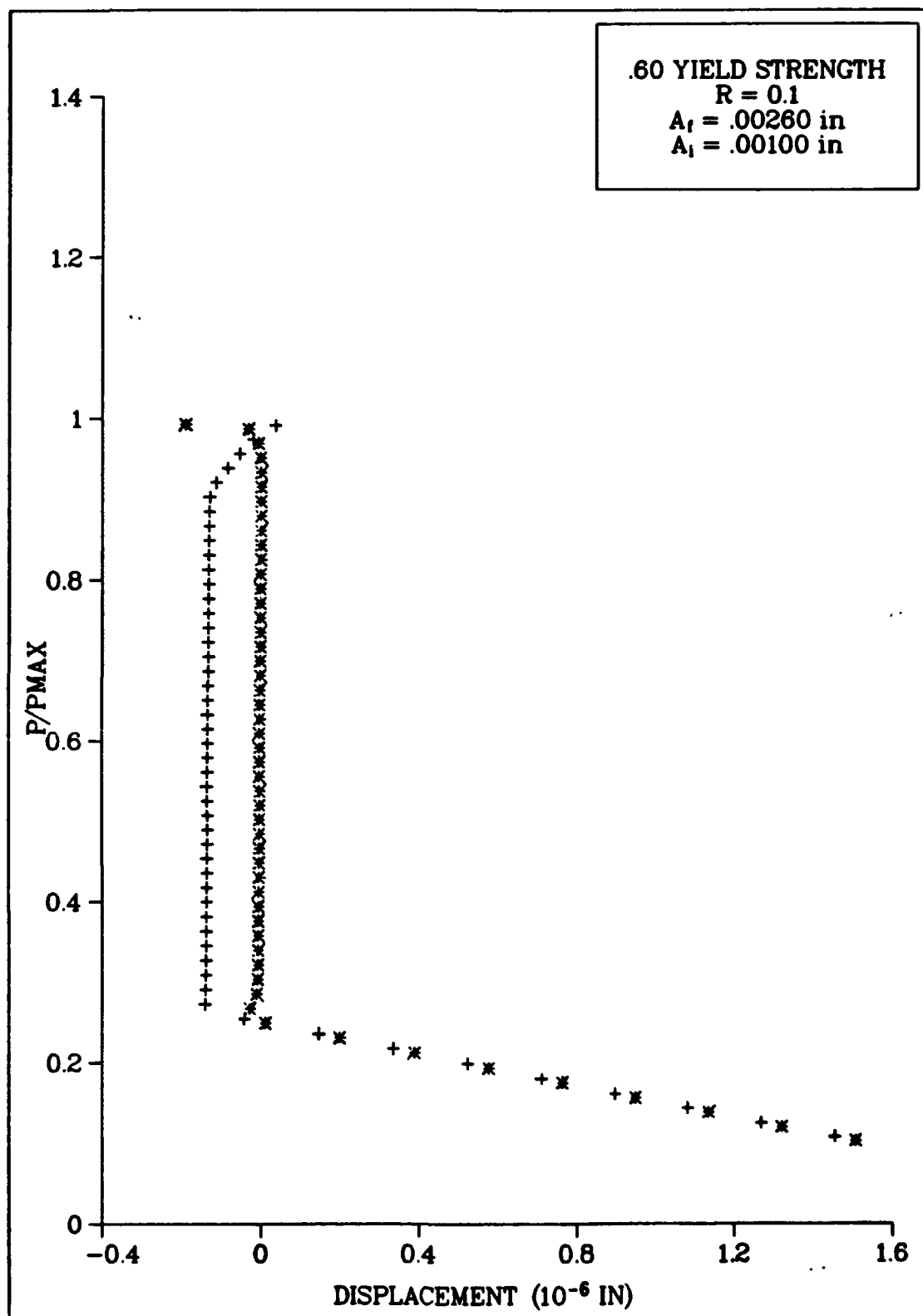
Fig 4.41: Load – Delta Displacement (Case B/Elem 206)

98
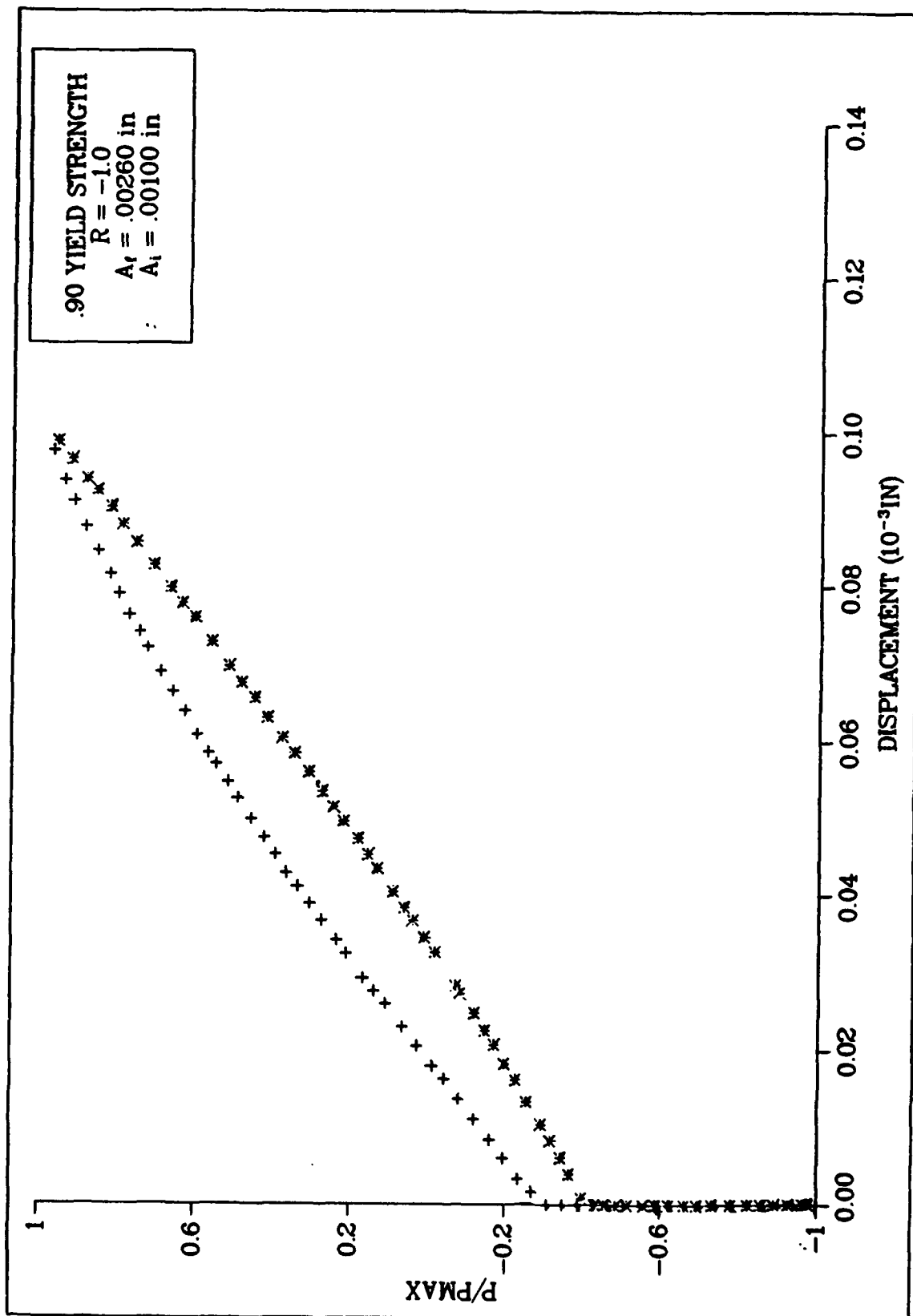
Fig 4.42: Load – Displacement (Case C/Elem 192)
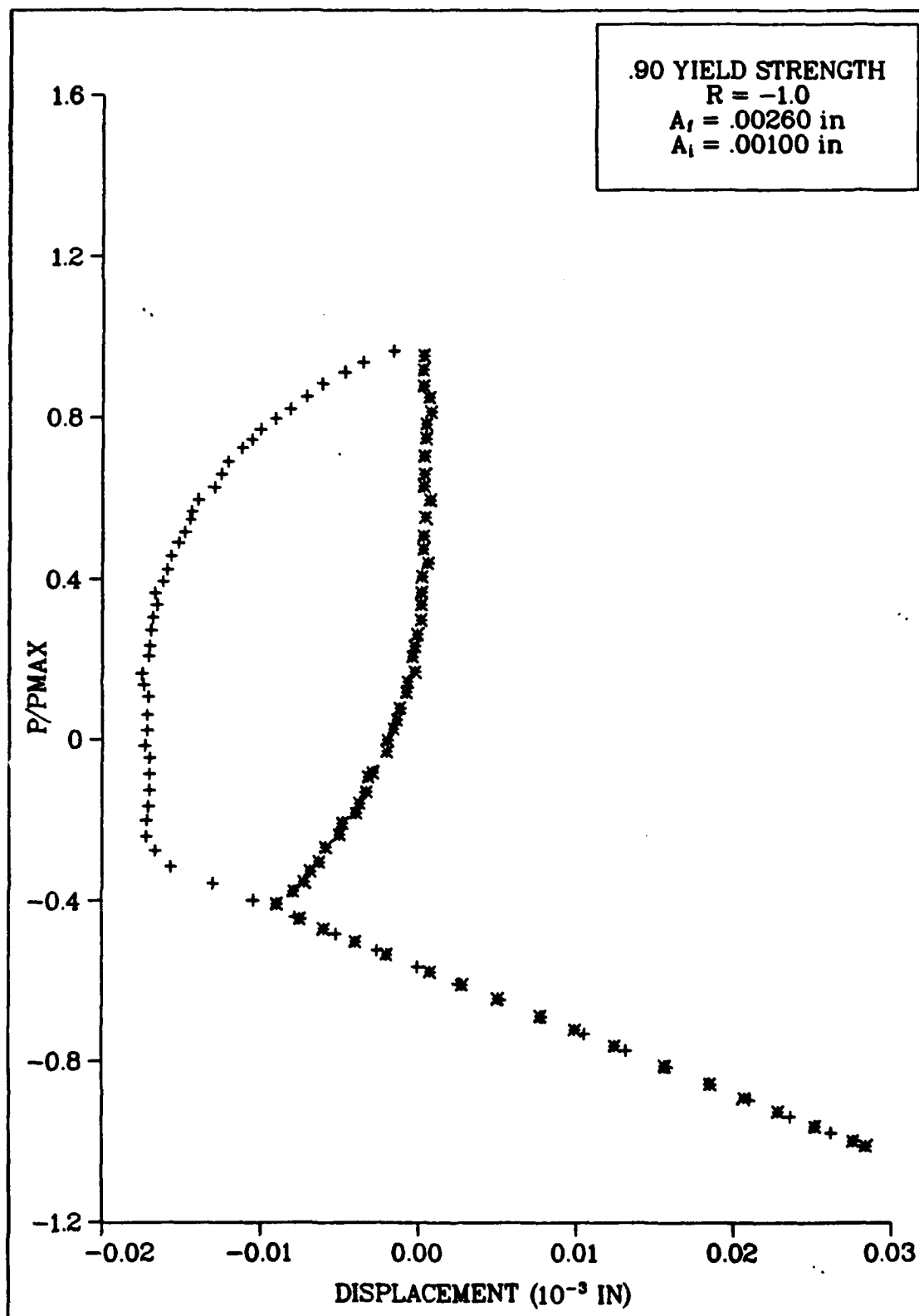
Fig 4.43: Load – Delta Displacement (Case C/Elem 192)
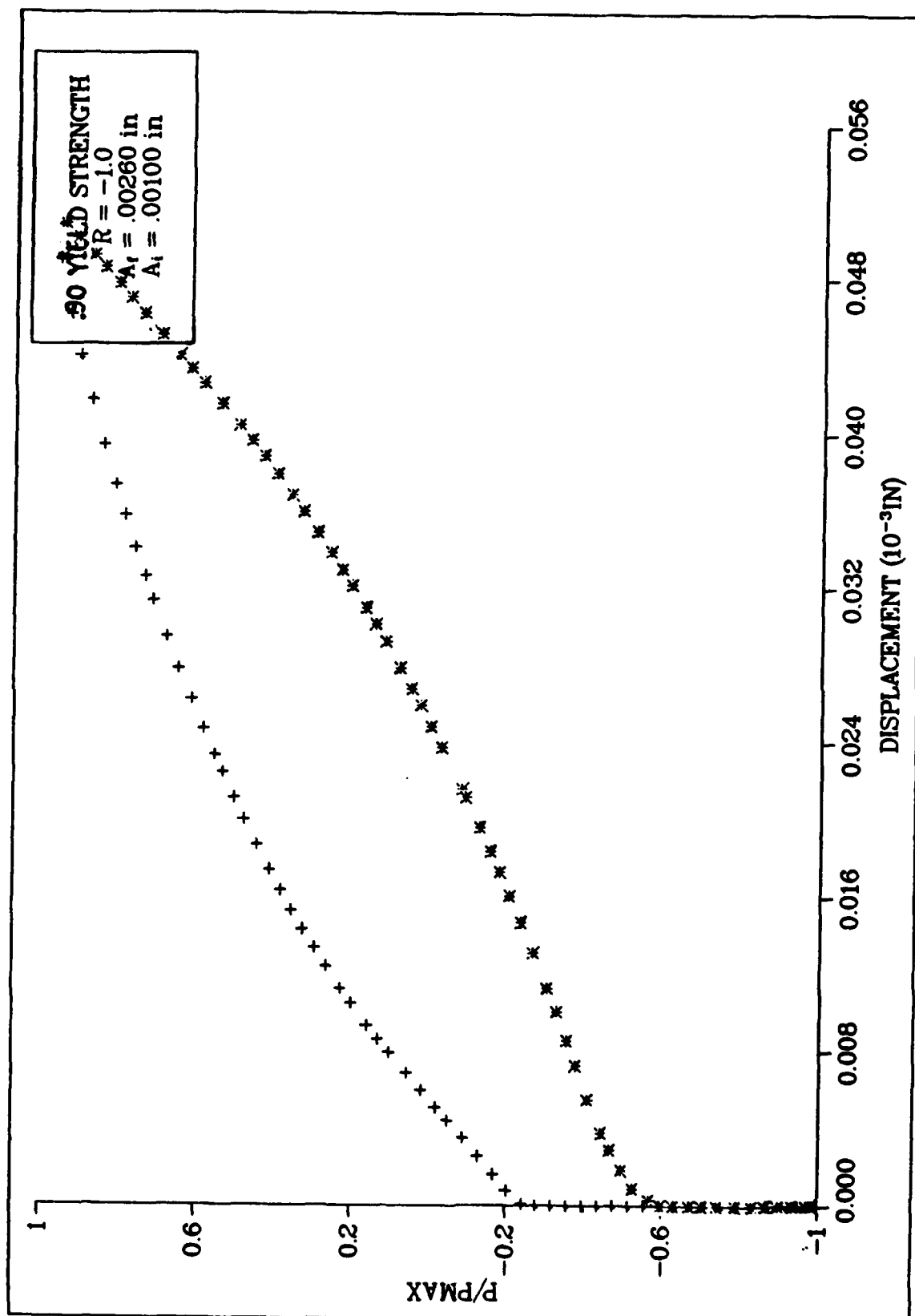
Fig 4.44: Load – Displacement (Case C/Elem 205)

101
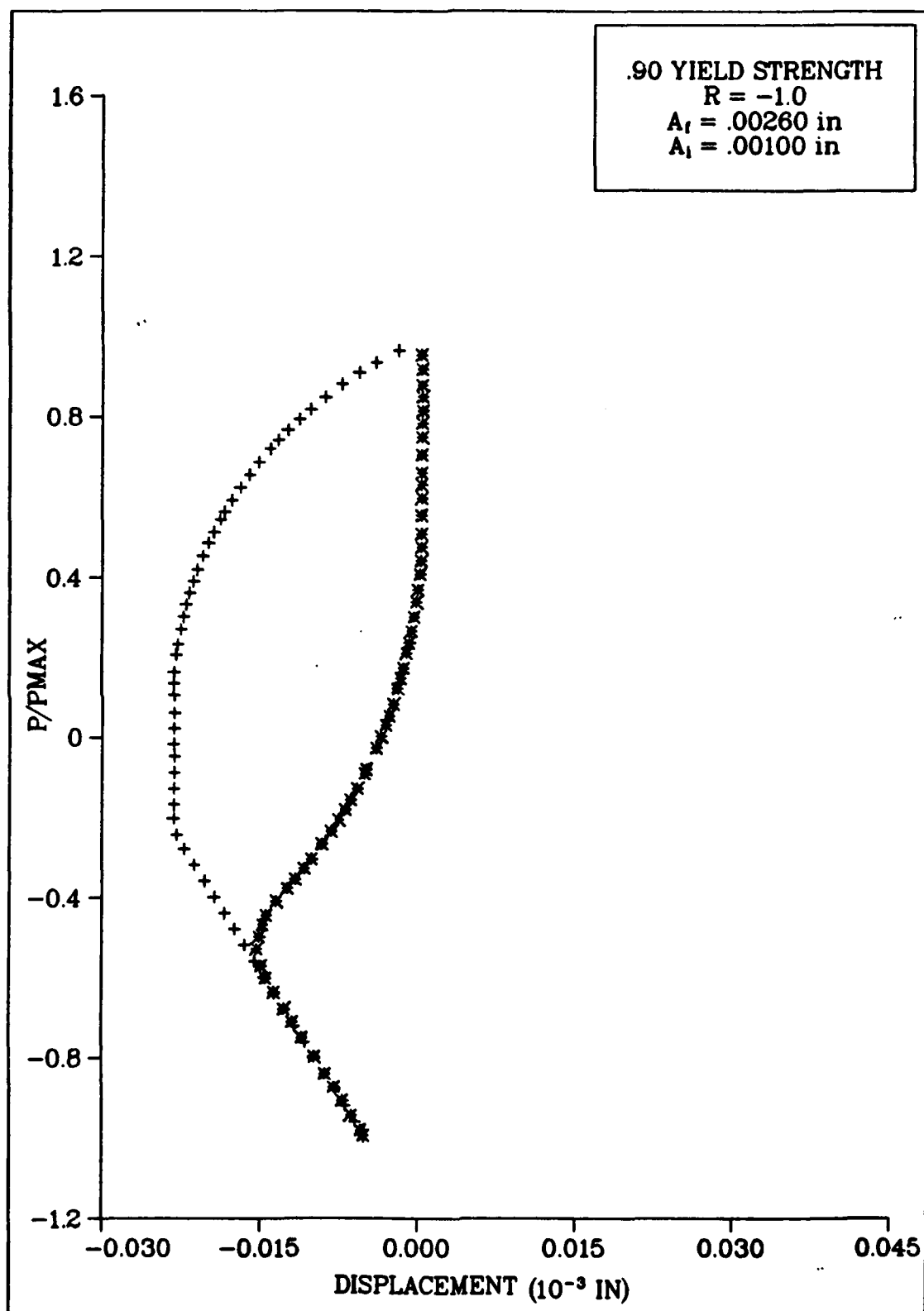
Fig 4.45: Load — Delta Displacement (Case C/Elem 205)

102
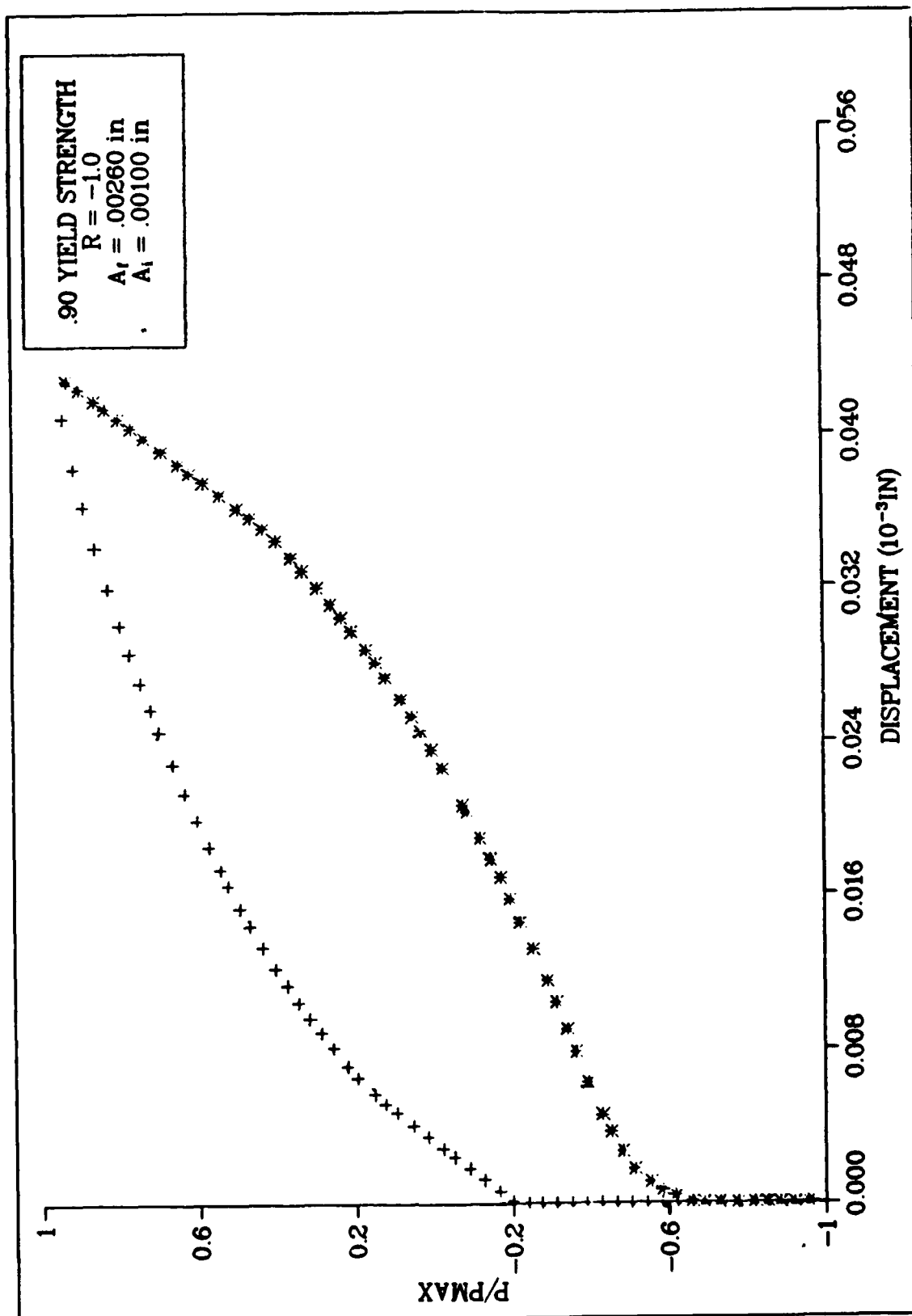
Fig 4.46: Load – Displacement (Case C/Elem 206)

103
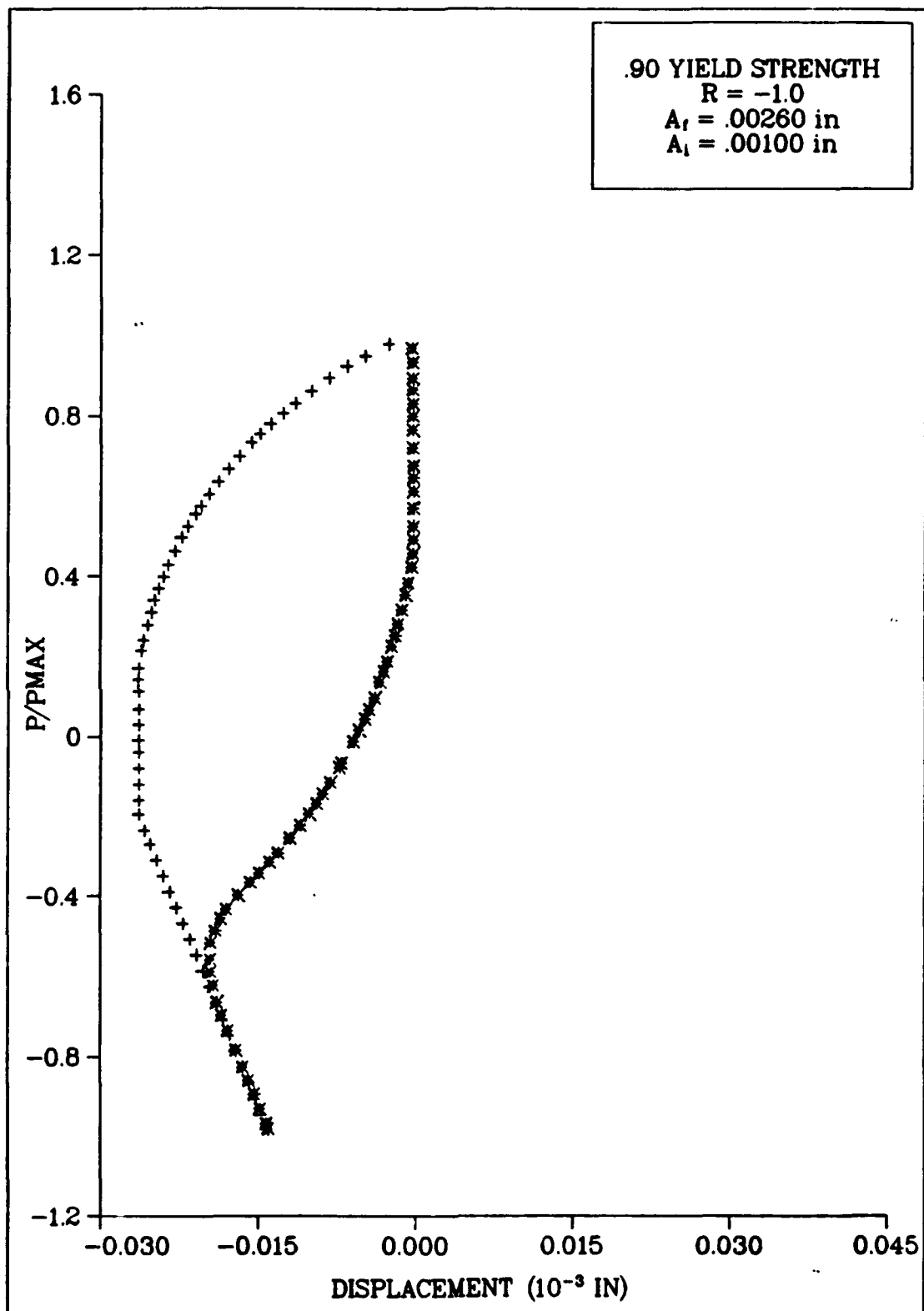
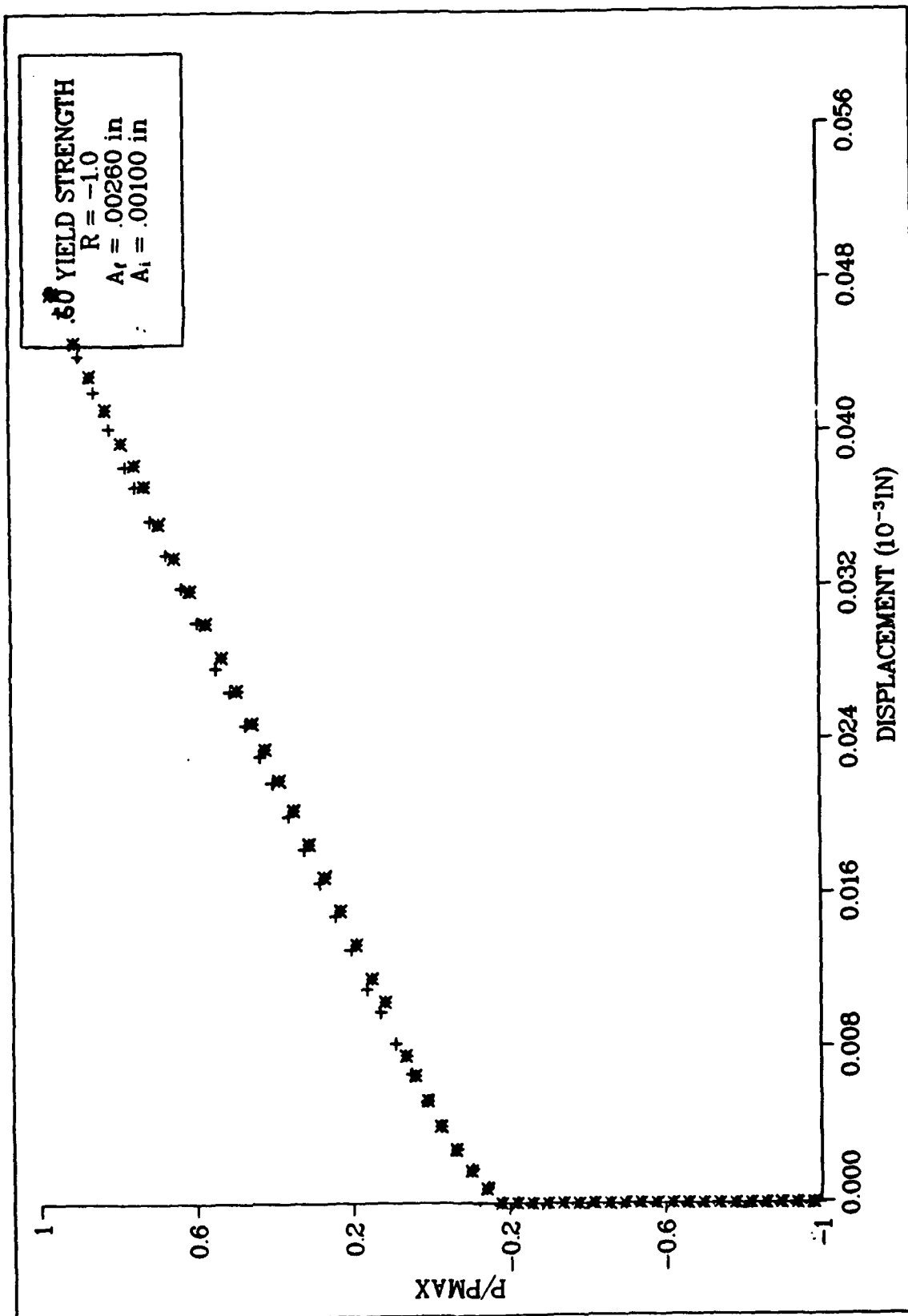Fig 4.47: Load – Delta Displacement (Case C/Elem 206)

104
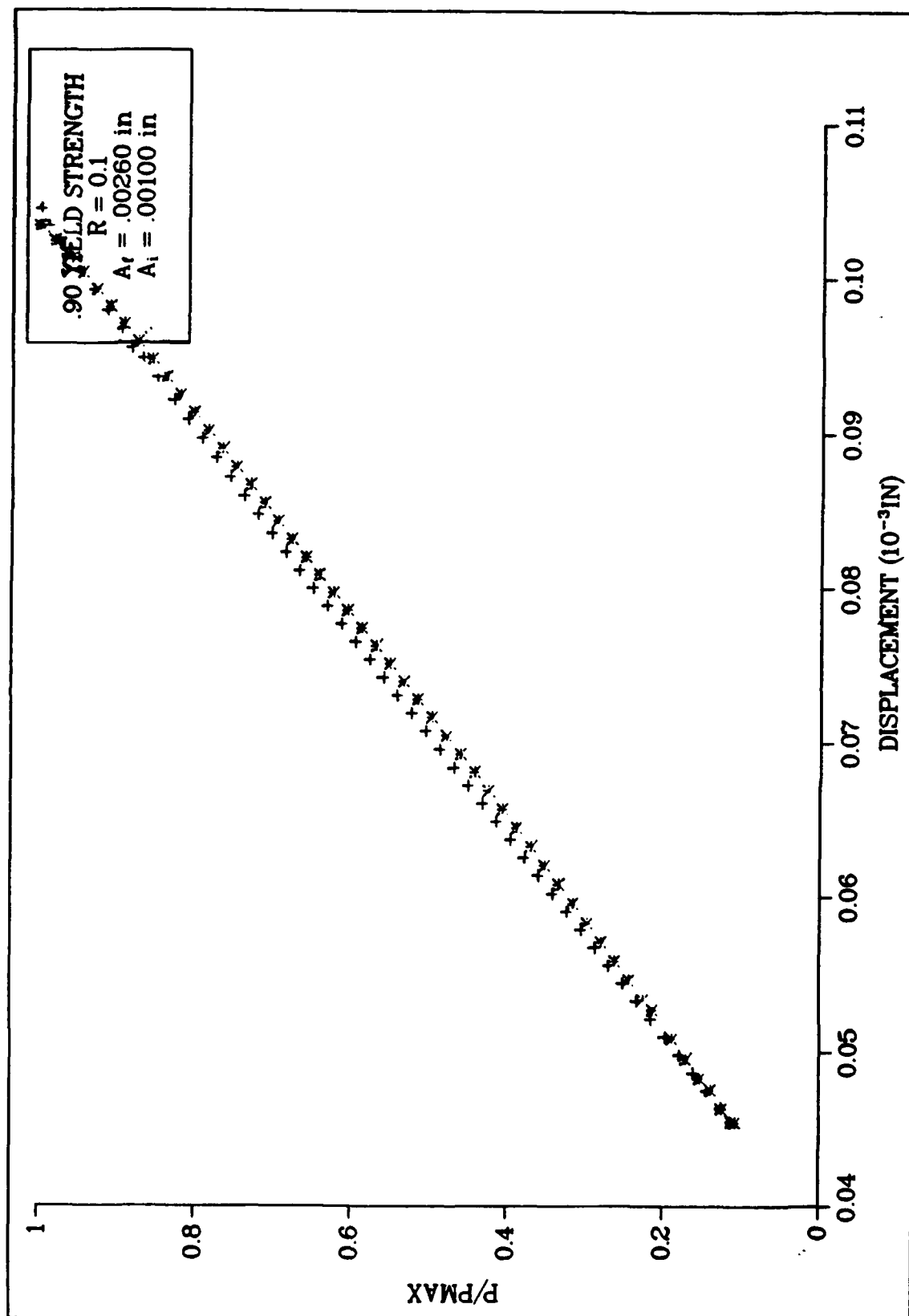
Fig 4.48: Load – Displacement (Case D/Elem 192)

Fig 4.49: Load − Delta Displacement (Case D/Elem 192)

106
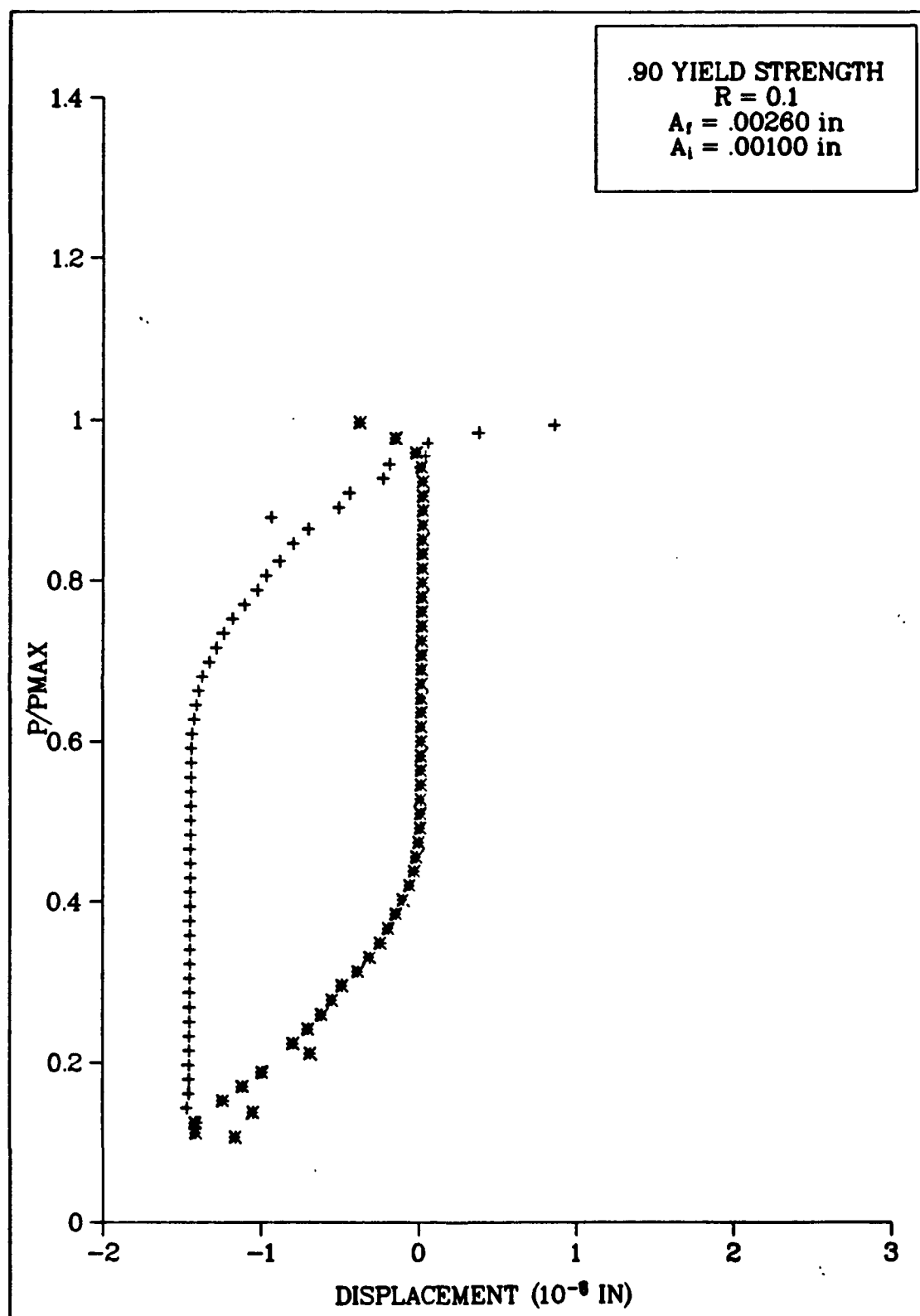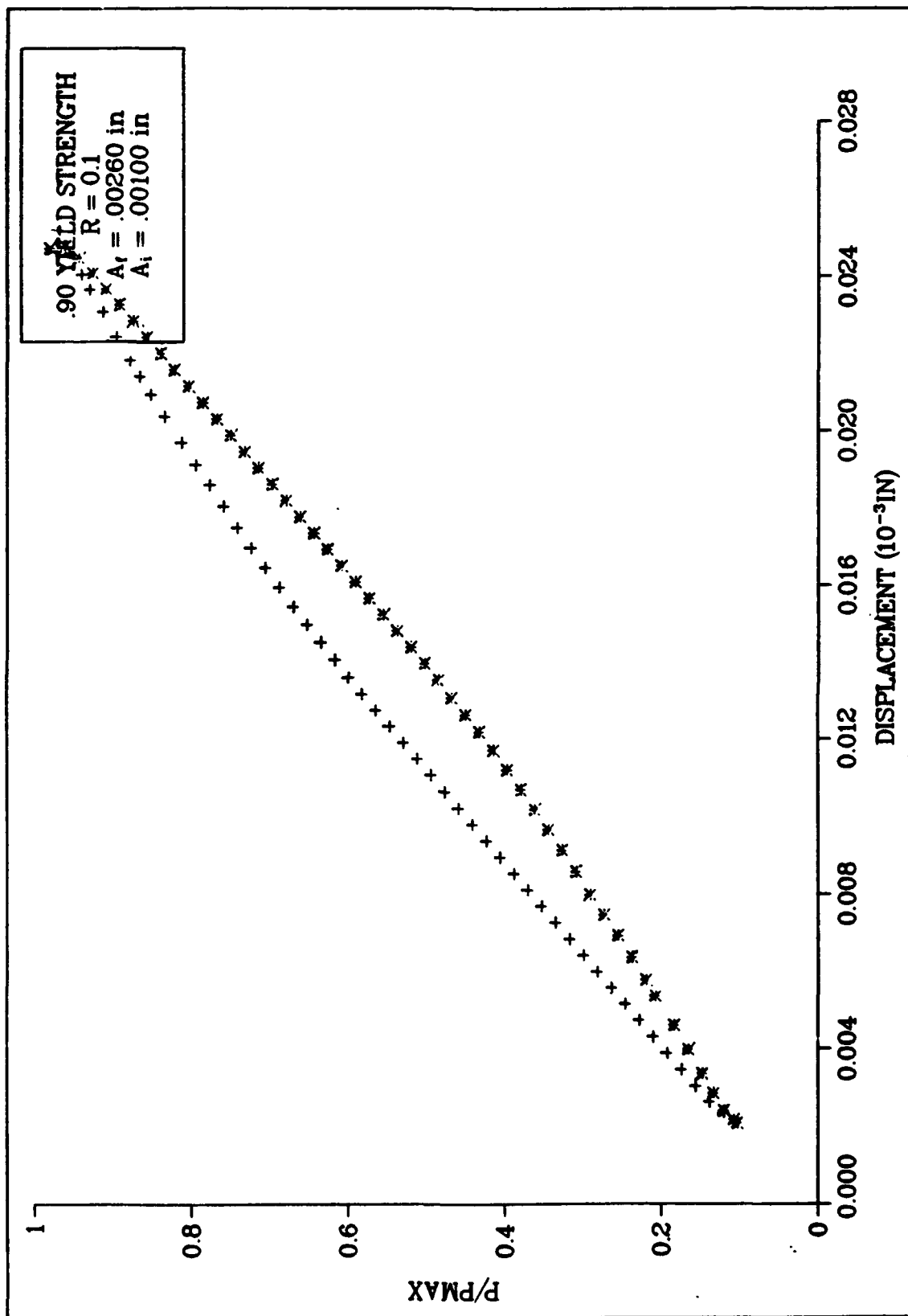
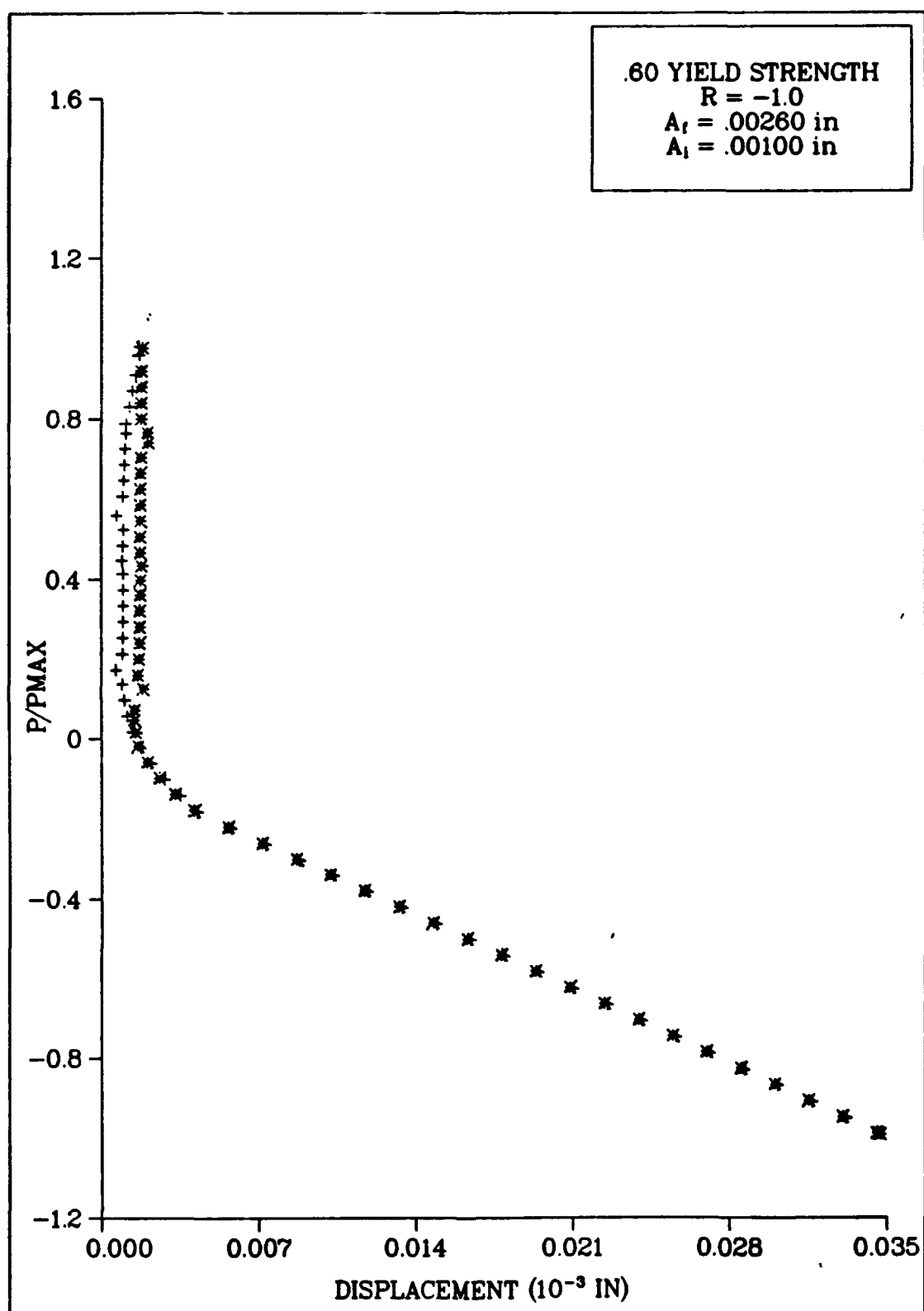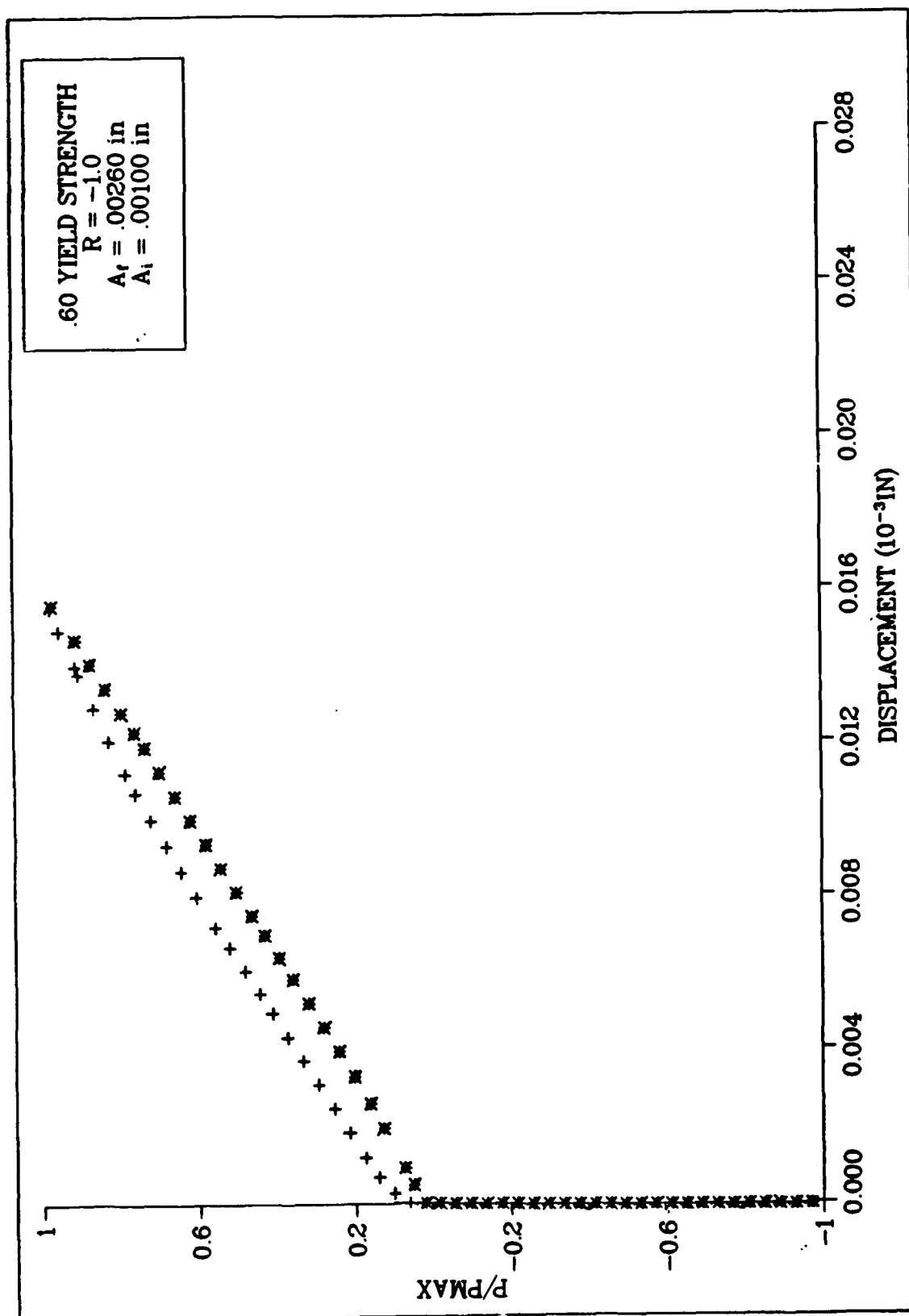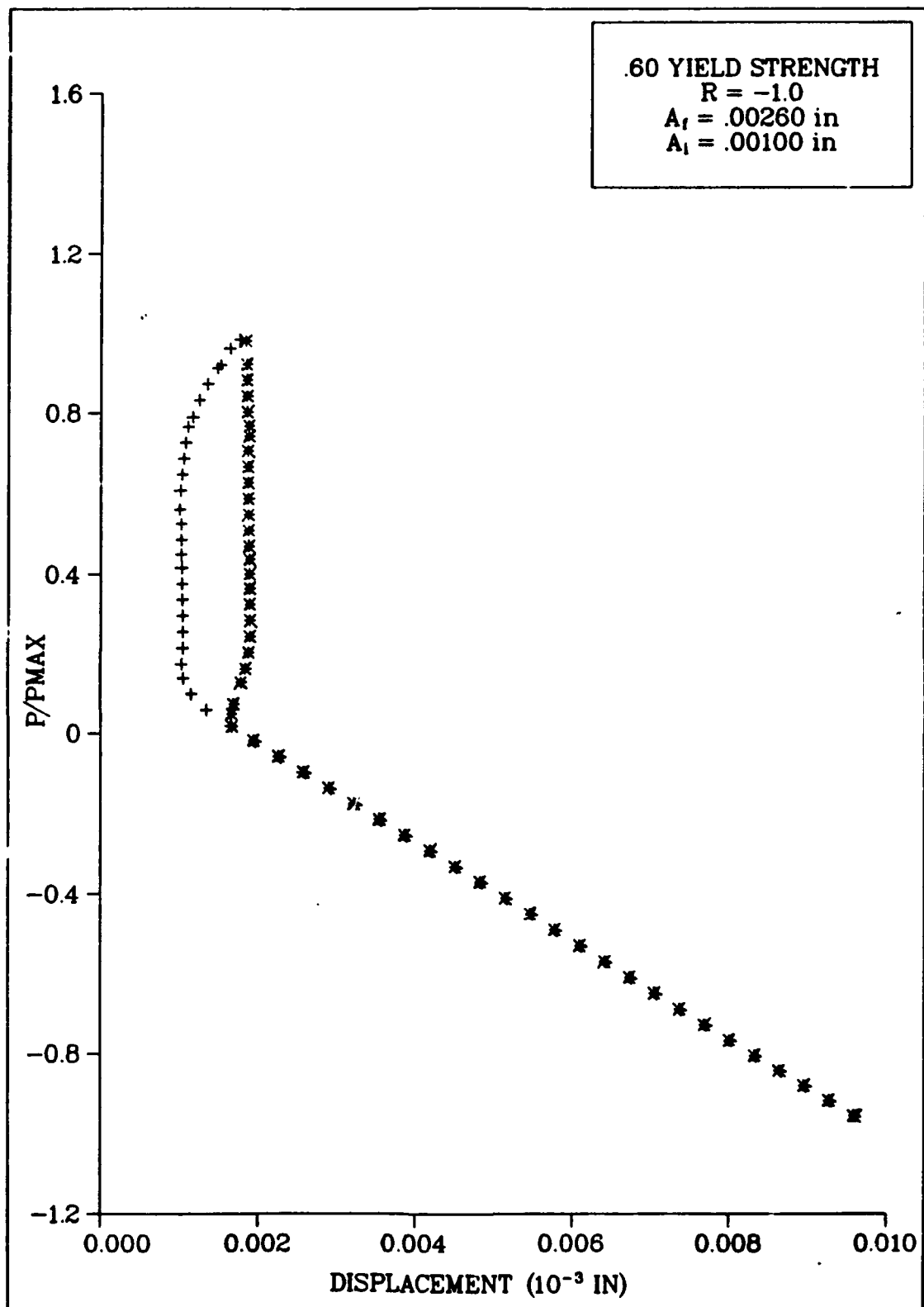Fig 4.50: Load – Displacement (Case D/Elem 205)

107
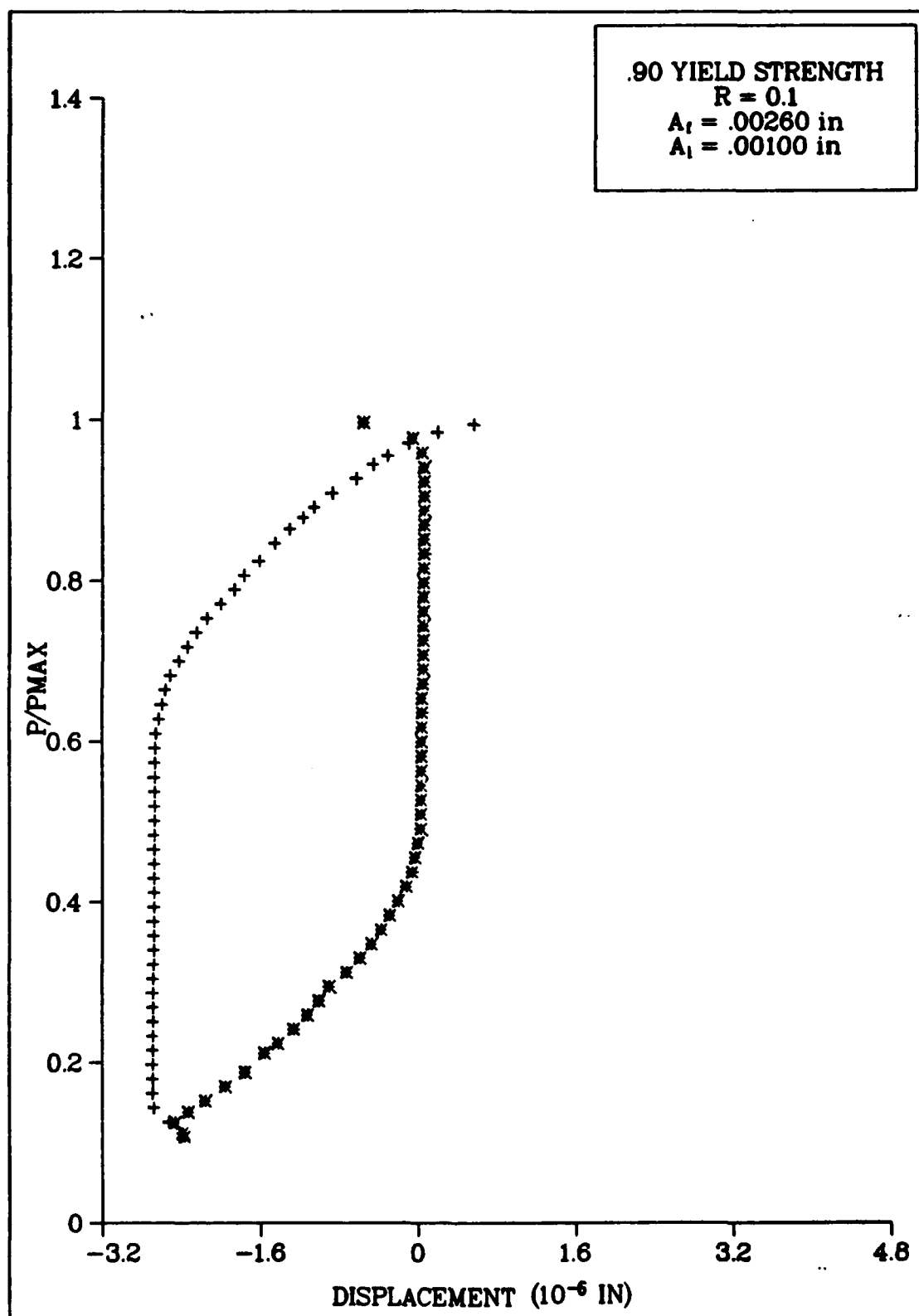
Fig 4.51: Load – Delta Displacement (Case D/Elem 205)

108
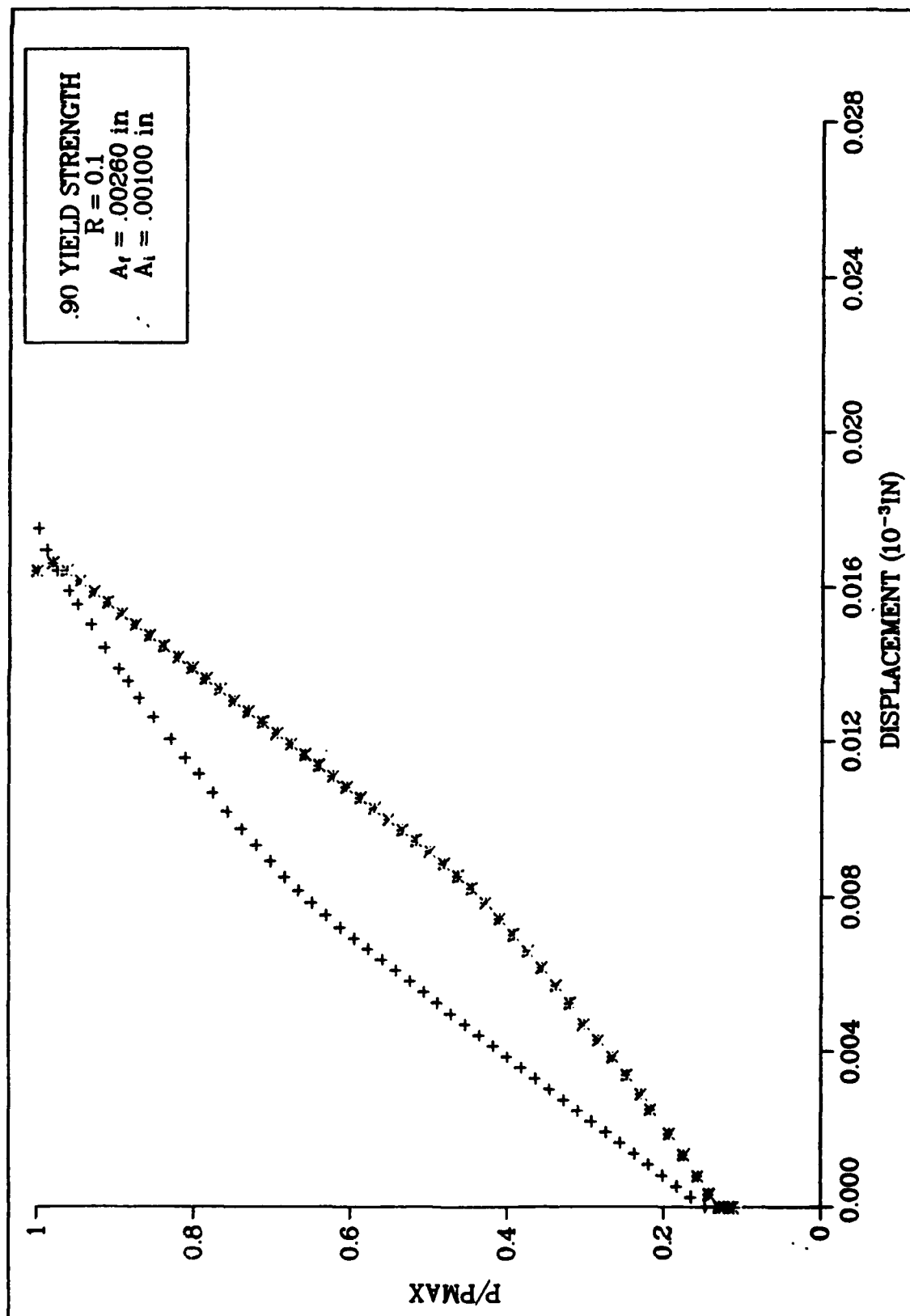
Fig 4.52: Load – Displacement (Case D/Elem 206)

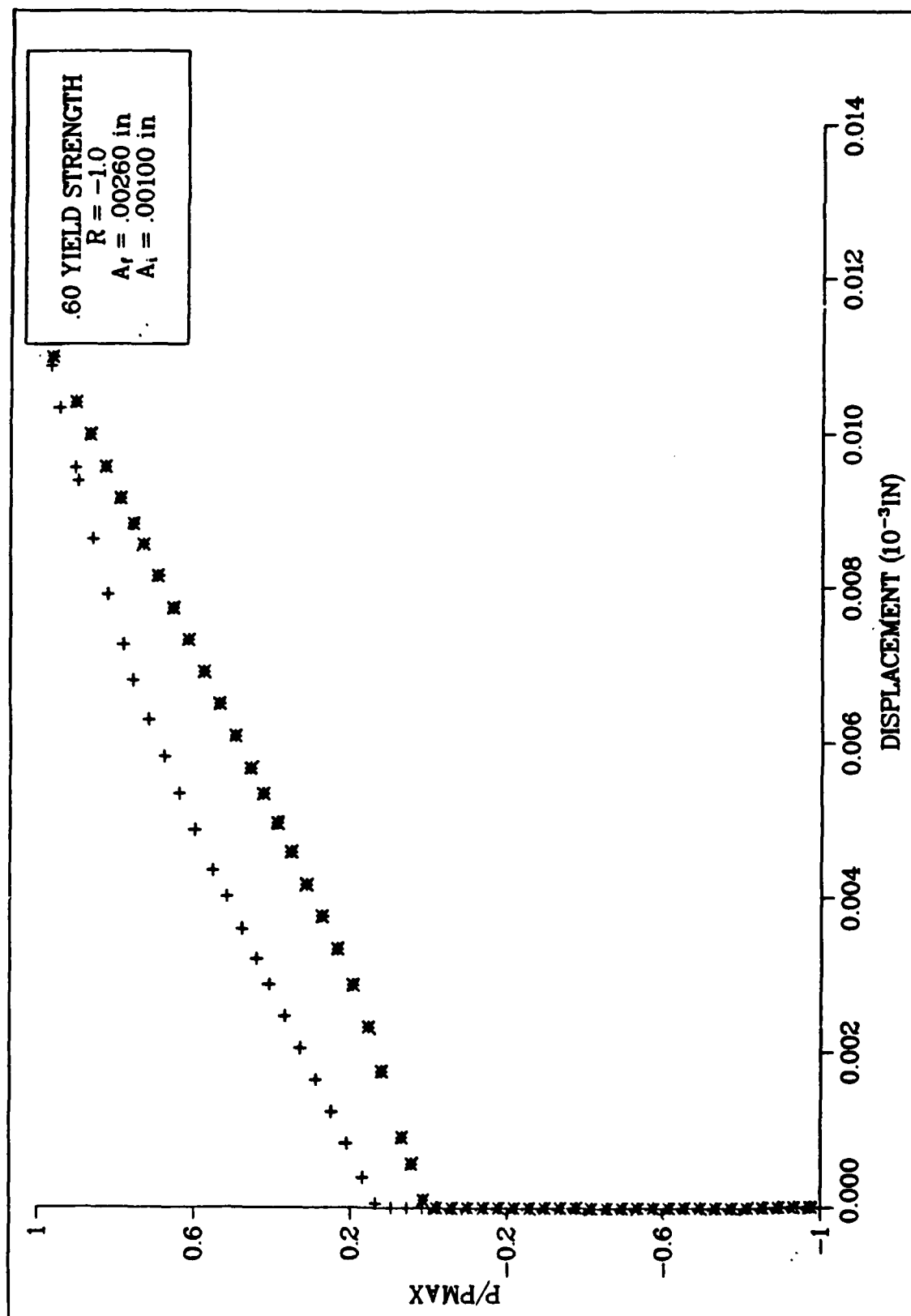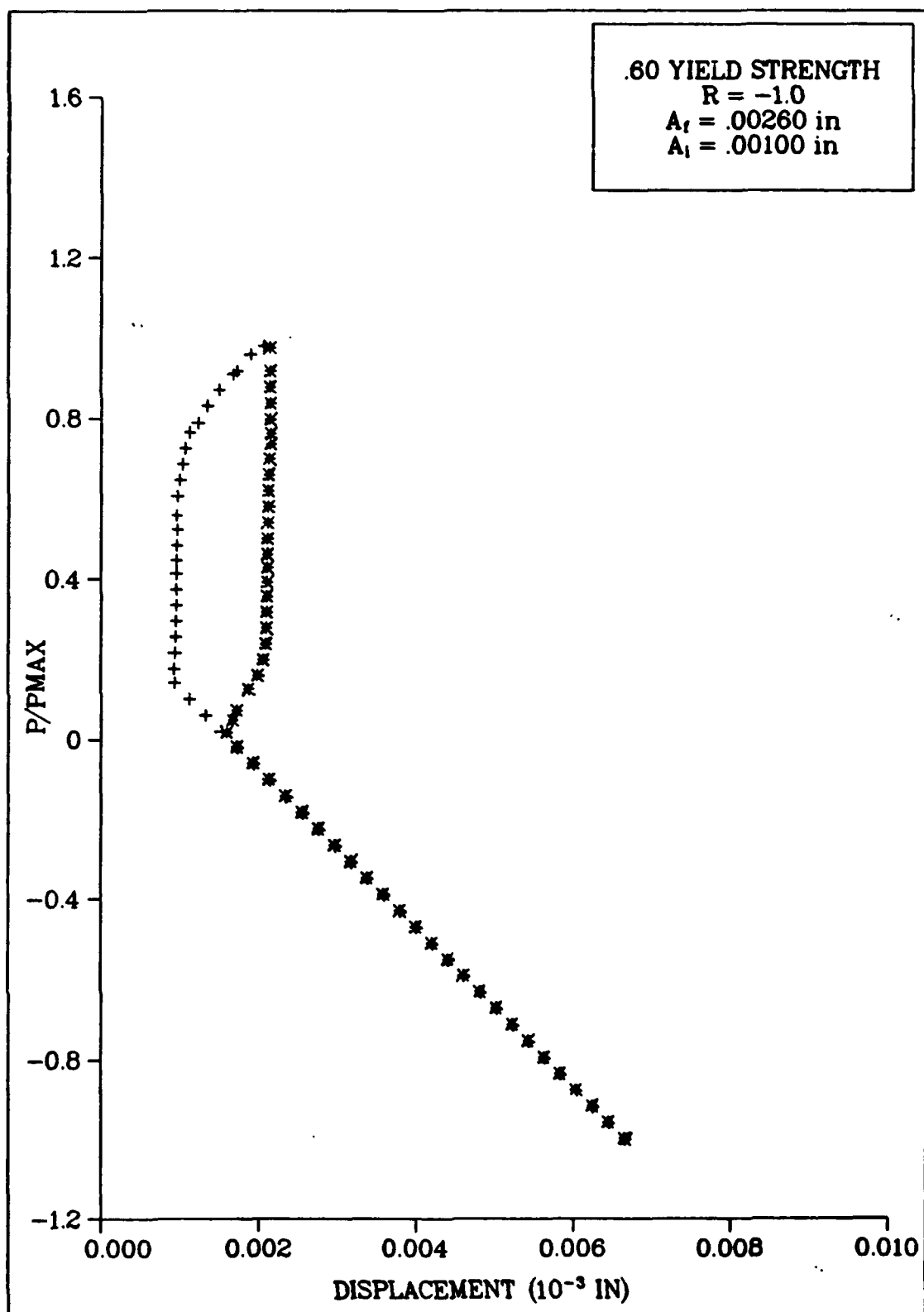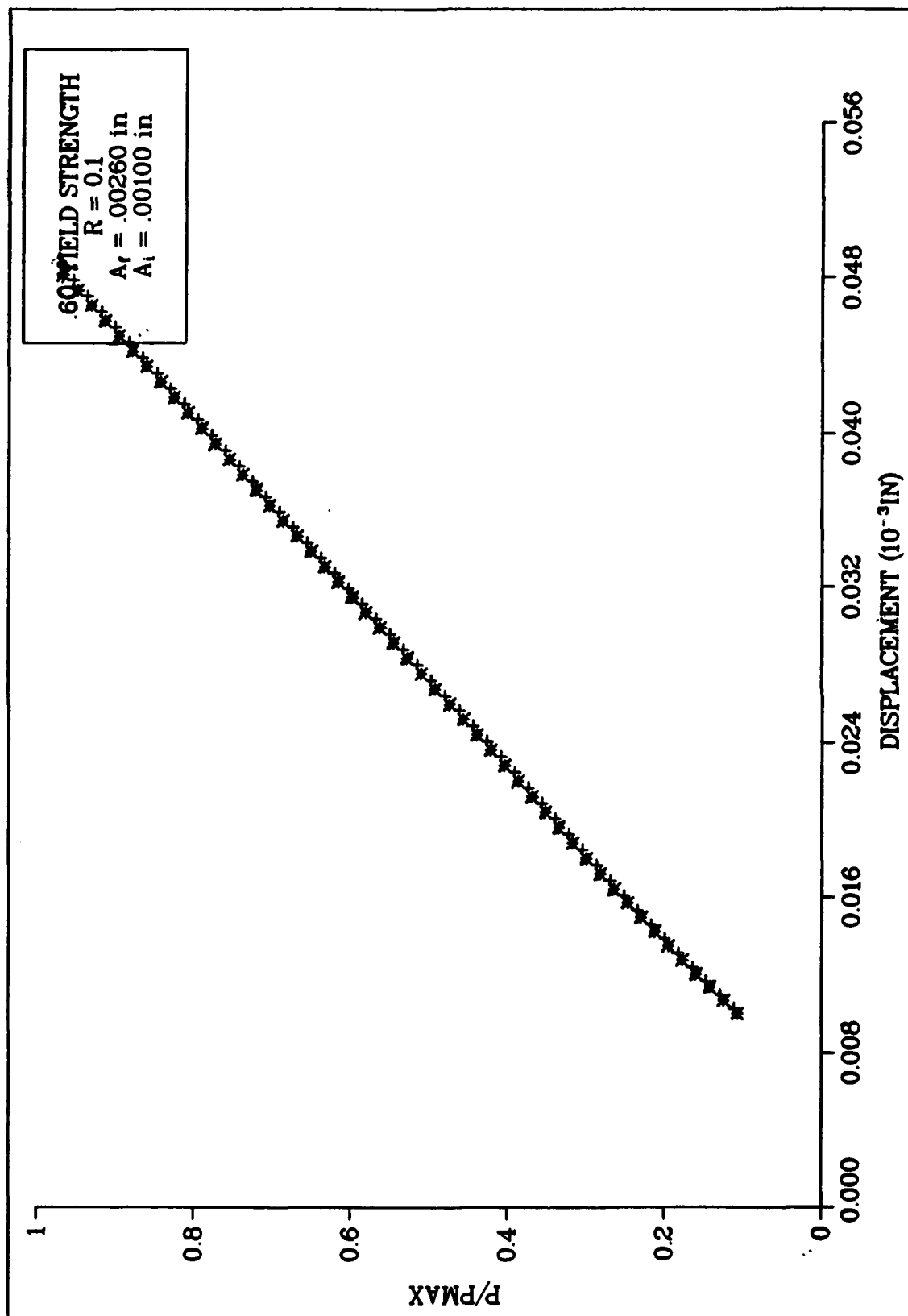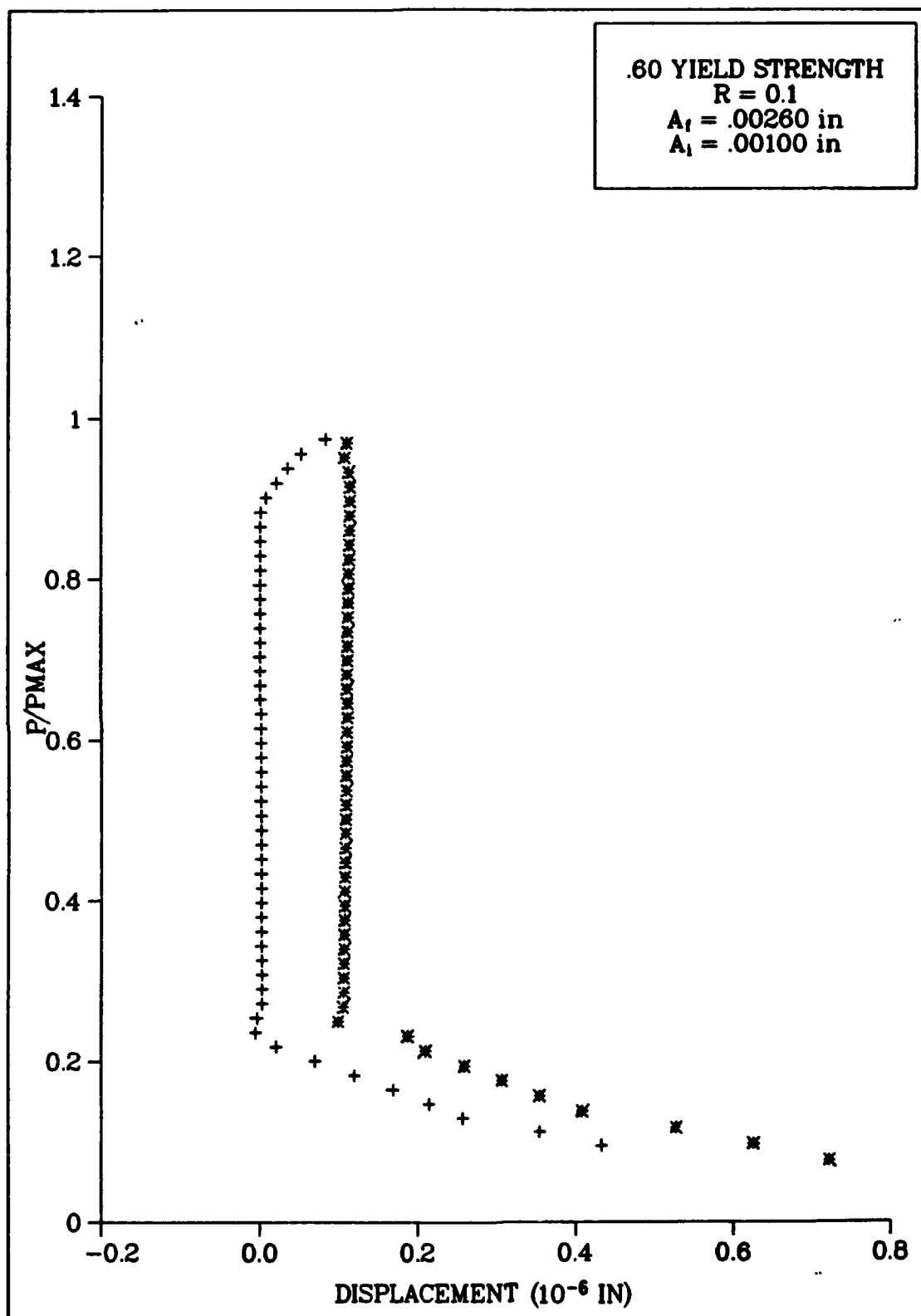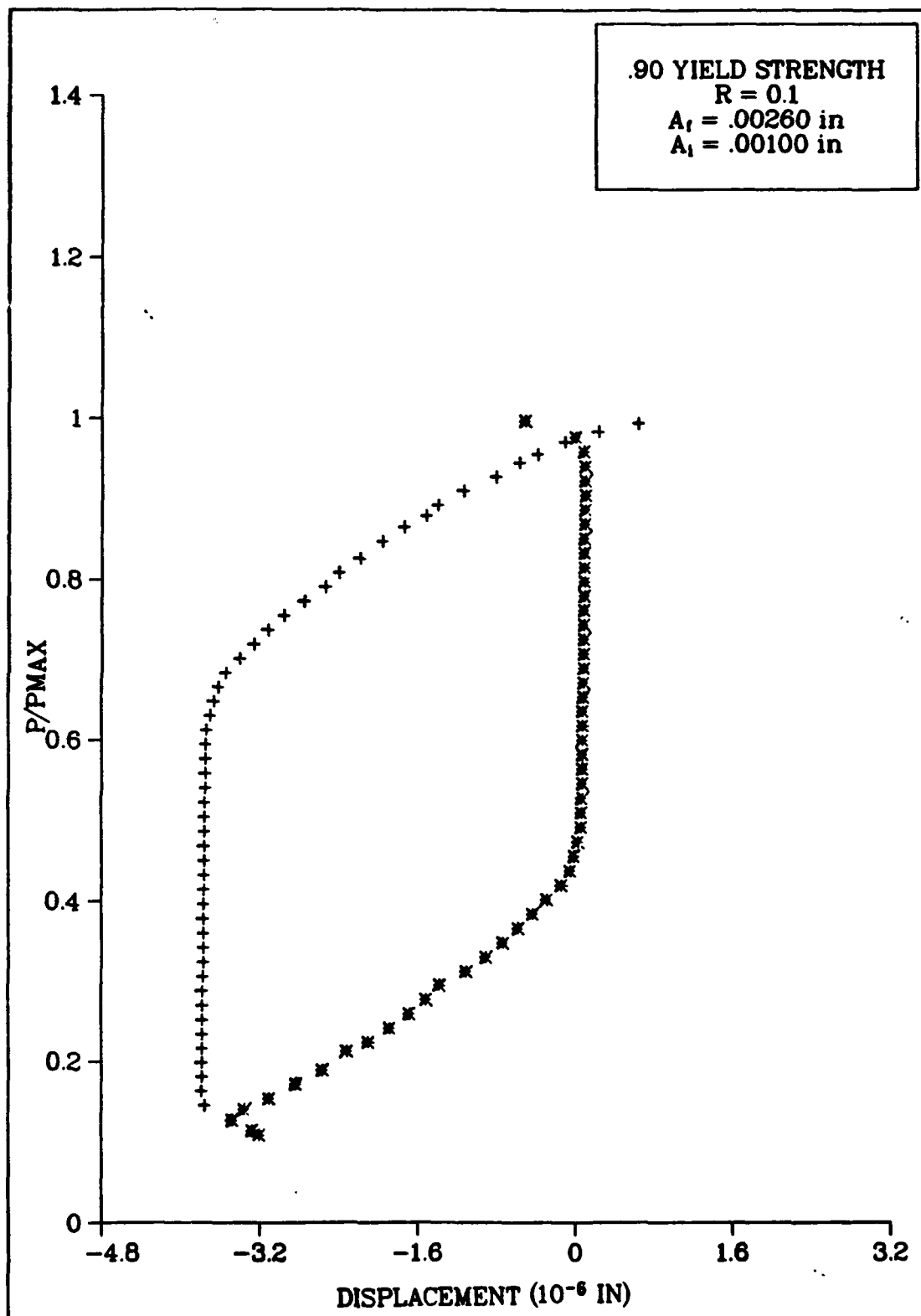Fig 4.53: Load – Delta Displacement (Case D/Elem 206)

110

point is difficult to determine because of the accumulation of plasticity effects between the crack tip and the point of displacement measurement. In each of the four cases presented, it is observed that the nearer to the crack tip that measurements are taken, the more distinct the change in linearity of the load-displacement curve. At nodes immediately behind the crack tip, very accurate determinations of crack closure can be obtained. Those further from the crack tip are less reliable.

An improvement to the load-displacement method of experimentally determining closure is to modify the data to obtain a load-delta displacement curve. As a specimen is initially unloaded, a measurement of the displacement curve is obtained. Deviations from the analytically derived slope are then used to determine when closure occurs. Although this technique improves the accuracy in determining the point of closure, far-field measurements are still obscured by the accumulation of plasticity. As measurements are taken closure to the crack tip, more accurate determinations of crack closure and opening are obtained.

Other observations regarding crack opening and closure can be made by further analysis of the load-delta displacement curves. During the time the crack is closed and external load is increasing, the slope of the curve remains constant until the crack opens. At this point, there is a distinct change in slope and the value of P(ope) is easily obtained. As the load continues to increase, the slope of the load-delta displacement curve is again constant representing the occurrence of elastic strains. When the applied load reaches its maximum value, plastic strains begin to occur and a third change in slope is observed.

During the unloading portion of the load cycle, the specimen initially undergoes an elastic reduction in strain which is represented by the vertical slope of the load-delta displacement curve. At the load corresponding to P(ope), a portion of that plastic strain is recovered until crack closure occurs. This is indicated by a reduction in the curve's slope. At the point of closure, the slope is once more distinctly reduced. Furthermore, the difference between the values of P(clo) and P(ope), coupled with the amount of recoverable plastic strain, determine the extent of hysteresis exhibited in the load-delta displacement curves.

Results for Inconel 718

The single-edge cracked specimen composed of high temperature Inconel 718 was subjected to a constant nominal stress value of 90 percent of the material yield strength and a load ratio of 0.1, whereas the frequency was varied between 1.0 and .01 Hz. In these cases, one crack was allowed to grow from an initial crack length of .001 inch to a final length of .0018 inch (five finite element nodes released), and the second crack had an initial crack length of .0018 inch. Through the use of the two load frequencies, the effects of viscoplasticity on plasticity induced closure, the formation of a plastic wake, and fatigue crack growth were investigated.

Figures 4.54 through 4.57 show the displacements behind the crack tip at both minimum and maximum loads. As expected, the displacements were less for the propagated cracks over the crack growth region. The differences in the displacements due to the nature of propagating and non-propagating cracks are nearly the same for each frequency. The
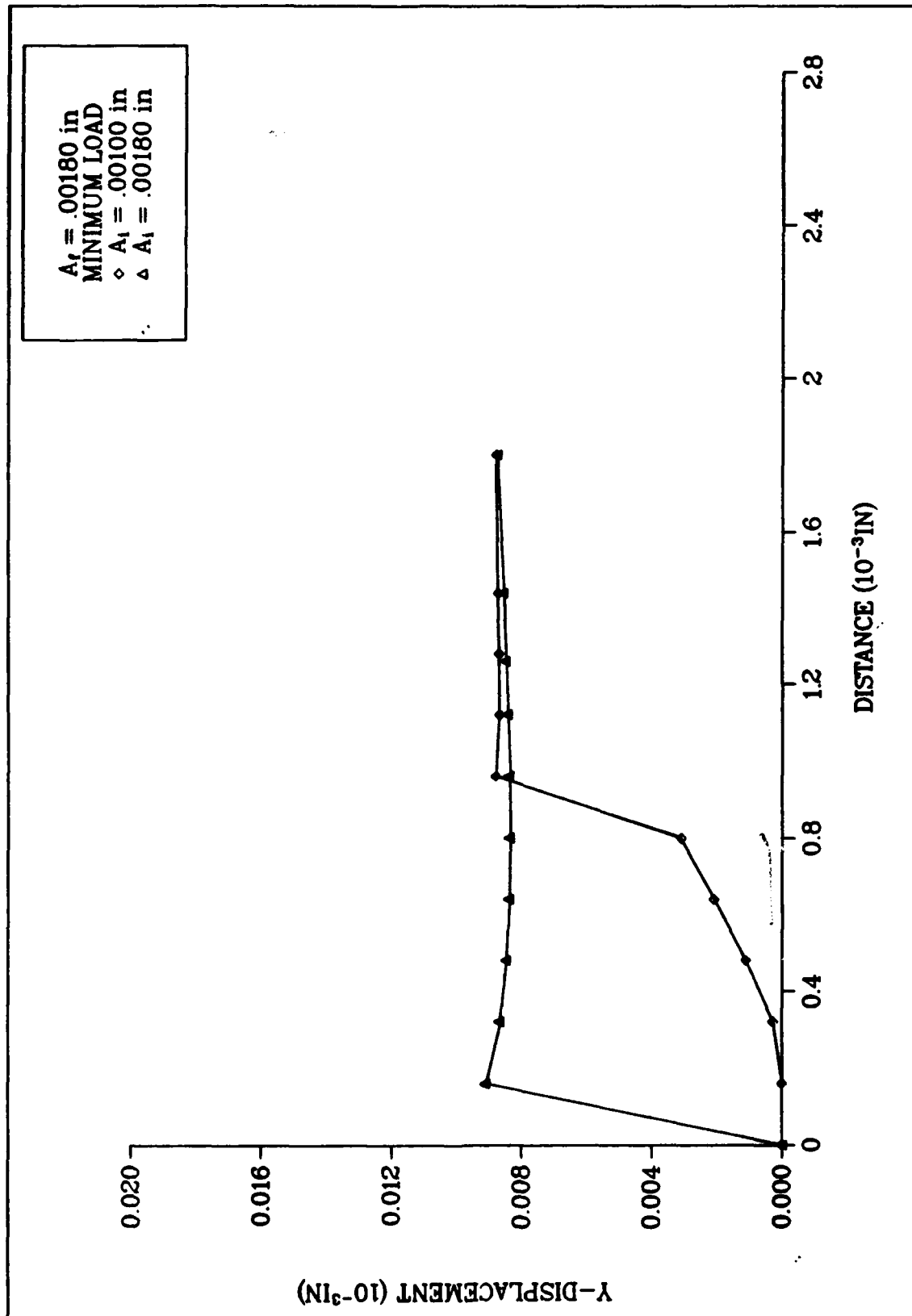
Fig 4.54: Displacements Behind Crack Tip (Case E/Min Load)

113
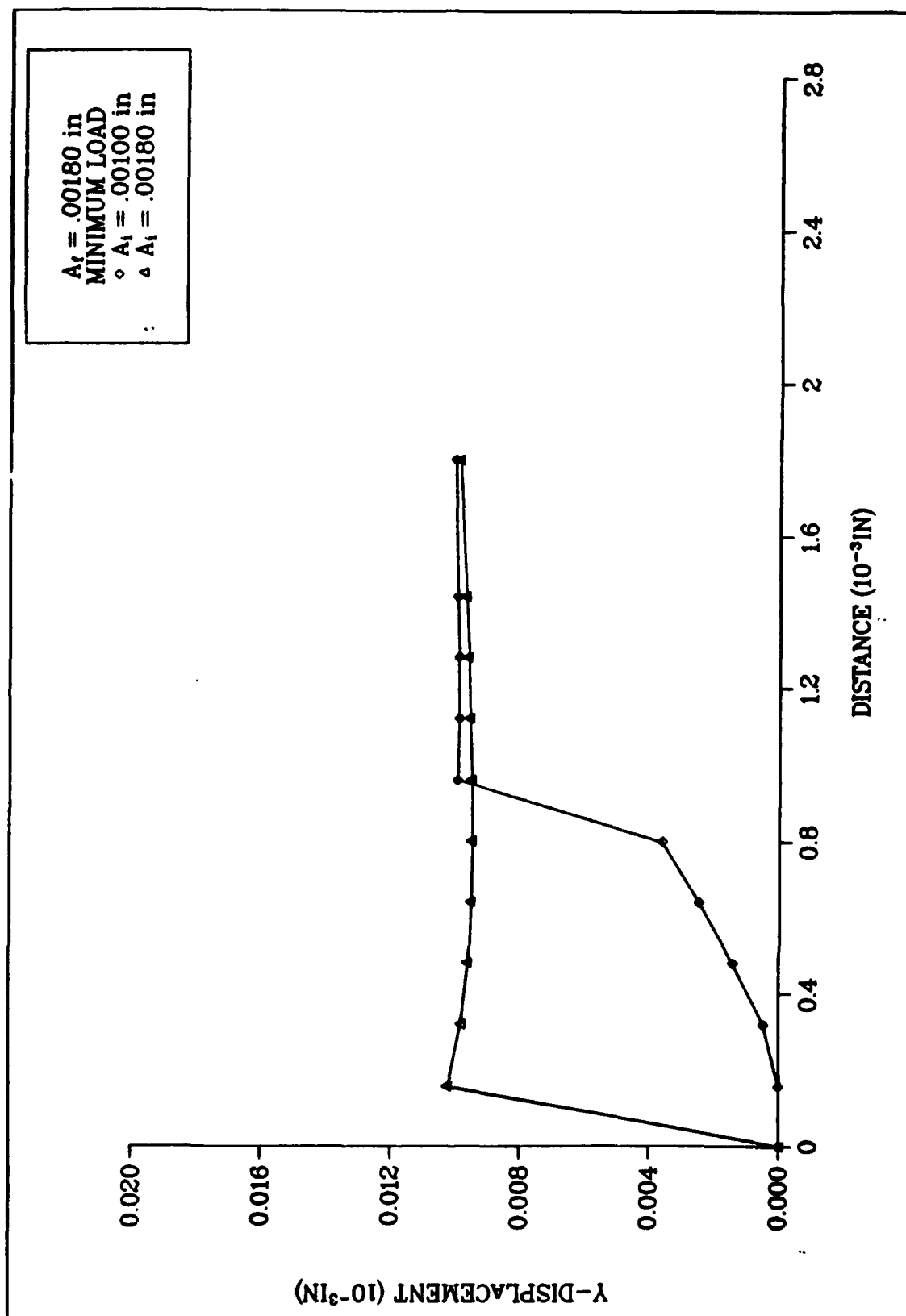
Fig 4.55: Displacements Behind Crack Tip (Case F/Min Load)

114
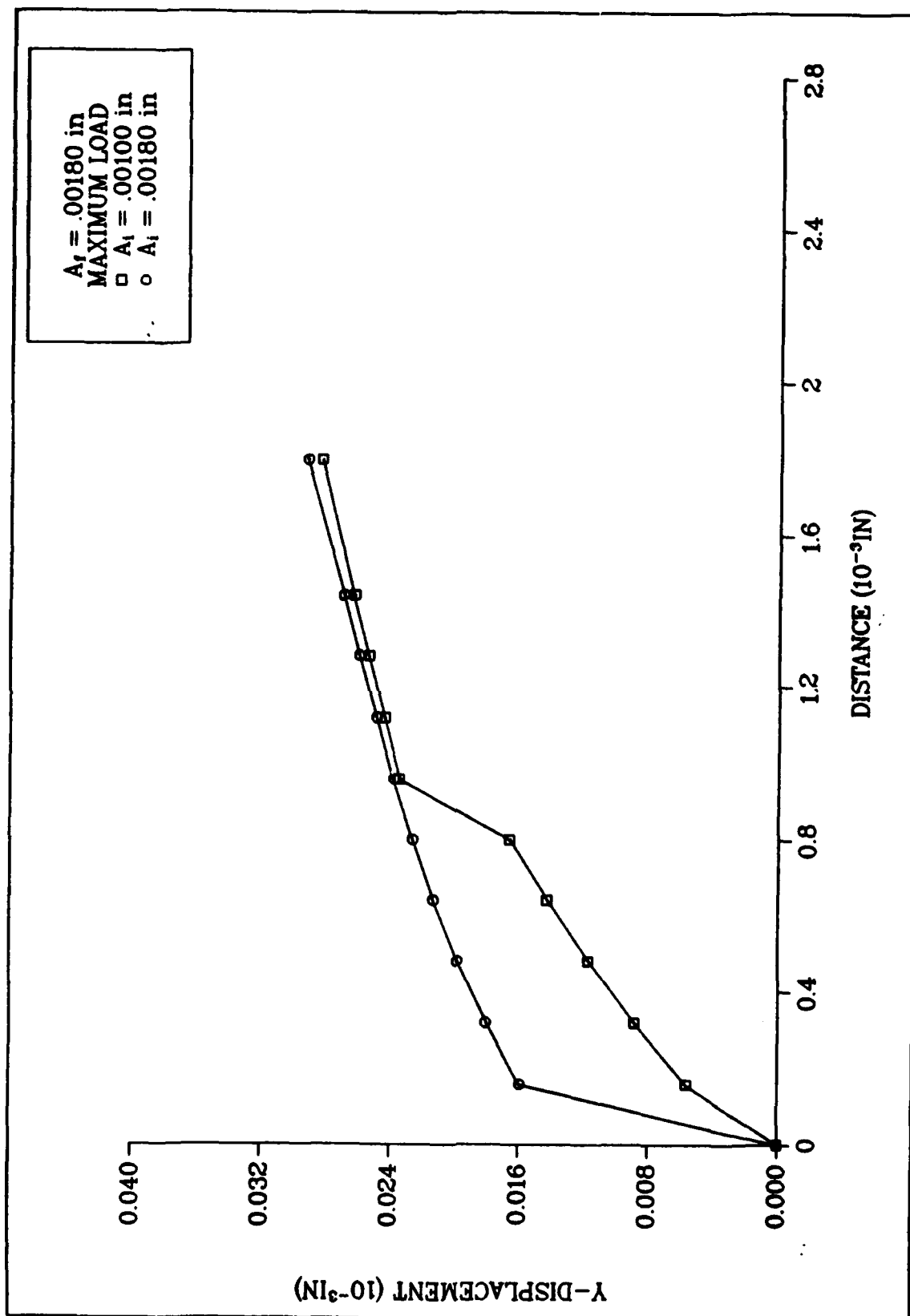
Fig 4.56: Displacements Behind Crack Tip (Case E/Max Load)
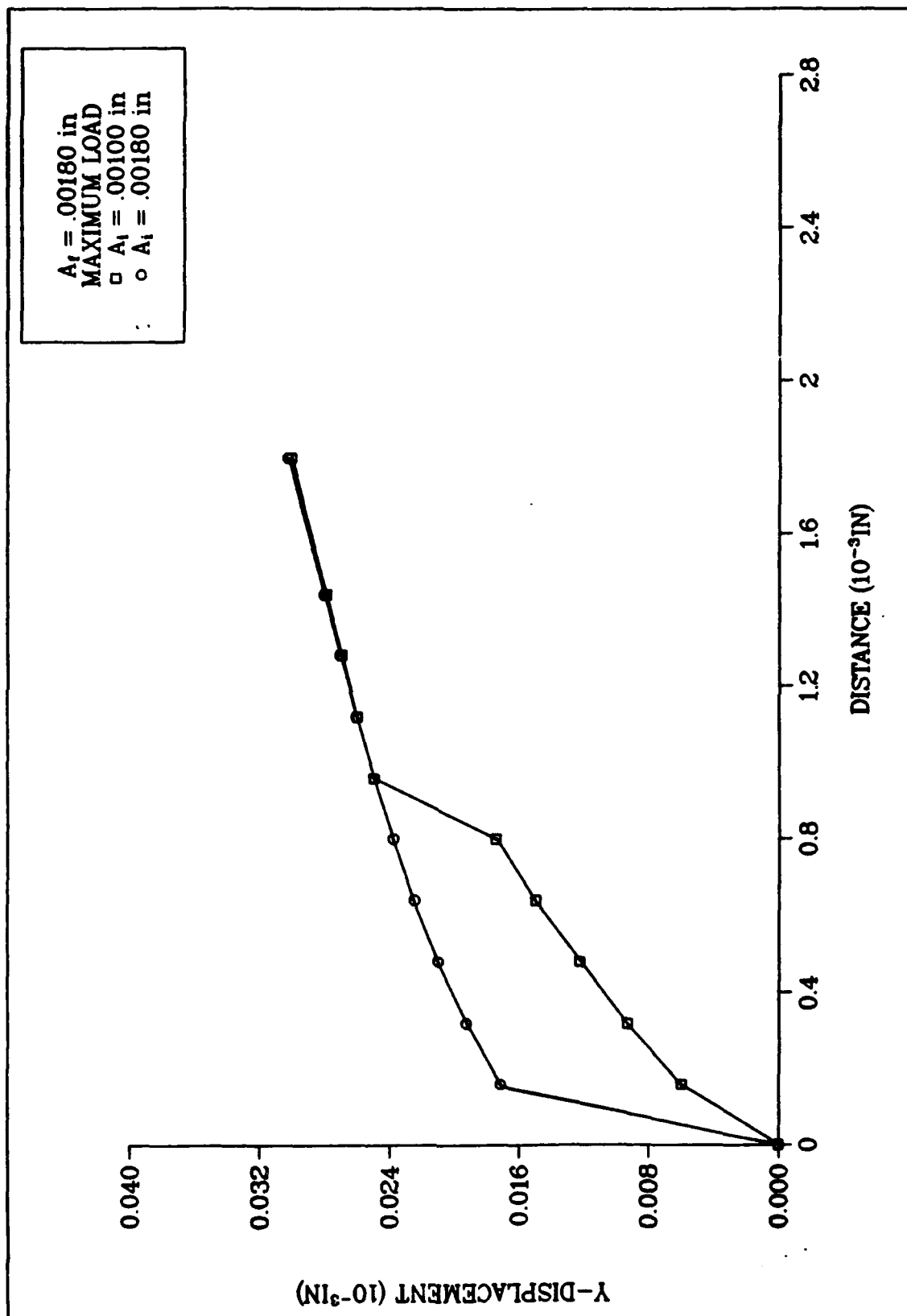
Fig 4.57: Displacements Behind Crack Tip (Case F/Max Load)

116

magnitudes of the displacements observed at the lower frequency (case F), however, are greater than the higher frequency. The viscoplastic properties at various load frequencies do not significantly affect the differences in propagated and non-propagated crack for this material.

The stress/strain hysteresis loops shown in Figures 4.58 and 4.59 show that stresses ahead of the crack tip are not significantly affected by previous crack growth. Further, these stresses do not differ with changes in load frequency. The strain values observed, however, are reduced as a result of crack propagation and the formation of the plastic wake. The amount of reduction in strain resulting from crack growth is less in case E, indicating that the higher frequency does not allow as much straining as the lower frequency.

As observed in the hysteresis loops previously discussed, the stress values ahead of the crack tip are only slightly affected by crack growth and viscoplasticity. In Figures 4.60 and 4.61 the distribution of stresses at minimum and maximum load values show a slight difference due to the fatigue crack growth and formation of the plastic wake. There is also a slight increase in all stress values in the vicinity of the crack tip for the higher load frequency which appears to be the result of viscoplastic material behavior of IN-718 at high temperature.

Figures 4.62 and 4.63 display the accumulation of plastic strain along and in front of the crack tip. As the crack propagates, the accumulation of plastic strain along the region of crack growth is evident as is the reduced strain immediately in front of the crack tip for the propagated crack. This phenomenon was also exhibited in the stress/strain curves previously discussed and appears to be a result of

117
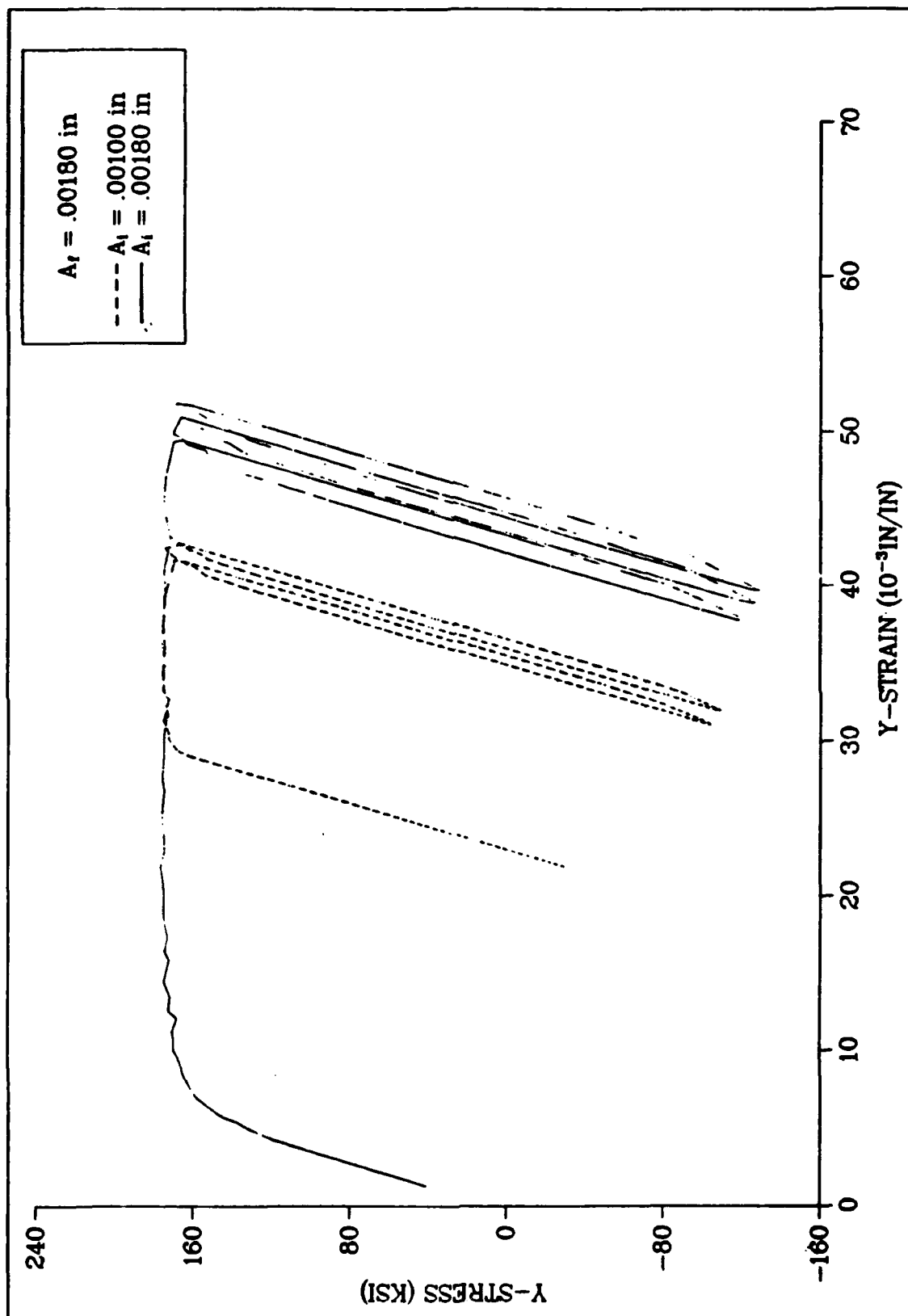
Fig 4.58: Stress/Strain Ahead of Crack Tip (Case E)

118
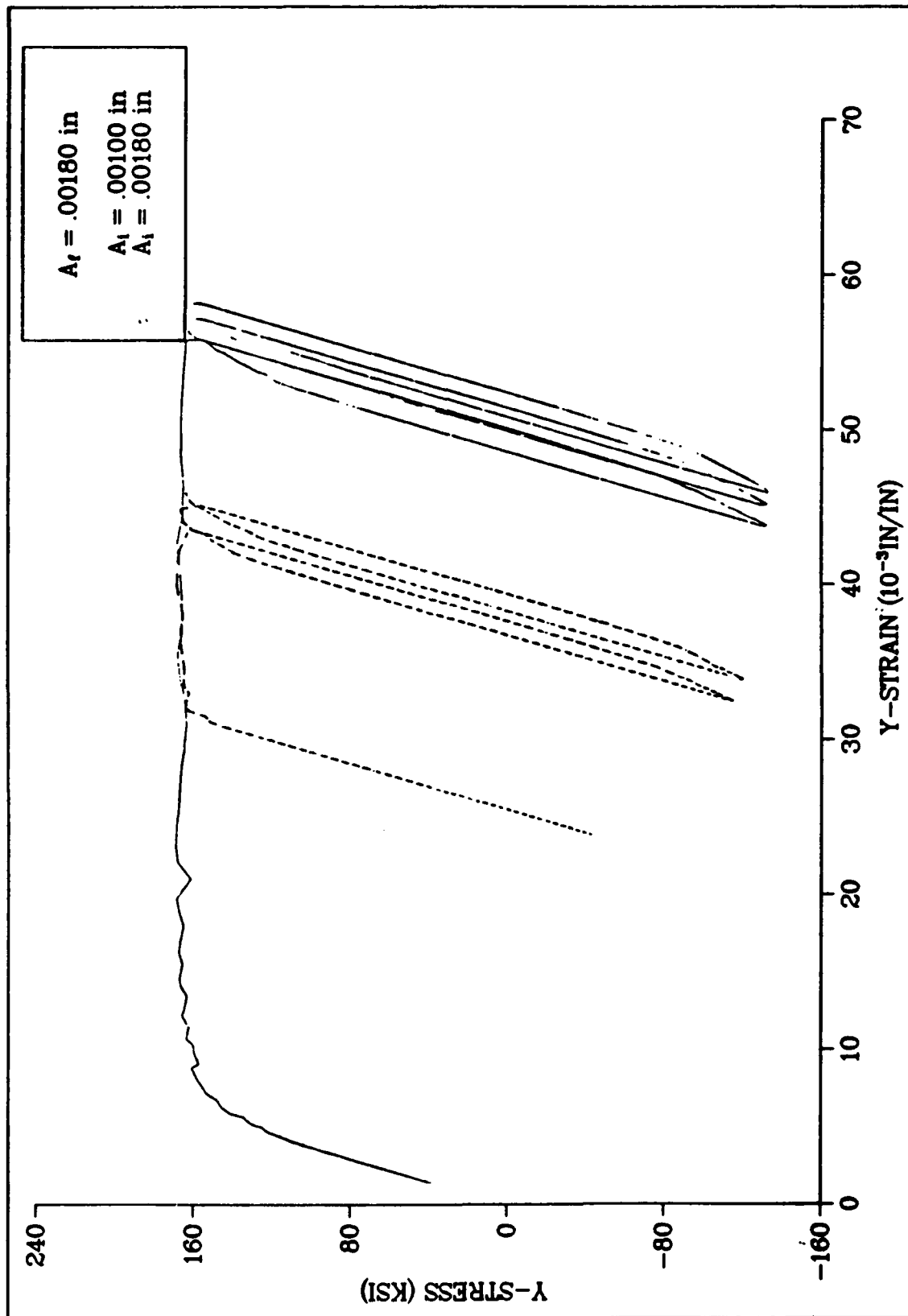
Fig 4.59: Stress/Strain Ahead of Crack Tip (Case F)

119
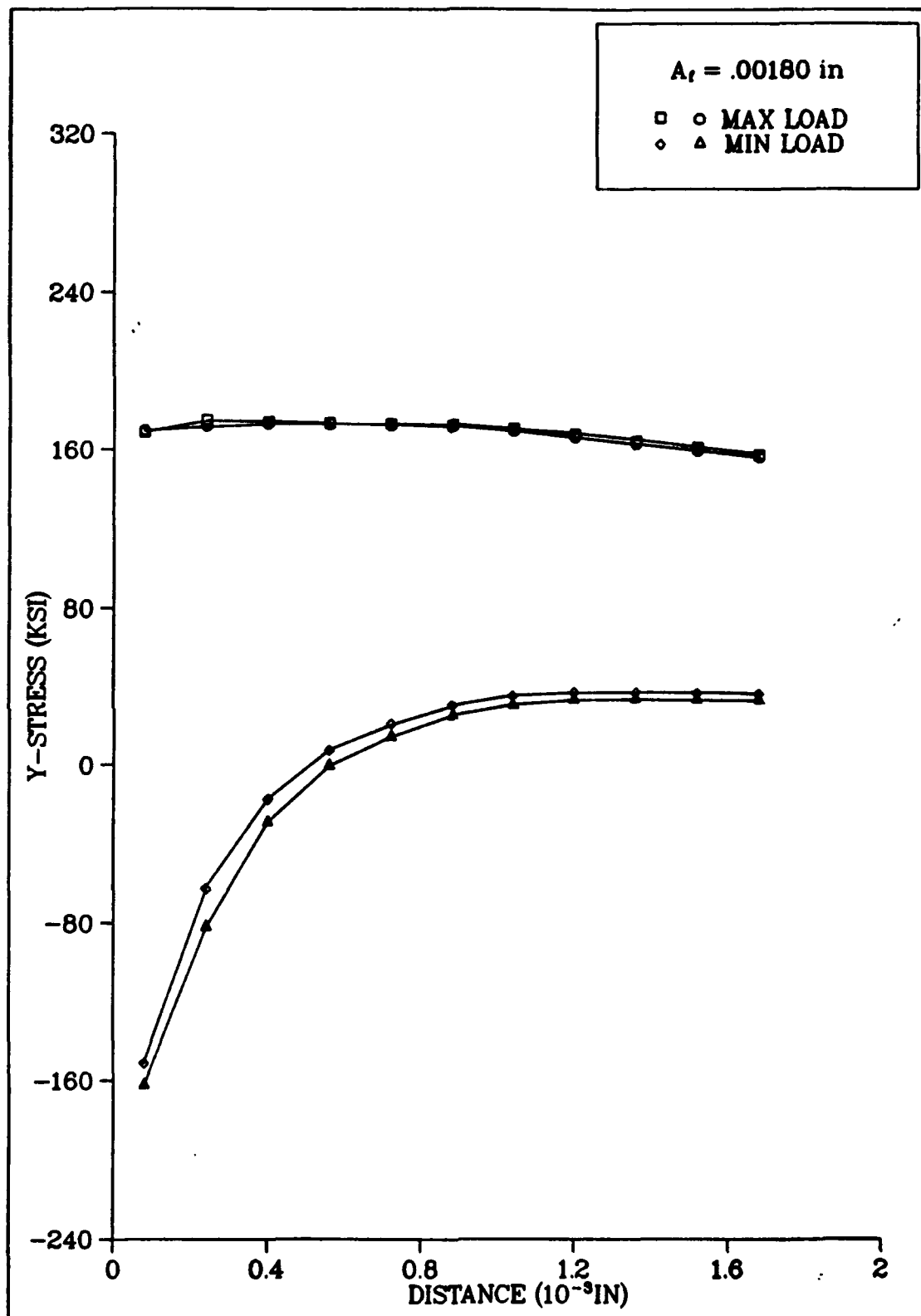
Fig 4.60: Stresses Ahead of Crack Tip (Case E)
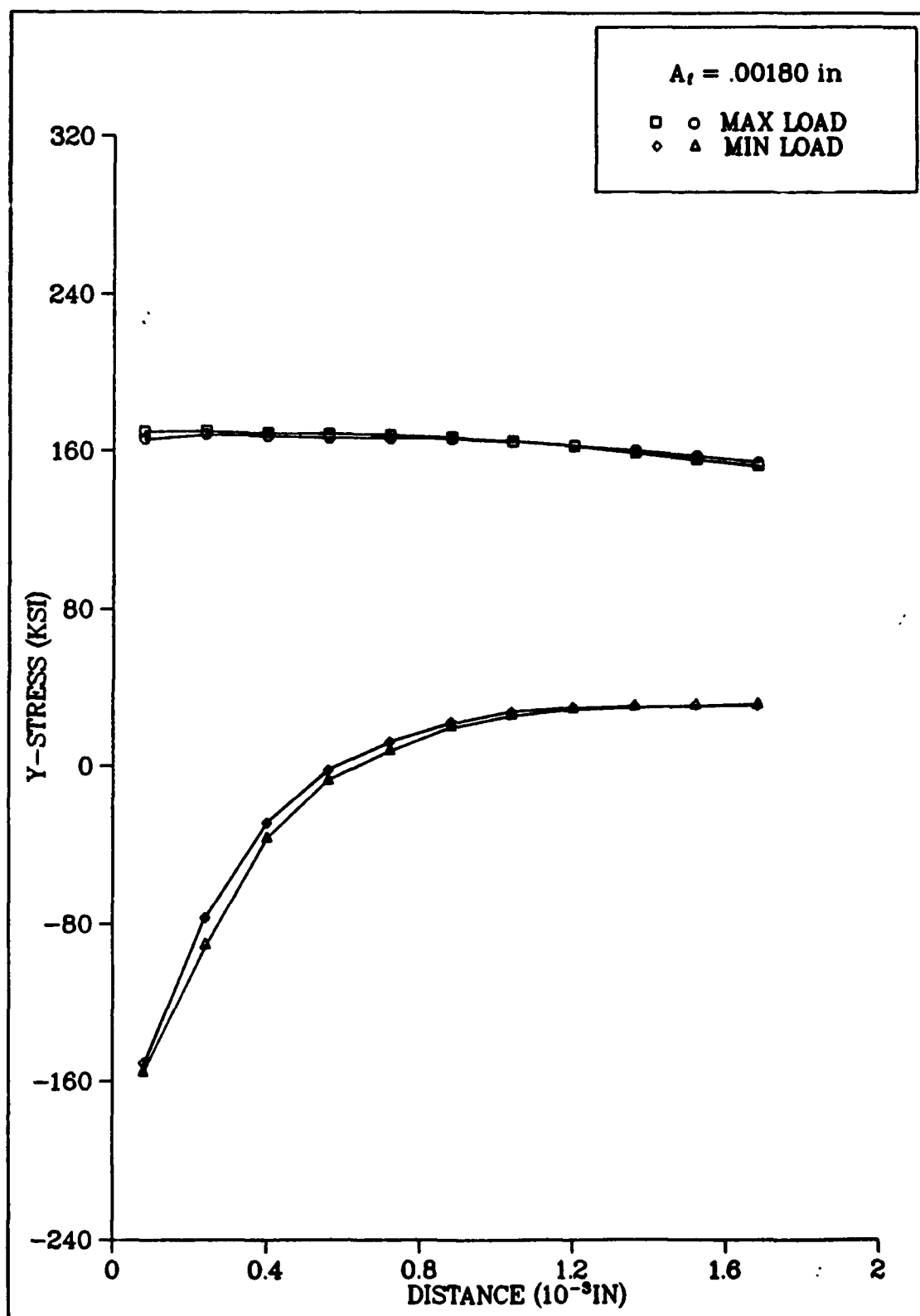
Fig 4.61: Stresses Ahead of Crack Tip (Case F)

121
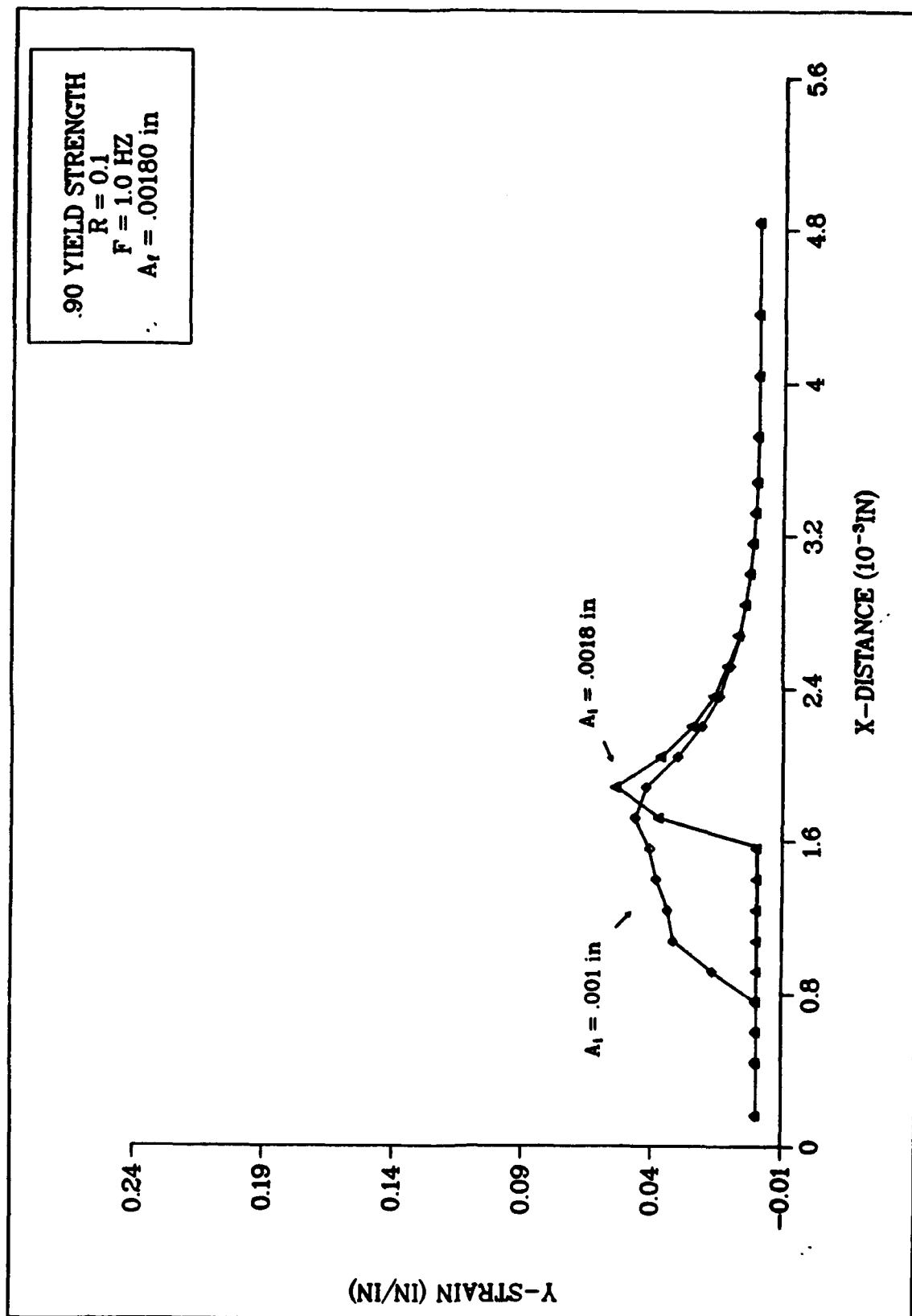
Fig 4.62: Plastic Strain Along X-Axis (Case E)

122
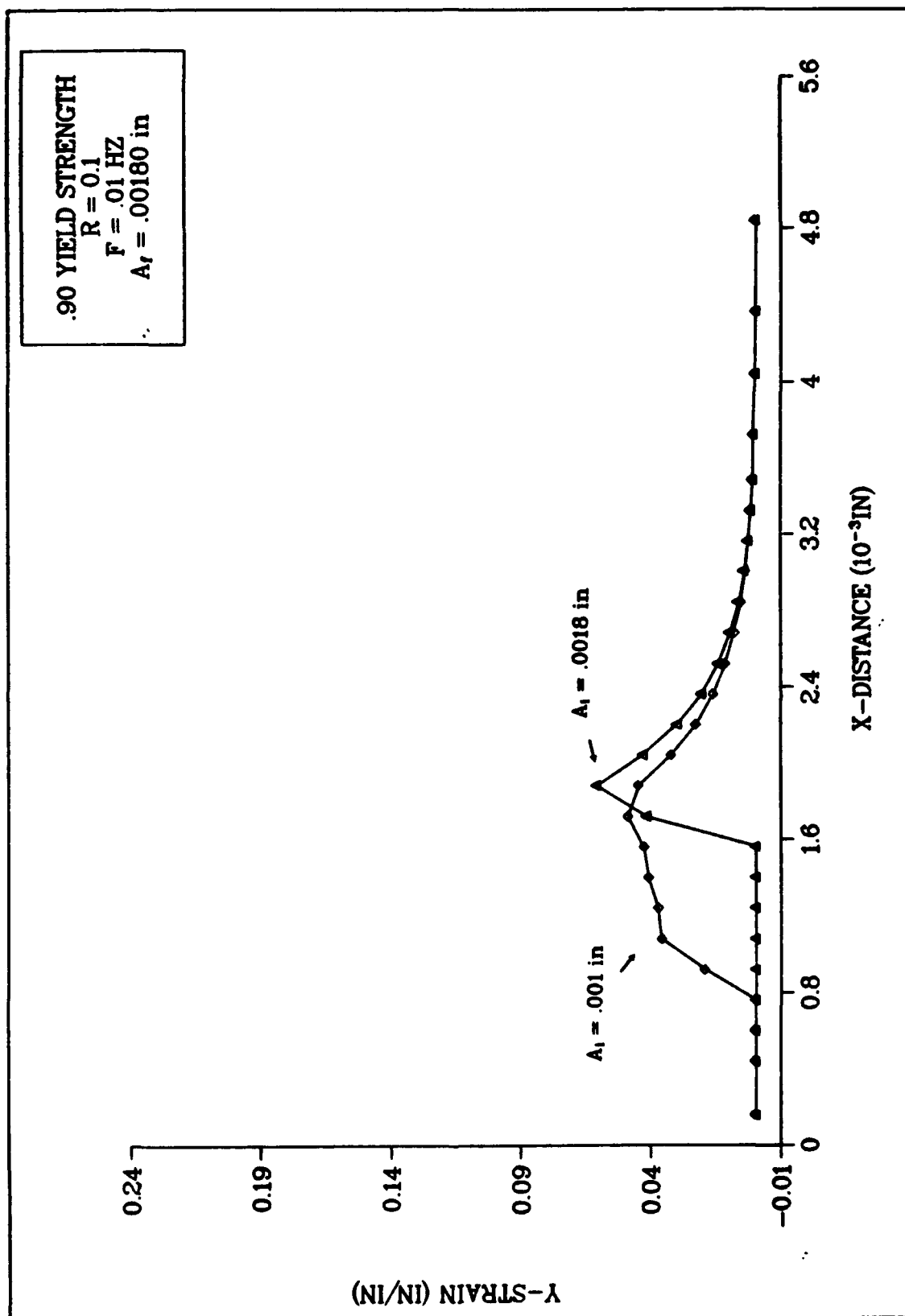
Fig 4.63: Plastic Strain Along X-Axis (Case F)

the plastic wake behind the crack tip. Further, by superimposing the plastic strains for these two cases as in Figure 4.64 the ef ect of viscoplasticity can be observed. At higher load frequencies the strains are slightly reduced along the entire crack length for both propagated and non-propagated cracks.

Closure data as related to crack length and maximum stress intensity factor are shown in Figures 4.65 to 4.68. In each case the closure and opening loads are reduced as the crack extends and K(max) increases. The viscoplastic behavior of the Inconel 718 material permits the growth of plastically deformed material which, in turn, increases residual compressive stresses. As a result, the cracks close at a higher external load during unloading than they would have in the absence of any plastic deformation. Similarly, during the subsequent loading portion of the fatigue cycle, crack opening occurs at a higher external load.

Load-displacement and load-delta displacement curves are presented for the Inconel 718 specimens in Figures 4.69 through 4.80. These have been obtained for three node locations. The crack mouth is represented by node 192, and the area immediately behind the crack tip by nodes 200 and 201. As discussed previously, it is apparent that the point of closure or opening is barely distinguishable when displacements are taken far-field, such as at the crack mouth. As the location of measurements moves closer to the crack tip more accurate estimations of crack closure and opening can be obtained.

In these curves for the Inconel 718 specimens, the same characteristics as were evident in the TI-6246 specimen are observed. During loading, the load-delta displacement slope remains constant as
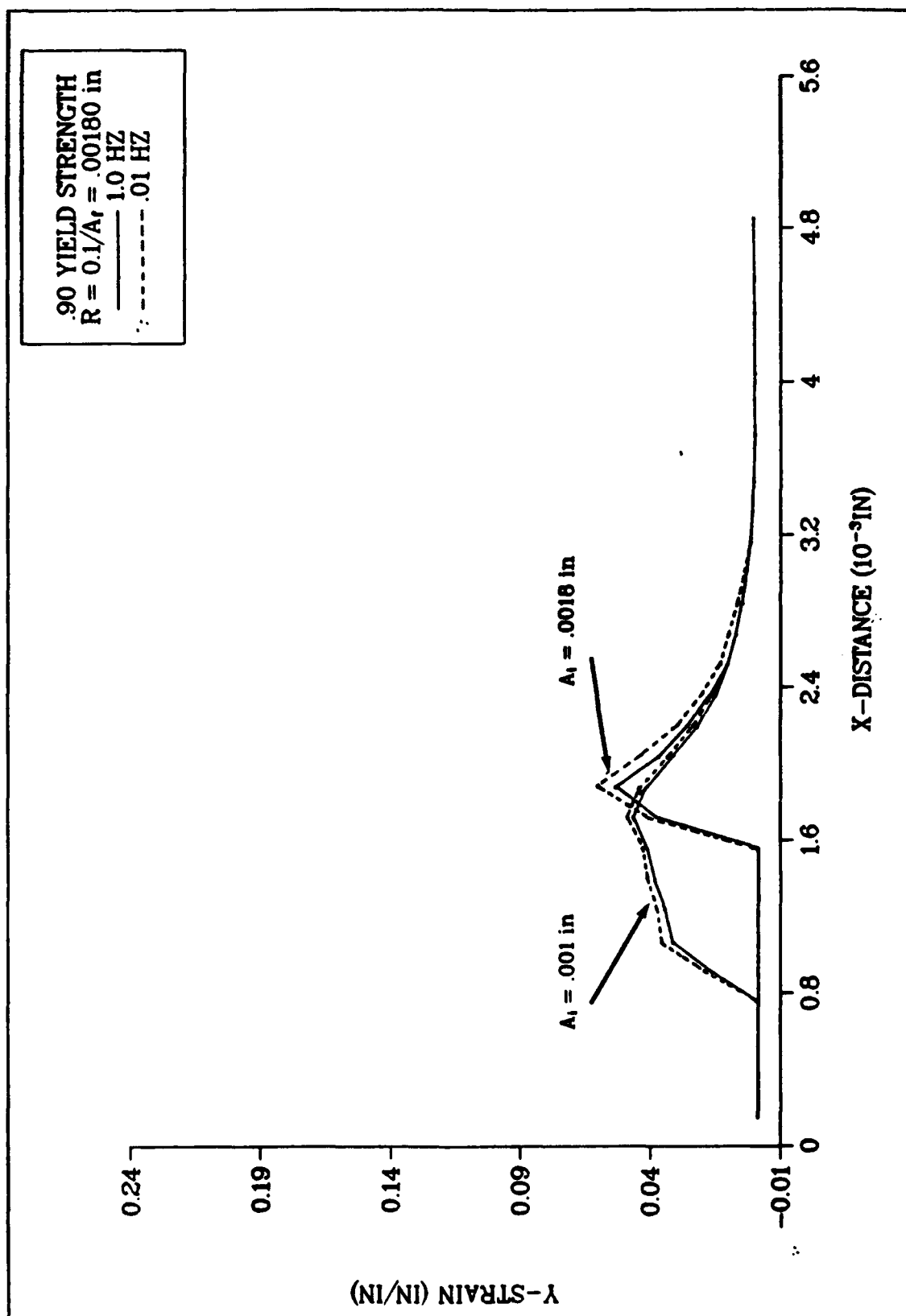
Fig 4.64: Affect of Frequency on Plastic Strain
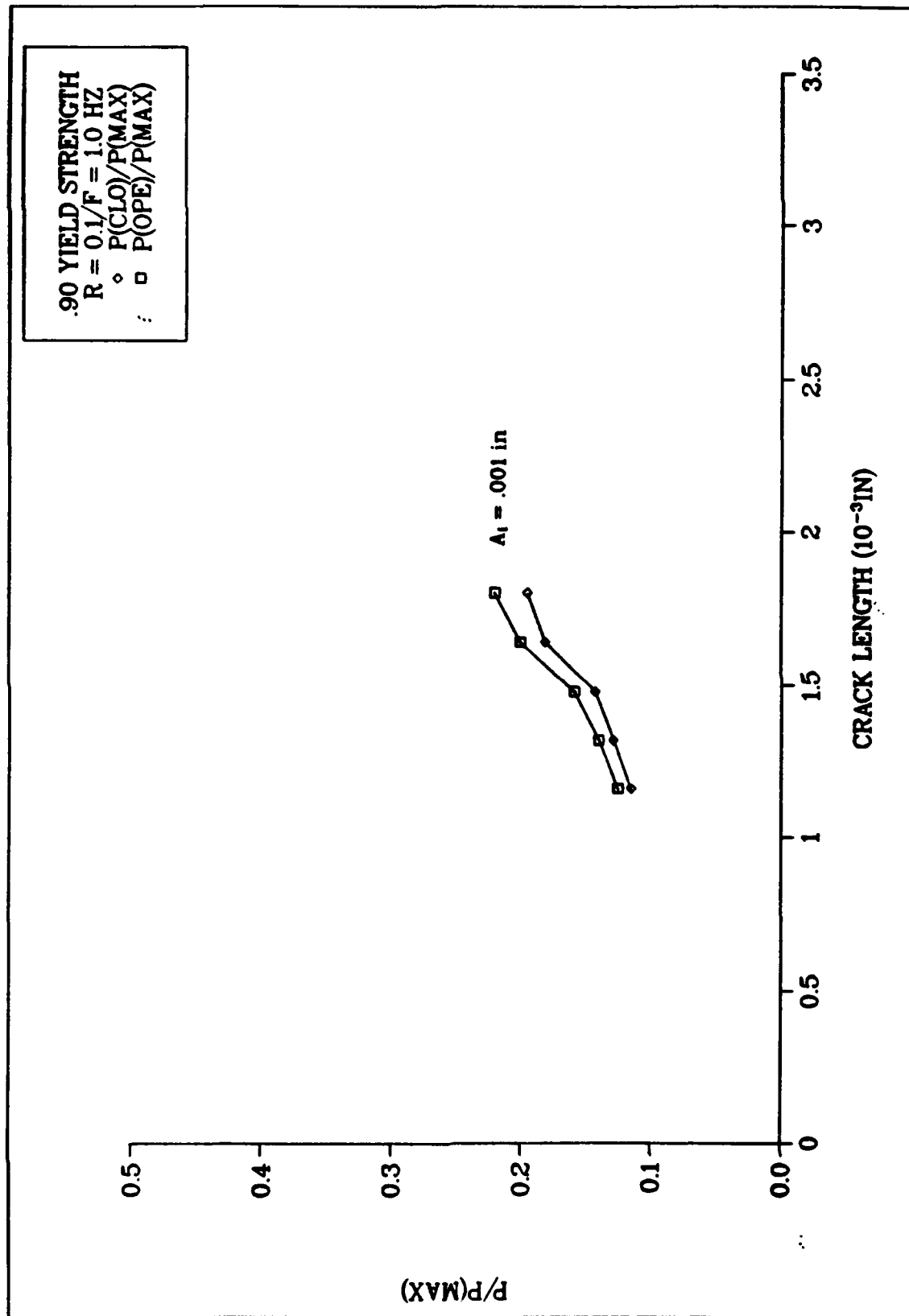
Fig 4.65: Crack Closure (Case E)
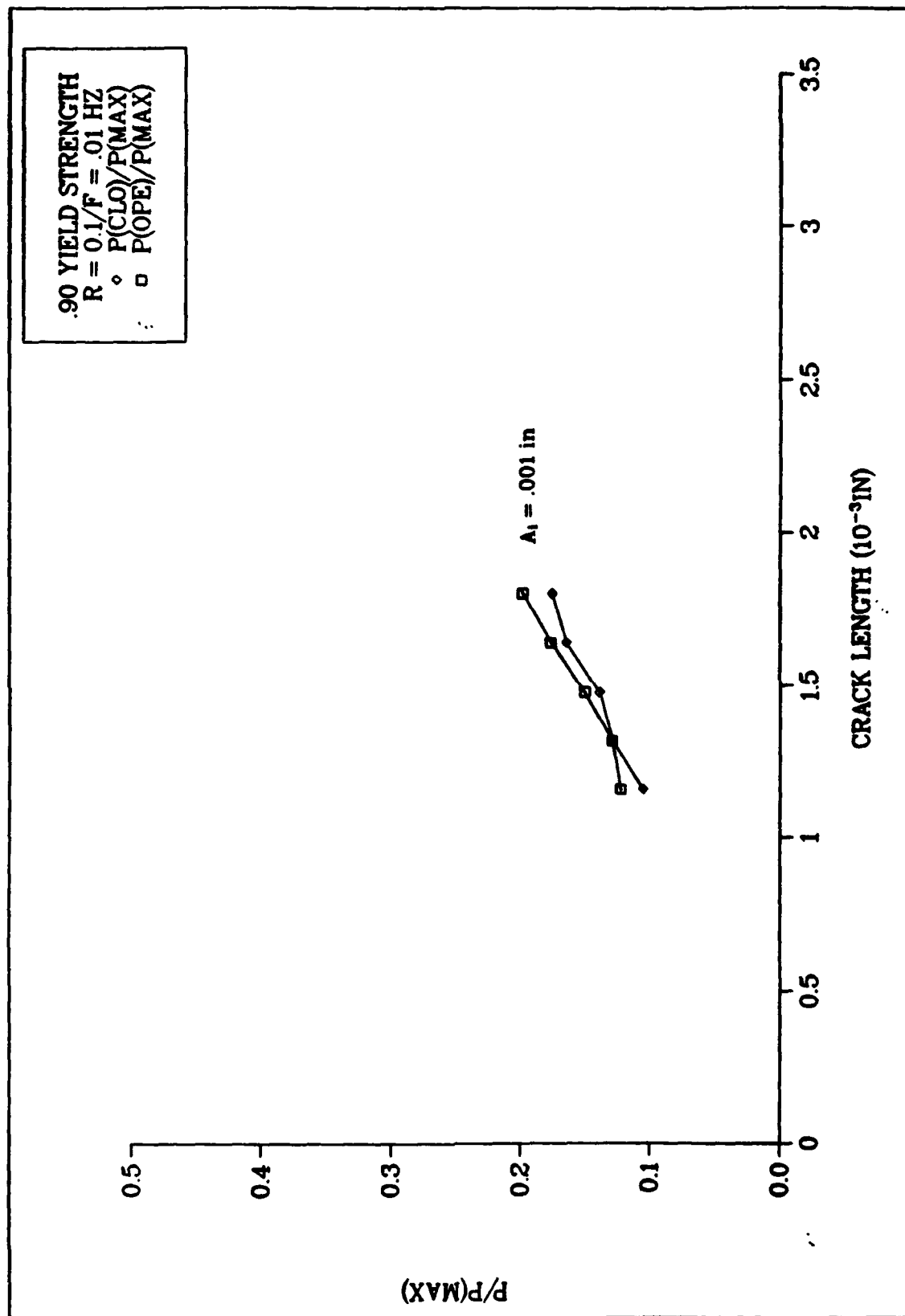
Fig 4.66: Crack Closure (Case F)
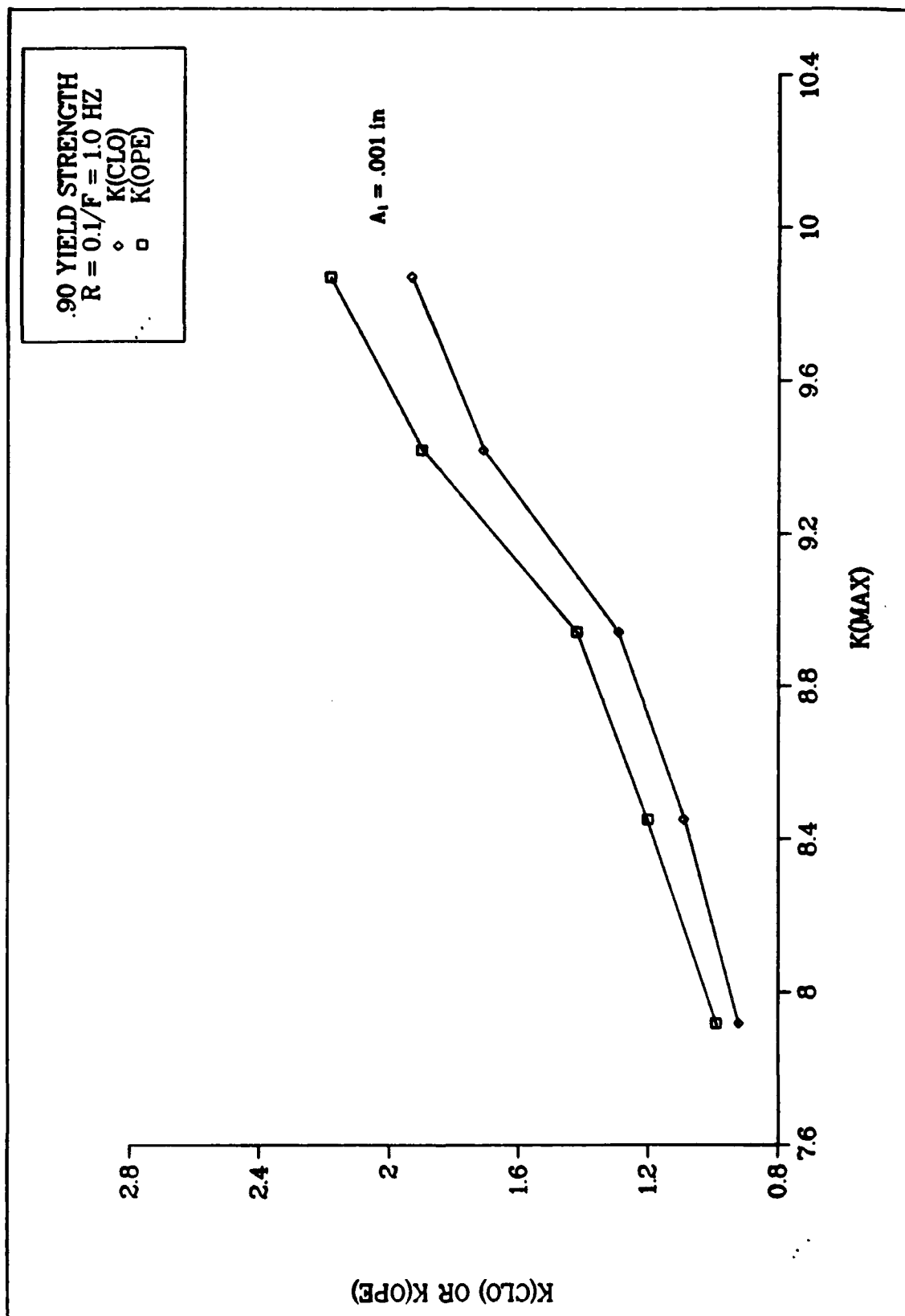
Fig 4.67: Crack Closure As a Function of K (Case E)

128
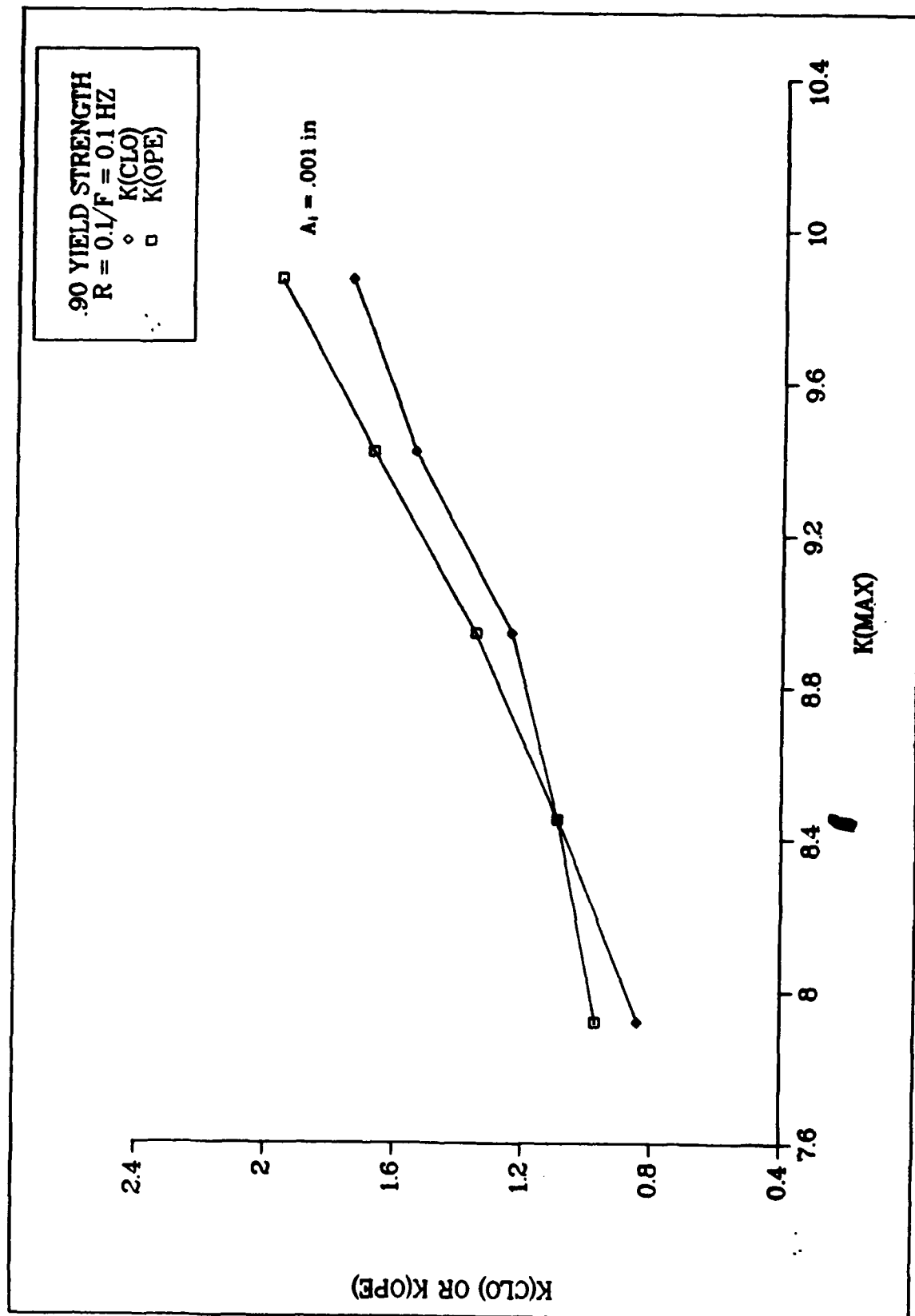
Fig 4.68: Crack Closure As a Function of K (Case F)
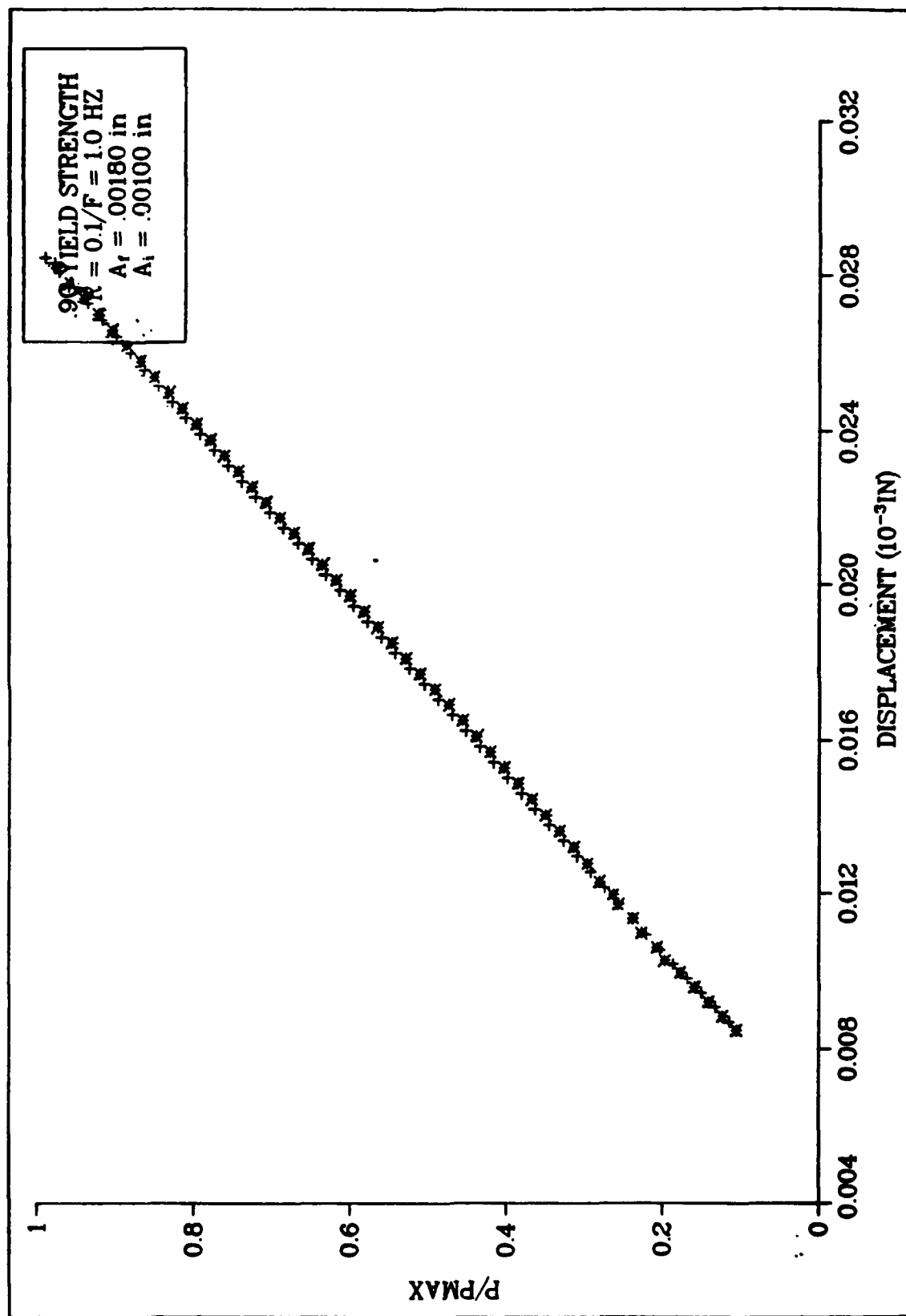
Fig 4.69: Load – Displacement (Case E/Elem 192)

130
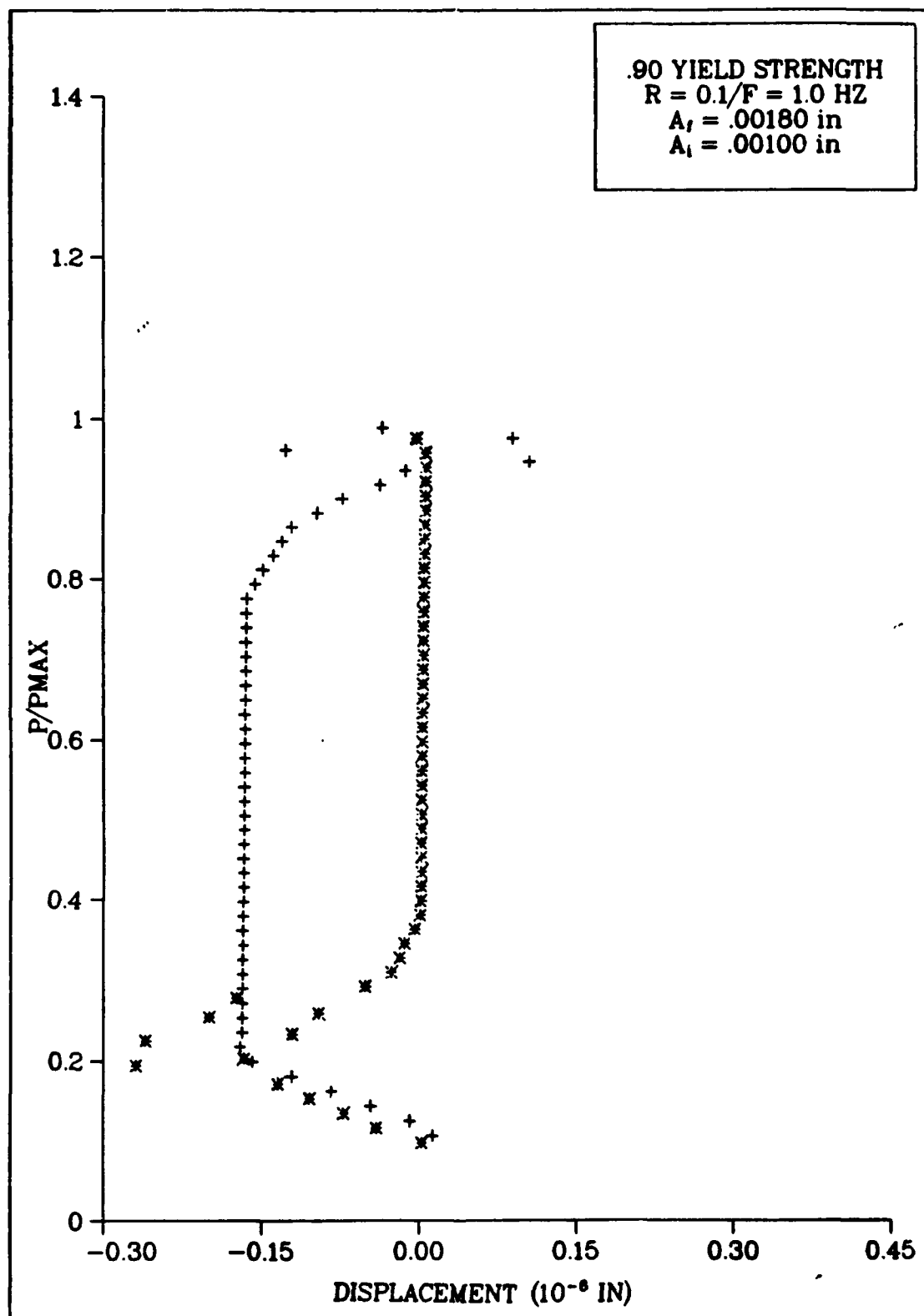
Fig 4.70: Load — Delta Displacement (Case E/Elem 192)
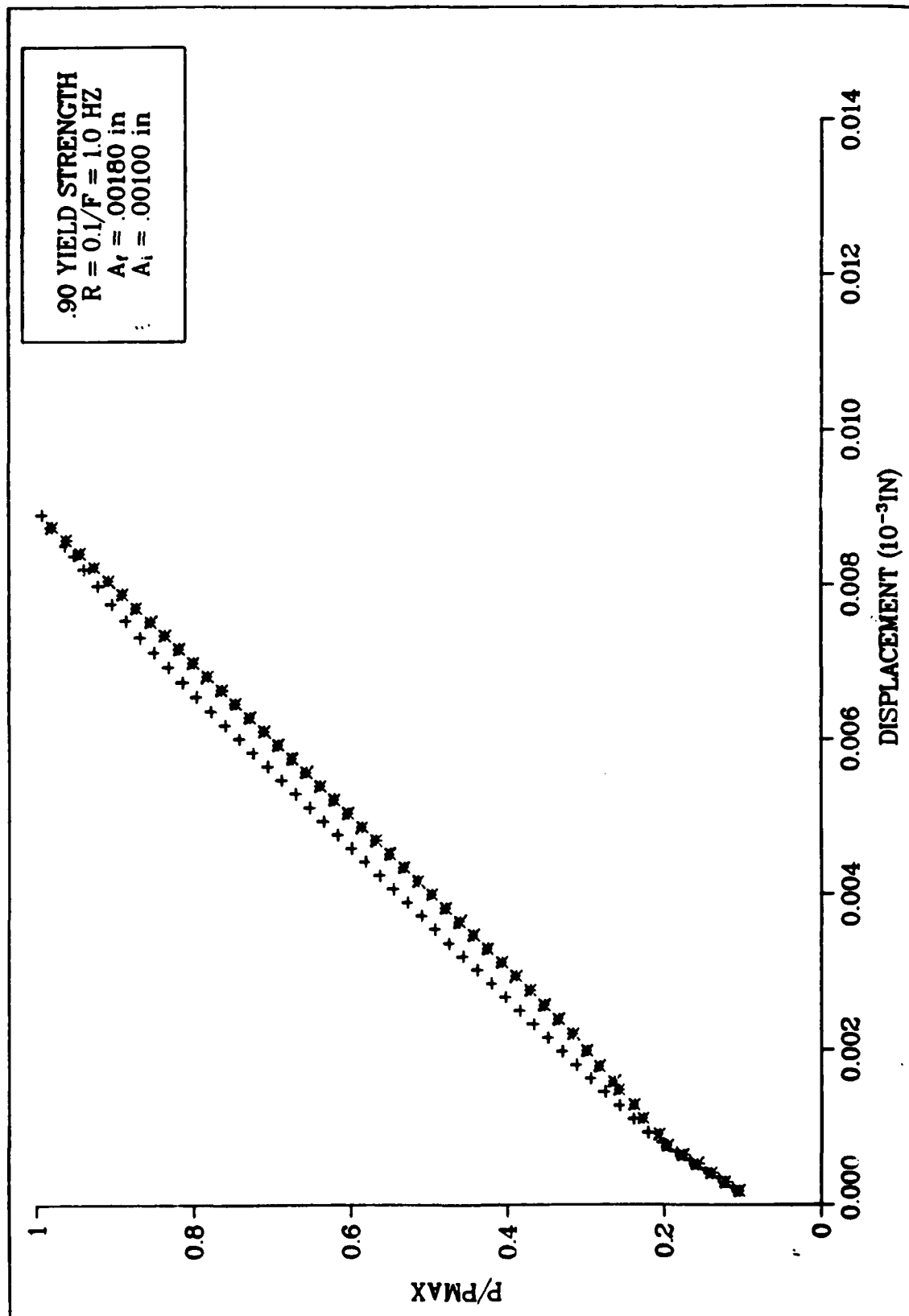
Fig 4.71: Load – Displacement (Case E/Elem 200)
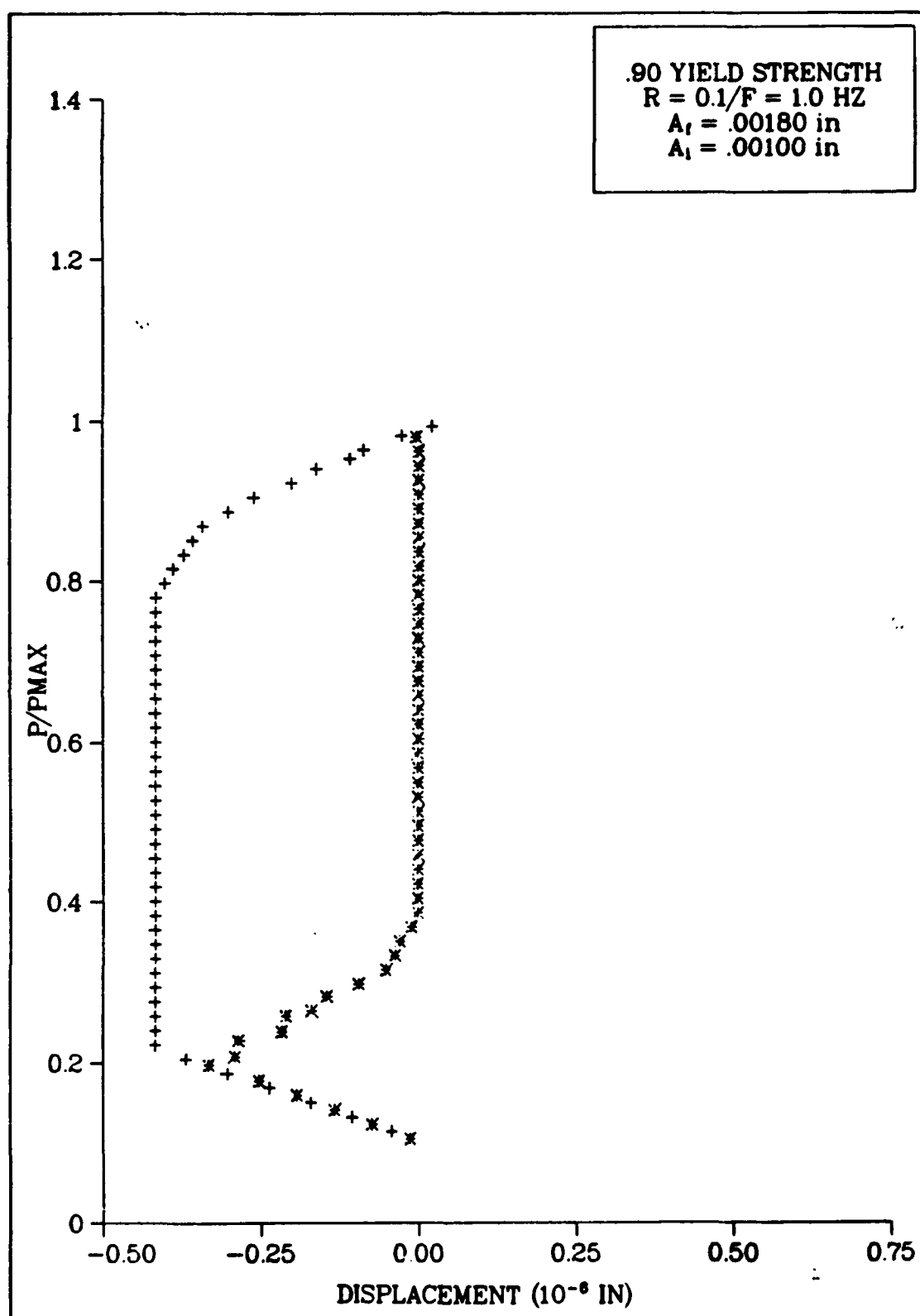
Fig 4.72: Load – Delta Displacement (Case E/Elem 200)

133
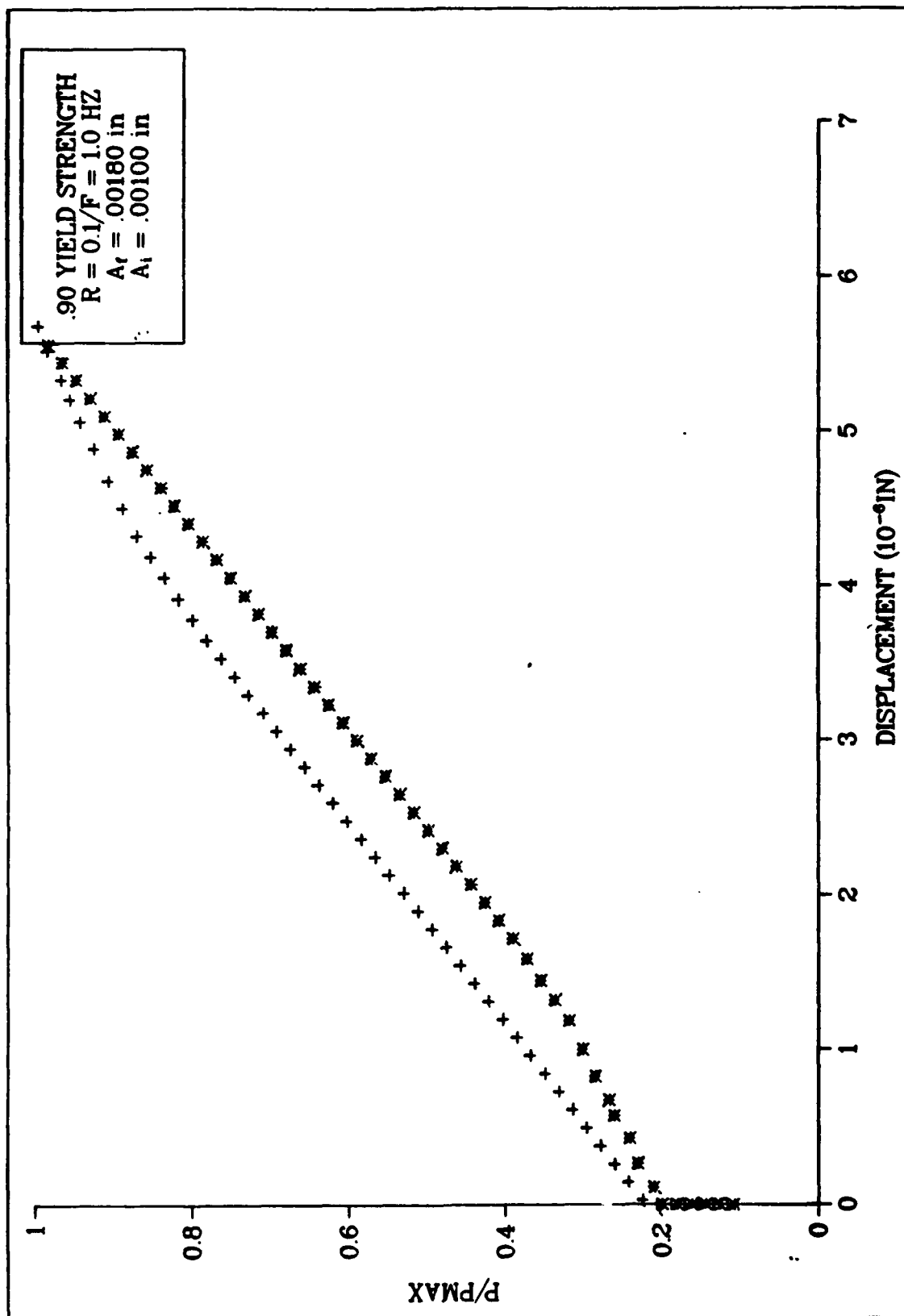
Fig 4.73: Load – Displacement (Case E/Elem 201)
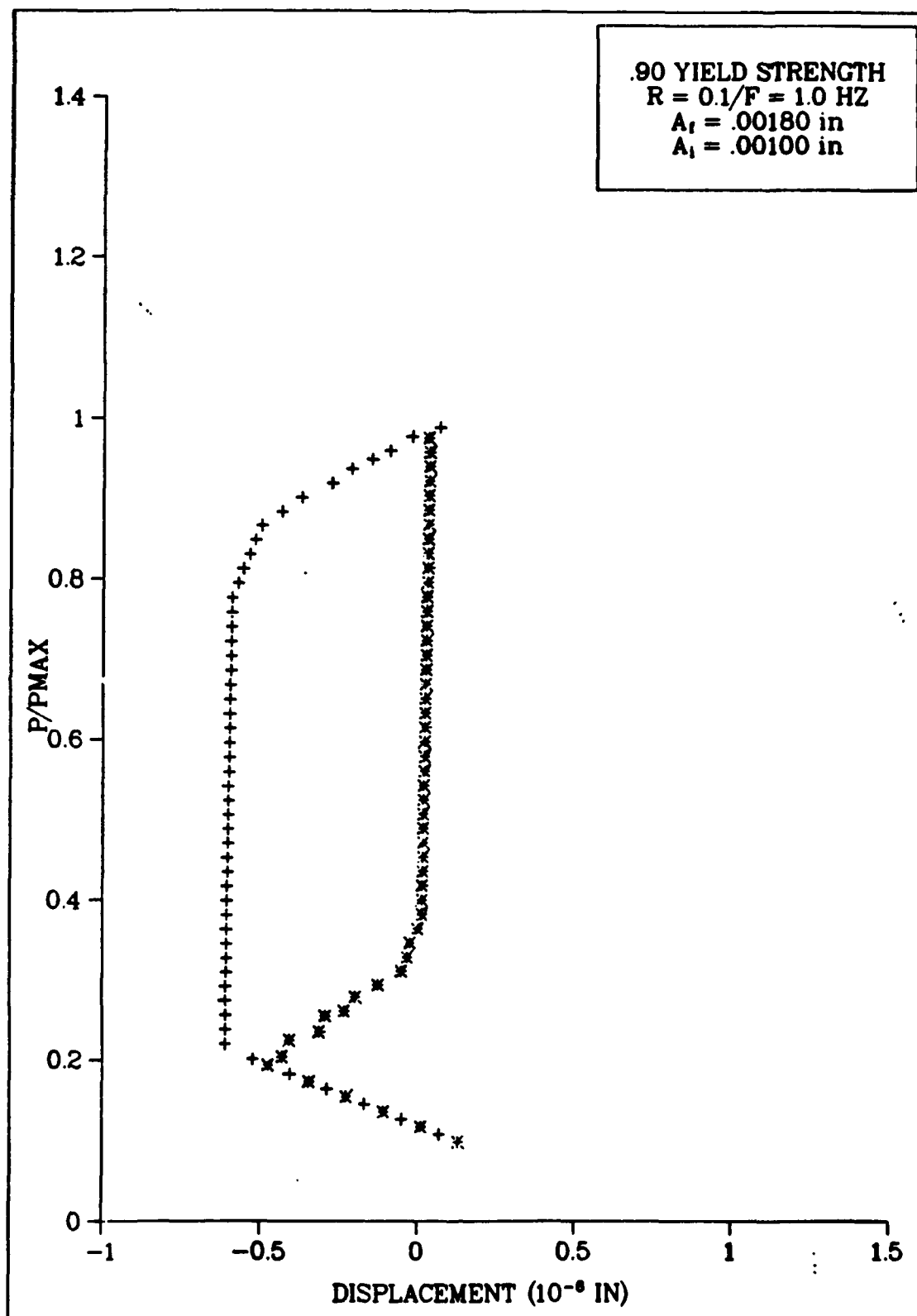
Fig 4.74: Load — Delta Displacement (Case E/Elem 201)
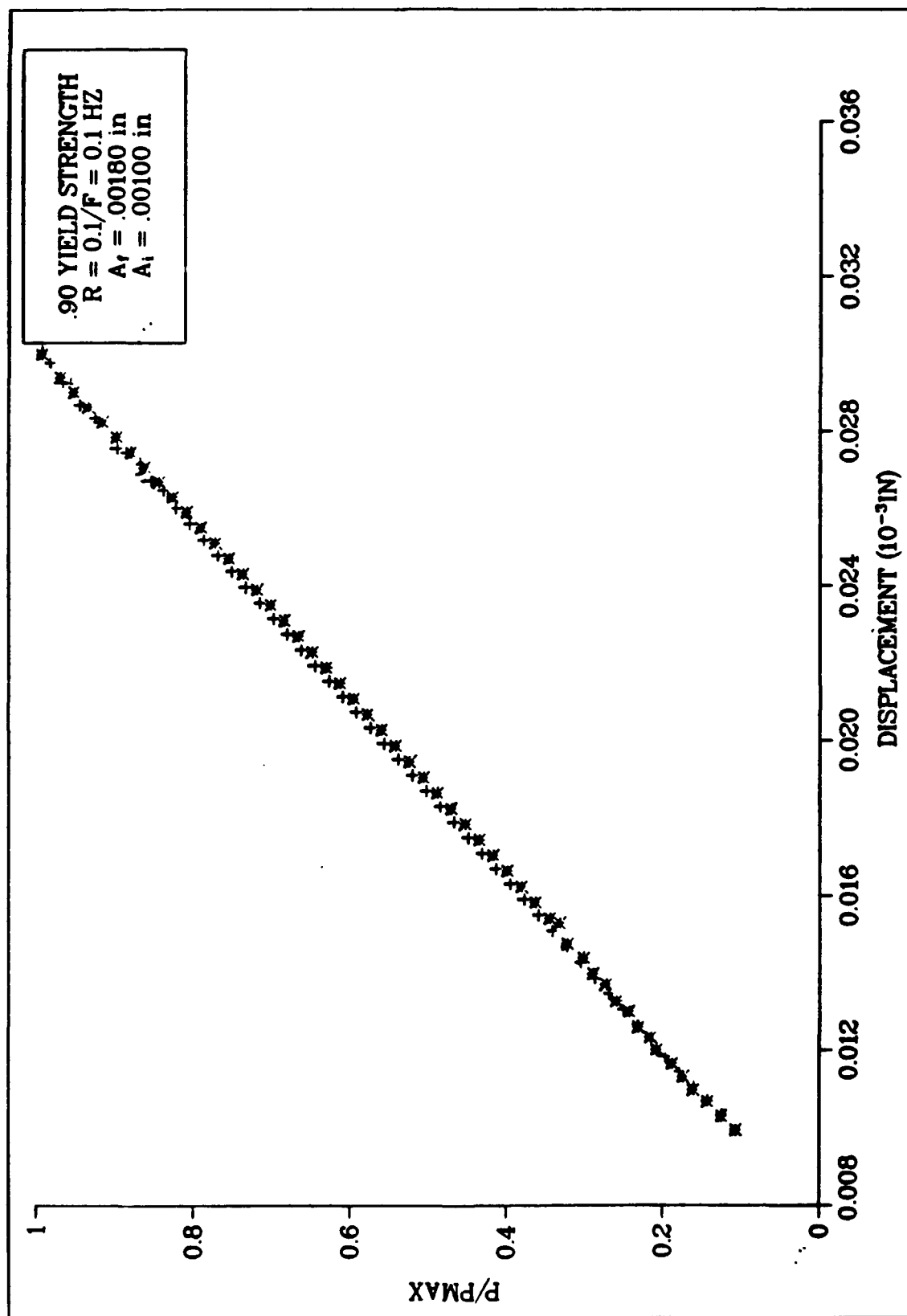
Fig 4.75: Load – Displacement (Case F/Elem 192)

136
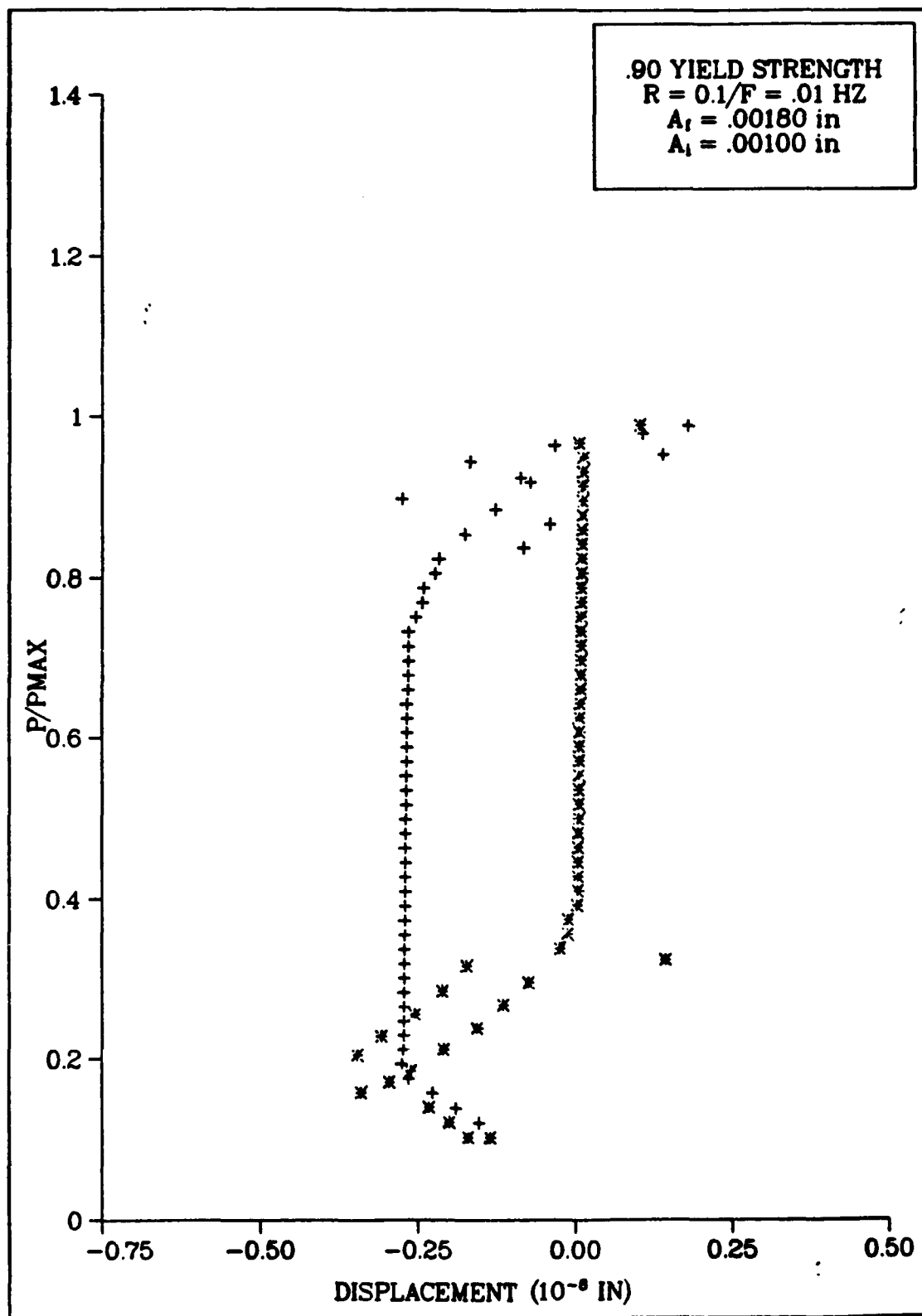
Fig 4.76: Load − Delta Displacement (Case F/Elem 192)
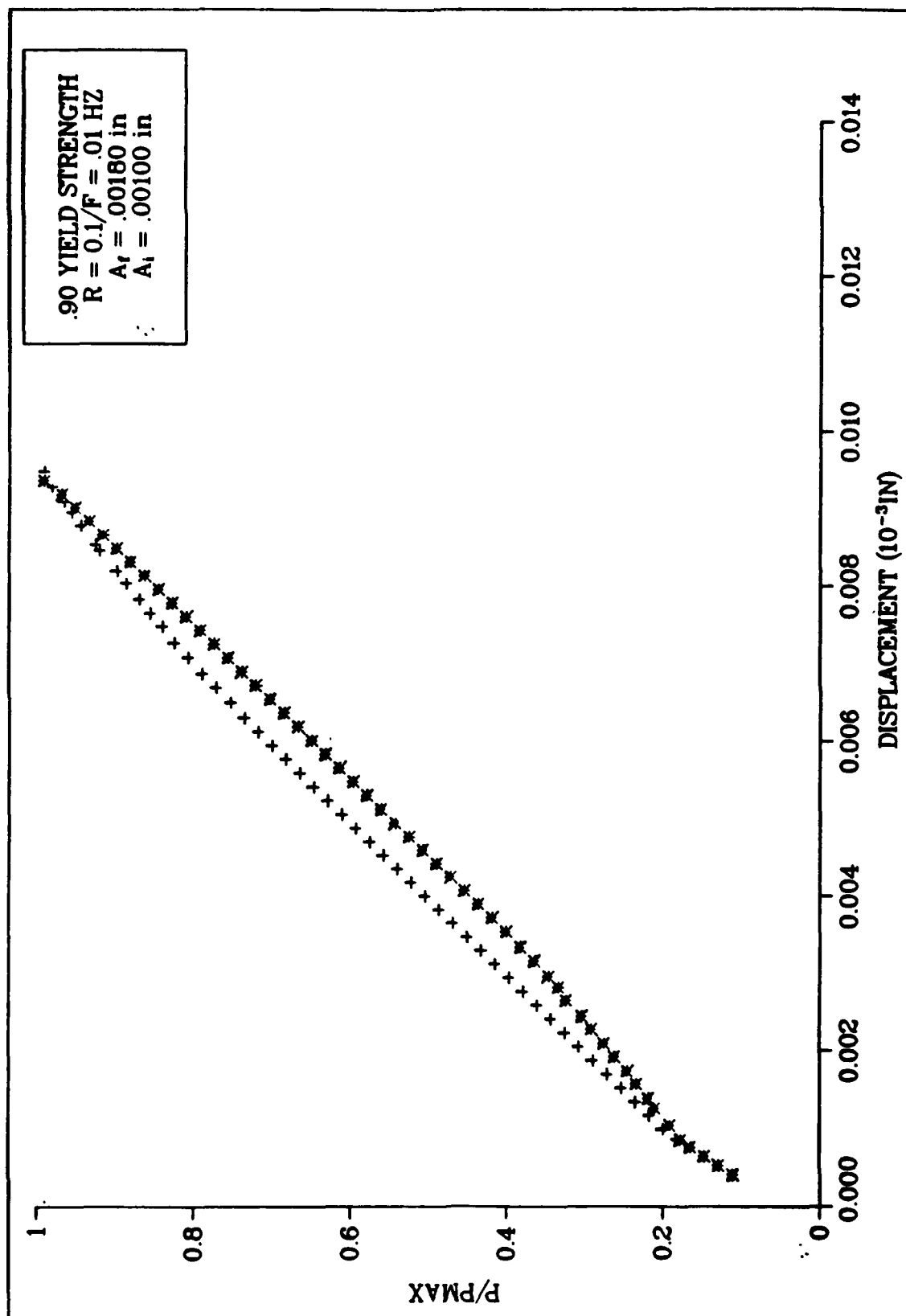
Fig 4.77: Load — Displacement (Case F/Elem 200)

The plot legend reads:

.90 YIELD STRENGTH
R = 0.1/F = .01 HZ
A_f = .00180 in
A_i = .00100 in

The vertical axis is labeled P/PMAX with values 0, 0.2, 0.4, 0.6, 0.8, 1.

The horizontal axis is labeled DISPLACEMENT (10^{-3}IN) with values 0.000, 0.002, 0.004, 0.006, 0.008, 0.010, 0.012, 0.014.

138
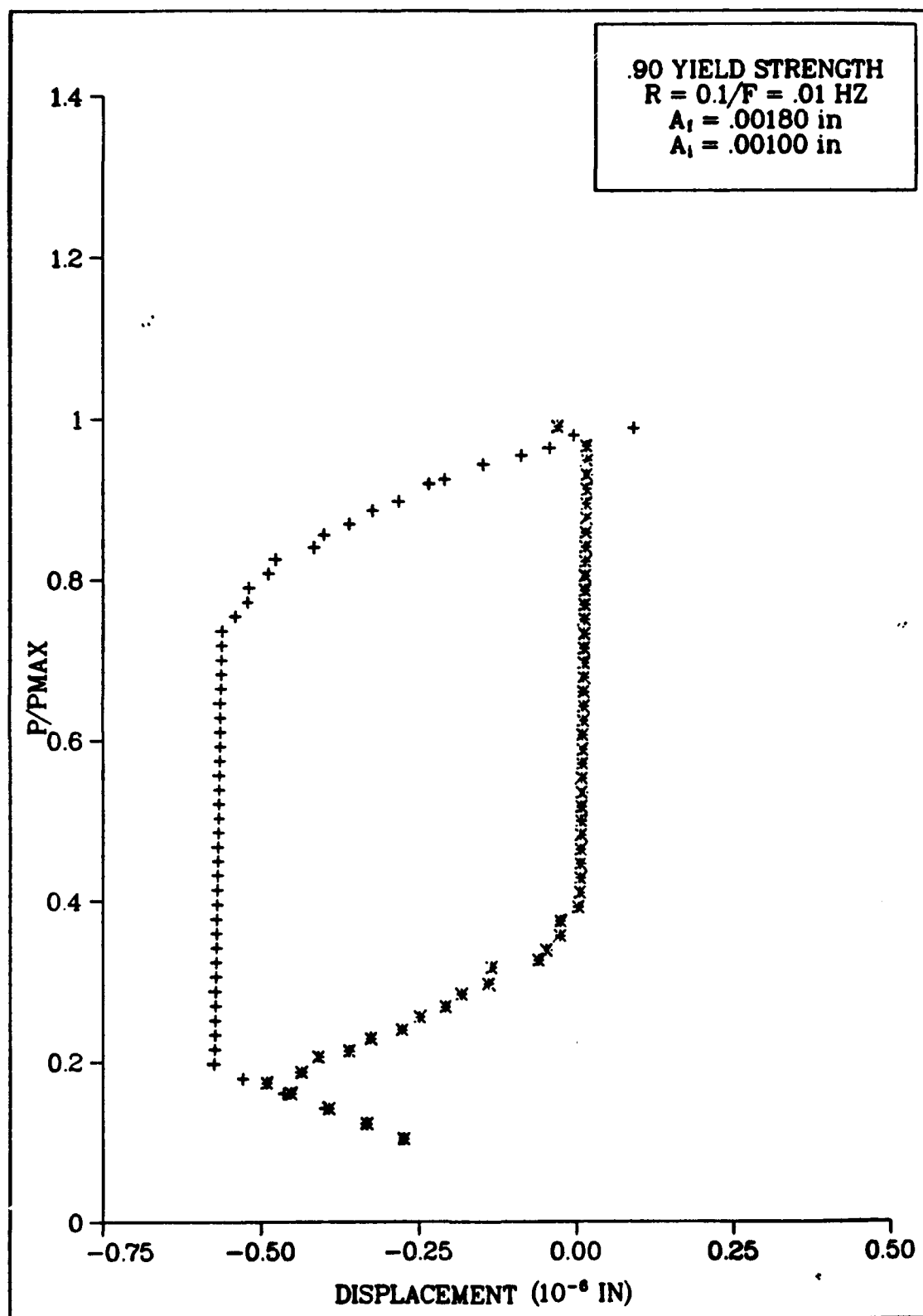
Fig 4.78: Load – Delta Displacement (Case F/Elem 200)

Fig 4.79: Load – Displacement (Case F/Elem 201)

140

.90 YIELD STRENGTH
R = 0.1/F = .01 HZ
A_f = .00180 in
A_i = .00100 in
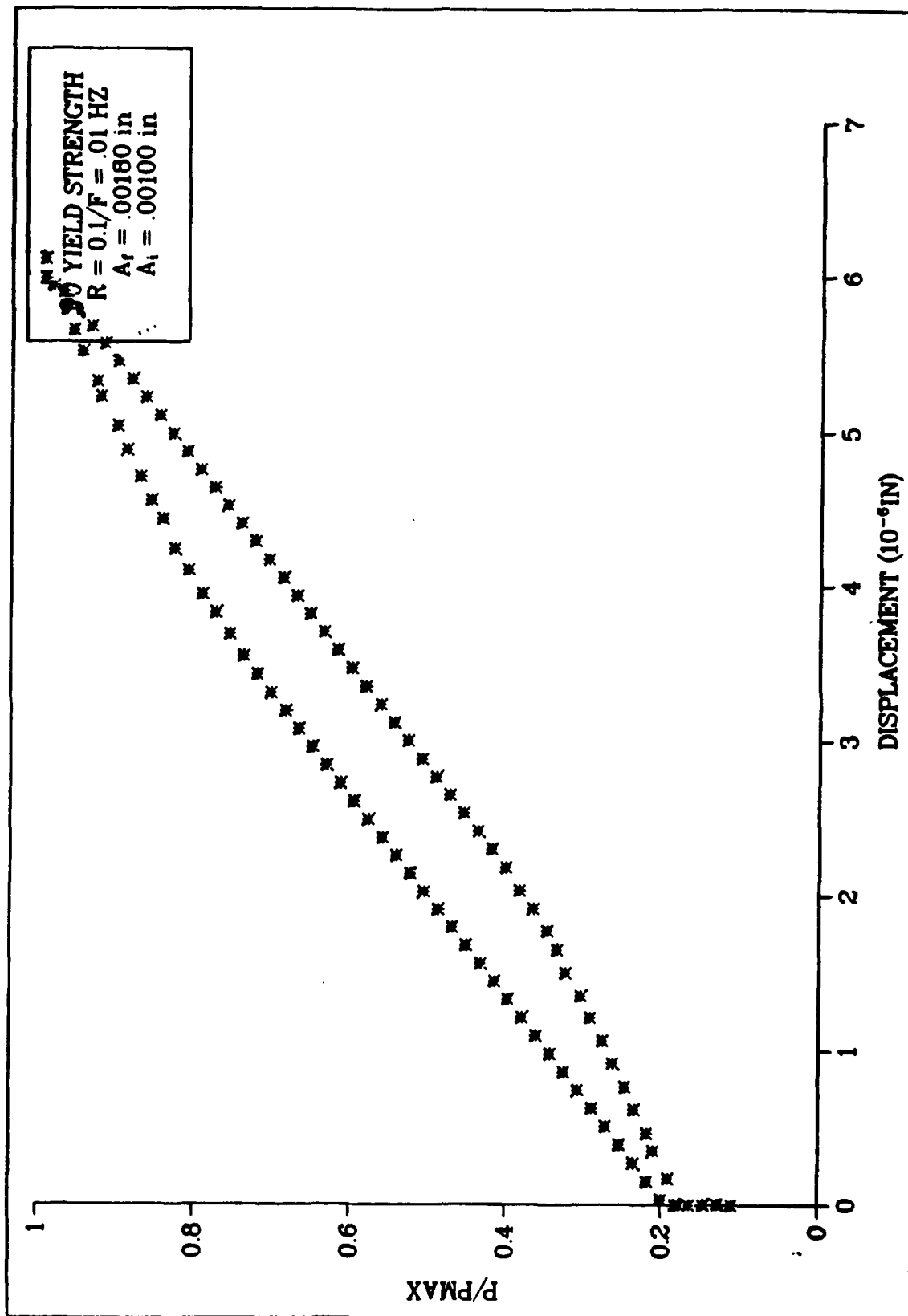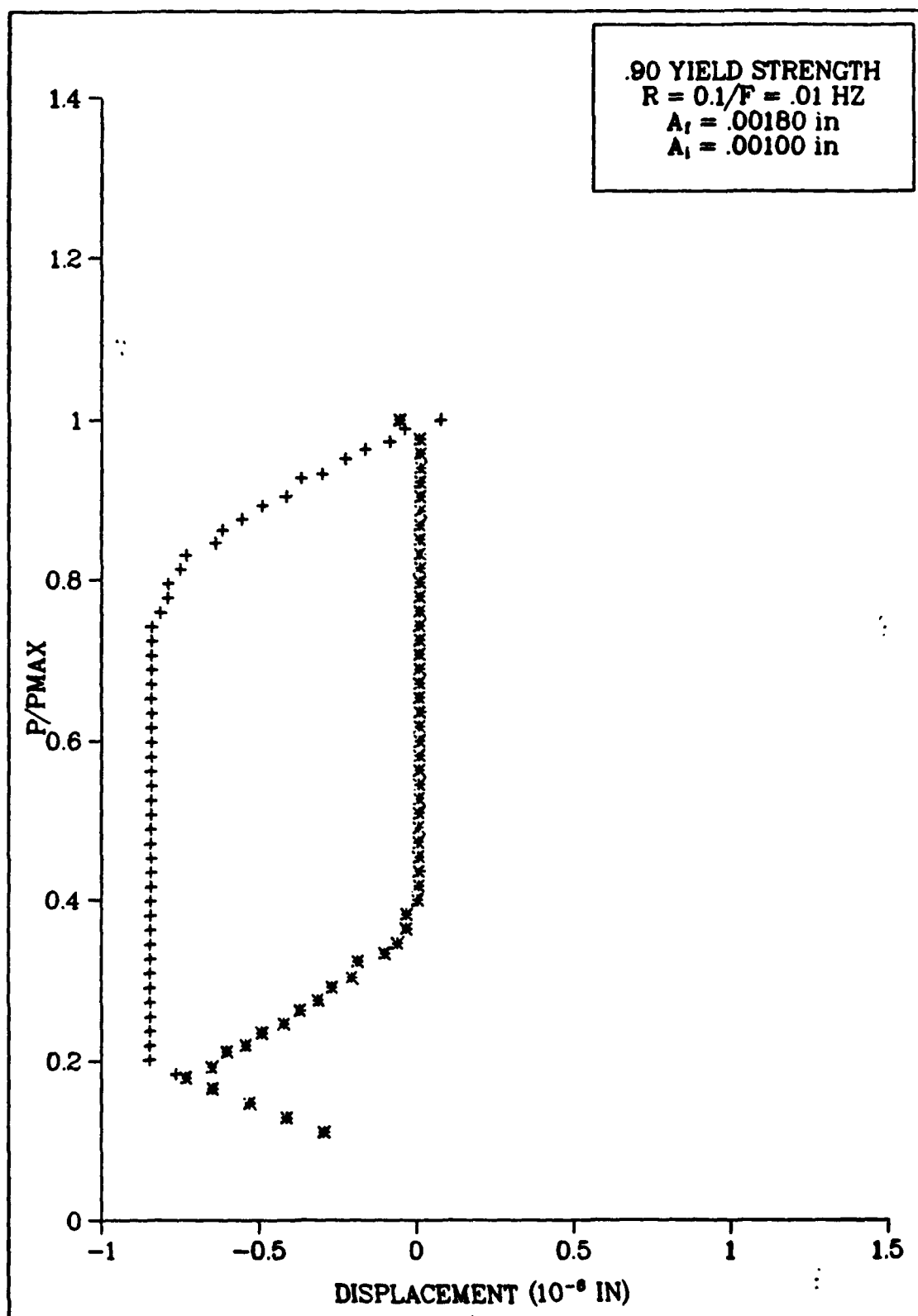
Fig 4.80: Load – Delta Displacement (Case F/Elem 201)

the crack remains closed, but at the point of crack opening, it increases dramatically. From this point, the elastic strains predominantly occur until plastic strains become evident near the point of maximum load. During subsequent unloading, a reduction in the elastic strains initially occurs, but then the recovery of plastic strains predominates as P(clo) is approached. The point of crack closure is indicated by a sharp change in the slope of the load-delta displacement curve.

The effects of viscoplastic material properties in Inconel 718 at high temperatures can be further seen in these curves. As an example, the load-delta displacement curve in Figure 4.74 shows that the width of the hysteresis loop is approximately $.6 \times 10^{-6}$ inches. This represents measurements taken at the node immediately behind the crack tip with a load frequency of 1.0 Hz. Similar measurements at a cyclic frequency of .01 Hz in Figure 4.80 reflect a width of $.85 \times 10^{-6}$ inches. A greater amount of recoverable plastic strain occurs at the lower frequency.

Discussion

Regardless of the materials involved, here TI-6246 at room temperature and Inconel 718 at $1200^{\circ}F$, as a crack propagates under cyclic loading, a plastic wake is formed along the crack surface. This wake is composed of plastically deformed material and has a definite effect of material behavior in the vicinity of the crack tip. In order to accurately describe this behavior, finite element analyses must be able to incorporate the development and effects of a plastic wake. As seen in this research, finite element modeling of plasticity induced closure in short cracks under fatigue loading requires some amount of

142

crack extension to develop closure. A non-propagating crack with no prior loading history or existence of residual strains behind the crack tip cannot provide the closure levels found in a propagating crack in a finite element analysis. A plastic wake over a finite crack length is necessary to develop and demonstrate crack closure.

Under most loading conditions, the formation of this plastic wake restricts crack surface opening displacements and reduces the total strain occurring immediately in front of the crack tip. These effects were observed in the finite element analysis over the region of crack growth from the original crack tip to its final location. If a specimen has been 'precracked' before the onset of fatigue loading without allowing for the development of a plastic wake, then displacements along the precrack will be less and total strains observed will be greater than one exhibiting a plastic wake effect. A 'precracked' specimen exhibiting no crack growth history, either experimentally or analytically, will not accurately demonstrate the effects of plasticity induced closure on fatigue crack growth.

The investigation conducted as part of this research effort indicates that this plastic wake effect develops rapidly for fully reversed loading but requires longer propagation distances to develop under a stress ratio of R = 0.1. As a result, plasticity induced closure is also observed to develop more rapidly at higher stress levels than lower stress levels. Further, the steady state closure loads, as a fraction of maximum load, decrease with increasing stress or decreasing stress ratios.

Because of this build-up of plastic material, residual compressive forces are exhibited during the unloading portion of the fatigue cycle.

This causes an increase in the amount of tensile load required to open a crack and, in a like manner, a decrease in the amount of external compression required to keep the crack closed. This plastic wake effect increases the values of P(clo) and P(ope), the closure and opening loads. This effect, however, is not the same for all cases. As discussed previously, the variations in crack opening stress intensities K(ope) with maximum stress intensity K(max) is neither a single-valued function nor a monotonically increasing function for short cracks under different stresses or stress ratios. For either value of R investigated, K(ope) decreases with increasing stress. Opening and closing stress intensities, K(ope) and K(clo), tend to diverge with increases in K(max) or crack length under constant amplitude fatigue at R = -1.0.

The determination of closure and opening loads requires displacement measurements at some point along the crack length. This investigation showed that closure is more easily determined using near-field displacements (those immediately behind the crack tip) than far-field (those at or near the crack mouth). Differential displacement plots, however, ease the determination of opening and closing loads. For high stress levels where significant hysteresis is observed, the inflection point in the unloading curve correlates with the closure load. These closure and opening loads, using either displacement measurements or differential displacement plots, do not depend on displacement measurement location, but the sensitivity and resolution required to determine these loads is greatly affected by location. Near-field measurements provide greater sensitivity to closure load determination.

These above observations regarding the effects of plasticity induced closure on fatigue crack growth are consistent over a wide range of load conditions. High compressive forces, however, which occur in a reversed loading condition tend to remove some of these effects. The recovery of some plasticity as a result of these forces along the crack surface reduces the size of the plastic wake and reduces the restriction of strain related conditions. These results appear highly dependent on the loading history of a specimen and are not easily predicted.

V. Summary and Conclusions

Visco II, a plane stress/plane strain finite element code has been developed from the original Visco program developed by Hinnerichs [71]. This modified version incorporates non-linear viscoplastic, as well as, elastic-plastic, material behavior, changing boundary conditions resulting from crack growth and crack closure, and a data storage/ restart capability. The overall solution technique is the residual force method which maintains a constant stiffness matrix and incorporates plasticity effects through the inclusion of a plastic load vector. Non-linear material behavior is handled by the Bodner-Partom Viscoplastic Flow Law, and an Euler extrapolation scheme is used to integrate these relations with respect to time. Further, a Gauss-Siedel iterative technique is used to solve for equilibrium conditions.

This finite element code was employed to study the effects of plasticity induced closure in short cracks by analyzing single-edge cracked specimens (a = .001 in) under various load conditions. Materials studied included TI-6246 at room temperature and Inconel 718 at $1200^{o}F$.

The following are summary statements and/or conclusions based upon the short crack fatigue analyses discussed herein:

1. A procedure was developed which accurately handles crack closure in a cyclically loaded specimen. This algorithm is initiated within the finite element code when negative displacements occur along the crack surface. A vector of closure loads, which is required to maintain zero displacements

146

where closure has occurred, is then incorporated into the equilibrium solution such that refactorization of the stiffness matrix is not required. This maintains the overall residual force method solution technique. This procedure produced substantial improvements in the accuracy of past finite element analyses of cyclically loaded center cracked specimens.

2. A procedure to accomodate a data storage/restart capability was incorporated into the Visco II finite element code. This modification allows for extensive finite element analyses which were previously unattainable due to computer restraints.

3. The crack growth algorithm included in previous forms of the Visco finite element code was modified and successfully used to analyze a cyclically loaded specimen for the first time. Previous analyses used this algorithm solely to study creep crack growth. The change in plastic strain exhibited immediately in front of the crack tip on subsequent load cycles was used as a criterion for crack growth. This significantly reduced computational requirements and satisfactorily modelled material behavior in a specimen exhibiting fatigue crack growth.

4. Material constants for TI-6246 at room temperature were determined for use in the Bodner model following procedures similar to those developed by Beaman [72] and Stouffer [74]. These values represent a rate-insensitive material at room temperature and demonstrate that the Bodner model, which incorporates both rate dependent plasticity and creep, can be successfully applied to such a material. These constants were

147

determined based upon minimal experimental stress/strain data
and were subsequently shown to satisfactorily model the
particular material behavior.

5. The Visco II code was used to model the growth of small cracks
   to represent the behavior of TI-6246. The numerical procedure
   allowed the study of the formation of a plastic wake, residual
   stresses, and deformation both behind and ahead of the crack
   tip. This constitutes the first detailed analytical study of
   the growth of short cracks from a free surface and the effects
   of plasticity induced closure.

6. At maximum tensile load, the non-propagating crack is fully
   open and maximum displacements in the vicinity of the crack tip
   occur at the node directly behind the tip. The displacement
   profile of the propagating crack, however, shows that the crack
   remains closed for several nodes behind the crack tip and then
   opens gradually. Under cyclic loading, the displacements take
   on unusually high values directly behind the crack tip when no
   history of crack extension is considered.

7. Plastic strains immediately ahead of the crack tip are higher
   for the non-propagating crack than for the propagating crack.
   Under fully reversed loading, a severe compression develops in
   the plastic wake and is most compressed at higher stress levels
   directly behind the crack tip.

8. Finite element modeling of plasticity induced closure in short
   cracks in fatigue requires some amount of crack growth to
   develop closure. A non-propagating crack with no prior loading
   history or residual strains behind the crack tip cannot provide

the closure levels present in a propagating crack using finite element simulations. The plastic wake effect develops rapidly for fully reversed loading but requires greater crack extension to develop under a stress ratio $R = 0.1$. Closure also develops more rapidly at high stress levels than at low stress levels. Steady-state closure loads, as a fraction of maximum load, decrease with increasing stress or decreasing load ratio.

9. The variation of crack opening stress intensity, K(ope), with maximum stress intensity, K(max), is neither a single-valued function nor a monotonically increasing function for short cracks under different stress levels or stress ratios. For either value of stress ratio considered, $R = -1.0$ or $R = 0.1$, K(ope) decreases with increasing stress as the nominal applied stress moves from 0.6 to 0.9 of the material yield stress. In addition, opening and closing stress intensities, K(ope) and K(clo), tend to diverge with increases in K(max) or crack length under constant amplitude fatigue at $R = -1.0$. This divergence is highest at a nominal stress value of 0.9 material yield stress.

10. Closure, as determined from deviations from linearity in a load-displacement plot, is more easily determined using near-field displacements (immediately behind the crack tip) rather than from far-field ones (at the crack mouth) in small cracks where the plastic zone size is of the same order as crack length. Differential-displacement plots make it easier to determine opening and closing loads. For high stress levels were significant hysteresis is observed in the load-displace-

ment curve, the inflection point in the unloading portion of the curve correlates with the closure load determined from the first contact of a node behind the crack tip in the finite element analysis. Closure and opening loads do not depend on displacement measurement location, but the sensitivity and resolution necessary to determine these loads are greatly affected by the measurement location. Near-field measurements provide this greater sensitivity and resolution in closure load determination.

11. The same general characteristics regarding the effects of plasticity induced closure in the growth of short cracks under fatigue loading for TI-6246 at room temperature (rate independent material behavior) were observed for Inconel 718 at $1200^{\circ}F$ (rate dependent material behavior). Viscoplastic effects were, however, observed when considering the difference in cyclic load frequency. At the higher load frequency, plastic strains are less along the crack length than for the lower cyclic frequency. The size of the plastic wake is smaller at higher frequencies resulting in less residual compressive stresses at the higher frequency. Crack opening and crack closing loads are therefore reduced as load frequency is increased.

Bibliography

1. United States Air Force. <u>Engine Structural Integrity Program</u>.
    Military Standard 1783. Aeronautical Systems Division. WPAFB, Ohio,
    1984.

2. United States Air Force. <u>Aircraft Structural Integrity Program</u>,
    <u>Airplane Requirements</u>. Military Standard MIL STD-1530A, (11).
    December 11, 1975.

3. United States Air Force. <u>Airplane Damage Tolerance Requirements</u>.
    Military Specifications MIL-A-83444. July 2, 1975.

4. Grandt, A.F. Jr. <u>Initiation, Growth and Coalescence of Small</u>
    <u>Fatigue Cracks</u>. AFOSR-TR-83-0867. Air Force Office of Scientific
    Research, Bolling AFB, D.C., May, 1983.

5. El Haddad, M.H., Smith, K.N., and Topper, T.H. "Fatigue Crack
    Propagation of Short Cracks". <u>Journal of Engineering Materials and</u>
    <u>Technology</u>, Vol 101: 42-46 (January, 1979).

6. Hudak, S.J. Jr. "Small Crack Behavior and the Prediction of Fatigue
    Life". <u>Journal of Engineering Materials and Technology</u>, Vol 103:
    26-35 (1981).

7. Lankford, J. "On the Small Crack Fracture Mechanic Problem".
    <u>International Journal of Fracture</u>, Vol 16: R7-R9 (1980).

8. Miller, K.J. "The Short Crack Problem". <u>Fatigue of Engineering</u>
    <u>Materials and Structures</u>, Vol 5, No 3: 223-232 (1982).

9. Stahle, P. "On the Small Crack Fracture Mechanics". <u>International</u>
    <u>Journal of Fracture</u>, Vol 22, No 3: 203-216 (1983).

10. Swain, M.H. and Newman, J.C. Jr. "On the Use of Marker Loads and
    Replicas for Measuring Growth Rates for Small Cracks". AGARD
    Specialists Meeting on Fatigue Crack Topography. Siena, Italy.
    April 4-5, 1984.

11. Leis, B.N. "Displacement Controlled Fatigue Crack Growth in
    Inelastic Notch Fields: Implications for Short Cracks".
    <u>Engineering Fracture Mechanics</u>, Vol 22, No 2: 279-293 (1985).

12. Miller, K.J. "The Propogation Behavior of Short Cracks".
    <u>Subcritical Crack Growth Due to Fatigue, Stress Corrosion, and</u>
    <u>Creep</u>. 151-166. Elsevier Applied Science Publishers, New York,
    N.Y., 1984.

13. Ritchie, R.O. and Suresh, S. "Mechanics and Physics of the Growth
    of Small Cracks". AGARD Conference on Behavior of Short Cracks in
    Airframe Components. Toronto, Canada. September 19-24, 1982.

14. Le May, I. "Fatigue Damage Mechanisms and Short Crack Growth". AGARD Conference on Behavior of Short Cracks in Airframe Components. Toronto, Canada. September 19-24, 1982.

15. Leis, B.N., Kanninen, M.F., Hopper, A.T., Ahmad, J., and Broek, D. A Critical Review of the Short Crack Problem in Fatigue. AFWAL-TR-83-4019. AFWAL Materials Laboratory, WPAFB, Ohio, January, 1983.

16. Talug, A. and Reifsnider, K. "Analysis and Investigation of Small Flaws". Cyclic Stress-Strain and Plastic Deformation Aspects of Fatigue Crack Growth, ASTM STP 639, American Society for Testing and Materials: 81-96 (1977).

17. Ritchie, R.O. and Lankford, J., Eds., Small Fatigue Cracks, The Metallurgical Society of AIME, Warrendale, PA, 1986.

18. Suresh, S. and Ritchie, R.O. "Propagation of Short Fatigue Cracks". International Metals Reviews, Vol 29, 1984, pp 445-476.

19. Morris, W.L. "The Noncontinuum Crack Tip Deformation Behavior of Surface Microcracks". Metallurgical Transactions, A, Vol 11A, 1980, pp 1117-1123.

20. Lankford, J., Davidson, D.L., and Chan, K.S. "The Influence of Crack Tip Plasticity in the Growth of Small Fatigue Cracks". Metallurgical Transactions, A, Vol 15A, 1984, pp 1579-1588.

21. Ritchie, R.O. and Suresh, S. "Some Considerations on Fatigue Crack Closure at Near-Threshold Stress Intensities Due to Fracture Surface Morphology". Metallurgical Transactions, Vol 13a: 937-940 (1982).

22. Larsen, J.M. "Advanced Experimental Methods for Monitoring the Behavior of Small Cracks". AGARD Structures and Materials Panel Specialists Meeting on 'Damage Tolerance Concepts for Critical Engine Components'. San Antonio, Texas, April, 1985.

23. Larsen, J.M., Jira, J.R., and Weerasoorlya, T. "Crack Opening Displacement Measurements on Small Cracks in Fatigue". ASTM 18th National Symposium on Fracture Mechanics. Boulder, CO. June, 1985.

24. Larsen, J.M. "An Automated Photomicroscopic System for Monitoring the Growth of Small Fatigue Cracks". Fracture Mechanics: Seven- teenth Volume, STP 905, J.H. Underwood, R. Chait, C.W. Smith, D.P. Wilhelm, W.A. Andrews, and J.C. Newman, Eds., American Society for Testing and Materials, Philadelphia, 1986, pp 226-238.

25. Bannerjee, S. A Review of Crack Closure. AFWAL-TR-84-4031. AFWAL Materials Laboratory, WPAFB, Ohio, April, 1984.

26. Suresh, S. and Ritchie, R.O. "A Geometric Model for Fatigue Crack Closure Induced by Surface Roughness". *Metallurgical Transactions*, Vol 13A: 1627-1631 (1982).

27. Suresh, S. "Crack Deflection: Implications for the Growth of Long and Short Cracks". *Metallurgical Transactions*, Vol 14A: 2375-2385 (1983).

28. Minakawa, K., Newman, J.C. Jr., and McEvily, A.J. "A Critical Study of the Crack Closure Effect on Near-Threshold Fatigue Crack Growth". *Fatigue of Engineering Materials and Structures*, Vol 6, No 4: 359-365 (1983).

29. Blom, A.F. and Holm, D.K. "An Experimental and Numerical Study of Crack Closure". *Engineering Fracture Mechanics*, Vol 22, No 6: 997-1011 (1985).

30. Elber, W. "Fatigue Crack Closure Under Cyclic Tension". *Engineering Fracture Mechanics*, Vol 2: 37-45 (1970).

31. Elber, W. "The Significance of Fatigue Crack Closure". *Damage Tolerance in Aircraft Structures*, ASTM STP 486, American Society for Testing and Materials: 230-242 (1971).

32. Allison, J.E. "Crack Closure Measurements During Fatigue Crack Growth". *Fracture Mechanics: 18th Symposium*, American Society for Testing and Materials, 1987, Philadelphia, pp 913-933.

33. Suresh, S. and Ritchie, R.O. "Near-Threshold Fatigue Crack Propagation: A Perspective on the Role of Crack Closure". *Fatigue Crack Growth Threshold Concepts*, D.L. Davidson and S. Suresh, Eds., The Metallurgical Society of AIME, Warrendale, PA, 1984, pp 227-261.

34. Ritchie, R.O. and Yu, W. "Short Crack Effects in Fatigue: A Consequence of Crack Tip Shielding". *Small Fatigue Cracks*, The Metallurgical Society of the AIME, Warrendale, PA, 1986, pp 167-189.

35. Nicholas, T., Palazatto, A.N., and Bednarz, E. "An Analytical Investigation of Plasticity Induced Closure Involving Short Cracks". *Mechanics of Fatigue Crack Closure, ASTM STP 982*, J.C. Newman, Jr. and W. Elber, Eds., American Society for Testing and Materials, Philadelphia, 1988, pp 361-379.

36. Newman, J.C., Jr. and Elber, W., Eds., *Mechanics of Fatigue Crack Closure, ASTM STP 982*, American Society for Testing and Materials, Philadelphia, PA, 1988.

37. Allen, R.J. and Sinclair, J.C. "The Behavior of Short Cracks". *Fatigue of Engineering Materials and Structures*, Vol 5, No 4: 343-347 (1982).

38. Hobson, P.D. "The Formulation of a Crack Growth Equation for Short Cracks". Fatigue of Engineering Materials and Structures, Vol 5, No 4: 323-327 (1982).

39. Taylor, D. and Knott, F. "Fatigue Crack Propagation Behavior of Short Cracks: The Effects of Microstructure". Fatigue of Engineering Materials and Structures, Vol 4, No 2: 147-155 (1981).

40. El Haddad, M.H., Dowling, N.E., Topper, T.H. and Smith, K.N. "J-Integral Applications for Short Fatigue Cracks at Notches". International Journal of Fracture, Vol 16, No 1: 15-30 (1980).

41. Trantina, G.G. and de Lorenzi, H.G. "Elastic-Plastic Fracture Mechanics Analysis of Small Cracks". Army Symposium on Solid Mechanics. September 21-23, 1982.

42. Newman, J.C. Jr. "A Finite Element Analysis of Fatigue Crack Closure". Mechanics of Crack Growth. ASTM STP 590: 280-301 (1976).

43. Dugdale, D.S. "Yielding of Steel Sheets Containing Slits". Journal of Mechanics and Physics of Solids, Vol 8, 1960, pp 100-104.

44. Newman, J.C. Jr. "A Non-Linear Fracture Mechanics Approach to the Growth of Short Cracks". AGARD Specialists Meeting on Behavior of Short Cracks. Toronto, Canada. September 20-21, 1982.

45. Ogura, K., Ohji, K. and Ohkibu, Y. "Cyclic Analysis of a Propagating Crack and Its Correlation with Fatigue Crack Growth". Engineering Fracture Mechanics, 9: 471-480 (1977).

46. Nakagaki, M. and Atluri, S.N. "Elastic-Plastic Analysis of FC Closure in Modes I and II". AIAA Journal, 18: 1110-1117 (1980).

47. Newman, J.C. Jr. A Crack Closure Model for Predicting Fatigue Crack Growth Under Aircraft Spectrum Loading. NASA Technical Memorandum 81941. Langley Research Center, Hampton, Virginia, January, 1981.

48. Newman, J.C. Jr. and Armen, H. Jr. "Elastic-Plastic Analysis of a Propagating Crack Under Cyclic Loading". AIAA/ASME/SAE 15th Structures, Structural Dynamics and Materials Conference. Las Vegas, Nevada. April 17-19, 1974.

49. Newman, J.C. Jr. "Finite Element Analysis of Crack Growth Under Monotonic and Cyclic Loading". Cyclic Stress-Strain and Plastic Deformation Aspects of Fatigue Crack Growth. ASTM STP 637. American Society for Testing and Materials: 56-80 (1977).

50. Newman, J.C. Jr. Finite Element Analysis of Fatigue Crack Propagation - Including the Effects of Crack Closure. Doctor of Philosophy Dissertation. Virginia Polytechnic Institute and State University, Blackburg, Virginia. 1974.

51. Wastberg, S. "A Finite Element Analysis of a Crack Growing Under Cyclic Loading". Fatigue of Engineering Materials and Structures, Vol 6, No 2: 149-158 (1983).

52. Sih, G.C. and Moyer, E.T. Jr. "Path Dependent Nature of Fatigue Crack Growth". Engineering Fracture Mechanics, Vol 17, No 3: 269-280 (1983).

53. Fuhring, H. and Seeger, T. "Fatigue Crack Growth Under Variable Amplitude Loading". Subcritical Crack Growth Due to Fatigue, Stress Corrosion, and Creep: 109-133. Elsevier Applied Science Publishers, New York, N.Y. 1984.

54. Newman, J.C. Jr. and Raju, I.S. Prediction of Fatigue Crack Growth Patterns and Lives in Three-Dimensional Cracked Bodies. NASA Technical Memorandum 85187. Langley Research Center, Hampton, Virginia. April, 1984.

55. Armen, H. "Assumptions, Models, and Computational Methods for Plasticity". Computers and Structures, Vol 10: 161-174 (1979).

56. Nayak, G.C. and Zienkiewicz, O.C. "Elasto-Plastic Stress Analysis. A Generalization for Various Constituitive Relations Including Strain Softening". International Journal for Numerical Methods in Engineering, Vol 5: 113-135 (1972).

57. Mendelson, A. Plasticity: Theory and Application. The MacMillan Company. New York, N.Y. 1968.

58. Owen, D.R.J. and Hinton, E. Finite Elements in Plasticity: Theory and Practice. Pineridge Press Limited. Swansea, United Kingdom. 1980.

59. Iyyer, N.S. and Dowling, N.E. "Opening and Closing of Cracks at High Cyclic Strains". Small Fatigue Cracks, The Metallurgical Society of the AIME, pp 213-223.

60. McEvily, A.J. and Minakawa, K. "Crack Closure and the Conditions for Fatigue Crack Propagation". Fatigue Crack Growth Threshold Concepts, D.L. Davidson and S. Suresh, Eds., The Metallurgical Society of the AIME, Warrendale, PA, 1984, pp 517-530.

61. Newman, J.C., Jr., "A Crack Opening Stress Equation for Fatigue Crack Growth". International Journal of Fracture, Vol 24, 1984, pp R131-R135.

62. Kanninen, M.F. and Popelar, C.H. Advanced Fracture Mechanics, Oxford University Press, New York, 1985, p 507.

63. Bodner, S.R. Review of a Unified Elastic-Viscoplastic Theory (The Bodner Equations). Interim Scientific Report. Grant Number: AFOSR-84-0042. Air Force Office of Scientific Research/NA. Bolling AFB, D.C. October, 1984.

64. Bodner, S.R. "Evolution Equations for Anisotropic Hardening and Damage of Elastic-Viscoplastic Materials". Symposium on Solid Mechanics. Udine, Italy. June, 1983.

65. Bodner, S.R. and Partom, Y. "Constituitive Equations for Elastic-Viscoplastic Strain-Hardening Materials". _Journal of Applied Mechanics_, Vol 42: 385-389 (1975).

66. Bohun, M.H. and Palazotto, A.N. "Comparisons of Viscoplastic Flow Laws". _Journal of Engineering Fracture Mechanics_, Vol 21, No 3: 503-519 (1985).

67. Wilson, R.E. and Palazotto, A.N. "Viscoplastic Fatigue in a Superalloy at Elevated Temperatures Considering a Zero Mean Stress". AIAA/ASME/ASCE/AHS 25th Structures, Structural Dynamics and Materials Conference. Palm Springs, CA. May 14-16, 1984.

68. Henkel, C.L. _Crack Closure Characteristics Considering Center Cracked and Compact Tension Specimens_. Master of Science Thesis. AFIT/GAE/AA/84D-9. Air Force Institute of Technology. WPAFB, Ohio. December, 1984.

69. Smail, J. and Palazotto, A.N. "The Viscoplastic Crack Growth Behavior of a Compact Tension Specimen Using the Bodner-Partom Flow Law". _Engineering Fracture Mechanics_, Vol 19, No 1: 137-158 (1984).

70. Wilson, R.E. and Palazotto, A.N. "Viscoplasticity in a Superalloy at Elevated Temperatures Considering Tension and Compressive Loading". _Engineering Fracture Mechanics_, Vol 22, No 6: 927-937 (1985).

71. Hinnerichs, T. _Viscoplastic and Creep Crack Growth Analysis by the Finite Element Method_. AFWAL-TR-80-4140. AFWAL Materials Laboratory, WPAFB, Ohio. July, 1981.

72. Beaman, R.L. _The Determination of the Bodner Coefficients for IN-718 and Their Effects on Cyclic Loading_. Master of Science Thesis. AFIT/GAE/AA/84M-1. Air Force Institute of Technology. WPAFB, Ohio. March, 1984.

73. Mercer, J.G. _Viscoplastic Analysis of Fatigue Cracks at Notches by the Finite Element Method_. Dissertation Submitted to the Department of Aeronautics and Astronautics, Air Force Institute of Technology in Partial Fulfillment of the Requirements for the Degree of Doctor of Philosophy, AFIT/DS/AA/86-2, 1986.

74. Stouffer, D.C. _A Constituitive Representation for IN-100_. AFWAL-TR-81-4039. Materials Laboratory. Air Force Wright Aeronautical Laboratory. WPAFB, Ohio. June, 1981.

75. Hinnerichs, T.D., Palazotto, A.N., and Nicholas, T. "Evaluation of Creep Crack Growth Criteria for IN-100 at Elevated Temperature". *AIAA Journal*. Vol 21, No 3: 438-445. March, 1983.

76. Hinnerichs, T., Nicholas, T., and Palazotto, A. "A Hybrid Experimental-Numerical Procedure for Determining Creep Crack Growth Rates". *Engineering Fracture Mechanics*, Vol 16, No 2: 265-277 (1982).

77. Hinnerichs, T., Palazotto, A.N., and Nicholas, T. "Application of a Numerical Procedure to Creep Crack Growth from Displacement Measurements in IN100". *Fracture Mechanics: Fourteenth Symposium - Vol II: Testing and Applications*. ASTM STP 791. American Society for Testing and Materials: II-166 - II-181 (1983).

78. Bar-Tikva, D., Grandt, A.F., and Palazotto, A.N. "An Experimental Weight Function for Stress-Intensity-Factor Calibrations". *Experimental Mechanics*. Vol 21, No 10: 371-378 (October 1981).

79. Broek, D. *Elementary Engineering Fracture Mechanics*. Martinus Nijhoff Publishers. Hingham, MA. 1983.

80. Rolfe, S.T. and Barsom, J.M. *Fracture and Fatigue Control in Structures - Applications of Fracture Mechanics*. Prentice-Hall Inc. Englewood Cliffs, NJ. 1977.

Appendix A: Determination of Bodner Constants for TI-6246

The constants used in the Bodner model are both material and temperature dependent and must therefore be evaluated for each material at the specific temperature of interest. Material constants for TI-6246 at room temperature have not been previously determined and must therefore be evaluated for use in this research effort. The procedure for evaluating the Bodner constants developed by Beaman [72], which built upon the works of Stouffer [74], is used in conjunction with experimental stress/strain data provided by the WRDC Materials Laboratory (Figure 2.1).

An initial assumption is the absence of thermal recovery of work hardening. The governing equation for determining the rate of work hardening,

$$\dot{Z} = m(Z_1 - Z)\sigma\dot{\epsilon}^p - AZ_1[(Z-Z_2)/Z_1]^r \tag{A.1}$$

can be written as

$$dZ = m(Z_1 - Z)dW_p \tag{A.2}$$

This equation is then integrated using the initial condition that $Z = Z_0$ at $W_p = 0$ to obtain

$$dZ/(Z_1 - Z) = mdW_p \tag{A.3}$$

$$\ln(Z_1 - Z) = \ln(Z_1 - Z_0) - mW_p \tag{A.4}$$

Appropriate strain rate data, graphed as $\ln(Z_1 - Z)$ versus W_p is then linearly approximated to obtain values of m (slope) and Z_0 (y-intercept).

158

The data used in this procedure was taken from the experimental stress-strain curve provided. The elastic modulus, E, is a reliable description of the material's elastic behavior and values of stress, strain, and strain plus 'offset' strain were determined from the experimental data and deviations from a plot of the elastic modulus. In order to calculate the plastic work, W_p, plastic strains were first derived from the total strains. This was accomplished using Hooke's Law to derive the plastic strains by

$$\epsilon^P = \epsilon - \sigma/E \qquad (A.5)$$

Using the values obtained here, the plastic work, W_p, was computed using the general form

$$W_p^n = W_p^{n-1} + \sigma^{n-1}(\epsilon^{P(n)} - \epsilon^{P(n-1)}) +$$

$$((\epsilon^{P(n)} - \epsilon^{P(n-1)})(\sigma^n - \sigma^{n-1}))/2 \qquad (A.6)$$

The x-coordinates of Equation (A.4) were thereby determined.

Evaluation of the y-coordinates begins with the evaluation of

$$Z = \sigma\left[(2n/(n+1))\ln(2D_0/\sqrt{3}\dot{\epsilon}^P)\right]^{n/2} \qquad (A.7)$$

which requires knowledge of the plastic strain rates. This was accomplished using

$$\dot{\epsilon}^e = \dot{\sigma}/E = \Delta\sigma/\Delta tE \qquad (A.8)$$

where $\dot{\epsilon} = \dot{\epsilon}^e + \dot{\epsilon}^P$ and $\dot{\epsilon} = 1.3 \times 10^{-5}$ in/sec. Since the experimental total strain rate is held constant, the time between data points can be computed using the change in total strain. Values for the plastic

159

strain rates are then computed over subsequent data point intervals.

In this procedure, D_0 was assumed to be 10^4 sec and the values of n and Z_1 were estimated using

$$\ln(-\ln(\sqrt{3}\dot{\epsilon}^P/2D_0)) = -2n\ln\sigma + (2n\ln Z_1 + \ln((n+1)/2n) \qquad (A.9)$$

The linear relationship between $\ln(-\ln(\sqrt{3}\dot{\epsilon}^P/2D_0))$ and $\ln\sigma$ permits the determination of n, and subsequently Z_1. Since only one set of stress-strain data was available, the values obtained were only approximations of the actual material values. Using this initial value of n, subsequent values were taken in the vicinity of this first approximation and corresponding values of Z_1 evaluated. Employing these values, subsequent evaluations of Equation A.7 led to several associated values of Z and $\ln(Z_1-Z)$.

At this point a two-element finite element model employing the above estimated values was used to evaluate the Bodner constants. Since it was assumed that there was no thermal recovery present, the values of Z_2, A, and r were set equal to zero. Additionally, D_0 was assumed to be 10^4 sec. The value of n was varied within a region near the approximated value determined above and a resulting value of Z_1 obtained. Using these two values, the constants m and Z_0 were evaluated. This procedure was repeated until the set of Bodner constants resulted in stress-strain data which resembled the experimental data as nearly as possible. These resultant constants are shown in Table 2.2 and the subsequent stress-strain curve in Figure 2.1.

The set of Bodner constants evaluated in this manner is only an approximation of the actual material values. The accurate determination of these coefficients requires, as a minimum, several experimental

stress-strain curves at high strain rates with no thermal recovery, and several data points involving lower strain rates [72]. The values of the coefficients determined above are highly subjective. As indicated, however, they produce a satisfactory representation of the experimentation provided.

Appendix B: Visco II Program Modifications

The finite element code, Visco II, is a modification of the program developed by Hinnerichs [71] in order to satisfy the requirements of this research. These changes, although important to this study, do not interfere with the computational procedures of the Bodner-Partom Viscoplastic Flow Law and the various solution techniques such as the Residual Force Method and the Gauss-Siedel iterative algorithm. The modified program has been verified by re-analyzing several cases previously studied by Henkel [68] and by comparisons with works by Mercer [73]. The modifications that are presented here are the data storage/restart capability and the crack closure algorithm.

The computer code involved in the data storage/restart capability is presented in Figure B.1. This procedure requires the input of the variable NCONT (00037) which indicates if data will be stored at the completion of a given analysis and whether or not this particular analysis is a continuation of a previous computer run (0 - not used, 1 = data storage only, 2 - both data storage and program restart required). If the computer analysis is exercising the restart capability, the input data is read from storage (00042-00083). New values of TMAX and STOPCY (00039-00041) must additionally be input at this point to place time limits on the current analysis. If, at the end of the current run, data will be stored for future use, then this is accomplished after the current analysis is complete (00371-00412).

The procedure shown here has been verified by duplicating Henkel's results [68] for a center cracked panel under load conditions of K_I - 45 KSI-IN$^{1/2}$ and R - -1.0

```
00034C        READ AND PRINT OF DATA
00035C
00036         WRITE(6,99)
00037         READ(5,*)NCONT
00038         IF((NCONT.EQ.0).OR.(NCONT.EQ.1)) GO TO 810
00039         READ(5,*)TMAX,STOPCY
00040         PRINT(6,*)"NEW MAX TIME = ",TMAX
00041 -       PRINT(6,*)"NEW STOP CYCLE = ",STOPCY
00042         READ(1,*)NDATA,MESHE,MESHN,MESHOLD,SCAL,MPRINT
00043         READ(1,*)PS,MAT,DZ2,EN,Z1,Z0,ZI,EMO,RN,AC
00044         READ(1,*)NUMBC,NCPIN,NOPIN,NCYCM,TOLER,XFAC
00045 -       READ(1,*)VP,YIELD,HP,VC,ALPHA,RAM,BERG,DTMAX,TPRINT,TPLOT
00046         READ(1,*)NC,PMAX,PO,PERIOD,TSTRESS,TEPS,VM,PE,SLOPEA
00047         READ(1,*)NF,FRATE,ACDE,OPE,CEPT,RT,CONV,ICRR,DTINIT
00048         READ(1,*)ICR,JPATH,T,TP,NUMEL,NUMNP,CJINT,DOT,DT,PI,PP,NN,TPL
00049         READ(1,*)(LM(I),I=1,3)
00050         READ(1,*)(AREA(I),I=1,NUMEL)
00051         READ(1,*)(NPI(I),NPJ(I),NPK(I),I=1,NUMEL)
00052         READ(1,*)(SIGXX(I),SIGXY(I),SIGYY(I),SIGZZ(I),I=1,NUMEL)
00053         READ(1,*)(DSIGXX(I),DSIGXY(I),DSIGYY(I),DSIGZZ(I),I=1,NUMEL)
00054         READ(1,*)(DX(I),DY(I),DXY(I),DZ(I),I=1,NUMEL)
00055         READ(1,*)(WPP(I),WPC(I),WPE(I),ET(I),XU(I),TH(I),I=1,NUMEL)
00056         READ(1,*)(EVPX(I),EVPY(I),EVPXY(I),EVPZ(I),I=1,NUMEL)
00057         READ(1,*)(EPEFF(I),DPEFF(I),I=1,NUMEL)
00058         READ(1,*)(NPB(I),NFIX(I),SLOPE(I),I=1,NUMBC)
00059         READ(1,*)(DSX(I),DSY(I),XLOAD(I),YLOAD(I),NAP(I),I=1,NUMNP)
00060         READ(1,*)(XORD(I),YORD(I),DXDT(I),DYDT(I),I=1,NUMNP)
00061         READ(1,*)(FX(I),FY(I),NFA(I),NFN(I),I=1,NF)
00062         READ(1,*)(SXXC(I),SXYC(I),SYXC(I),SYYC(I),TCRACK(I),
00063        1VLOD(I),I=1,29)
00064         DO 820 J=1,9
00065         READ(1,*)(SXX(I,J),SXY(I,J),SYX(I,J),SYY(I,J),I=1,NUMNP)
00066         READ(1,*)(NP(I,J),I=1,NUMNP)
00067 820     CONTINUE
00068         DO 830 J=1,10
00069         READ(1,*)JEL(J)
00070         READ(1,*)(JN(J,I),XN(J,I),YN(J,I),I=1,13)
00071 830     CONTINUE
00072         IF(ICR.EQ.0) GO TO 845
00073         DO 840 J=1,4
00074         READ(1,*)(NCR(I,J),I=1,ICR)
00075 840     CONTINUE
00076 845     READ(1,*)CTOL,NCLC
00077         IF (NCLC.EQ.0) GO TO 847
00078         DO 846 I=1,NCLC
00079 846     READ(1,*)(NCLOS(I,J),J=1,5)
00080 847     CONTINUE
00081         DO 850 J=1,6
00082         READ(1,*)(B(I,J),D(I,J),S(I,J),I=1,6)
00083 850     CONTINUE
00084         CALL OUTPUT(NUMEL,NUMNP,T,DT,NN,PP)
00085         GO TO 300
00086 810     CONTINUE
```

Figure B.1

Visco II - Data Storage/Restart

163

```
00370          IF(NCONT.EQ.0) GO TO 890
00371      .   WRITE(2,*)NJATA,MESHE,MESHN,MESHOLD,SCAL,MPRINT
00372          WRITE(2,*)PS,MAT,D22,EN,Z1,ZS,ZI,EMJ,RN,AC
00373      .   WRITE(2,*)NUMBC,NCPIN,NOPIN,NCVCM,TOLER,XFAC
00374          WRITE(2,*)VP,YIELD,HP,VC,ALPHA,RAM,BERG,DTMAX,TPRINT,TPLOT
00375          WRITE(2,*)NC,PMAX,PO,PERIOD,TSTRESS,TEPS,VM,PE,SLOPEA
00376          WRITE(2,*)NF,FRATE,NJDE,OPE,CEPT,RT,CONV,ICRR,DTINIT
00377      --  WRITE(2,*)ICR,JPATH,T,TP,NUMEL,NUMNP,CJINT,DDT,DT,PI,PP,NN,TPL
00378          WRITE(2,*)(LM(I),I=1,3)
00379          WRITE(2,*)(AREA(I),I=1,NUMEL)
00380          WRITE(2,*)(NPI(I),NPJ(I),NPK(I),I=1,NUMEL)
00381          WRITE(2,*)(SIGXX(I),SIGXY(I),SIGYY(I),SIGZZ(I),I=1,NUMEL)
00382          WRITE(2,*)(DSIGXX(I),DSIGXY(I),DSIGYY(I),DSIGZZ(I),I=1,NUMEL)
00383          WRITE(2,*)(DX(I),DY(I),DXY(I),DZ(I),I=1,NUMEL)
00384          WRITE(2,*)(WPP(I),WPC(I),WPE(I),ET(I),XU(I),TH(I),I=1,NUMEL)
00385          WRITE(2,*)(EVPX(I),EVPY(I),EVPXY(I),EVPZ(I),I=1,NUMEL)
00386          WRITE(2,*)(EPEFF(I),DPEFF(I),I=1,NUMEL)
00387          WRITE(2,*)(NPB(I),NFIX(I),SLOPE(I),I=1,NUMBC)
00388          WRITE(2,*)(DSX(I),DSY(I),XLOAD(I),YLOAD(I),NAP(I),I=1,NUMNP)
00389          WRITE(2,*)(XORD(I),YORD(I),DXDT(I),DYDT(I),I=1,NUMNP)
00390          WRITE(2,*)(FX(I),FY(I),NFA(I),NFN(I),I=1,NF)
00391          WRITE(2,*)(SXXC(I),SXYC(I),SYXC(I),SYYC(I),TCRACK(I),
00392       1YLOJ(I),I=1,29)
00393          DO 870 J=1,9
00394          WRITE(2,*)(SXX(I,J),SXY(I,J),SYX(I,J),SYY(I,J),I=1,NUMNP)
00395          WRITE(2,*)(NP(I,J),I=1,NUMNP)
00396  870    CONTINUE
00397          DO 875 J=1,10
00398          WRITE(2,*)JEL(J)
00399          WRITE(2,*)(JN(J,I),XN(J,I),YN(J,I),I=1,13)
00400  875    CONTINUE
00401          IF(ICR.EQ.0) GO TO 882
00402          DO 880 J=1,4
00403          WRITE(2,*)(NCR(I,J),I=1,ICR)
00404  880    CONTINUE
00405  882    WRITE(2,*)CTOL,NCLC
00406          IF (NCLO.EQ.0)GO TO 884
00407          DO 883 I=1,NCLO
00408  883    WRITE(2,*)(NCLCS(I,J),J=1,5)
00409  884    CONTINUE
00410          DO 885 J=1,6
00411          WRITE(2,*)(B(I,J),D(I,J),S(I,J),I=1,6)
00412  885    CONTINUE
00413  890    CONTINUE
00414          END
```

Figure B.1 (cont)

Visco II - Data Storage/Restart

The crack closure algorithm developed in this computer code is divided into two parts and these are presented in Figure B.2. The first of these is the input data (00171-00179) which includes the closure tolerance (CTOL), the number of nodes that will be checked for closure (NCLO), and a matrix (NCLOS(N,J)) identifying the specific nodes of interest and the surrounding elements.

The second portion of the closure modification is the additional set of computer statements within the equilibrium solution. In lines 00808 to 00814 the nodes identified are checked for negative displacements. If negative displacements have occurred, they are reset to zero and resultant closure loads are calculated (00846-00881). Convergence of the closure loads is checked in lines 00882-00885. If the difference in closure loads is within the closure tolerance, CTOL, then the analysis continues. If not, the program reinitiates the equilibrium solution and subsequent recalculation of closure loads based upon a new set of nodal displacements.

As previously stated, these algorithms have been verified through comparisons with other works. The results obtained using the above procedures agreed well with Mercer [73] when analyzing a 35 KSI-IN$^{1/2}$ loaded center cracked panel. Additionally, an analysis of a 45 KSI-IN$^{1/2}$ loaded center cracked panel agreed with the results obtained by Henkel [68]. In both cases, the use of the above algorithm significantly reduced the residual forces in the equilibrium solutions.

```
00148          READ (5,*)ICR,TCRACK(1)
00149          PRINT (6,*)"THE NUMBER OF NODES TO BE CRACKED=",ICR
00150          IF (ICR .EQ. 0)GO TO 940
00151          DO 2000 I=1,ICR
00152          READ (5,*)(NCR(I,K),K=1,4)
00153 2000 PRINT (6,*)(NCR(I,K),K=1,4)
00154          READ(5,*)(TCRACK(I),I=1,ICR)
00155          DO 930 I=1,ICR
00156          PRINT(6,*)"NODE   ",NCR(I,1),"POPS AT TIME    ",TCRACK(I)
00157 930  CONTINUE
00158 940  CONTINUE
00159          READ (5,*)JPATH
00160          PRINT(6,*)"NUMBER OF J INTEGRAL PATHS=",JPATH
00161          IF (JPATH .EQ. 0)GO TO   910
00162          DO 900 I=1,JPATH
00163          READ (5,*)JEL(I)
00164          PRINT (6,*)"NUMBER OF ELEMENTS IN PATH",I,"EQUALS",JEL(I)
00165          M=JEL(I)
00166          READ (5,120)(JN(I,K),XN(I,K),YN(I,K),K=1,M)
00167 120  FORMAT (I5,2E10.2)
00168          DO 905 K=1,M
00169 905  PRINT (6,*)"JN=",JN(I,K)," XN= ",XN(I,K)," YN= ",YN(I,K)
00170 900  CONTINUE
00171 910  READ(5,*)CTOL,NCLO
00172          PRINT(6,*)"CLOSURE TOLERANCE= ",CTOL
00173          PRINT(6,*)"NODES ALONG CRACK= ",NCLO
00174          IF(NCLO.EQ.0) GO TO 925
00175          DO 920 N=1,NCLO
00176          READ(5,*)(NCLOS(N,J),J=1,5)
00177 920  PRINT(6,*)"NODE= ",NCLOS(N,1),"   ELEMENTS ARE: ",NCLOS(N,3),
00178       1" ",NCLOS(N,4)," ",NCLOS(N,5)
00179 925  CONTINUE
00180 C
```

Figure B.2

Visco II - Closure Algorithm

```
00777 ·      DIMENSION B(6,6),D(6,6)
00778        ICLOS=0
00779 ··     DO 100 N=1,NUMNP
00780        PLOAD(1,N)=0.
00781        PLOAD(2,N)=0.
00782 100    PLOAD(3,N)=0.
00783 105    DDT=DT
00784        NPRINT=0
00785 ·      NUMPT=NCPIN
00786        NUMOPT=NOPIN
00787        NCYCLE=0
00788        RTF=PI+T*FRATE
00789        IF(RTF .LT. 1.)FTOLER=RTF*TOLER
00790        IF(RTF .GE. 1.)FTOLER=TOLER
00791 327    SUM=0.
00792        INTTC=0
00793        DO 290 M=1,NUMNP
00794        NUM=NAP(M)
00795        IF (NUM .EQ. 1)PRINT (6,*)"NODE POINT  ",M," IS UNCONNECTED "
00796        IF(SXX(M,1)+SYY(M,1))275,290,275
00797 275    FRX=XLOAD(M)  -- ···
00798        FRY=YLOAD(M)-PLOAD(2,M)
00799        DO 280 L=2,NUM
00800        N=NP(M,L)
00801        FRX=FRX-SXX(M,L)*DSX(N)-SXY(M,L)*DSY(N)
00802 280    FRY=FRY-SYX(M,L)*DSX(N)-SYY(M,L)*DSY(N)
00803        DX=SXX(M,1)*FRX+SXY(M,1)*FRY-DSX(M)
00804        DY=SYX(M,1)*FRX+SYY(M,1)*FRY-DSY(M)
00805        IF(PLOAD(1,M).GT.0.)DY=0.
00806        DSX(M)=DSX(M)+XFAC*DX
00807        DSY(M)=DSY(M)+XFAC*DY
00808        IF (PLOAD(1,M).GT.0.) DSY(M)=0.
00809        DO 65 INTT=192,215
00810        IF(DSY(INTT).GE.0.)GO TO 65
00811        DSY(INTT)=0.
00812        INTTC=1
00813        PLOAD(1,INTT)=1.
00814 65     CONTINUE
00815 10     IF (SYY(M,1))20,40,20
00816 20     IF (SYY(M,1))285,30,285
00817 30     SUM=SUM+ABS(DX/SXX(M,1))
00818        GO TO 290
00819 40     SUM=SUM+ABS(DY/SYY(M,1))
00820        GO TO 290
00821 285    SUM=SUM+ABS(DX/SXX(M,1))+ABS(DY/SYY(M,1))    — ···· ·· ·
00822 290    CONTINUE
```

Figure B.2 (cont)

Visco II - Closure Algorithm

167

```
00846C          DETERMINATION OF CLOSED NODAL LOADS
00847C
00848           ITER=0
00849           ICLOS=1
00850           DO 195 M=1,NUMNP
00851           IF (PLOAD(1,M).EQ.0.)GO TO 195
00852           PLOAD(3,M)=0.
00853           DO 140 N=1,NCLO
00854           IF (NCLOS(N,1).EQ.M)L=N
00855 140       CONTINUE
00856           LN=NCLOS(L,2)+2
00857           DO 150 N=3,LN
00858           I=NPI(NCLOS(L,N))
00859           J=NPJ(NCLOS(L,N))
00860           K=NPK(NCLOS(L,N))
00861           CALL BMATRIX(NCLOS(L,N),B)
00862           EPX=B(1,1)*DSX(I)+B(1,3)*DSX(J)+B(1,5)*DSX(K)
00863           EPY=B(2,2)*DSY(I)+B(2,4)*DSY(J)+B(2,6)*DSY(K)
00864           GAM=B(3,1)*DSX(I)+B(3,2)*DSY(I)+B(3,3)*DSX(J)
00865          1+B(3,4)*DSY(J)+B(3,5)*DSX(K)+B(3,6)*DSY(K)
00866           CALL DMATRIX(NCLOS(L,N),D)
00867           EPXX=EPX-EVPX(NCLOS(L,N))
00868           EPYY=EPY-EVPY(NCLOS(L,N))
00869           GAMM=GAM-EVPXY(NCLOS(L,N))
00870           X=D(1,1)*EPXX+D(1,2)*EPYY
00871           Y=D(2,1)*EPXX+D(2,2)*EPYY
00872           XY=D(3,3)*GAMM
00873           IF(I.EQ.M)GO TO 160
00874           IF(J.EQ.M)GO TO 165
00875           IF(K.EQ.M)GO TO 170
00876 160       PLOAD(3,M)=PLOAD(3,M)+B(1,2)*X+B(2,2)*Y+B(3,2)*XY
00877           GO TO 175
00878 165       PLOAD(3,M)=PLOAD(3,M)+B(1,4)*X+B(2,4)*Y+B(3,4)*XY
00879           GO TO 175
00880 170       PLOAD(3,M)=PLOAD(3,M)+B(1,6)*X+B(2,6)*Y+B(3,6)*XY
00881 175       CONTINUE
00882 150       CONTINUE
00883           IF(PLOAD(2,M).EQ.0.)PLOAD(2,M)=.01
00884           DIFF=ABS((PLOAD(3,M)-PLOAD(2,M))/PLOAD(2,M))
00885           IF(DIFF.GT.CTOL)ITER=1
00886 195       CONTINUE
00887 196       CONTINUE
00888           IF(ITER.EQ.0)GO TO 200
00889           DO 185 M=1,NUMNP
00890 185       PLOAD(2,M)=PLOAD(3,M)
00891           GO TO 105
00892 200       DO 210 M=1,NUMNP
00893           IF (PLOAD(1,M).EQ.0.)GO TO 205
00894           PRINT(6,*)M,"  ",PLOAD(3,M)
00895 205       CONTINUE
00896 210       CONTINUE
00897           RETURN
00898           END
```

Figure B.2 (cont)

Visco II - Closure Algorithm

Eugene J. Bednarz ████████████████████████████████████
████████████████ He graduated from Chicopee Comprehensive High School in
June 1970. He then attended the United States Air Force Academy at
Colorado Springs, Colorado. In 1974, he graduated with a B.S. degree
in Engineering Mechanics and was commissioned as a Second Lieutenant in
the U.S. Air Force. He was assigned to the 351st Strategic Missile
Wing at Whiteman AFB, Missouri and served as a Missile Combat Crew
Commander (MCCC) and as an Instructor MCCC for the Minuteman II
Modernized weapon system. During this time, he earned an M.B.A. degree
degree from the University of Missouri at Columbia through the
Minuteman Education program. In 1980, he was assigned to the 544th
Intelligence Analysis Squadron, HQ Strategic Air Command, Offutt AFB,
Nebraska. Here he performed duties as an intelligence analyst for
antiballistic missile systems and served as Chief, Technology Section.
In June 1981, he entered the Air Force Institute of Technology, School
of Engineering. He graduated in December 1982 with a Master of Science
degree in Systems Engineering and remained at the School of Engineering
to pursue a doctorate in Aeronautical Engineering. He is currently
assigned to the Air Force Weapons Laboratory, Kirtland AFB, New Mexico.